This is to certify that the
dissertation entitled

ELECTRONICALLY INDUCED STRUCTURE TRANSFORMATIONS IN GRAPHITE & SILVER, STUDIED USING ULTRAFAST ELECTRON CRYSTALLOGRAPHY

presented by

RAMANI K. RAMAN

has been accepted towards fulfillment
of the requirements for the

Ph.D. degree in Physics

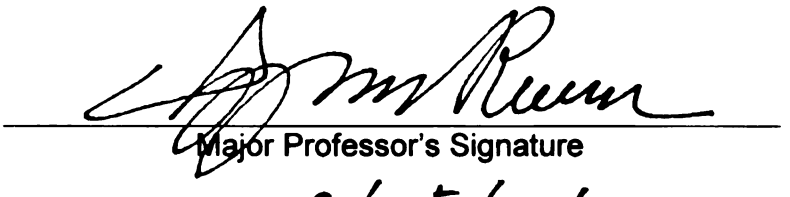

Major Professor's Signature

08/25/2010

Date

ELECTRONICALLY INDUCED STRUCTURE TRANSFORMATIONS IN GRAPHITE & SILVER, STUDIED USING ULTRAFAST ELECTRON CRYSTALLOGRAPHY

By

Ramani K. Raman

A DISSERTATION

Submitted to
Michigan State University
in partial fulfillment of the requirements
for the degree of

DOCTOR OF PHILOSOPHY

Physics

2010

ABSTRACT

ELECTRONICALLY INDUCED STRUCTURE TRANSFORMATIONS IN GRAPHITE & SILVER, STUDIED USING ULTRAFAST ELECTRON CRYSTALLOGRAPHY

By

Ramani K. Raman

Electronically induced structure transformations are a unique class of phenomena in which material transformation can be effected by impulsive excitation of the electronic system, often resulting in exotic structural phases and transformation pathways inaccessible to thermodynamic channels. Using ultrafast electron crystallography (UEC), we have directly observed such photodinduced atomic dynamics in two systems - graphite and silver nanocrystals (Ag NC) that appear to be driven by the strong coupling between the laser excitation and lattice perturbations in the form of strongly coupled optical phonons and laser induced electron redistribution.

In graphite, structural changes resulting from photoexcitation with p-polarized, near-IR, femtosecond laser pulses are observed to lead to the nonthermal creation of a transient state with sp^3 like bonding characteristics. At laser fluences approaching, but below the damage threshold, the average inter-layer spacing contracts along with creation of new inter-layer distances at $\approx$ 2 Å while the lattice is only moderately heated. The advantage of using electrons (which carry a charge) as a probe is demonstrated, as it reveals the transformation to be driven by a hitherto unobserved surface dipole field, observed here via a Coulomb refraction shift of the scattered electrons within the sub-surface region. *Ab initio* density functional theory calculations are employed to relate these structural changes to a nonthermal heating of the electrons, followed by a photoinduced charge separation causing a compressive Coulomb stress.

To quantify the role and dynamics of electrons emitted from photoexcited surfaces, a novel 'point-projection method' is introduced, capable of directly imaging

the spatiotemporal evolution of such photoemitted electron bunches. The method is shown to provide sufficient sensitivity to image electron bunches (as small as 10^{10} e/cm^3) and permit quantitative investigation of the electron emission from photoexcited graphite surface. It is shown that such photoemission plays a minor role in the refraction shifts observed in the UEC study and a sub-surface dipole field is sufficient to explain the structural and charge relaxations observed. Investigations utilizing scanning electron microscope imaging of structures generated from laser ablation of graphite reveals the creation of geometrically faceted crystalline features, whose Raman spectrum exhibit sp^3 like characteristics, though unambiguous identification of diamond structures generated requires further study.

In the case of silver nanocrystals (Ag NC), photoexcitation near the surface plasmon resonance (SPR) is observed to lead to fragmentation at fluences below their melting threshold. By isolating each NC from other neighboring NCs in a surface supported geometry, the normally irreversible process becomes reversible and amenable to multi-shot pump-probe diffraction investigations just below the fragmentation threshold. Transient structural, thermal and Coulombic signatures of the pre-fragmented state are extracted from the UEC investigation and combined with a *progressive* Reverse Monte-Carlo structure refinement scheme to visualize the atomic dynamics leading up to the fragmentation. Such multi-faceted analysis reveals the fragmentation to proceed through the creation and growth of undercoordinated defect sites along which the lattice is weakened. These defects are likely seeded by the strong coupling between SPR dephasing pathways and inter-band transitions that can lead to bond-softening effects and local valence instabilities. The creation of sufficient number of such defect sites at elevated fluences are believed to lead to the eventual fragmentation of the entire NC.

This thesis also details the design and principle of UEC systems employed in a surface probing geometry for the study of nanostructures and interfaces.

To *Amma, Appa and my 'Jaan'*

ACKNOWLEDGMENT

The work presented here is truly collaborative in nature and would not have been possible without the help of many individuals. First and foremost, I would like to thank my adviser Prof. Chong-Yu Ruan for his guidance, support and gentle rebukes at times when I strayed too far off course. I have learned a great deal from him about how to 'do' science and realized the need to have the courage to dream big.

In Ryan Murdick and Yoshie Murooka, I was fortunate to find fantastic lab colleagues, and the genial camaraderie we shared made working in and building up the lab a joy. They have had their hands in many experiments in too many diverse capacities to list individually. My grad school experience would not have been half as enjoyable without Ryan. I thank him for all his help both inside the lab and outside of it. We will always be buddy.

To Prof. Bhanu Mahanti for the support and guidance he extended in his capacity as graduate chair and mentor throughout my stay here at MSU and also to Prof. Norman Birge for being a great mentor while I was a teaching assistant.

I acknowledge my colleagues and collaborators who have contributed in various measures to the results reported here. Thanks to Prof. Tománek, Teng Yang and Savas Berber for the DFT calculations on photoexcited graphite and the extensive discussions during the preparation of the manuscript. Aric Pell performed the calculations to optimize the pole-piece geometry for the improved 2^{nd} generation proximity coupled femtosecond electron gun presented here. Richard Worhatch had an extensive hand in the Reverse Monte-Carlo refinement of silver nanocrystal data. Prof. Lawrence Drzal and Sanjib Biswas provided the graphene nanoplatelets samples used in the UEC investigations and laser ablation studies reported here. Thanks to Zhensheng Tao for his contributions in the analysis of vacuum space charge imaging data and to Terry Han for assisting in various experiments in the final years.

The machine shop staff Tom Palazzolo, Tom Hudson, Jim Muns and Rob Bennett

were instrumental (no pun intended) in the design of many precision miniature components fabricated for the UEC system, all of which would not have been possible without their skill and patience. Reza Loloee and Baokang Bi helped me in great measure to utilize the various experimental facilities in the basement while Xudong Fan at the MSU Center for Electron Microscopy was extremely patient while introducing me to the TEM. Thanks are also due to Cathy Cords and Debbie Barratt for their fantastic administrative support throughout. Finally, a note of thanks to Prof. Clifford Weil in the MSU math department, whose LaTeX thesis template was of immense help in the preparation of this manuscript.

On the personal front, I have been fortunate to befriend some genuine individuals who have made my stay at MSU cherished. Hersh Sisodia, Apar Maniar, Dipti Jain, Archana Basu and Amy Murdick - thanks for all the great times and wonderful memories.

Finally, I would not, and could not have undertaken this arduous journey without the constant support and unconditional love from my parents. It is to them that I owe my being. Last, but by no means the least, a huge thanks to my wife Shivani for her support and unflinching faith in my abilities when I had little in them myself.

I am humbled and grateful to have worked alongside such fantastic mentors, colleagues and friends, and leave MSU with the fondest of memories. Thank you to one and all.

TABLE OF CONTENTS

List of Tables x

List of Figures xi

1 Introduction **1**
1.1 Electronically Induced Structure Transformation 3
1.2 Ultrafast Laser-Matter Interaction 4
1.2.1 The Pump-Probe Paradigm 6
1.3 Non-Thermal Melting in Semiconductors 8
1.4 Ultrafast Solid-Solid Phase Transformations 14
1.5 Graphite-Diamond Transition 18
1.5.1 Thermodynamic Pathways 19
1.5.2 Electronically Induced Diamondization 21
1.6 Photoinduced Fragmentation of Silver Nanocrystals 24
1.7 Summary 26

2 Diffraction Theory & Data Reduction Procedures **28**
2.1 Diffraction Basics 28
2.1.1 Scattering & Momentum Transfer 30
2.1.2 Scattering from a 1-D Lattice - the Laue Function 32
2.1.3 Equivalence of Laue Function Formalism and Bragg Law . . . 36
2.1.4 Reciprocal Space & The Ewald Construction 37
2.1.5 Diffraction From Lattice With Basis - Form Factor & Structure Factor 41
2.2 Diffraction Data Extraction & Analysis 45
2.2.1 Data Reduction: Surface Supported Nanocrystals 46
2.2.2 Data Reduction: Graphite 50

3 Experimental Apparatus - Design & Development **54**
3.1 The Laser System 58
3.2 The Ultra High Vacuum Chamber 60
3.2.1 UHV Chamber Instrumentation 60
3.2.2 Chamber Pumping Schematics 62
3.3 Proximity Coupled Pulsed Electron Gun 64
3.4 5-Axis Cryogenic Sample Holder 68
3.4.1 Overall Design 69
3.4.2 Sample Stage Construction 71
3.4.3 Sample Docking & Rotation 73

3.5 Pump-Probe Alignment . . . 75
3.6 Diffraction Acquisition System . . . 79
3.6.1 Intensified CCD Camera . . . 79
3.6.2 Time-Gated Data Acquisition . . . 81
3.7 Optical Experiment Station . . . 83
3.7.1 Detection System . . . 85
3.7.2 Optical Pump-Probe Alignment . . . 87
3.7.3 Choice Of Detector: Photodiode Or PMT? . . . 89

4 Ultrafast Dynamics Of Graphite At Near-IR Photoexcitation . . 94
4.1 Experimental Details . . . 95
4.2 Ground State Characterization . . . 96
4.2.1 Why Surface Diffraction is not RHEED . . . 98
4.3 Time-Resolved Raw Diffraction Data . . . 101
4.4 Coulomb Refraction . . . 104
4.5 Fourier Phasing Technique . . . 107
4.6 HOPG Structural Dynamics . . . 109
4.6.1 Low Fluence Response . . . 109
4.6.2 High Fluence Response . . . 112
4.6.3 Observation Of Transient sp^3-Bonds in Graphite . . . 113
4.6.4 Density Functional Theory Calculations . . . 117
4.7 Role Of Surface Charge: Photoemission Imaging Study . . . 120
4.7.1 The Point-Projection Imaging Technique . . . 121
4.7.2 Imaging VSC Cloud Over HOPG Surface . . . 123
4.7.3 Qualitative Analysis Of Shadow Image Data . . . 126
4.7.4 Quantitative Analysis: VSC Cloud Dynamics . . . 129
4.8 Optical Investigation of HOPG . . . 135
4.9 Summary . . . 138

5 Further investigations of Graphite-Diamond Transition . . . 140
5.1 Pulsed Laser Ablation Of HOPG . . . 141
5.2 Graphite Nanoplatelets . . . 145
5.2.1 xGNP Laser Ablation . . . 145
5.3 UEC Investigations Of GNP . . . 151
5.4 Summary . . . 153

6 Photoinduced Fragmentation In Silver Nanocrystals . . . 154
6.1 Ultrafast Electron Nanocrystallography . . . 155
6.1.1 Sample Preparation . . . 157
6.1.2 Importance Of SAM layer . . . 160
6.2 Silver Nanocrystals - Ground State Characterization . . . 162
6.3 Diffraction Signatures From Pre-Fragmented State . . . 165
6.3.1 Thermal Signatures of Fragmentation . . . 167
6.3.2 Role of Charges in Fragmentation . . . 170
6.4 Progressive Reverse Monte-Carlo Modeling . . . 175

6.5 Proposed Fragmentation Pathway 177

7 Conclusion **180**

A Graphite Structure Factor **184**

References **188**

LIST OF TABLES

2.1 List of Nobel prizes awarded for diffraction-related work 29

4.1 Results of fitting experimental data to the projected Gaussian model. 133

LIST OF FIGURES

Images in this dissertation are presented in color

1.1 Sequence of processes following ultrafast excitation of solids. Adapted from Ref. [11] 5

1.2 Experimental appraoch to study ultrafast phenomena: The pump-probe paradigm 7

1.3 Optical signature of non-thermal melting in silicon. (a) Increased linear reflectivity; From Ref. [29] (b) Polar plot of SHG signal; From Ref. [30] (c) From Ref. [31] - (i) Crystalline-order dependent and (ii) and order-independent SHG signal. (iii) Pump-probe autocorrelation signal (iv) Linear p-polarized reflectivity. 9

1.4 Ultrafast X-ray diffraction studies of non-thermal melting. (a) From Ref. [48] - Normalized X-ray diffraction intensity from InSb excited at $\approx$ 120 mJ/cm^2 for three probing depths: 3500 Å (open circles), 1700 Å (filled circles) and 1200 Å (open triangles). (b) From Ref. [49]. Atomic root mean square displacements of InSb atoms along the 111 and 220 directions. (c, d) From Ref. [50]; (c)Diffraction signal from photoexcited Bi, showing generation of coherent A_{1g} phonons at increasing excitation fluences. Inset shows measured phonon frequency as a function of inversion asymmetry (x=0.5 = perfectly symmetric), which is measured by the baseline shift in intensity. (d) Calculated inter-atomic potentials as a function of carrier density n. 12

1.5 Theoretical modeling of Nonthermal melting in silicon. (a, b) From Ref. [56]. Time evolution of (a) average atomic displacement from the ideal 'diamond lattice' positions and (b) average kinetic energy of Si atoms following photoinduced creation of e-h plasma of density ξ =0.15. (c) From Ref. [60]. Time evolution of ionic temperature T_{ion}, free energy F and atomic mean square displacement R^2 following initial electronic temperature T_e set to 25000 K, corresponding to photoexcitation at $\approx$ 2.15 eV. 15

1.6 Ultrafast Solid-Solid Phase Transformations. (a, b) From Ref. [13]. Amorphous-to-crystalline transformation in GeSb films. (a) Time evolution of reflectivity from three positions A, B and C corresponding to local excitation fluence of 45, 20 and 12 mJ/cm^2 respectively. (b) Cross sections of time-resolved reflectivity across a pump-excited region at 3 different time delays. (c, d) From Ref. [16]. Ionic-to-Neutral phase transformation in a molecular charge transfer crystal. X-ray diffraction patterns recorded before (c) and after (d) photoexcitation. Emergence of the (030) peak on the ns timescale suggests macroscopic phase transformation. 16

1.7 Thermodynamic Pathways For Graphite - Diamond Transitions. (a) Carbon phase diagram, from Ref. [64]. A = region for catalytic transformation of graphite(g) to diamond(d). B = spontaneous fast g-d. C = spontaneous fast d-g. D = spontaneous slow martensitic tranformation of hex-g to hex-d. (b) Cartoon depicting the sliding and buckling of graphite layers, necessary for its conversion into diamond. 20

1.8 Graphite - diamond transitions through electronically induced pathways. (a, b) Complete transformation of carbon onions into diamond under 1.25 MeV electron beam irradiation inside a TEM [77] (c, d) Formation of nanodiamond following electron injection into Ar^{8+} irradiation damaged area [2]. (c) STM images and (d) Scanning tunneling spectroscopy I-V curves. 22

1.9 NC fragmentation pathways - explosive boiling and Coulomb explosion. 25

2.1 (a) Elastic scattering from 2 identical scatterers. Vectors $\mathbf{k_i}$ and $\mathbf{k_f}$ denote the initial (incident) and final (scattered) wave vectors. (b) Pictorial definition of *momentum transfer* **s** - the vectorial change in the wave-vector of incident wave as a result of scattering along a given direction. 30

2.2 (a) Scattering geometry for a 1-D chain of N identical scatterers. (b) Diffraction intensity expected from the geometry in (a) and described by the Laue function (Eqn. 2.2), graphed for N = 10 (solid blue) and N=5 (dashed red). The two curves are vertically displaced for clarity. 33

2.3 (a) Laue formalism of scattering, for the special case of *specular* scattering where $\theta_i = \theta_o = \theta_{Sc}/2$. (b) The same scattering geometry of (a), with multiple rows of atoms, highlighting the essential equivalence between the Laue and Bragg formalisms of diffraction. The vertical line indicate the lattice planes 36

2.4 (a) Ewald construction concept for a 2D lattice. (b) Ewald construction for a RHEED geometry. (c) RHEED pattern obtained from a clean Si(111) surface, from Ref. [121]. 39

2.5 The lattice & basis for an (a) honeycomb lattice and (b) fcc lattice . 43

2.6 Diffraction geometry employed, along with the accompanying ground state diffraction patterns from (a) surface supported nanocrystals and (b) graphite. 46

2.7 Data reduction procedures employed in UEC studies of surface supported NCs, illustrated here with a specific example of 2 nm Au NCs. (a) Diffraction intensity I_{Tot} recorded from ring-averaging of UEnC diffraction data along with empirically fitted polynomial background I_{Bkg}. The arrow points to the sharp turn-around introduced in the intensity profile due to surface absorption effects. (b) Background subtracted intensity. (c) $M(s) = (I_{Tot} - I_{Bkg})/I_{Bkg}$ along with secondary background fitting to remove offsets introduced due to inelastic scattering. (d) $sM(s)$ curve obtained from (c). (e) $G(r)$ obtained from sine transform of $sM(s)$ in (d). 49

2.8 Data reduction procedures employed in case of graphite. (a) Intensity profile along central (00) rod (boxed in inset), along with the empirically fitted background. (b) Normalized structure function $S(s)$ extracted from (a). (c) Cosine transform of (b) to yield layer density function (LDF), $\mathcal{L}(z)$. 50

3.1 Global layout of various sub-systems comprising the UEC Lab 56

3.2 Conceptual construction of an ultrafast laser system utilizing regenerative chirped pulse amplification, similar to the system in use in the MSU UED lab. 58

3.3 Details of experimental and sample characterization tools incorporated into the UED chamber at MSU, broken down by each level. The UED experiment is carried out at level 2. 61

3.4 Pumping schematics for the UHV chamber. The actual components inside the chamber, such as the electron gun, the sample holder and others have been omitted for sake of clarity. For details of the molecular doser, see Ref. [156] 63

3.5 Design of the proximity coupled fs electron gun. (a) Conceptual layout of the gun. (b) Cross section CAD drawing of the optimized fs gun design currently in use. (c) Photograph of the actual electron gun, fully assembled just prior to installation within the UHV chamber. . 65

3.6 Characterization of the proximity coupled electron gun. (a) Comparison of 1^{st} and 2^{nd} generation electron gun performances. (b) Knife edge scan of the electron beam-size (2^{nd}-gen gun) at sample location showing $\sim$ 5μm FWHM. (c) Estimation of detector (CCD) response to a single electron event. Inset is a CCD image acquired at low-light levels showing 'blips' representing isolated single electron events. . . 67

3.7 (a) Overview of the cryogenic sample holder, with sample transfer and sample-plane ϕ rotation capability. All dimensions shown are in inches. (b) Close-up of the sample stage on which the sample is mounted and ferried in and out of the chamber. (c) Front & side-view photographs of the docking station. (d) Measure of low temperatures attained by the sample stage with and without the radiation shield. Solid line represents the time taken for the sample stage to warm up once the cryostat has been switched off. 70

3.8 Construction of the dockable sample holder. (a) An exploded view of the docking station, showing the sandwich style construction to allow rotation. See Sec. 3.4.2 for detailed explanation of the features. (b) Transverse cross-section of the assembly, showing the location of the ball-bearings to enable smooth rotation of the entire station relative to the cold-finger extension. 72

3.9 Sample docking mechanism. (a, b) The docking stage, engaged by the transfer arm, is hooked onto the docking station. The mounting screws prevent rotation of the system while the transfer arm is disengaged by unscrewing. The transfer arm tip, can be then used to tighten the mounting screws. (c) A still picture acquired from the video camera monitoring of the sample docking process. 74

3.10 Coarse pump-probe alignment procedures. (a) View of the sample surface seen b the optical camera mounted outside the chamber. See Fig. 3.3(b). (b) Cartoon depicting the method adopted to intercept the electron beam with the sharp tip (diameter$\sim$ 75 μm) of an *in situ* mounted needle. (c) Plot of normalized integrated intensities of the electron beam as the needle cuts across its path. The inset show the appearance of the electron beam on the CCD at two representative needle locations as marked. The electron beam is clearly seen to be occluded by the needle tip at $x \sim$ -14.56 mm. (d) Directing the 2 non-collinear diode laser beams to intersect on the needle tip while the needle tip intercepts the electron pulse path in the chamber. (e) Overlapping the pump laser with the probing electron beam on the sample surface while using the intersection of the two diode lasers (DL1 & DL2) as guides. 76

3.11 Fine pump-probe alignment procedures. (a) Raster scan pump laser (red spot) across the surface region probed by the electron pulse (green spot) by moving the focusing lens mounted on stepper-motor controlled stage. (b) Graphite diffraction pattern. We acquire diffraction pattern at a fixed pump-probe delay for a sequence of 2DY and 2DX lens positions. In each pattern, we integrate the intensity along s_x direction within the central streak region specified by the dashed box to produce a 1D curve, which are all then stacked in sequence to form a 2D map image shown in (c) that visualizes the change in diffraction pattern. The location of maximum change defines optimal pump-probe overlap. (d, e) The variation in intensity and position of the brightest Bragg spot seen in (b) as a function of 2DX and 2DY position. Both plots suggest an optimal overlap of pump and probe at (2DX, 2DY)=(-0.4, 0.5) 78

3.12 Construction of the *Intensified* CCD detector, capable of single electron detection. (a) The Intensified CCD camera (b) Image Intensifier (c) Electron multiplication in a Microchannel plate array. 80

3.13 Operation Principle Of The IC LS123. (a) Connection Diagram. (b) Function Table. [Source: Fairchild Semiconductors DM74LS123 Data sheet] 81

3.14 Circuit layout of the timing generator For Time-Gated Diffraction Acquisition 82

3.15 Optical experiment station. (a) Optic table layout of components. The numbers along axis are inch markers, used to approximately locate each component. (b) Box diagram outlining the detection system; Time-gated data acquisition and exponential averaging of data performed by a box-car integrator. (c) Response time of the integrator over which the average output settles to a new value when the input signal changes. 10k sample averaging provides best S/N but requires longer sampling periods to reach true average value. 84

3.16 Effect of exponential moving average (EMA) option of the box-car integrator. Fluctuation in averaged integrator output for 3 different EMA options while using (a) Photomultiplier tube (PMT) with control gain set to 1.0 V and (b) Photodiode (PD) to probe the unperturbed ground state of HOPG. (c) Standard deviation of data in (a) and (b) expressed in % Note: The data was acquired at the rate of 1 sample per ms using a DAQ board (*National Instruments*), though (a) and (b) plot only selected data points 500 ms apart. The numbers in (c) are estimated based on the complete data. 87

3.17 Overlapping pump & probe pulses. (a) Align pump and probe lasers through a 100μm aperture. (b) Detect using photodiode (PD), the simultaneous pump and probe scatter from a business card placed at the experimental position. (c) Evolution of PD response in (b) as the translational delay stage is scanned, showing the merging of pump & probe signals. The numbers (in ps) indicate delay stage position. (d) Width of the 1-Gaussian fit to the oscilloscope traces (points) along with a quadratic polynomial fit (solid line). The insets shows the signal profile and the fitted Gaussian curve at two select time points. (e) Determining time-zero with fs resolution based on monitoring *in situ* pump-probe change in reflectivity signal from graphite. Time-zero is clearly established as 2667.5 $\pm$ 0.1 ps 88

3.18 (a) Pump-probe dynamics from graphite excited at $F = 5$ mJ/cm^2 using photodiode (PD) and PMT as detectors. At high gain, the PMT saturates, and is insensitive to the pump-induced reflectivity drop. (b) Maximum dR/R measured at $t = 400$ fs while varying the PMT's internal gain via the supply voltage. (c) The PMTs gain curve while using a CW He-Ne Laser (1 mW average power). Data points (right axis) represent the gain obtained at different supply voltage relative to that at 700 V, while the dashed line represents typical gain (left axis) provided by manufacturer. (d) The same as (c), except using the fs probe laser pulse now. Deviation from the linear behavior is seen even at the lowest of light levels. 91

3.19 Baseline drift of signal. 3 delay scans, acquired in rapid succession show the shift of the reference baseline during the data acquisition. Each scan is composed of 31 time-points and requires about 5 minutes to complete. 92

4.1 Ground state UEC characterization of HOPG. (a) Raw diffraction pattern from graphite and (b) the corresponding maxima indexing scheme. The (00) and (10) rods in (a) are digitally attenuated to reduce contrast and simultaneously view all diffraction maxima. (c) The two characteristic zone axis (ZA) in graphite basal plane giving rise to strong diffraction maxima. Dashed line represents the Ewald sphere. (d) Ground state structure function $M(s)$ obtained from (00) rod in (a). (e) Layer density function (LDF) obtained from the Fourier transform of M(s). Peaks at multiples of 3.35 Å represent inter-layer spacings in graphite. 97

4.2 Surface Diffraction vs. RHEED. (a) Ewald sphere construction in a RHEED geometry. Inset shows an Si-111 RHEED pattern from Ref. [121]. (b) Surface diffraction from a rough surface. (c) Rocking curve expected from flat, pristine surfaces studied in RHEED and (d) from surface diffraction off rough surfaces, such as this study. (e) Rocking curve 'map' of the (00) rod for surface diffraction from Si-111 surface and (f) HOPG surface, both obtained using the UEC setup. Insets show the gating of the (00) rod. 100

4.3 Diffraction difference images from HOPG at various pump-probe time delays as labeled, along with the ground state diffraction pattern used as reference. 101

4.4 Raw data from UEC investigation of HOPG. (a) Diffraction evolution maps from the central streak in the HOPG diffraction pattern for 3 fluences of 18, 40 and 90 mJ/cm^2. Horizontal axis represents pump-probe delay time. (b) Shift of the (006) maxima for various excitation fluences. The inset plots the maximum shift observed at different fluence. (c) Diffraction evolution map for $F = 21$ mJ/cm^2. (b) Center-position of maxima, tracked from (c) 103

4.5 Cartoon depicting the Coulomb refraction of a grazing incidence electron beam as it interrogates a sub-surface region where a laser-induced transient surface voltage V_S exists. The refraction shift is exaggerated here for clarity. Adapted from Ref. [156] 104

4.6 Demonstration of the Fourier phasing technique to correct TSV induced effects in diffraction patterns. (a) HOPG ground state structure function $M(s)$ and the distorted (see text) $M'(s)$ curve. (b) LDF curves and (c) high-resolution LDF * curves obtained from Fourier transform of curves in (a). Asymmetry in LDF* obtained from M' is apparent. (d) The Fourier phasing algorithm along with the plot of χ^2 used to correct the TSV-effect introduced within $M'(s)$. (e) The 'phase-corrected' $M''(s)$ compared with $M(s)$ and $M'(s)$. (f) The LDF curves and (g) LDF* curves corresponding to the $M(s)$ curves in (e). The Fourier phasing algorithm recovered the original M(s) from the shifted $M'(s)$. 108

4.7 Low fluence response of HOPG: Debye-Waller analysis. (a) Decay of diffraction intensities for $F = 21$ mJ/cm^2. (b) Mean-square amplitude of vibration $\langle \Delta \bar{u}_C^2 \rangle$ estimated from (a) via the Debye-Waller relation Eqn. 4.3 (c) Experimentally measured mean-square vibration amplitudes from different maxima on the (00) rod for a range of excitation fluences. Dashed line only a guide to the eye. (d) Experimental measure of temperature dependent vibrational amplitudes in graphite using X-ray scattering corrected for thermal diffuse scattering - from Ref. [174] 111

4.8 Charging dynamics near photoexcited HOPG surface (a) The transient surface voltage V_S measured in the case of 3 excitation fluences, as labeled (b) Maximum V_S as function of excitation fluence showing linear trend. (c) Log-log plot of the V_S relaxation dynamics (dots) with fit to a drift-diffusion model (lines) demonstrating power-lay decay of V_S with exponent $\sim$ -1. 113

4.9 Interlayer structural dynamics in graphite. (a) Contraction of primary LDF peak at various fluences for short times and (b) for long times. (c) The maximum contraction of LDF peak at short times, and maximum expansion (overshoot) at longer times. (d) Correlation of the measured TSV with inter-layer contraction at $F = 77$ mJ/cm^2. 115

4.10 Signature of sp^3-like bonding in HOPG. (a) Molecular interference pattern $M(s)$ and the corresponding LDF curves at selected time stances following strong photo-excitation. The transient peak at 1.9 Å in the LDF indicates formation of an interlayer bond. (b) Ratio of peak intensities obtained from the diffraction patterns. The enhancement of the (00 12) with respect to the (00 10) peak cannot be explained by thermal vibrations and indicates a transient structure consistent with sp^3 bonding. (c) Ratio of peak intensities at $R = 1.9$ Å and 3.35 Å in the LDF. 116

4.11 Electronic structure changes during photo-excitations in graphite. (a) Schematic view of the structure. (b) Electronic density of states (solid line) and the Fermi-Dirac distribution of graphite at $T = 0$ (dashed line) and $k_BT = 1.0$ eV (dotted line). (c) Total pseudo-charge density $\rho(\mathbf{r})$ and (d) change in the pseudo-charge density $\Delta\rho(\mathbf{r})$ due to an electronic temperature increase to $k_BT = 1.0$ eV. The plane used in (c) and (d) intersects the graphene layers along the dashed lines in (a). 119

4.12 Schematics of the electron point-projection imaging technique. Typical values are $x_0 \approx 1$ - 4 mm, $L \approx 150$ mm. The dashed arrows illustrate the effect of the photo-emitted electron bunch on the coherently scattered electrons constituting the diffraction maxima. 122

4.13 Shadow images obtained from a photoexcited HOPG surface (using offset distance $x_0 = 2.4$ mm), illustrating the creation, emergence and evolution of vacuum space charge (VSC). The numbers indicate the pump-probe delay in ps. 124

4.14 Time-evolution map of VSC Cloud at $F = 75$ mJ/cm^2. (a) Typical shadow image obtained. Dashed boxes indicate the regions chosen to create the diffraction evolution map shown in panels (b) and (c) as labeled. (b) The dark streak in panels (b) and (c) represents the propagation trajectory of VSC cloud with time on abscissa. The maxima show a clear shift as each is crossed by the VSC at separate time instances marked by the arrows in (c). 125

4.15 Qualitative analysis of VSC induced changes in diffraction pattern. (a-c) Angular shift of (00 2l) diffraction maxima at $F = 35$ mJ/cm^2 in (a) and $F = 56$ mJ/cm^2 in (b, c) for different offset distances x_0, as illustrated by the inset cartoons. (d) Dynamics of integrated intensity and (e) angular shift of the diffraction maxima, with $F = 23$ mJ/cm^2 and $x_0 = 2.4$ mm. (f) Angular shift of (008) maxima at different excitation fluence while holding $x_0 = 2.4$ mm constant and (g) the same at different x_0 while holding $F = 56$ mJ/cm^2 constant. (h) Angular shift of (006) maxima at 2 different fluences, showing a unique double-hump feature that is as yet unexplained. The two curves are vertically offset for clarity; dashed lines represent respective zero-level. 127

4.16 (a) Snapshot shadow images of photoemitted electron bunch obtained with $x_0 = 4.3$ mm. The cross-sectional line profiles (black curves) are extracted along the dashed line in the second panel. (b) Model used to construct an analytical expression for the shadow image z line scans in Eqn. 4.4. The shadow intensity on CCD is related to the integrated strength of the Gaussian VSC cloud along the probe electron propagation trajectory. (c) Fitting curves (lines) of cross-sectional line-profile data (circles) using a Gaussian model considering the projection geometry. 130

4.17 Photoemission from graphite surface: Dynamics along the z-direction, with $x_0 = 2.4$ mm. (a) Time-evolution of the electron bunch's center-of-mass (CoM) and (b) $1/e$-width. (c) Spatiotemporal evolution of the diffraction maxima and the electron bunch at $F = 56$ mJ/cm^2, showing the bunch CoM (black dots) and its spread ($1/e$-width) relative to the CoM (gray circles). 132

4.18 Comparison of TSV and VSC effects in UEC investigations of HOPG. (a) Shift of the (006) maxima in case of perfect pump-probe alignment ($x_0 = 0$) and projection imaging geometry with ($x_0 = 2.4$ mm). (b) Comparison of the TSV measured by the probing electron beam submerged beneath the HOPG surface in the UEC study (Ref. [153]) along with the estimated effect of VSC in that study, based on the VSC dynamics extracted here. 134

4.19 Optical reflectivity data from HOPG. (a-d) Transient reflectivity $\delta R/R$ at different fluences, as labeled. (e) Reflectivity data at various fluences with maximum change in $\delta R/R$ self-normalised to unity. The timescales of initial reflectivity drop and subsequent relaxation are largely fluence independent. (f) Maximum change in reflectivity plotted as a function of irradiated fluence, showing saturation beyond 10 mJ/cm^2. 136

4.20 (a) Optical reflectivity data acquired with good S/N (70 scans) for 2 fluence limits with fits to convoluted growth & decay $\sim \{1-exp(t/\tau_1)\}\, exp\{(t-t_1)/\tau_2\}$. (b) Transient reflectivity from HOPG at $F = 13$ mJ/cm^2 reported by Downer & co-workers [197]. (c) Long-time dynamics at $F = 17$ mJ/cm^2, showing no long-term response (note the break in the abscissa). The optical signal relaxes completely within 10 ps. A weak oscillatory signal, possibly due to acoustic waves triggered in the graphite surface layers is detected. Solid line represents fit to a decaying sine function. (d) Long time optical response from HOPG. No noteworthy dynamics are observed at these long timescales. 137

5.1 Morphology of laser-ablated graphite at F=100 mJ/cm^2. (a) Low-mag SEM image of the entire spot. (b, c) Higher magnification views of the centrally ablated area marked by a square in (a), showing creation of crystalline like nanostructures. (d) Similar result obtained by Huang & co-workers at $F = 170$ mJ/cm^2 [204]. 141

5.2 Morphology of nanostructure created from fs laser ablation ($F = 100$ mJ/cm^2) of graphite, in areas surrounding the central ablation spot. (a) Low-mag SEM image of the ablation spot. (b-e) Magnified views of nanostructures from different surrounding regions labeled in (a). The nanostructures exhibit regular crystalline facets suggesting the creation of sp^3 bonded diamond-like carbon structures. (f) The 'cauliflower' like texture commonly observed in ns pulsed laser diamond-like-carbon films obtained from ns pulsed laser deposition using 248 nm KrF laser [205]. The film texture produced in this study in (b-e) resembles this 'cauliflower' pattern. 142

5.3 Raman spectrum from laser-ablated HOPG. (a) Optical micrograph of the laser ablated region with 4 regions labeled. (b) Raman spectrum obtained from the 4 regions labeled in (a). (c) Raman spectrum obtained from pristine HOPG and from region 4 in (a) in this study overlayed on top of that recorded by Meguro *et al.* [2]. Meguro characterized their spectrum as originating from creation of nanodiamonds. 144

5.4 Electron energy loss spectrum acquired from 3 types of carbon - graphite, amorphous carbon and diamond. The absence of π^* peak along with the the rather sharp dip around 300 eV can be used as a fingerprint of diamond-like structures. 146

5.5 Analysis of laser-ablated xGNP sample. (a) SEM Image of xGNP sample on the lacey carbon grid. Inset shows 1 full grid covered in xGNP. (b) Diffraction pattern from a small select area ($\approx$ 100 nm) acquired in a TEM from the unablated sample. Dashed quadrilateral marks the reciprocal cell expected from the honeycomb structure of graphite layers. (c) Low-mag image of the edge of laser-induced damage. Investigations were carried out within this grid, just inside the edge. (d) A small region adjacent to the laser damage edge (as marked by the arrow emanating from (c), which showed interesting results summarized in following panels. (e) Diffraction pattern from spot 2 labeled in (d) showing the presence of new spots marked by arrows, created symmetrically on either side of the dashed line suggesting lattice contraction. The central (00) spot is digitally added for reference. (f) Normalized EEL spectra acquired from spots labeled 1, 2, 3 in (d), showing the change in intensity of the π^* peak. 148

5.6 Analysis of diffraction and EELS signatures from unablated GNP. (a) High resolution TEM image of GNP, with 3 spots marked. (b) Normalized EEL spectra recorded from adjacent regions labeled in (a), showing change in the π^* peak. (c-e) Diffraction patterns recorded from spots labeled in (a). Diffraction from spot 1 agrees well with pristine graphite, whereas those from spots 2 & 3 show distortions such as creation of multiple Bragg spots and stretching of the hexagon along directions marked by the arrows, which are features similar to those seen in the ablated sample. (f-h) Simulation of TEM diffraction pattern from a perfect graphite lattice, for varying angles (θ) between the graphite's $c-$axis and the electron beam direction. Note the creation of additional spots in (g) and the stretching of the hexagon in (h). 149

5.7 (a-c) High resolution TEM images of 3 different crystalline nanostructures with size in the 10-20 nm range observed near the laser ablated region within the xGNP samples. Each nanostructure appears to be surrounded by few layers of amorphous-carbon. (d) A high-resolution TEM image of a flat xGNP sheet, provided for comparison. 150

5.8 UEC investigations of exfoliated graphite nanoplatelet (xGNP) samples. (a) Ground state transmission UEC diffraction pattern. (b) 1d diffraction curve obtained from radial averaging of rings in (a) (c) Mean-square atomic vibrations within the basal plane, extracted from (100) and (220) maxima in (b) compared with that along c-axis dynamics acquired from HOPG. Fluence in both cases is $F = 20$ mJ/cm^2 (e) Comparison of rms vibrations along the basal and the c-axis. Dashed lines only a guide to the eye. 152

6.1 Sample geometry employed in the UEC investigation of nanopaticles. 156

6.2 Steps to deposit colloidal nanocrystals on silicon surface. (a) Hydroxyl terminated silicon surface. (b, c) Surface functionalization (d, e) Nanocrystal deposition. (f) SEM image showing typical sample morphology obtained using 20 nm Au NCs here as example. 159

6.3 Controlling areal density of NCs on organosilane covered Si-111 substrate. (a-b) Changing pH of Ag colloidal suspension using acetic acid. (c-f) Changing hydrophobicity of Ag colloidal suspension using ethanol. (g) NC counting statistics averaged over two separate 1 μm^2 areas. . 160

6.4 Importance of Buffer SAM layer for UEC investigations of surface supported nanoparticles. (a) Sample morphology obtained with unsuccessful or incomplete surface functionalization, with corresponding diffraction pattern (b) and rocking curve (c). (d) Ideal sample morphology, showing uniform coverage of isolated NPs, with corresponding diffraction pattern (e) and rocking curve (f). 161

6.5 Ground state characterization of 40nm Ag NC using UEC. (a) SEM images of the Ag NC sample. (b) Theoretical distance list for fcc Ag lattice using lattice constant $a_0 = 4.08$ Å (c) UEC diffraction pattern obtained from ground state of sample in (a). (d) $sM(s)$ pattern obtained from radial averaging of diffraction pattern in (b), as described in Sec. 2.2.1. Characteristic fcc peaks are labeled. (e) Atom-atom pair correlation function $G(r)$ in the ground state, obtained through Fourier analysis of (c). The peaks agree well with theoretical predictions in (b). 163

6.6 SEM Investigation of Ag NC fragmentation. (a) Sample before irradiation (b-f) Random areas of the sample within the laser footprint. Excitation at 400nm, F=30 mJ/cm^2. (g) Similar fragmentation of Ag NCs observed in the solution based study by Kamat *et al.* [99]. (A) - before; (B) after excitation by a 355 nm ps laser. 164

6.7 UEC Data (a) Time evolution map of the normalized structure factor *sM(s)* of Ag NCs excited at SPR at $F = 17$ mJ/cm^2, with *sM(s)* at select times explicitly overlayed. (b) Pair correlation function $G(r, t)$, corresponding to the select times in (a). The arrows point to the medium range order peaks, which completely dephase by $t = +13$ ps, before their eventual revival at long times. 166

6.8 Thermal signatures of NC fragmentation process. NC temperature estimated from Debye-Waller analysis of peak intensity drop in (331) and (311)+(220) peaks. Inset shows $W = (1/s^2)\ ln\,(I/I_0)$ determined for the same two peaks, and exhibits anisotropy at short times. The oscillatory curve is drawn as a guide to the eye, representing acoustic oscillations of the NC. 167

6.9 Simulation of Ag NC fragmentation and associated signatures in diffraction pattern. (a) Planar slice along the center of a Ag $15 \times 15 \times 15$ supercell, that is progressively subdivided into smaller pieces. The individual fragments are displaced from each other and oriented randomly to remove any correlation between the fragments. (b) W parameter estimated from the computed $sM(s)$ from these fragmented NC. (c) Computed $sM(s)$ from these fragmented NCs for select fragmentation degree, showing the similar dramatic drop in (111) & (220) peaks as observed in the UEC data shown in (d). 170

6.10 Determining photoemission (PE) yield from Ag NC sample using the point-projection imaging technique described in section 4.7.1. (a) Normalized shadow images of the PE cloud. The cloud profile is shown on the right. (b) Evolution of PE cloud profiles along z direction normal to Si-111 surface both with and without the Ag NCs. Significant enhancement of PE is seen in presence of Ag NCs. 171

6.11 Monitoring NC charging dynamics through SAM (001) peak shift. (a) Refraction shift of SAM (001) peak due to interfacial charge transfer. (b) Total shift of the SAM (001) peak along with the TSV-induced shift deduced from Fourier phasing algorithm. Difference between the two yields the contribution to the interfacial field from the SAM layer alone. (c) The shift of the SAM peak correlated to the degree of NC charging, based on the calculations in (d, e). (d) Finite element simulations of the field generated by the NC charged to unit positive voltage. The SAM layer $\approx$ 1 nm is too small to be seen on this scale. (e) 2D surface plot of the interfacial voltage, and its effect on the SAM peak. Note the intensity of the SAM peak relative to the Debye-Scherrer rings from Ag. 172

6.12 (a-h) Prefragmentation states of Ag NC at select times, determined using the PRMC structure refinement scheme described in the text. Growth of local disorder is apparent from the increase in number of undercoordinated atoms (black) (i) Final G(r) fits obtained after PRMC convergence. 174

6.13 Growth and decay dynamics of defect sites in the PRMC refined supercell structure. (a) Evolution of the number of atoms with given coordination number following photoexcitation. Counts of Perfect fcc coordinated atoms ($N_C = 12$) decreases as the number of undercoordinated sites increase. (b, c) Evolution of total number of defect sites characterized by $N_C \leq 10$ showing their growth and percolation at short times, and decay at long times. Long time decay in (c) is fit to a biexponential function, with the $1/e$ timescales shown. 176

A.1 Graphite Unit Cell. (a) Views along the 001 (top) and 010 (bottom) to help visualize the 3D structure of graphite, showing the $ABAB\ldots$ stacking of the individual graphene layers. The shaded pink region represents the unit cell and the green atoms labeled 1-4 are the basis atoms comprising one unit cell. (b) Magnified view of the unit-cell and the constituent basis atoms. 185

Chapter 1

Introduction

Structural changes are commonly achieved by applying pressure or heat. In such cases, the system absorbs energy from the external agency, evolving slowly under quasi-equilibrium conditions, driven by the principle of free-energy minimization. With the advent of short-pulse lasers capable of producing intense bursts of photon packets of femtosecond (fs) durations, it is now possible to deposit significant amount of energy in to a system within a very short time. This offers controlled exploration of the complex energy landscape of materials. The intense femtosecond (fs) laser pulse can 'shock' the electrons in the material by exciting the valence electrons into non-equilibrium configurations before the atoms (which are heavier) have any time to respond. Since the lattice structure is predominantly determined by the valence electrons that participate in bonding, the modified far-from equilibrium electronic configurations can result in strongly perturbed inter-atomic potentials, affecting bond strength and sometimes even bond orders. This can lead to structural change, melting or even a solid-solid phase transformation on very short time scales. Such phenomena, where phase transformations are triggered on timescales shorter than the electron-phonon coupling times cannot be explained by a thermal picture, and are broadly classified as *electronically induced phase transitions.* This offers a powerful method

to access novel states of matter that might not be accessible through conventional thermodynamic means. Furthermore, even if complete structural transformation is not evidenced, perturbation of the system and the consequent relaxation mechanisms can provide fundamental insights into the nature of bonding in materials, and the intimate couping between electrons on the lattice on the ultrafast timescales. Such studies gain even more importance with the emergence of strongly correlated materials where novel physics arises from the strong coupling between the electronic, spin, and lattice degrees of freedom.

The study reported here focuses on electronically induced structure transformations in two systems - graphite, and silver nanocrystals. In graphite, recent studies have pointed toward the possibility of inducing a graphite - diamond transition via an ultrafast destabilization of the graphite lattice [1, 2]. Using ultrafast electron crystallography as a probe of transient structures, we will show that such a transformation is indeed possible, and appears to be driven by hitherto unexpected transient hole-doping effects caused by charge redistribution in the graphite layers. In silver, we explore the photoinduced fragmentation of surface-supported silver nanocrystals (Ag NC) excited at surface-plasmon resonance. By combining the diffraction probes with structure refinement schemes, we are able to 'image' the fragmented domains within a photoexcited Ag NC. The fragmentation is found to be seeded by inhomogeneous creation of defect sites within the Ag NC whose growth and percolation lead to fragmentation of the NCs well below their melting threshold. As in the case of graphite, interfacial charges are also observed to play an important role in these transformations.

1.1 Electronically Induced Structure Transformation

The concept of electronically induced structure transformation has its roots in the discovery of laser annealing in the 1970s [3–5]. Efforts to understand the underlying mechanisms of laser-induced material transformation in semiconductors such as Si and GaAs led to two contrasting viewpoints - the thermal model [6, 7] which involved laser induced heating of the material leading to melting and eventual recrystallization, and the more intriguing plasma annealing (PA) model. Proposed by Van Vechten *et al.* [8, 9], the PA model attributed laser annealing to lattice instabilities resulting from the photoinduced promotion of a large number of (bonding) valence band electrons into the (anti-bonding) conduction band. The sudden depletion of bonding electrons was shown to lead to the weakening of covalent bonds, allowing the atoms enhanced mobility to anneal any defects. Since then, several experimental and theoretical efforts [10], have shown that for pulse durations of ns or several tens of ps, the thermal model satisfactorily describes the laser induced phase transformations. Since electronic energy relaxations typically occur within sub-ps timescales, the entire energy carried by a ps or ns laser pulse can be transferred to the lattice within the pulse duration itself. Any subsequent phase transformations then proceed with a hot lattice, through thermal channels.

The situation becomes more complex however, when pulse durations approach the fs domain. Femtosecond lasers allow the impulsive excitation of a large number of electrons to elevated energies well-before any appreciable transfer of energy to the lattice has commenced. In such cases, the plasma annealing model becomes more appealing. Electronically induced lattice instabilities could conceivably trigger structural phase transitions on the sub-ps timescales even as the lattice remains vibrationally cold. A simple calculation is instructive here - a gold nucleus (mass number

$\sim$ 196) at room temperature of 300 K posses an an average nuclear thermal velocity of $\sim$ 130 m/s (estimated from classical equipartition theorem). If the bonds holding the Au atoms in place in its lattice were to momentarily vanish, the Au atoms could move in 0.5 ps as much as 0.6 Å, which is close to 20% of the bond-length. Lighter atoms like Si would move even more on account of their increased thermal velocity. It is easy to see that such a scenario could lead to significant disorder in the lattice without ever heating it up.

Several phase transitions have been identified that are evidenced to be electronically initiated, such as nonthermal melting in semiconductors [11], amorphous-to-crystalline transformations in films [12, 13], ionic-neutral switching in organic molecular crystals [14–16], insulator-metal transitions in Mott insulators [17, 18], melting of charge-ordered states in perovskite manganites [19] & charge density wave materials [20], and possible transition to superconducting states in high-T_c cuprates [21]. However, despite a large body of work in this area, the fundamental origins and the driving force behind of electronically induced structure transformations remains elusive, in part due to the multitude and complexity of ultrafast processes in solids that involve non-equilibrium dynamics of both electronic and the lattice sub-systems. Hence, before we attempt a mini-review of this field, it is worthwhile to briefly examine the complex processes that occur on such short time scales and various methods devised to probe these processes.

1.2 Ultrafast Laser-Matter Interaction

The interaction of ultrashort laser pulses with matter involves a complex cascade of energy relaxation processes as illustrated in Fig. 1.1 (adapted from Ref. [11]). When a photon is incident on a solid, the energy is first absorbed by the electrons, causing the electrons to be promoted from their ground state to an excited state at

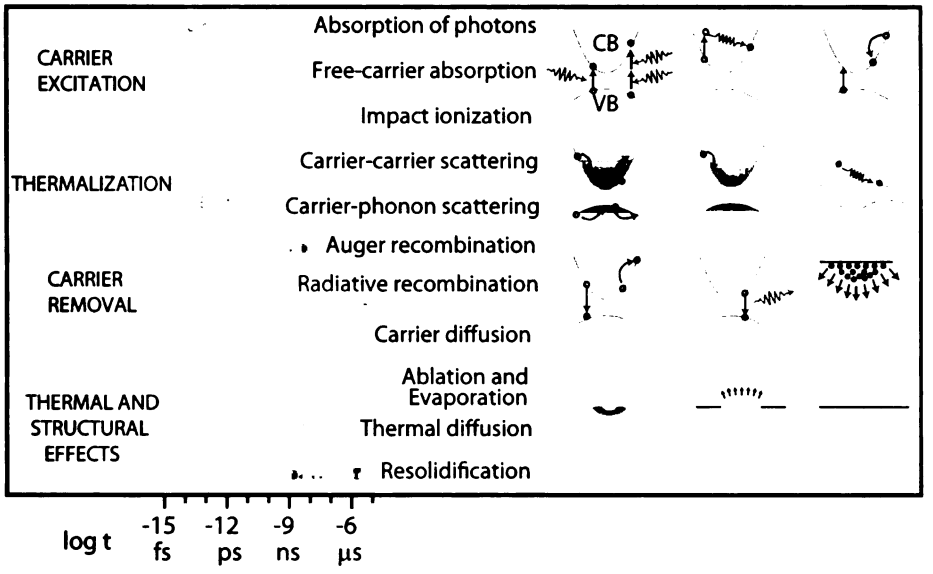

Figure 1.1: Sequence of processes following ultrafast excitation of solids. Adapted from Ref. [11]

higher energies. In semiconductors, this translates to a promotion from the valence band into the conduction band across the band gap whereas in metals, free-carrier absorption promotes electrons to higher energies within the same (conduction) band. This electronic excitation is nearly instantaneous, occurring on the 1-10 fs timescale, and hence completed within the duration of the pulse. It results in the creation of a non-thermal distribution of electrons whose population is not describable by a conventional Fermi-Dirac (FD) distribution. The excited electrons 'thermalize' (typically on the 10 - 100 fs timescale) via carrier-carrier scattering and relax back to the band-edge. At this point, the carrier population can be described by a FD distribution function with a well defined electronic temperature T_e - the carriers are said to have 'thermalized'. Concurrent with this carrier-carrier scattering processes, carrier-phonon scattering processes also commence leading to transfer of energy to the lattice vibration modes via emission of incoherent phonons. Phonons typically carry very little energy and so, the transfer of energy to the lattice requires many phonon

emissions ranging over several ps. This energy transfer between the electronic and lattice sub-systems allows them both to come into thermal equilibrium with each other at a common temperature T. Finally, the excess carriers in the conduction band are removed by recombination (radiative and non-radiative such as Auger) or by carrier diffusion out of the photoexcited volume.

These processes, as evident in Fig. 1.1 do not occur sequentially, but often in parallel. Electron-phonon scattering commences even before carrier thermalization is complete. Process such as impact ionization and Auger recombination alter carrier densities in complex ways. The high carrier densities modify the effective ionic potential and hence the bonding parameters. In some systems, carrier relaxation might be preferentially coupled to a subset of phonon modes termed strongly coupled optical phonons that drive the lattice in a coherent fashion. Thus, mapping the electronic and structural dynamics of photoexcited solids from start to finish requires experimental investigations of many different processes occurring over a wide time scale ranging from the first few fs following photoexcitation to longer ns, along with accurate theoretical modeling of the various energy relaxation processes.

1.2.1 The Pump-Probe Paradigm

Investigation of ultrafast phenomena require experimental methods capable of resolving events occurring on the fs-ps time scale. With the significant advancement in short-pulse laser technology over the last 3 decades [22], ultrafast lasers have served as an ideal tool in such investigations. A plethora of experimental approaches have been formulated and perfected, each with their unique advantages. While the specifics of different approaches may vary, most of them rely on the fundamental concept of the pump-probe paradigm illustrated in Fig. 1.2. Two laser pulses are employed - one acting as a 'pump' and another as the 'probe'. The pump pulse serves to initiate the ultrafast process of interest by providing an impulsive kick to the (electronic) system

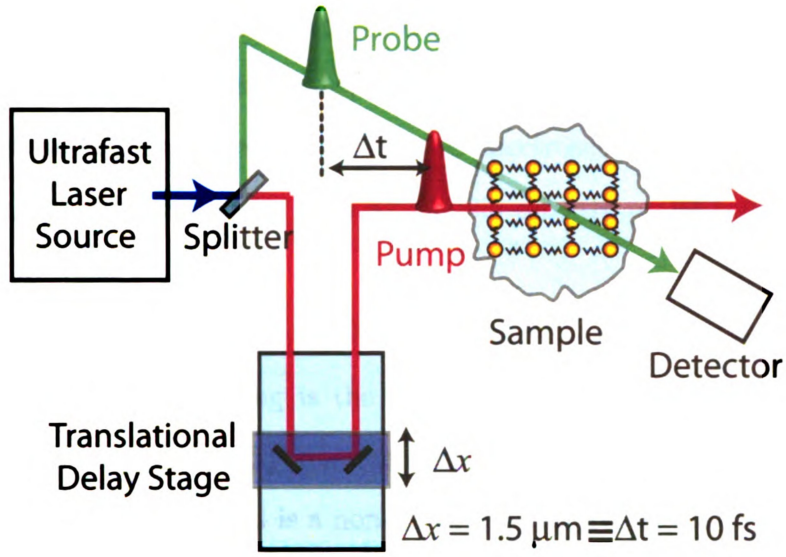

Figure 1.2: Experimental appraoch to study ultrafast phenomena: The pump-probe paradigm

away from its ambient equilibrium condition. The arrival of the pump pulse at the sample position thus fixes the 'time-zero' for the experiment. As the system relaxes back to the ground state, a time-delayed probe pulse interrogates the sample and the response is recorded using appropriate detectors. The ultrashort duration of the probing pulse ensures that the sample response depends solely on the instantaneous state of the system at the moment of interrogation, thus lending the ultrafast time resolution to the experiment. Data is accumulated for a series of pump-probe delay settings that can be controlled by the use of translational delay stage as illustrated in the figure, thus mapping out the complete temporal response of the system over timescales of interest.

This probing paradigm is almost universal amongst all ultrafast experimental techniques. The diversity in pump-probe approaches arises purely by varying the nature of the probe. Experiments utilizing optical probes relate the time-resolved reflectivity or transmission signals from the photoexcited sample to the electronic configuration based on suitable *a priori* assumptions on the material's dielectric function. Ad-

vanced optical probes such as 2-angle broadband reflection/transmission go a step further and measure the dielectric response of the material. Electron spectroscopy methods such as angle resolved photoemission spectroscopy (ARPES) [20, 23] and electron energy loss spectroscopy (EELS) [24, 25] directly probe the transient electronic configurations.

Structural dynamics on the other hand, require alternate approaches. One approach based on optical probing is the detection of 'second harmonic generation' (SHG), where the experimentally relevant signal is the second harmonic of the fundamental probe frequency. SHG is a non-linear optical process [26] in which the EM fields of two photons of fundamental frequency ω couple through the non-linear polarization induced in a material to generate a photon of frequency 2ω. The process is mediated through the second order susceptibility $\chi^{(2)}$, which is an intrinsic quantity that reflects the crystalline symmetry of the material. Thus, changes in the second harmonic signal can be related to the structural symmetry of the crystal. The most direct approaches however to study structural dynamics utilize scattering of X-rays [27] or electrons [28] from a photoexcited solid. An optical probe-pulse is used as the generator of ultrafast X-rays/electron packets which are made to diffract off the sample in either reflection or transmission geometries. Since these diffraction patterns (collected on a CCD) serve as fingerprints of the instantaneous lattice structure, any change in them with the pump-probe delay carries information on structural dynamics of the system.

1.3 Non-Thermal Melting in Semiconductors

Non-thermal melting in semiconductors has served as a quintessential test-bed for the study of electronically induced structure transformation in materials. The first reports came from Shank & co-workers in 1983 [29] who observed a rapid sub-ps rise in

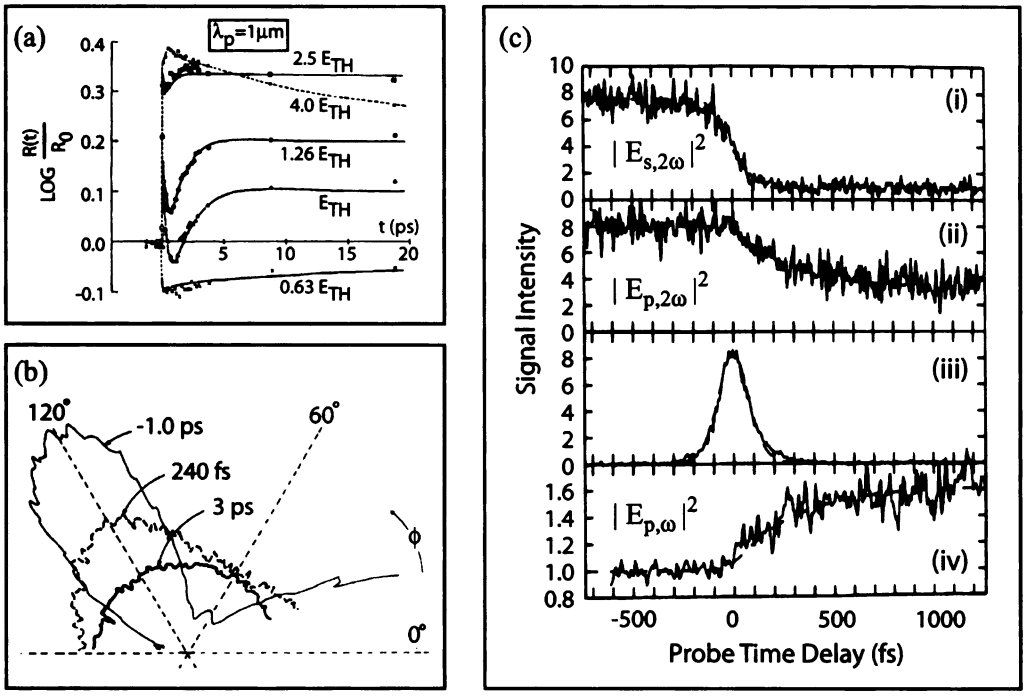

Figure 1.3: Optical signature of non-thermal melting in silicon. (a) Increased linear reflectivity; From Ref. [29] (b) Polar plot of SHG signal; From Ref. [30] (c) From Ref. [31] - (i) Crystalline-order dependent and (ii) and order-independent SHG signal. (iii) Pump-probe autocorrelation signal (iv) Linear p-polarized reflectivity.

reflectivity from silicon surface excited by a 90 fs laser pulse as shown in Fig. 1.3(a). This rise was attributed to a Drude-like response from a dense electron-hole (e-h) plasma that causes the refractive index to go negative on account of the increased carrier density. The subsequent short-time modulation and eventual saturation in reflectivity was attributed to the creation of a layer of molten silicon. This interpretation was supported by second harmonic generation (SHG) studies. Since atoms on Si-111 are arranged in a hexagonal pattern, the SHG signal exhibits 3-fold symmetry about the surface normal (maxima every 120°). The SHG signal from Si-111 was observed to become nearly isotropic within 1 ps following photoexcitation [30] [See Fig. 1.3(b)] thus suggestive of a loss in crystalline order. In an improvement of this technique, Tom, Aumiller and Brito-Cruz reported the vanishing of the crystalline-

order-dependent s-polarized SHG signal from Si-111 surface in less than 150 fs [31] [See Fig. 1.3(c)]. Similar rapid disappearance of SHG signal within 100 - 200 fs indicating ultrafast lattice disordering has been observed in GaAs as well [32].

While these observations offer compelling evidence, observing macroscopic structural disorder in times as short as 150 fs is rather surprising, as they are comparable to a single atomic vibration period in solids that typically range of a few hundred fs timescale [33, 34]. Since, optical probes interact directly with the electronic system and not the lattice, any conclusions about photoinduced structural transformations are inferred indirectly, and non-structural sources of optical response need to be accounted for. For example,

1. In case of solid-liquid transitions, an increase in reflectivity need not necessarily suggest transition to a molten metal-like state since the properties of a dense electron-hole plasma resemble those of a simple metallic liquid.

2. At high pump-fluences, the depopulation of a large number of electrons from the valence band can lead to signal 'bleaching' effects in which the probe-pulse is unable to excite any transitions due to lack of electrons in the valence band. This can lead to increased transmission or reduced SHG signals.

3. Free-carrier effects such as screening of the lattice ionic potential (which could occur in a structurally intact solid), could alter the dielectric function $\epsilon(\omega)$ and hence the optical response, in a time-dependent manner as the carriers relax. As a result, the linear reflectivity response may not be related to a Drude-like response of e-h plasma, but to band-structure changes [35]. Similarly, the SHG signal may not be related only to crystal symmetry, as it depends not only on $\chi^{(2)}$, but also indirectly on the linear dielectric constants at both fundamental and second harmonic frequencies [36].

Several optical experiments that have accounted for these effects have revealed the

complexity of electronically induced processes. Mazur & co-workers reported a band-gap collapse in photoexcited GaAs on the 0.5 ps timescale based on their explicit determination of the transient dielectric function $\epsilon(\omega, t)$ [35, 37], and related this to structural disorder [38]. Free-carrier effects were discounted, as these effects would be most dominant at time-zero when the carrier density is at its maximum. However, the similarity in timescales over which SHG intensity vanishes for all materials including the lighter Si [31], heavier GaAs [32, 39] and the much heavier InSb [40] have led to a two-step model of order-disorder transitions. In this model [39], the initial optical responses ($\leq$ 100 fs) are shown to arise largely from significant modifications of the optical constants, while the structural disorder proceeds later on the timescales of several hundreds of femtoseconds or longer. Experiments employing optical [41] and time-resolved microscopy probes [42] have also supported this view.

From these reports, it is apparent that while optical probes are extremely adept in resolving the early fs response of a system, the attribution of the observed changes to a causative phenomena, particularly when it entails structural change, relies on a careful choice of appropriate theoretical models and *a priori* assumptions as to the behavior of material's dielectric function and band structure.

The development of ultrafast X-ray [27, 43] and electron [28] probes have thus offered a powerful alternative to directly probe lattice dynamics of photoexcited solids. In such diffraction studies, lattice disorder and melting is normally inferred via the Debye-Waller (DW) drop in Bragg peak intensities that occurs on account of increased atomic vibrations. Based on this, nonthermal melting has been reported in many systems such as organic films [44], Ge [45], GaAs [46] and InSb [47, 48], where the relevant Bragg peaks show abnormally large DW drops that are unaccountable from a superheated lattice. However, the extent of lattice disorder induced in these processes is unclear. The Bragg peaks never completely diffuse as they should for a liquid, [See Fig. 1.4(a)], thereby suggesting the retention of some degree of long range order.

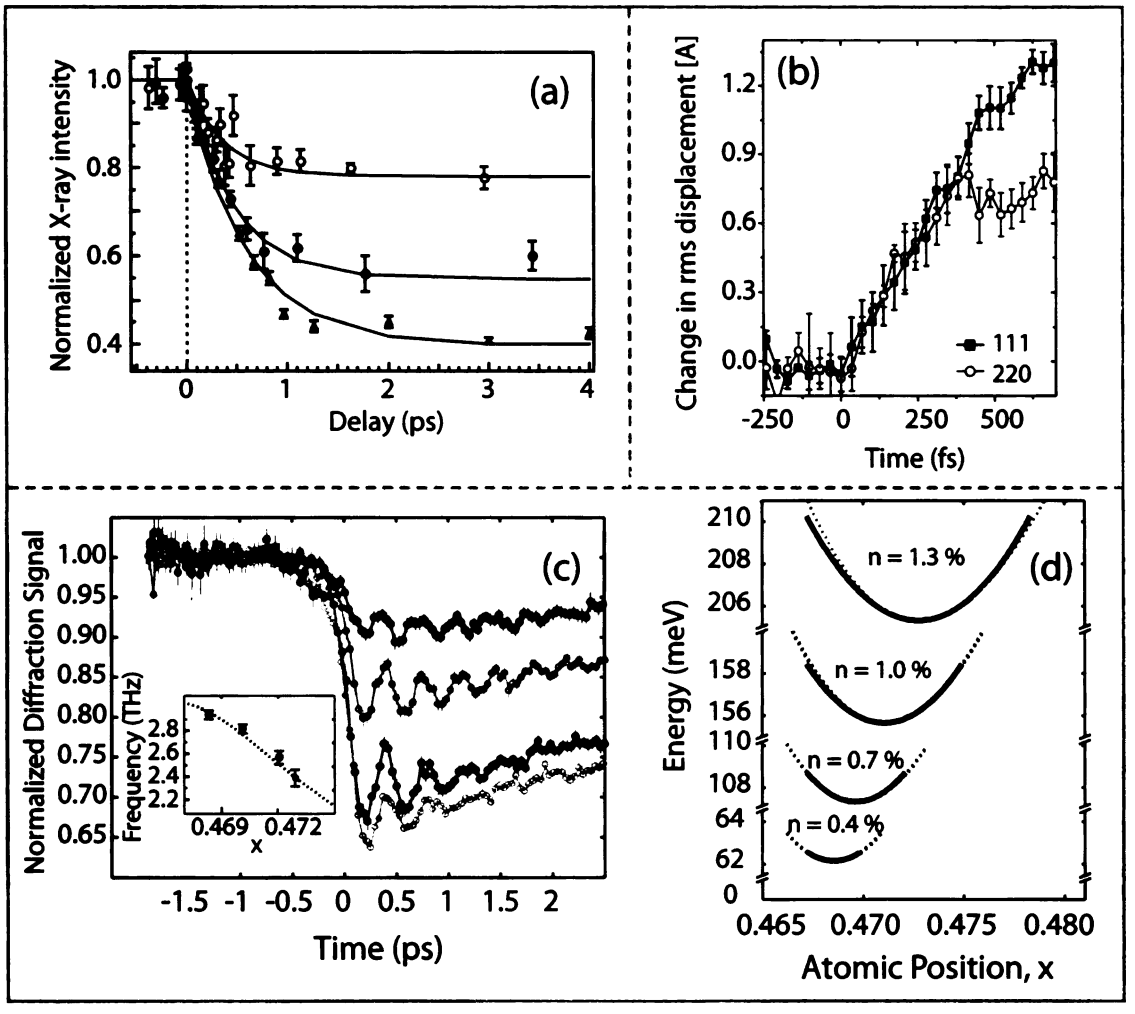

Figure 1.4: Ultrafast X-ray diffraction studies of non-thermal melting. (a) From Ref. [48] - Normalized X-ray diffraction intensity from InSb excited at $\approx$ 120 mJ/cm^2 for three probing depths: 3500 Å (open circles), 1700 Å (filled circles) and 1200 Å (open triangles). (b) From Ref. [49]. Atomic root mean square displacements of InSb atoms along the 111 and 220 directions. (c, d) From Ref. [50]; (c)Diffraction signal from photoexcited Bi, showing generation of coherent A_{1g} phonons at increasing excitation fluences. Inset shows measured phonon frequency as a function of inversion asymmetry (x=0.5 = perfectly symmetric), which is measured by the baseline shift in intensity. (d) Calculated inter-atomic potentials as a function of carrier density n.

X-ray studies have also identified the importance of coherent phonons [34, 46, 47, 51–53] and bond-softening effects [49, 50] in driving these processes. Lindenberg *et al.* [49] reported the atomic dynamics in InSb following photoexcitation to be *inertial*, in that, the atomic displacements increased linearly for several hundred femtoseconds with room temperature thermal velocities [Fig. 1.4(b)]. This was attributed to the lattice evolving over a modified potential energy surface (PES) with 'softened' restoring forces, before large scale phonon excitations perturb the lattice. Fritz *et al.* [50] on the other hand have studied photoinduced structural dynamics in Bismuth along the Peierls distorted body diagonal. Photoexcitation leads to impulsive oscillation of the atoms about this Pierls distorted configuration which they attribute to a carrier denisty dependent 'displacive' shift of the PES to a new minima accompanied by bond-softening effects evident from the red-shift of coherent A_{1g} phonons. [See Fig. 1.4(c, d)].

There has also been a significant thrust from the theoretical side to understand the origins of such nonthermal processes. Initial approaches utilizing the plasma annealing model attempted to relate the phonon frequencies to increased carrier density (albeit under equilibrium conditions) and minimize the electron-phonon component of the free-energy [54]. The free energies thus calculated indicated possibility of phase transition at elevated carrier density despite only nominal increase in lattice temperatures. More recently, Stampfli & Bennemann have used molecular dynamics (MD) simulations to model the non-equilibirum aspects of these processes [55–57]. Calculations are based on a tight-binding Hamiltonian that employs phenomenological force field models for bonding in semiconductors. Importantly, their model incorporates a carrier density dependent repulsive interaction between the atoms that was not addressed in the PA model. They observed [See Fig. 1.5(a, b)] that promotion of 15% of the charges in silicon can lead to the atoms gaining significant kinetic energy within 100 fs with average atomic displacements as large as 1 Å [56]. On the

other hand, Parinello & co-workers have performed *ab initio* MD simulations based on finite-temperature density functional theory (DFT) to model the laser melting of Si [58]. The approach incorporates self consistently the effects of electronic excitations and fractionally occupied states without the need for any phenomenological force-field models [59]. Their calculations also reveal [See Fig. 1.5(c)] a rapid increase in atomic displacement along with a concomitant rise in lattice temperature, which they differentiate from a simple transfer of energy from electrons to lattice [58, 60]. The liquid-like phase thus generated on the ps timescale has properties unlike ordinary liquid Si [61] and is hence proposed to be a unique transient state. While Benneman *et al.* attribute the lattice instabilities to softening of phonon modes [55–57], Parrinello *et al.* do not observe significant effects of photoexcitation on the phonon modes and instead attributes the phase transformation to the forces generated by a modified PES [60].

Despite some disagreement over the disorder initiating mechanisms within the first 100 - 200 fs, there is overall consensus that order-disorder transitions in semiconductors at fluences exceeding the damage threshold are nonthermal in nature. The key idea emerging from these studies is that under the right excitation conditions, lattice disorder can proceed under the impetus of room-temperature thermal motion. It is however important to remember that complete obliteration of bonds is unlikely on the ultrafast timescales as *ab initio* MD simulations have shown that covalent bonding character is preserved even in the liquid state [61].

1.4 Ultrafast Solid-Solid Phase Transformations

The studies reported thus far concentrated on matter under intense excitation, often at limits twice over the damage threshold. Recently, another interesting avenue of materials research has opened up involving solid-solid phase transitions that occur at

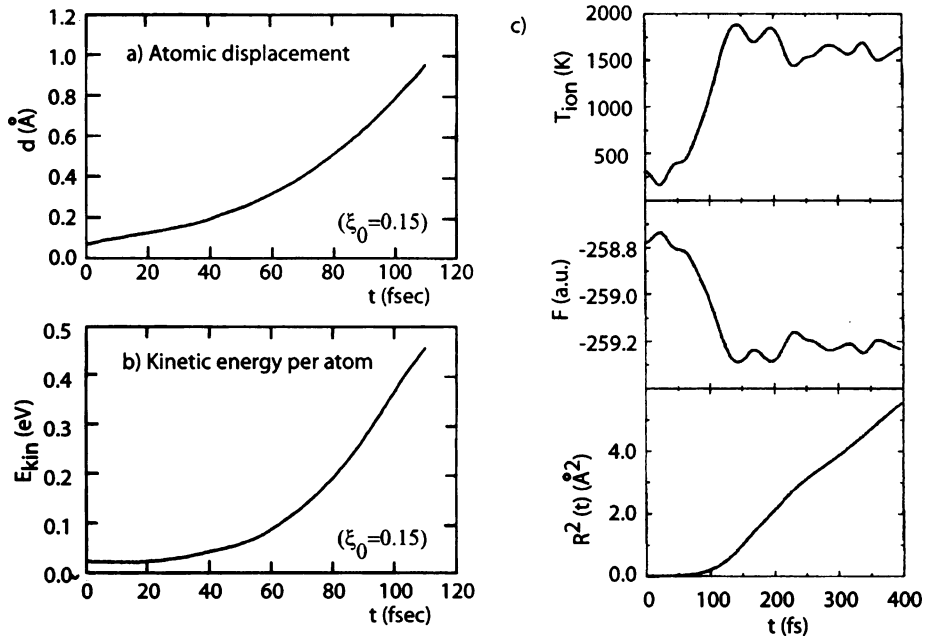

Figure 1.5: Theoretical modeling of Nonthermal melting in silicon. (a, b) From Ref. [56]. Time evolution of (a) average atomic displacement from the ideal 'diamond lattice' positions and (b) average kinetic energy of Si atoms following photoinduced creation of e-h plasma of density ξ =0.15. (c) From Ref. [60]. Time evolution of ionic temperature T_{ion}, free energy F and atomic mean square displacement R^2 following initial electronic temperature T_e set to 25000 K, corresponding to photoexcitation at $\approx$ 2.15 eV.

fluences below the material damage threshold without melting.

Solis & co-workers have observed the *enhanced* crystallization of amorphous GeSb films when excited by sub-ps laser pulses [12]. The reflectivity from amorphous film rose following photoexcitation to *exactly* crystalline-like values (thus discounting e-h plasma effects) within 250 fs [13] [See Fig. 1.6(a, b)]. While the complete phase transformation occurred on the ns timescale, they observed a strong spatial correlation between the region that exhibited initial fs reflectivity rise and that which eventual transformed completely on the ns timescale [panel (b)]. The lattice thus seemed to 'remember' the spatial region over which the sub-ps phase transformation was initiated.

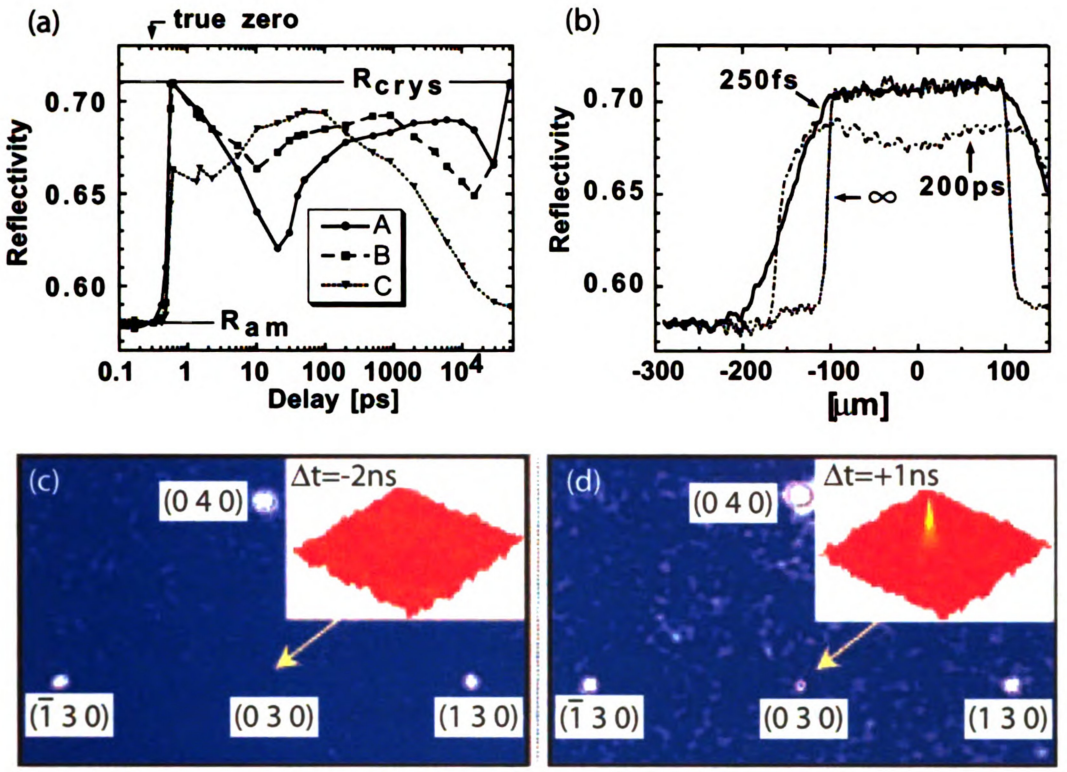

Figure 1.6: Ultrafast Solid-Solid Phase Transformations. (a, b) From Ref. [13]. Amorphous-to-crystalline transformation in GeSb films. (a) Time evolution of reflectivity from three positions A, B and C corresponding to local excitation fluence of 45, 20 and 12 mJ/cm^2 respectively. (b) Cross sections of time-resolved reflectivity across a pump-excited region at 3 different time delays. (c, d) From Ref. [16]. Ionic-to-Neutral phase transformation in a molecular charge transfer crystal. X-ray diffraction patterns recorded before (c) and after (d) photoexcitation. Emergence of the (030) peak on the ns timescale suggests macroscopic phase transformation.

Another interesting example of such electronically induced phase transformations is the reversible phase change between ionic and neutral phases of molecular charge transfer crystals. Optical experiments have reported the macroscopic conversion from ionic to neutral phases on the tens of ps timescales [14, 15] when the excitation exceeds a certain critical threshold intensity. This has been confirmed by time-resolved X-ray studies of the process [16], where the appearance of a new Bragg peak identified the structural transformation [See Fig. 1.6(c, d)]. The process has been explained by the concept of macroscopic cooperativity where the creation of a critical number of neutral

domains allows the system to act in a concerted fashion, triggering a macroscopic change.

Recently, Cavalerri and coworkers using optical reflectivity in conjunction with time-resolved X-ray diffraction have identified an optically driven solid-solid insulator-to-metal phase transitions in VO_2 [62]. At fluences of 25 mJ/cm^2 (sample damage threshold $\approx$ 63 mJ/cm^2) the phase transition was initiated within 300 fs. Experiments involving extremely short 15 fs pump pulses revealed the phase transition to be delayed relative to the pulse excitation [17], thus indicating a structural origin to the observed change. This was further confirmed by diffraction signatures obtained from ultrafast electron crystallography (UEC) study. UEC allows the tracking of multiple Bragg reflections simultaneously, in contrast to X-rays studies where often only one or two Bragg peaks are co-present. By studying the time-evolution of multiple VO_2 Bragg peaks following photoexcitation, Zewail and co-workers revealed [18] that the initial mechanism responsible for the structural change lies in the V-V bond dilation. Since the initiating 1.55 eV excitation primarily involves the *d*-band which arises from bonding between the vanadium pairs, excitation of this d-band weakens the bonding between adjacent V-V pairs, leading to the bond dilation and unit cell shearing that triggers the phase transformation. Furthermore, while the bond-dilations were observed on the fs timescale, lattice shearing, which is essential for the phase transformation proceeded on much longer ns timescales.

These studies raise important unresolved questions. On what timescales do macroscopic structural changes occur within photoexcited systems? While it is undeniable that they are initiated on the fs timescale, how long does it take for the initiated processes to come to fruition on the macroscopic scale? The persistence of Bragg peaks under nonthermal melting conditions suggest that some degree of long range lattice order may preserved even on longer ps timescales. Furthermore, what is the driving force behind such atomic motion? Is it a displacive excitation that shifts the

PES minima, or bond-softening that alters the inter atomic forces, or both? What is the role of coherent phonons in mediating these processes?

In this study, we will utilize UEC to examine two such electronically induced structural transitions - the photoinduced graphite-to-diamond transition and the photoinduced fragmentation of silver nanocrystals.

1.5 Graphite-Diamond Transition

The interconversion between graphite and diamond is important from a technological as well as scientific viewpoint on account of the widely contrasting properties of the two, despite the chemical similarity. Graphite is soft, opaque, black, and good electrical conductor, whereas diamond is hard, transparent, lustrous, and an electrical insulator. These differences arise solely from their different structural motifs.

Graphite is a layered structure composed of sp^2 hybridized carbon atoms engaged in strong in-plane σ-bonds to form a planar hexagonal net structure. The loosely bound electrons in the out-of-plane π-oribitals are delocalized over the entire sheet and form weak van der Walls bonds with adjacent layers [63]. The relatively weak inter-layer bonds renders the material soft with easy cleaving properties and the delocalized π electrons make it a very good electrical conductor. Diamond, on the other hand is composed of sp^3 hybridized C atoms in which all 4 valence electrons are engaged in strong σ-bonds. Each C atom is tetrahedrally coordinated and the lattice structure can be described as 2 inter-penetrating fcc structures with one fcc cell displaced by 1/4th along the body diagonal. This rigid crystalline structure imparts to diamond its industrially prized hardness and the lack of any loosely-bound or free electrons makes it an excellent electrical insulator.

1.5.1 Thermodynamic Pathways

Both graphite and diamond are extremely stable forms of carbon and are separated by a large activation barrier between them. The phase diagram of carbon [64] shown in Fig. 1.7(a) reveals that while lower pressures favor graphite, the high pressure region is dominated by diamond. Thus, artificial synthesis of diamond has relied on creating extreme temperature and pressures in laboratories to produce what are termed as HPHT (high pressure high temperature) diamonds. The first such successful and *reproducible* synthesis of HPHT diamonds was reported by a team at General Electric research lab in 1950s [65, 66]. Subsequently, diamond was also produced by shock-compression of graphite [67] and the use of elevated temperatures saw the creation of a novel hexagonal form of diamond [68]. Such process relied on the spontaneous crystallization of carbon into the preferred diamond structure at high pressures. They thus lacked precision, and were almost always accompanied by atomic defects - nitrogen, in particular. Of late, chemical vapor deposition (CVD) techniques have been utilized to grow diamond-like thin films in which a gaseous source of carbon, such as methane (CH_4) is dissociated under application of RF fields, and the carbon allowed to condense on a substrate in the diamond-form. Inhibitors such as atomic hydrogen are used to suppresses the formation of sp^2 bonded graphitic structures. CVD diamond films are typically of nm thickness. Pulsed laser ablation using ns lasers have also yielded diamond in the micron scale [69]. A recent study involving compression of graphite within diamond anvil cell up to pressures of $\approx$ 25 GPa revealed that ordinary graphite turned into a transient super hard graphite with almost 50% bonds reportedly converted into sp^3 like state [70]. However, complete diamond structure was not attained and the super hard graphite reverted to ordinary graphite once the pressure was released.

The need for such extreme conditions for diamond conversion has its roots in the

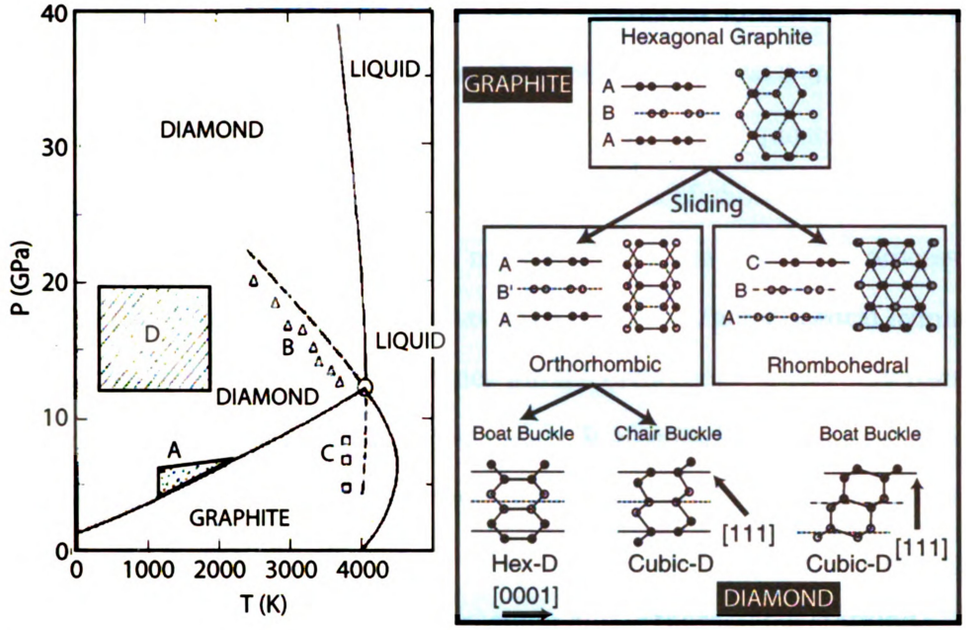

Figure 1.7: Thermodynamic Pathways For Graphite - Diamond Transitions. (a) Carbon phase diagram, from Ref. [64]. A = region for catalytic transformation of graphite(g) to diamond(d). B = spontaneous fast g-d. C = spontaneous fast d-g. D = spontaneous slow martensitic tranformation of hex-g to hex-d. (b) Cartoon depicting the sliding and buckling of graphite layers, necessary for its conversion into diamond.

enormous activation barrier between the two phases. A look at the relative structures of graphite and diamond reveals that graphite-to-diamond conversion requires two essential steps as illustrated in Fig. 1.7(b). (1) The relative sliding of two adjacent layers followed by (2) buckling of the layers to form interlayer tetrahedral bonds. Both of these steps appear to be energetically costly from the thermodynamic viewpoint. Energy minimization calculations within the framework of *ab initio* DFT have shown that at ambient temperatures and pressures, graphite and diamond structures sit at a PES minima separated by a significant activation barrier of 0.33 eV/atom [71]. In the same study, graphite was 'observed' to transform into diamond under isotropic pressures of 80 GPa, provided persistence of rhombohedral symmetry (ABC stacking) was enforced. At this pressure, the interlayer distance approached a critical value of $\approx$ 2.1 Å at which, significant inhomogeneity in π-orbital charge density tended

to favor the formation of tetrahedral sp^3 bonds. Diamond formation through the rhombohedral structure has been observed in experiments as well involving pulsed laser ablation of graphite in a liquid environment [72]. The rapid quenching of ablated products in this experiment have revealed the presence of rhombohedral graphitic (ABC stacking) forms, presumably frozen midway during the conversion process. On the other hand MD simulations that relaxed the stringent rhombohedral symmetry preservation condition reported a preference for the orthorhombic pathway resulting in hexagonal diamonds [73] as realized by Bundy & Kasper [68]. However, the MD calculation also reported similar conversion pressures of 80 GPa as the DFT study, at which, the interlayer sliding was observed to become barrierless, with the graphite layers freely transforming between the hexagonal and orthorhombic stacking.

1.5.2 Electronically Induced Diamondization

The difficulty in implementing *in situ* monitoring of structure modifications during the graphite-diamond transformation has limited the understanding of the process at the atomic level, and the subject has been mainly addressed theoretically [1, 71, 73–75]. Recently, Banhart and colleagues have made significant contributions in monitoring nanoscale diamond synthesis under electron beam irradiation inside a TEM [See Fig. 1.8(a, b)]. Under conditions of high temperature and intense irradiation from a highly energetic ($\sim$ 1.25 MeV) electron beam, carbon onions were found to undergo self-compression leading to nucleation of diamond crystals within the core, where pressures could exceed 100 GPa [76]. Surprisingly, once a diamond structure nucleated within the core, diamond formation proceeded unhindered even in the outer layers of the onion where high pressures are not expected [77]. The only essential criteria for the sustenance of the conversion process was continual generation of defects under constant irradiation. The authors proposed that radiation induced bond-breaking in carbon specimens due to electronic excitations and knock-on effects

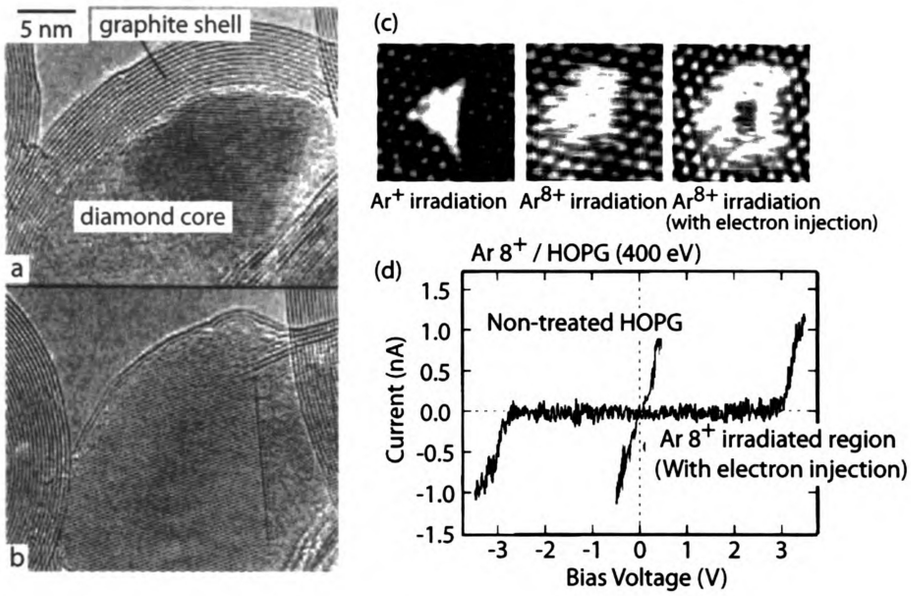

Figure 1.8: Graphite - diamond transitions through electronically induced pathways. (a, b) Complete transformation of carbon onions into diamond under 1.25 MeV electron beam irradiation inside a TEM [77] (c, d) Formation of nanodiamond following electron injection into Ar^{8+} irradiation damaged area [2]. (c) STM images and (d) Scanning tunneling spectroscopy I-V curves.

together with the increased temperatures of 850-1050 K may lower the energy barrier for graphite-diamond conversion. Such irradiation induced diamond formation was also observed on planar graphite surfaces [78], suggesting that the graphite-diamond transition might be feasible on a general scale and not restricted to carbon structures with specific geometry.

Around the same time, Meguro and co-workers also reported the creation of nanodomains of diamond within an extended graphite lattice [2] following electron injection (using an STM) into an area damaged by highly charged Ar^{8+} ion irradiation [See Fig. 1.8(c, d)]. The need for electron injection suggested that the diamond formation proceeded through some sort of modification of the local electronic states. Wang and co-workers were also able to synthesize nanocrystalline diamond purely by Ar^{+} irradiation of graphite. A first principles time-dependent DFT study modeling these

processes has suggested that enhanced charge transfer from the collision of Ar^{8+} with the carbon atoms perturbs the lattice significantly leading to creation of vacancies and large atomic displacements leading to not only sp^3-like bonds but also a variety of other structures [79].

These studies have revealed the promise of inducing the graphite-diamond transition via an electronic destabilization of the graphite lattice. Interestingly, a first principles DFT calculation has suggested that graphite structure becomes greatly destabilized when holes are excited in the valence π band [1]. As the π electrons stabilize the in-layer σ bonds, the generation of holes within this valence π band can break the σ bonds and allow the atoms to diffuse vertically, providing the possibility of sp^3 bond formation. The study found that at a critical hole density of 0.1 per atom, the graphite-diamond transition became barrierless.

Thus, as mentioned earlier, it appears that formation of diamond requires two essential conditions - (1) The sliding of the layers relative to one another and (2) Seeding of valence holes that can distort the lattice, creating defect sites around which new diamond structures can nucleate. Laser photoexcitation of graphite lattice can serve as an ideal way to generate both criteria necessary for diamondization. Ultrafast photoexcitation in graphite is known to be strongly coupled to the E_{2g} phonons that represents the interlayer shearing mode that can effect local layer sliding [33, 80, 81]. This allows efficient concentration of the energy within these layer shearing modes. Additionally, p-polarized light preferentially interacts with the π-electrons, and can be used to generate valence holes to seed defects within the graphite lattice. As will be shown in this study, such electronic excitation of the graphite system triggered by our p-polarized laser can indeed lead to the creation of new $sp^2 - sp^3$ hybrid structures evidenced via our diffraction probing of transient structures. Similar formation of nanodomains of sp^3 structures in photoexcited graphite has since been evidenced using STM investigations as well [82].

1.6 Photoinduced Fragmentation of Silver Nanocrystals

Nanostructures are another class of promising system for the study of such electronically induced transformations. They exibit novel electronic configurations and enhanced coupling between the electronic and atomic degrees of freedom on account of their reduced size and dimensionality. Significant effort has been expended on understanding the interaction of these NCs with light in the ultrafast regime. It is now well known that the photophysics of metal NCs is dominated by the creation of *surface plasmon resonance* (SPR), which is a collective oscillation of the conduction electrons within the NC in response to the incident electromagnetic radiation [83, 84]. Excitation of metallic NCs at SPR is highly selective, with the NC response dependent on their shape, size and dielectric environment [85–89] which affect their structural [90], optical [91] and sensing [92] capabilities.

At low power levels, SPR excitations can lead to the triggering of impulsive coherent oscillations of the NCs, which are experimentally observed through the resulting modulation of dielectric constants of the NC [93, 94]. Most of the optical studies have focussed on elucidating fundamental material properties such as electron-electron [87, 89, 95] and electron-phonon scattering rates [96, 97] and heat dissipations [88], which can be temperature dependent. Consequently, most of these studies have been conducted in the regime of low excitation levels.

Upon turning up the laser power levels, further interesting physics can be uncovered. At SPR excitation, the optical near field can build up values far exceeding those illuminating the NC, causing in the process, charging [98], fragmentation[99–103], and surface ablation [104] even at moderate fluences. Such optically induced fragmentation of nanoparticles has been a source of debate and has been attributed variously to thermal ablation, in which the NPs recondense from vapor following explosive boiling

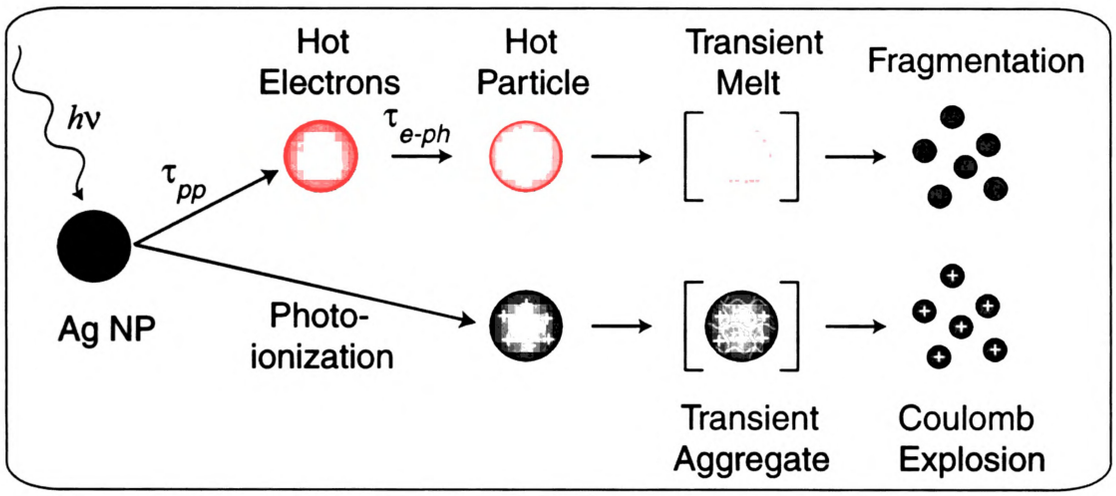

Figure 1.9: NC fragmentation pathways - explosive boiling and Coulomb explosion.

[100] and also to Coulomb explosion, in which rapid NP charging is induced either by thermionic [102] or multiphoton ionizations [99, 103] forming transient charged aggregates, as outlined in Fig. 1.9. For bulk materials, both pathways have been extensively investigated [105], and the threshold for laser ablation was found to be an order of magnitude higher than the limits for material melting, depending on the pulse duration of the laser. Using nanosecond (ns) pulse irradiation, the thermal mediated process usually dominates, whereas with pulse duration less than 100 femtosecond (fs), nonthermal channels were considered, such as plasma formation and optical breakdown phenomena in dielectrics [105], and bond softening caused by interband transitions in metals [106], reached within the timescales for electron-phonon and lattice thermalizations. In contrast, for NPs, significant reduction of the threshold for photoinduced disintegration was observed [99, 101, 104], especially near SPR, representing a new class of phenomena.

The reaction pathway of such light - NC interactions on the atomic scale has remained elusive, in part due to the inability of optical probes to *directly* trace atomic motions. As a result, the mechanism bridging the femtosecond (fs) optical seeding to the picosecond (ps)-to-nanosecond (ns) macroscopic structural changes remains a

central topic to be elucidated, With the development of ultrafast X-ray sources, scattering based experimental techniques have forged in, attempting to fill this gap by providing direct access to the atomic structures. Plech and co-workers have investigated the structural dynamics of photoexcited, surface supported nanoparticles using time-resolved X-Ray diffraction and observed particle heating by fs laser and subsequent cooling on the nanosecond time scales. They have also observed evidence for initial nonthermal effects in the NC response, though the instrumental resolution of 100 ps has prevented a detailed study of the initial structural dynamics. More recently, diffractive imaging using coherent ultrashort X-rays from free-electron lasers is fast emerging as an attractive technique to obtain 3-dimensional snap-shots of nanoscale structures [107, 108], though atomic scale resolution has not yet been achieved.

1.7 Summary

Understanding the dynamics of such complex structure rearrangement processes on the nanoscale from the femtosecond initiation to their eventual conclusion on longer ns timescale requires the ability to image the atomic rearrangements [14, 16, 109] and their redistribution along with dynamics of charges in real time. Diffractive structure probes can fill in major pieces of the puzzle, augmenting optical investigations to elucidate the complete material transformation pathway. Here we have used ultrafast electron crystallography (UEC) [110], to directly probe the photoexcited transient structures in graphite and Ag NC up to the ablation limit, and identified the transient dynamical structures and the charge states. UEC offers some desirable advantages over X-ray and optical approaches. (1) It is a structure probe that directly follows atomic dynamics. (2) Experiments are on table-top scale allowing high degree of instrumentation flexibility. (3) Since electrons interact strongly through the Coulombic interaction with the nuclei and electrons in a material, the scattering

cross-sections are orders of magnitude larger than that for X-rays allowing sensitive probing of nanostructures and materials with low mass (such as carbon). (4) Due to this strong interaction, the scattering depth of electrons in systems better matches the optical penetration depth ($\sim$ 10-50 nm) leading to reduced contamination of the time-resolved signal from unpumped regions of the sample. (5) Electron bunches are easier to manipulate than X-rays leading to well-developed schemes to strongly focus them along transverse (spatial) as well as longitudinal (time) directions and thus obtain tightly focused femtosecond electron probes. (6) The charged electrons interact with, and are sensitive to the dynamics photoinduced interfacial charges which play an important role in structure transformation processes occurring on or near surfaces.

For these reasons, the development of ultrafast electron diffraction (UED) [28, 111, 112], crystallography (UEC) [113] and microscopy (UEM) [114] along with that of the Dynamic Transmission Electron Microscope (DTEM) [115] serve as powerful tools to study structural dynamics of systems ranging from gaseous molecular to nanoscale condensed phases and bulk materials.

Chapter 2

Diffraction Theory & Data Reduction Procedures

Diffraction has served as one of the most powerful experimental tools in determining unknown structures, and has been part of pivotal moments in scientific history (See table 2.1). It is hardly a new concept and several seminal references provide a detailed and rigorous treatment of the subject [116–120]. Nevertheless, an attempt has been made in the following sections to provide an intuitive feel for diffraction and the interpretation of diffraction patterns. The aim here is to provide a conceptual introduction to the phenomena of diffraction, which the experts may conveniently overlook. Mathematical rigor has been suppressed in favor of conceptual clarity. Following the basics, Sec. 2.2 lays down the data-reduction formalisms specific to the experimental geometry employed in this study.

2.1 Diffraction Basics

Diffraction is a term given to the interference of waves scattered by a collection of objects or *scatterers* placed in its path. When these scatterers are arranged in

Year	Recipients	Field	Citation
1914	Max Von Laue	Physics	*for the discovery of diffraction of X-rays by crystals*
1915	Sir William H. Bragg, William L. Bragg	Physics	*for their services in the analysis of crystal structures by means of X-rays*
1937	Clinton J. Davisson, George P. Thomson	Physics	*for their experimental discovery of the diffraction of electrons by crystals*
1962	Francis H. C. Crick, James D. Watson, Maurice H. F. Wilkins	Medicine	*for their discoveries concerning the molecular structure of nucleic acid and its significance for information transfer in living material*
1962	Max F. Perutz, John C. Cowdery	Chemistry	*for their studies of the structures of globular proteins*
1964	Dorothy C. Hodgkin	Chemistry	*for her determinations by X-ray techniques the structures of important biochemical substances*
1994	Bertram N. Brockhouse & Clifford G. Shull	Physics	*for pioneering contributions to the development of neutron scattering techniques for studies of condensed matter*

Table 2.1: List of Nobel prizes awarded for diffraction-related work

a regular periodic arrangement, such as atoms in a crystal lattice, then there exist certain specific directions along which the waves scattered from the different scatterers are *in-phase* with each other and interfere constructively. This gives rise to a pattern on a screen / detector placed far away that comprises of bright maxima and dark minima. The directions of maxima and minima of scattered waves and consequently their location on the screen depends on the internal arrangement of the scatterers. It is in this sense that the analysis of diffraction patterns can, in principle, provide insights into the internal structure of the material that scatters the waves.

2.1.1 Scattering & Momentum Transfer

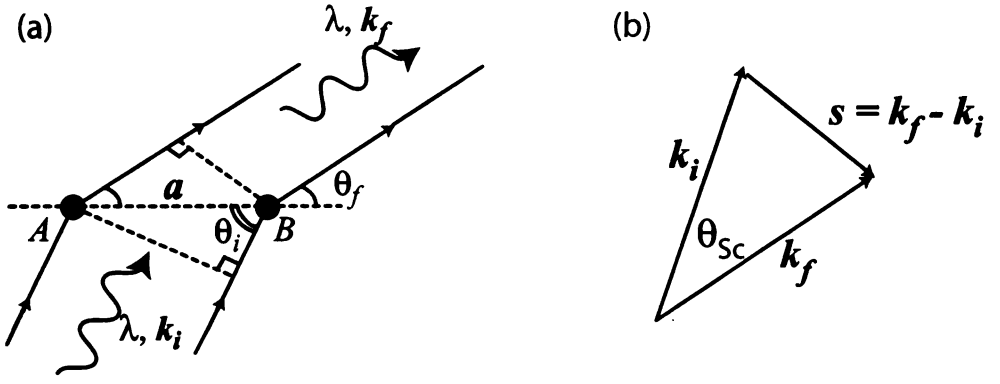

Figure 2.1: (a) Elastic scattering from 2 identical scatterers. Vectors $\mathbf{k_i}$ and $\mathbf{k_f}$ denote the initial (incident) and final (scattered) wave vectors. (b) Pictorial definition of *momentum transfer* **s** - the vectorial change in the wave-vector of incident wave as a result of scattering along a given direction.

Consider a simple scattering geometry consisting of 2 scatters located at A and B separated by vector **a** as shown in Fig. 2.1. Let radiation of wavelength λ be incident upon them at an angle θ_i. The condition for constructive or destructive interference along any specific direction θ_f in the far-field region would depend on the relative

phase ϕ between the waves scattered from points A and B, which is given by

$$\begin{aligned}
\phi &= \frac{2\pi}{\lambda}\,(\text{path difference}) \\
&= \frac{2\pi}{\lambda}\,(a\cos\theta_f - a\cos\theta_i) \\
&= ka\cos\theta_f - ka\cos\theta_i \qquad \text{where } k = 2\pi/\lambda \\
&= \mathbf{k_f}\cdot\mathbf{a} - \mathbf{k_i}\cdot\mathbf{a} \\
&= \mathbf{s}\cdot\mathbf{a} \qquad \text{where } \mathbf{s} = \mathbf{k_f} - \mathbf{k_i}
\end{aligned}$$

$\mathbf{k_i}$ and $\mathbf{k_f}$ represent the initial (incident) and final (scattered) wave-vectors, and the quantity $\mathbf{s} = \mathbf{k_f} - \mathbf{k_i}$ is conventionally called *momentum transfer.* This is because $\mathbf{s}$ is a measure of the vectorial change in the *de Broglie momentum* $\mathbf{p} = \hbar\mathbf{k}$ of the wave due to scattering, as illustrated in Fig. 2.1(b) and serves as a convenient and indeed *appropriate* measure to parameterize scattering process. While absolute values of $\mathbf{k_f}$ and $\mathbf{k_i}$ are specific to the experimental geometry and choice of reference frames, $\mathbf{s}$, which denotes *the relative change* in the wave propagation direction is not, and is thus an intrinsic descriptor of the scattering process. As a result, diffracted intensities are always expressed as a function of momentum transfer s.

For now, we will be concerned only with *elastic* scattering, in which the scatterer merely alters the direction of propagation of the incident wave, without absorbing / rejecting any energy from / to the wave. This type of interaction is the dominant contributor to the strong Bragg peaks observed in various diffraction patterns. *Inelastic* scattering, in which the incident wave exchanges energy with the lattice affects the intensities of these Bragg peaks and is certainly an important effect to be considered in quantitative diffraction studies. However, such energy transfer typically occurs on much smaller eV energy scales, which is negligible compared to the keV probes used in this study. Hence, the energies of the incoming and outgoing waves are nearly equal with $k_f = k_i = k = 2\pi/\lambda$. In such a scenario, it is useful to relate the magnitude s of

momentum transfer **s** to the scattering angle θ_{Sc}. From Fig. 2.1(b), we can deduce using the trigonometric law of cosines

$$\begin{aligned} s^2 &= k_f^2 + k_i^2 - 2k_f k_i \cos\theta_{Sc} \\ &= 2k^2(1 - \cos\theta_{Sc}) \\ &= 4k^2 \sin^2(\theta_{Sc}/2) \end{aligned}$$

Thus the momentum transfer s and scattering angle θ_{Sc} are related in elastic scattering as

$$s = \frac{4\pi}{\lambda} \sin\left(\frac{\theta_{Sc}}{2}\right) \tag{2.1}$$

2.1.2 Scattering from a 1-D Lattice - the Laue Function

Let us now augment the two scatters by adding more identical scatters at a uniform repeat distance of a, forming a 1-D *lattice* along the x-axis as shown in Fig. 2.2. Without loss of any generality, let us assume the first scatterer to be located at the origin $x = 0$. The basis vector defining this lattice is $\mathbf{a} = a\hat{x}$, and the location of m^{th} scatterer is given by $m\mathbf{a}$. Then, the total phase of the scattered wave along any direction indexed by **s** would be given by

$$\begin{aligned} \Phi &= \sum_{m=1}^{N-1} e^{im(\mathbf{s}\cdot\mathbf{a})} \\ &= \left(1 + e^{2i\mathbf{s}\cdot\mathbf{a}} + e^{4i\mathbf{s}\cdot\mathbf{a}} \ldots + e^{2(N-1)i\mathbf{s}\cdot\mathbf{a}}\right) \end{aligned}$$

This is a simple geometric series, which can be analytically summed to give

$$\begin{aligned} \Phi &= \frac{1 - e^{i2N\beta}}{1 - e^{i2\beta}} \qquad \text{where} \quad \beta = \mathbf{s}\cdot\mathbf{a}/2 \\ &= e^{iN\beta}\left(\frac{\sin(N\beta)}{\sin(\beta)}\right) \end{aligned}$$

If A_0 were to denote the scattering due to a single scatterer, then the total scattering amplitude, and the corresponding intensity along the momentum transfer direction specified by s is given by

$$A(\mathbf{s}) = A_0(\mathbf{s})\, e^{iN\beta}\, \frac{\sin(N\beta)}{\sin(\beta)} \quad ; \quad I(\mathbf{s}) = I_0(\mathbf{s})\, \frac{\sin^2(N\beta)}{\sin^2(\beta)} \quad ; \quad \beta = \frac{\mathbf{s}\cdot\mathbf{a}}{2} \tag{2.2}$$

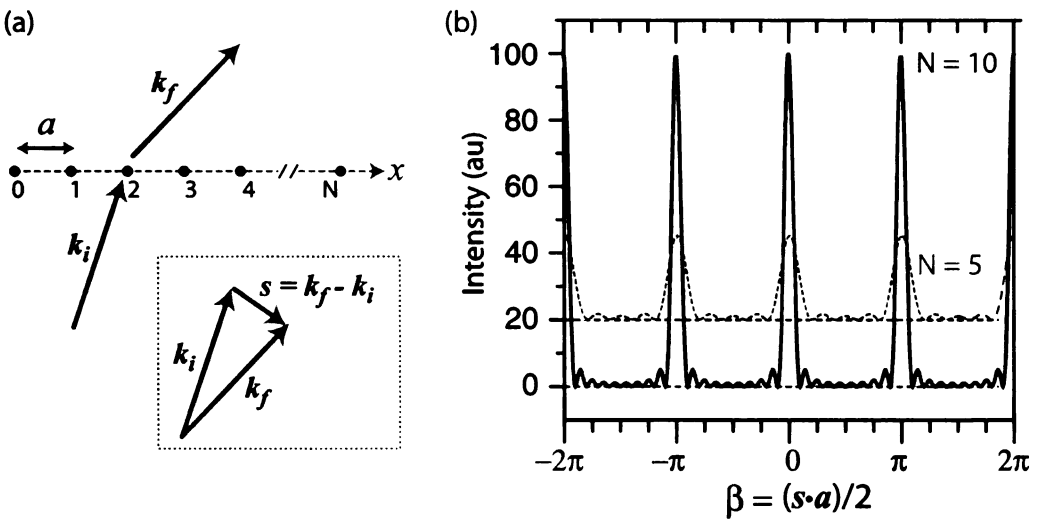

Figure 2.2: (a) Scattering geometry for a 1-D chain of N identical scatterers. (b) Diffraction intensity expected from the geometry in (a) and described by the Laue function (Eqn. 2.2), graphed for N = 10 (solid blue) and N=5 (dashed red). The two curves are vertically displaced for clarity.

The functional form of I_0 in Eqn. 2.2 is sometimes referred to as the *Laue function* and occurs frequently in analysis of diffraction patterns, including those obtained from a diffraction grating. It is worthwhile to examine the analytic behavior of the Laue function as its provides conceptual insights in the interpretation of diffraction patterns.

The Laue functions for $N = 5$ and $N = 10$ are graphed in Fig. 2.2(b). They are composed of a series of strong *primary maxima*, separated by many weaker *secondary maxima*. To examine how this pattern arises, let us consider for sake of mathematical simplicity, the functional form of scattering amplitude in Eqn. 2.2, instead of the Laue

function itself.

$$\xi(\beta) = \frac{\sin(N\beta)}{\sin(\beta)} \tag{2.3}$$

- *Primary maxima*: ξ attains a sharp maxima whenever β approaches a multiple of π.

$$\lim_{\beta \to m\pi} \frac{\sin(N\beta)}{\sin\beta} \to \lim_{\beta \to m\pi} \frac{N\cos(N\beta)}{\cos\beta} = \pm N \tag{2.4}$$

- *Zeroes*: ξ reaches zero whenever $\sin(N\beta) = 0$ while $\sin\beta \neq 0$, which occurs whenever $N\beta$ is a multiple π while β is not i.e. $\beta = m\pi/N$ where m/N is not an integer.

$$\frac{\sin(N\beta)}{\sin\beta} = 0 \quad \text{if } \beta = \frac{\pi}{N}, \frac{2\pi}{N}, \frac{3\pi}{N}, \ldots \frac{(N-1)\pi}{N}, \frac{(N+1)\pi}{N}, \ldots \tag{2.5}$$

  This tells us that between any two consecutive primary maxima of ξ, there exist $N-1$ zeroes. Since any analytic function must posses at least one maxima/minima between two zeroes, the Laue function (i.e. $\sim \xi^2$), will exhibit $N-2$ secondary maxima between any two primary maxima.

- *Secondary maxima* The location of secondary maxima of ξ are determined by the condition

$$\frac{d}{d\beta}\left(\frac{\sin(N\beta)}{\sin\beta}\right) = 0 \quad \Rightarrow \quad \frac{\sin(N\beta)}{\sin\beta} = N\,\frac{\cos(N\beta)}{\cos\beta} \tag{2.6}$$

This is an example of *transcendental equation* which is not analytically solvable, and often solved numerically. However, it can be shown that the intensity of these secondary maxima varies as N, as opposed to the intensity of primary maxima that varies as N^2 as suggested by Eqn. 2.4.

Based on these observations about the behavior of the Laue function, the following important conceptual insights are apparent.

1. **Diffraction contrast ratio**: From equations 2.4 and 2.6, as the intensity of primary maxima (referred to henceforth as *diffraction maxima*) varies as $\sim N^2$, while that of the secondary maxima varies as $\sim N$, an increase in the number of scatterers N will lead to an increase in the contrast ratio between the primary and secondary peaks, making the primary peaks *stand out* better.

2. **Diffraction maxima width**: The zero immediately following any diffraction maxima at $\beta = m\pi$ occurs at $\beta = m\pi + \pi/N$. Thus the width of the primary maxima varies as $\sim 1/N$. Hence, an increase N makes the primary maxima sharper.

3. **Diffraction as a measure of lattice periodicity**: Any two successive diffraction maxima are separated in the β-space by $\Delta\beta = \Delta\mathbf{s}\cdot\mathbf{a}/2 = \pi$, where $\Delta\mathbf{s}$ denotes the difference between the momentum transfer vectors associated with each maxima. Given that our 1-D chain of scatters was oriented along x direction, we can then write

$$a = \frac{2\pi}{\Delta s_x},$$

where Δs_x denotes the projection of the change in momentum transfer associated with adjacent diffraction maxima along the x direction. To state this in more general terms, if the diffraction pattern obtained from any unknown structure exhibits a *family* of bright maxima equidistant in the s or β space, then that periodicity in s-space is inversely related to the periodicity of the real-space lattice *along the same direction.* This is the essence of diffraction. By measuring the spacing between the maxima in the s-space, we can determine the unknown structure of materials.

2.1.3 Equivalence of Laue Function Formalism and Bragg Law

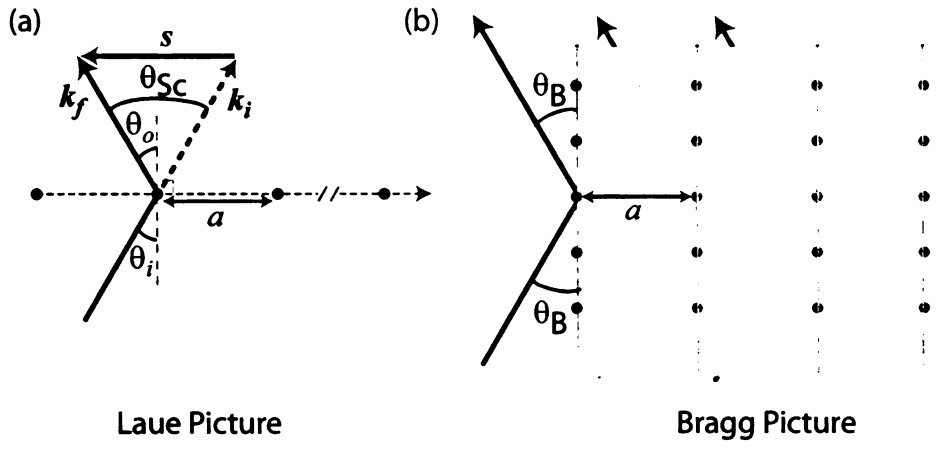

Figure 2.3: (a) Laue formalism of scattering, for the special case of *specular* scattering where $\theta_i = \theta_O = \theta_{Sc}/2$. (b) The same scattering geometry of (a), with multiple rows of atoms, highlighting the essential equivalence between the Laue and Bragg formalisms of diffraction. The vertical line indicate the lattice planes

It can readily shown that the maxima predicted by the Laue function are exactly equivalent to the celebrated Bragg equation. The Laue function, as we saw above, predicts a diffraction maxima whenever

$$\beta = \frac{\mathbf{s}\cdot\mathbf{a}}{2} = m\pi \Rightarrow \mathbf{s}\cdot\mathbf{a} = 2m\pi \tag{2.7}$$

Consider Fig. 2.3, where we explicitly look for a diffraction maximum along the specular direction defined by $\theta_i = \theta_0 = \theta_{Sc}/2$. This results in the condition that $\mathbf{s} \parallel \mathbf{a}$, and so, $\mathbf{s}\cdot\mathbf{a}$ in Eqn. 2.7 reduces to a product of the scalar magnitudes of $\mathbf{s}$ and $\mathbf{a}$. Then, combining Eqns. 2.1 & 2.7 we get,

$$s\,a = \frac{4\pi}{\lambda}\sin\left(\theta_{Sc}/2\right)\; a = 2m\pi \qquad \Rightarrow \qquad 2a\sin\theta_B = m\lambda \tag{2.8}$$

θ_i has been renamed here [and in the Bragg picture in Fig. 2.3] as θ_B as this angle

is conventionally referred to as the *Bragg angle*. Starting from the condition for Laue maxima in Eqn. 2.7, we have thus obtained the well-known Bragg condition. This equivalence becomes apparent in Fig. 2.3(b), where the row of scatterers in the Laue picture, when reproduced along the $y-$direction, will essentially generate a *family* of lattice planes that Sir William H. and William L. Bragg originally envisaged to describe the diffraction from crystalline lattices.

Additionally, Eqn. 2.8 highlights another important aspect of diffraction. Diffraction maxima will be *clearly* apparent *if and only if* $a \sim \lambda$. If this condition is not satisfied and if $\lambda \gg a$, then there will be no θ_i capable of satisfying the Bragg equation. On a fundamental level, what this means is that if $\lambda \gg a$, the relative path differences between the waves scattered from different atoms will be much smaller than λ (and consequently the phase difference much less than 2π) resulting in the interference effect getting washed out with no diffraction pattern visible. One can now appreciate why it required the discovery of X-rays (1901) that are characterized by $\lambda \sim$Å to enable the observation of diffractions from crystals (1913), in which the inter-atomic spacings indeed vary on the Å scale.

2.1.4 Reciprocal Space & The Ewald Construction

Atoms in such crystalline materials are arranged in a regular, well-defined, *periodic lattice*. Such lattices can be defined as an infinite array of points whose positions are given by

$$\mathbf{R} = n_1\mathbf{a} + n_2\mathbf{b} + n_3\mathbf{c} \tag{2.9}$$

where, (n_1, n_2, n_3) are integers and vectors $(\mathbf{a}, \mathbf{b}, \mathbf{c})$ are linearly-independent vectors referred to as *primitive vectors* or *lattice vectors*. While such a 3D structure appears more complex than a single 1-D chain we have considered so far, the fundamental principles of diffraction still hold, in that, the scattered intensity along any given

direction is determined by the sum of the phase-factors introduced along that direction by each atom. Using subscript m to index the atoms, the diffracted intensity may be evaluated as

$$I(s) \sim \left| \sum_{m=1}^{\infty} exp\,(i\,\mathbf{s}\cdot\mathbf{R_m}) \right|^2$$
$$= \sum_{m,n=1}^{\infty} exp\,(i\,\mathbf{s}\cdot\mathbf{R_{mn}})$$

where $\mathbf{R_{mn}} = \mathbf{R_m} - \mathbf{R_n}$ defines a lattice vector connecting two lattice sites. From this expression, it is apparent that the most intense maxima would be observed for those values of $\mathbf{s}$ which satisfy the condition $\mathbf{s}\cdot\mathbf{R_{mn}} = 2m\pi$ *simultaneously* for all vectors $\mathbf{R_{mn}}$. To perform such a check quickly and elegantly, we utilize the symmetry inherent to the lattice. $\{\mathbf{R_{mn}}\}$ is essentially an infinite set of vectors that can be generated by the set of primitive vectors $(\mathbf{a_1}, \mathbf{a_2}, \mathbf{a_3})$ by a process of integral multiplication. Such a construct in mathematics is termed as a *vector space* that is *spanned* by $(\mathbf{a_1}, \mathbf{a_2}, \mathbf{a_3})$. Let us, for a moment, consider another vector space spanned by a new set of vectors $(\mathbf{b_1}, \mathbf{b_2}, \mathbf{b_3})$ such that

$$\mathbf{a_i}\cdot\mathbf{b_j} = 2\pi\delta_{ij} \quad \text{where, } i,\, j = 1,\, 2,\, 3 \tag{2.10}$$

Then, if $\mathbf{s}$ belongs to this new dual space, i.e. $\mathbf{s} = h\mathbf{b_1}+k\mathbf{b_2}+l\mathbf{b_3}$, where h, k, l are some integers, then for every lattice vector $\mathbf{R_{mn}} = n_1\mathbf{a} + n_2\mathbf{b} + n_3\mathbf{c}$,

$$\mathbf{s}\cdot\mathbf{R_{mn}} = 2m\pi \quad \text{with } m = hn_1 + kn_2 + ln_3$$

This implies that a diffraction maxima will be observed for those scattering directions along which momentum transfer vector $\mathbf{s}$ is a member of this dual space spanned by $(\mathbf{b_1}, \mathbf{b_2}, \mathbf{b_3})$. Noting from Eqn. 2.10 that $b_i \sim 1/a_i$, the dual space is suitably termed *reciprocal space*, and the corresponding lattice generated by it is termed a *reciprocal*

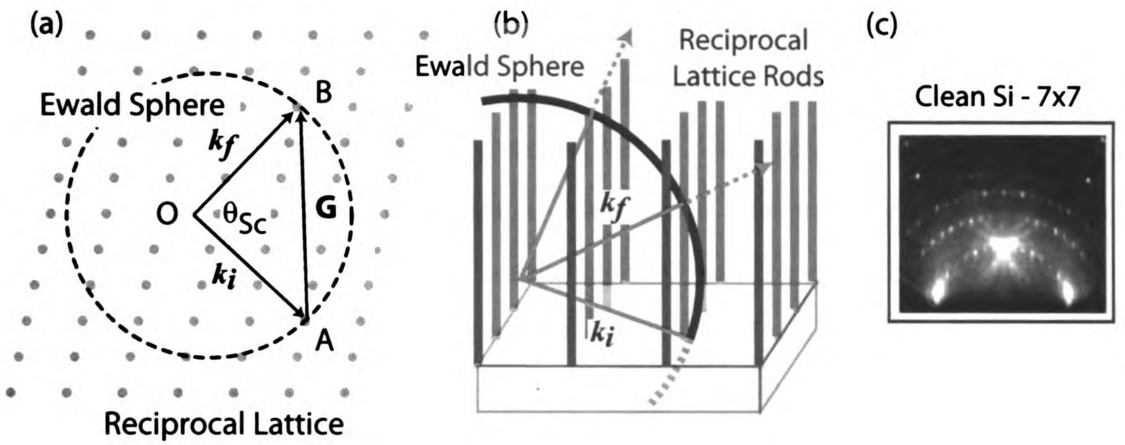

Figure 2.4: (a) Ewald construction concept for a 2D lattice. (b) Ewald construction for a RHEED geometry. (c) RHEED pattern obtained from a clean Si(111) surface, from Ref. [121].

lattice. Equation 2.10 forms the fundamental definition of the reciprocal space and can be used to obtain $\{\mathbf{b_i}\}$ for any given $\{\mathbf{a_i}\}$ using the following relations:

$$\mathbf{b_1} = \frac{2\pi\,(\mathbf{a_2} \times \mathbf{a_3})}{\mathbf{a_1} \cdot (\mathbf{a_2} \times \mathbf{a_3})} \quad \mathbf{b_2} = \frac{2\pi\,(\mathbf{a_3} \times \mathbf{a_1})}{\mathbf{a_1} \cdot (\mathbf{a_2} \times \mathbf{a_3})} \quad \mathbf{b_3} = \frac{2\pi\,(\mathbf{a_2} \times \mathbf{a_3})}{\mathbf{a_1} \cdot (\mathbf{a_2} \times \mathbf{a_3})} \tag{2.11}$$

Thus, if $\mathbf{G}$ represents a reciprocal lattice vector, the condition for observation of diffraction maxima can be expressed as

$$\mathbf{s} = \mathbf{k_f} - \mathbf{k_i} = \mathbf{G} \quad \rightarrow \quad \text{Condition for diffraction maxima} \tag{2.12}$$

This result motivates the formulation of an important and useful geometrical construct termed *Ewald construction* that facilitates in the interpretation of often complex diffraction patterns. This is illustrated in Fig. 2.4 for a simplified square lattice. Consider a 2D reciprocal lattice and a circle of radius k_i positioned such that the tip of the vector $\mathbf{k_i}$ coincides with some arbitrary reciprocal lattice site A. Since we are considering only elastic scattering, all other points on the circle represent different scattering directions $\mathbf{k_f}$. Now, if the circle were to pass through

any other reciprocal lattice point B, by the nature of the construction, the vector $\overrightarrow{AB}$ which represents the momentum transfer $\mathbf{s}$ shall also represents some reciprocal lattice vector $\mathbf{G}$. Thus a diffraction maxima will be observed along the direction $\overrightarrow{OB}$ along which the diffraction condition $\mathbf{s} = \mathbf{G}$ is satisfied. Generalizing to 3 dimensions, the reciprocal lattice becomes a 3-dimensional grid and the circle is now the Ewald sphere. As in the 2D case, the intersection of this Ewald sphere with any reciprocal lattice will represent a scattering direction (relative to the origin O) along which a diffraction maximum will be observable. This Ewald sphere construction proves extremely useful in the interpretation of diffraction patterns.

For example, in the case of diffraction from a 2D surface, the reciprocal lattice is no longer 3D grid of discrete points, but a 2D array of infinite rods. Recall that the reciprocal lattice is nothing but the composition of spatial periodicity defined by the Laue function along the 3 independent lattice repeat directions. For a 3D system which involves numerous scatters (very large N) in all 3 directions, this 3D Laue function is composed of sharp peaks that represent the discrete reciprocal lattice sites. However, when we go from a 3D to a 2D surface diffraction scenario, the number of scatterers along the surface normal direction is severely reduced, which implies that the Laue function along this direction is broadened. In the extreme case where only one surface layer contributes, there is no inter-layer interference and we end up with reciprocal lattice 'rods' (also called 'crystal truncation rods') that extend to ∞ in the surface normal direction, as shown in Fig. 2.4(b). The Ewald sphere would intersect multiple rods at different heights leading to a diffraction pattern similar to that shown in Fig. 2.4(c) (from Ref. [121]). It is important to note that these diffraction patterns do not contain any information on the lattice repeat along the surface normal and represent purely the lattice periodicity within the 2D planar surface. Such a probing geometry is employed in reflection high energy electron diffraction (RHEED) setups which is often used to quantify the degree of surface order in thin films. It will be

shown later in Sec. 4.2.1 that the surface probing UEC geometry differs from a pure RHEED setup in that, UEC can probe the sub-surface periodicity as well that is inacessible through RHEED.

2.1.5 Diffraction From Lattice With Basis - Form Factor & Structure Factor

So far, we have only considered the effect of scattering from a discrete set of lattice sites without any attention to 'how' the scattering happens. Inherent to our discussion has been the assumption that scattering along different directions is equally probable. However, this assumption is not entirely valid. The scattered intensity will posses a directional dependence based on how the incoming radiation interacts with the scatterer. This directional dependence of scattering is parametrized in a functional form known as the *atomic form factor* commonly denoted by $f(s)$. To determine $f(s)$, one needs to model the interaction forces that lead to the scattering process, which requires quantum mechanical picture of scattering. In the case of electron diffraction, where the probe is an electron wave, the incident electron wave function $\psi_0(r)$ is scattered by the interaction potential $V(r)$ to a new scattered state $\psi'(r)$. The stationary state wave-function of the electron waves in the far-field region is then represented by $\phi = \psi + \psi'$ which should satisfy the Schrödinger equation

$$-\frac{\hbar^2}{2m}\nabla^2\phi - eV(r)\phi = E\phi \tag{2.13}$$

where $V(r)$ defines the interaction potential between the incident radiation and the scatterer i.e. atom. For electrons, this interaction potential is the Coulomb potential of the outer valence electrons surrounding the lattice sites. The steady-state solution can be obtained by assuming a plane-wave solution of the form $\psi_0 = exp(i\,\mathbf{k_0}\cdot\mathbf{r})$

which yields [119] the asymptotic solution in the far-field limit as

$$\phi \sim \psi_0 + \frac{exp(ik_0 r)}{r} f(s) \tag{2.14}$$

where $f(s)$ is given by the relation

$$f(\mathbf{s}) = \frac{1}{4\pi} \int \frac{2me}{\hbar^2} V(r)\, exp(-i\,\mathbf{s}\cdot\mathbf{r})\, d\Omega \tag{2.15}$$

The integration here is over all space. In essence, $f(s)$ is a Fourier transform of the interaction potential $V(r)$. Once $f(s)$ is known, the scattering amplitude due to a lattice described by the vectors $\{\mathbf{R_n}\}$ can be written as

$$A(s) = \sum_n f_n(\mathbf{s})\, exp\,(i\,\mathbf{s}\cdot\mathbf{R_n}) \tag{2.16}$$

The exact form of $f(s)$ has been calculated theoretically by Doyle & Turner for various elements [122] by determining the interaction potential $V(r)$ for various elements within the Hartree-Fock framework of calculating ground state electron wave functions. They also expanded $f(s)$ into a Gaussian series whose coefficients are now known as *Doyle-Turner coefficients*, which are an indispensable tool in computational modeling and in fitting electron and X-ray diffraction patterns.

Another aspect we have so far ignored in the discussion of diffraction is that often, a crystal lattice may not be a *Bravais lattice*, i.e. it may not be describable by a choice of three vectors as demanded by Eqn. 2.9. In such cases however, the lattice can be described by a composition of two sub-lattices in which each Bravais lattice site described by $\mathbf{R_l}$ is connected to additional finite number of sites by the translation vector $\mathbf{u_b}$ called the *basis*. For example, the honeycomb lattice adopted by the carbon layers in graphite shown in Fig. 2.5(a) cannot be described by one set of primitive vectors. Using the edges of the hexagon as lattice vectors would generate

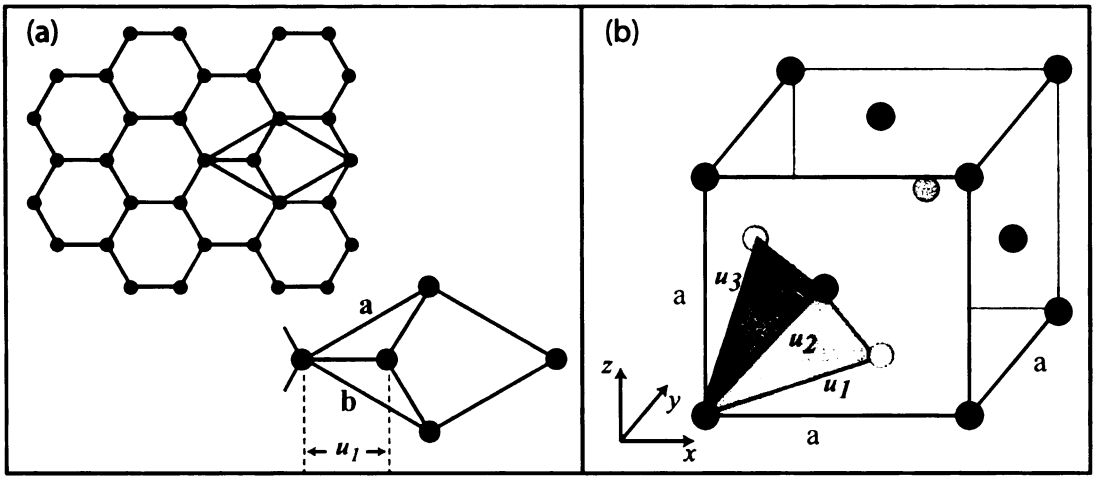

Figure 2.5: The lattice & basis for an (a) honeycomb lattice and (b) fcc lattice

additional lattice sites at the hexagon centers, which is not a part of the honeycomb lattice. Instead, by decomposing the lattice into a sub-unit (shown by the shaded rhombus) that repeats along to the lattice vectors (**a**, **b**), with each sub-unit being associated with the basis (**0**, $\mathbf{u_1}$), one can reproduce the entire honeycomb lattice exactly. In other cases, the set of Bravais lattice vectors describing a given crystal lattice may not be a convenient representation of the lattice and it may be suitable to adopt a different convention involving a basis. For example, in the case of an fcc lattice shown in Fig. 2.5(b), while the vectors ($\mathbf{u_1}$, $\mathbf{u_2}$, $\mathbf{u_3}$) can describe the entire lattice, it is often convinient to adopt the cubic unit cell of side-length a as shown, with (**0**, $\mathbf{u_1}$, $\mathbf{u_2}$, $\mathbf{u_3}$) forming the basis. In all such cases involving a lattice and a basis, the scattering amplitude $A(s)$, which is a summation of phase factors over all the atoms can be broken down into contributions from the lattice $\{\mathbf{R_l}\}$ and basis $\{\mathbf{u_b}\}$ as follows.

Assuming homonuclear lattice for simplicity, where all sites are occupied by the same atomic species and hence can be represented by identical atomic form factors $f(s)$

$$A(\mathbf{s}) = \sum_{l,b} f(s)\, exp\left\{i\mathbf{s}\cdot(\mathbf{R_l}+\mathbf{u_b})\right\}$$
$$= f(s)\left\{\sum_{b} exp(i\mathbf{s}\cdot\mathbf{u_b})\right\}\sum_{l} exp(i\mathbf{s}\cdot\mathbf{R_l})$$

In the case of heteronuclear lattice, $f(s)$ is replaced by $\langle f(s)\rangle_{cell}$ that represents the atomic form factor averaged over all the different atoms within one unit cell. The second term in this equation is the lattice sum, which leads to the Laue formalism of diffraction as discussed earlier. The first term in brackets that sums up the contribution to the phase from the basis atoms is called as the *structure factor*, commonly denoted by $F(\mathbf{s})$. As is evident from the expression, F modulates the intensities of the Bragg peaks whose directional location is determined by the lattice sum. Often cases arise in which the internal symmetry of the unit cell causes the structure factor along certain Bragg directions (defined by the lattice sum) to be 0. Such Bragg peaks which are expected for the given lattice, but are missing on account of the structure factor being 0 are termed *kinematically forbidden* (See Appendix A for example). Furthermore, note that a change in the long range lattice repeat of the unit-cell will affect the Bragg peak positions, whereas a change within the unit cell that does not affect the long range order (such as the generation of an optical phonon, say) will only affect the Bragg intensities, and not their position.

While this concept of lattice & a basis helps in understanding the qualitative aspects of diffraction, computational fitting/modeling of diffraction patterns does not require such a segregation into lattice and basis, and the total diffraction intensity can be expressed simply as a summation over all the atomic sites in the crystal lattice as:

$$I(\mathbf{s}) = |A(\mathbf{s})|^2 = \sum_{m,n} f_m\, f_n^*\, exp\,(i\,\mathbf{s}\cdot\mathbf{R_{mn}}) \tag{2.17}$$

where m and n range over all atomic sites. Since we are dealing only with homonuclear

lattice, $f_m = f_n = f$, and the above expression for $I(s)$ can be broken down into two contributions - those arising from $n = m$, which are the isotropic self-scattering terms, and the other from $n \neq m$, which represent the interference of waves scattered from different atoms.

$$I_{Tot}(\mathbf{s}) = I_A(s) + I_M(\mathbf{s}) \tag{2.18}$$

where

$$I_A(s) = N\langle f \rangle^2 , \qquad I_M(\mathbf{s}) = \sum_{m \neq n} f_m f_n^* \, exp\,(i\,\mathbf{s} \cdot \mathbf{R_{mn}}) \tag{2.19}$$

where N denotes the number of scatterers. I_A does not posses any structure-related information and purely forms an incoherent background signal in the diffraction pattern. All the information about the internal structure of the material is buried within I_M. Furthermore, in practical cases, I_A also includes contributions from inelastic scattering that does not have (under normal circumstances) any directional preference. Hence, it contributes toward the isotropic background signal within any diffraction pattern.

2.2 Diffraction Data Extraction & Analysis

We now discuss the data reduction procedures adopted in the UEC lab to extract structural information from the diffraction patterns. While the specifics of data reduction procedures usually depend on the choice of probe (X-ray, electron, neutron) and diffraction geometry (reflection, transmission), they essentially involve distilling from raw diffraction intensity $I_{Tot}(\mathbf{s})$, the probe-independent normalized structure function $S(s)$ via the removal of incoherent background and atomic self-scattering contributions followed by normalization using the probe scattering form factor. $S(s)$ is then directly related to the pair correlation function $G(r)$ by a Fourier transform. We will focus on scattering from two different samples - (a) silver nanocrystals de-

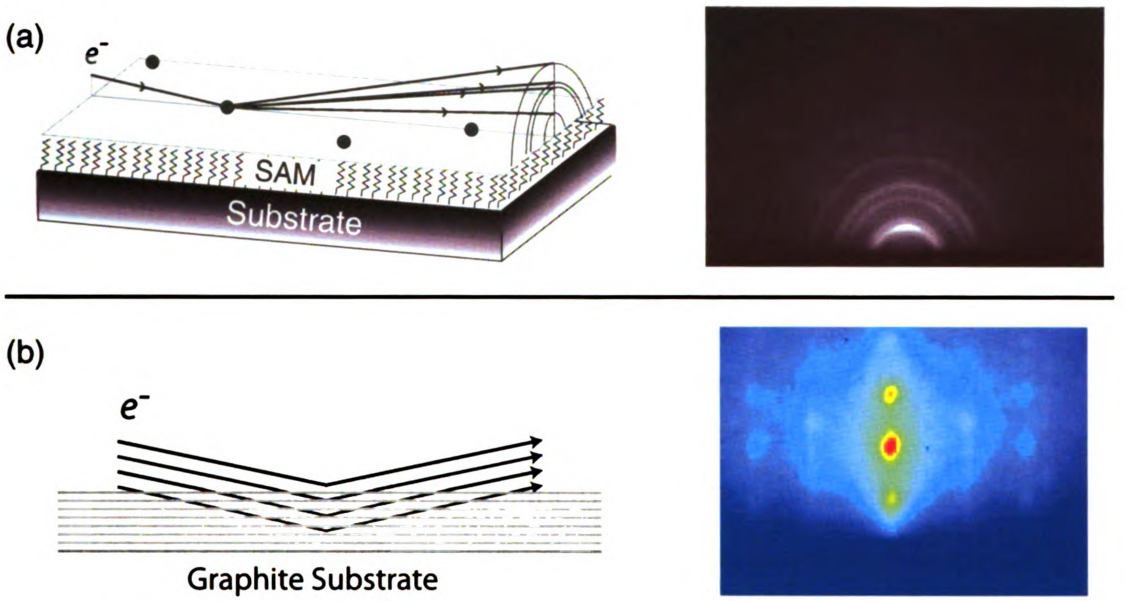

Figure 2.6: Diffraction geometry employed, along with the accompanying ground state diffraction patterns from (a) surface supported nanocrystals and (b) graphite.

posited on a silicon substrate, and (b) graphite surface. In both cases, the diffraction patterns are acquired from an electron beam incident on the sample at glancing angles as shown in Fig. 2.6. In such cases, the background signal arising from self scattering terms also contains other systematic surface artifacts such as absorption of scattered electrons and diffusive background from surface scattering, which does not permit the direct use of the well-tabulated Doyle-Turner coefficients to extract the coherent scattering signal from these patterns. We have developed empirical data reduction procedures that allow us to extract structural information from such small-angle electron diffraction patterns. The procedures outlined below are specific to this geometry and follow from Ref. [123].

2.2.1 Data Reduction: Surface Supported Nanocrystals

The electron diffraction patterns from the surface supported NCs are similar to powder-diffraction patterns, consisting of Debye-Scherrer rings as shown in Fig. 2.6(a).

This is because the NCs are randomly oriented on the surface allowing the electron beam to probe various crystal orientations in one shot. To model this diffraction pattern, we convert the summation in Eqn. 2.19 over the discrete lattice sites into a continuum integral over the isotropic atomic number density $\rho(r)$ by effecting the following substitution:

$$\sum_m \rightarrow \int_{\text{all space}} \rho(r) r^2 dr\, d(-cos\theta)\, d\phi \quad \text{where} \quad \mathbf{R_{mn}} \rightarrow (r,\, \theta,\, \phi)$$

As all unit cells are identical (by definition), the second summation in Eqn. 2.19 serves only to provide a multiplicative factor of N. Furthermore, since the NCs are randomly oriented, all orientations of θ are equally probable. I_M in Eqn. 2.19 can hence be expressed as

$$I_M(s) = N\langle f^2 \rangle \int_0^\infty r^2 \rho(r)\, dr \int_0^\pi exp\,(isr\cos\theta)\, d(-\cos\theta) \int_0^{2\pi} d\phi$$

which leads to the relation

$$I_M(s) = N\langle f^2 \rangle \int_0^\infty R(r)\, \frac{\sin(sr)}{sr}\, dr \tag{2.20}$$

where $R(r) = 4\pi r^2 \rho(r)$, $\langle f^2 \rangle$ is the average atomic form factor for the unit cell, and the sine term is a result of orientation averaging over θ. We can then relate the normalized structure function $S(s) = sM(s)$ where $M(s) = I_M(s)/N\langle f^2 \rangle$ to the atom-atom pair correlation function $G(r)$ by a simple sine Fourier transform as follows:

$$G(r) = \frac{2}{\pi} \int_0^\infty S(s) \sin(sr) ds \tag{2.21}$$

where $G(r) = 4\pi r \rho(r)$.

$G(r)$ is a measure of the probability of finding two atoms separated by a distance r and closely related to the pair-distribution function formalism prevalent in X-ray and neutron diffraction literature [124]. $G(r)$ is in effect a 1D representation of the 3D lattice distances. While not a unique descriptor of the 3D lattice structure, it is nevertheless enormously useful in interpreting structural dynamics in solids.

In light of this model, the data reduction procedure for UEnC outlined in Fig. 2.7 is aimed at deducing $S(s)$ from the experimentally recorded diffraction pattern. The first step is to obtain the total scattering intensity function $I_{Tot}(s)$ by a radial averaging of the Debye-Scherrer rings in the powder diffraction patterns. To do this, we need to locate the center of these rings, which is done using a guided theoretical simulation. The simulation recreates the theoretical polycrystalline diffraction rings from a known bulk fcc ground state structure of the NC on the diffraction imaging plane. It takes into account the electron incidence angle, sample orientation, camera distance, and the projection onto the imaging plane. These parameters are then fine tuned so as to match three key features in the observed and simulated diffraction pattern - (a) the main beam location, which is recorded prior to the experiment, (b) the substrate shadow edge and (c) the diffraction pattern themselves (location of Bragg peaks / rings etc). Once a satisfactory fit is obtained, the ring center is known and the ring averaging performed to determine $I_{Tot}(s)$.

To extract the structure function $S(s)$, we first evaluate $M(s)$ as $(I_{Tot}-I_{Bkg})/I_A$. The incoherent background I_{Bkg} is composed of contributions from both atomic self-scattering $I_A = N\langle f\rangle^2$ and inelastic scattering $I^{inelastic}$. I_A is a smoothly varying, monotonically decreasing function described by Doyle-Turner coefficients [122]. However, in case of small-angle surface diffraction geometries, the scattering is strongly modified by near-surface effects such as surface absorption. This is evident in the sharp turn-around of the background profile in Fig. 2.7(a) near the shadow edge. This effect is multiplicative, modifying I_A, and hence I_{Tot}. Since I_{Bkg} is largely

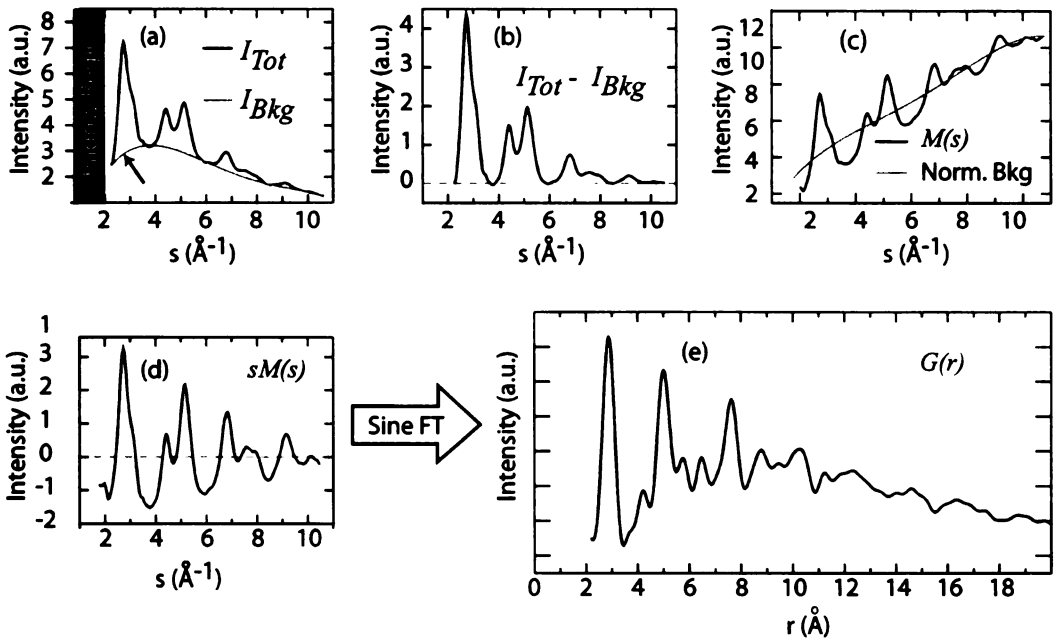

Figure 2.7: Data reduction procedures employed in UEC studies of surface supported NCs, illustrated here with a specific example of 2 nm Au NCs. (a) Diffraction intensity I_{Tot} recorded from ring-averaging of UEnC diffraction data along with empirically fitted polynomial background I_{Bkg}. The arrow points to the sharp turn-around introduced in the intensity profile due to surface absorption effects. (b) Background subtracted intensity. (c) $M(s) = (I_{Tot} - I_{Bkg})/I_{Bkg}$ along with secondary background fitting to remove offsets introduced due to inelastic scattering. (d) $sM(s)$ curve obtained from (c). (e) $G(r)$ obtained from sine transform of $sM(s)$ in (d).

contributed from I_A, it too is affected by these effects to a similar degree. Since this effect is difficult to model precisely, we use an empirical background removal procedure. We fit a polynomial background I_{Bkg} to I_{Tot} by requiring the background to pass through the baselines of observable peaks. Normally, I_{Bkg} should pass through the center of the oscillation pattern, but since the center is ill defined here, we find it more robust to fit the baselines. This is followed by a second stage of low-order polynomial background removal to correct for the offset, and the resulting curve multiplied by s to yield the $sM(s)$ curve, shown in Fig. 2.7(d). Finally, $G(r)$ can then be deduced via Eqn. 2.21. Other background subtraction procedures involving different functional forms for the fitted background and fitting procedures through the

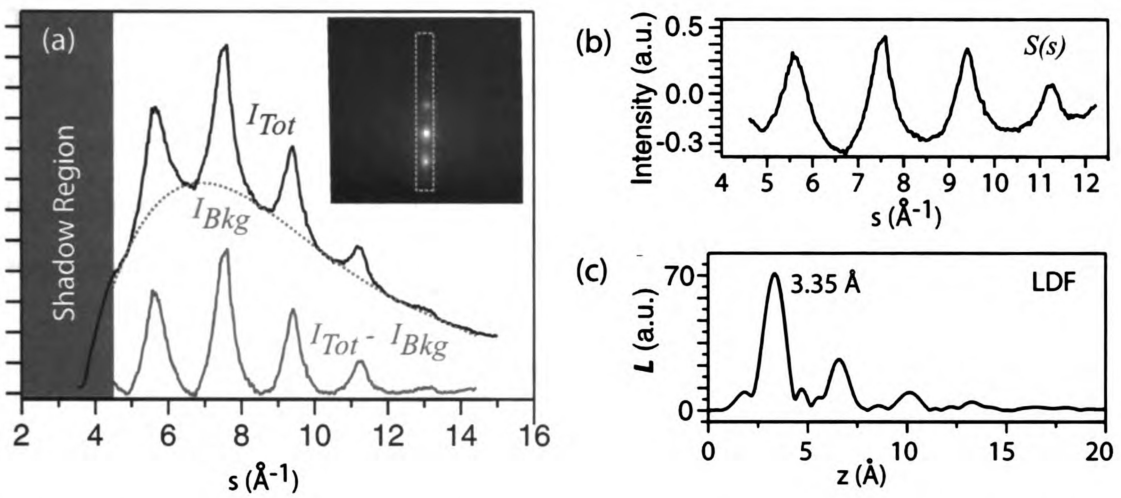

Figure 2.8: Data reduction procedures employed in case of graphite. (a) Intensity profile along central (00) rod (boxed in inset), along with the empirically fitted background. (b) Normalized structure function $S(s)$ extracted from (a). (c) Cosine transform of (b) to yield layer density function (LDF), $\mathcal{L}(z)$.

centers of oscillation pattern have also been produced. It is seen that the $sM(s)$ so determined is robust agaisnt adoption of these various schemes [110, 125].

While empirical, this formalism has been remarkably successful in distilling the structural data from diffraction patterns of surface supported NCs, which can also be treated by standard crystallographic refinement software used in X-ray and neutron diffraction studies [125]. UEnC investigation of 2 nm and 20 nm Au NCs employing this data extraction methodology has enabled clear identification of the Au NCs to possess cuboctahedral structures, distinct from other possible structural motifs such as decahedra and icosahedra [126]. Furthermore, the $G(r)$ obtained in the ground state of Au NCs agrees very well with the theoretical distance list expected from an fcc lattice.

2.2.2 Data Reduction: Graphite

The diffraction pattern from graphite shown in Fig. 2.6(b) consists of diffraction maxima along the central (00) streak accompanied by weaker streaks on the side.

The origin of this pattern is discussed in detail in Sec. 4.2. For now, it suffices to note that these peaks, which are oriented along the surface normal direction, arise from the constructive interference between electron waves scattered from the different layers of graphite. The orientation averaging as applied in the case of NCs is no longer applicable, and this diffraction pattern is conveniently modeled as follows.

$$\begin{aligned} I_M(s) &= f^2 \sum_{m \neq n} exp\,(i\,\mathbf{s} \cdot \mathbf{R_{mn}}) \\ &= f^2 \sum_{m \neq n} \frac{exp\,(i\,\mathbf{s} \cdot \mathbf{R_{mn}}) + exp\,(-i\,\mathbf{s} \cdot \mathbf{R_{mn}})}{2} \\ &= f^2 \sum_{m \neq n} \cos\,(\mathbf{s} \cdot \mathbf{R_{mn}}) \end{aligned}$$

Here, we have utilized the fact that for each scattering pair (m, n), the summation also takes into account the pair (n, m). Interchange of indices leads to $\mathbf{R_{nm}} = -\mathbf{R_{mn}}$. Explicit summing of both these terms will lead to double counting over the (m, n) indices, and so the factor of 1/2 is introduced to negate this double-counting, resulting in the cosine term. In this study, we primarily focus on the periodicity of the graphite lattice along the c-axis, perpendicular to the basal planes. This periodicity is represented by the diffraction maxima occuring on the (00) rod, along which, we can express $\mathbf{s} = (0, 0, s)$. Adopting a cylindrical (r, ϕ, z) coordinate system whose z axis is oriented along graphite $\mathbf{c^*}$ (or equivalently $\mathbf{c}$) axis that is perpendicular to graphite's basal planes, we obtain

$$I_M(s) = f^2 \sum_{m \neq n} \cos(s z_{mn}) \tag{2.22}$$

where z_{mn} denotes the projection of $\mathbf{R_{mn}}$ along the $\mathbf{c^*}$ axis. As before, we can convert the discrete summation into a continuum intergal by effecting the following substitution.

$$\sum_{m} \rightarrow \int_{\text{all space}} \rho(r,z)\, r\, dr\, d\phi\, dz \quad \text{where} \quad \mathbf{R_{mn}} \rightarrow (r,\, \phi,\, z)$$

Once again, as in the case of nanocrystals, the second summation in Eqn. 2.22 merely yields a multiplicative factor N, which is the total number of scatterers. Furthermore, the anisotropy of graphite's structure implies that the atomic number density $\rho(r,\, z)$ can be completely decoupled into a product of two atomic number densities - one within the basal plane $\rho_r(r)$ and that perpendicular to it $\rho_z(z)$ such that

$$\int_{r=0}^{\infty}\int_{\phi=0}^{2\pi} \rho_r(r)\, r\, dr\, d\phi = N_r \quad ; \quad \int_{z=0}^{\infty} \rho_z(z)\, dz = N_z \quad ; \quad N_r\, N_z = N$$

where N_r represents the number of scatterers in a single plane, N_z is the number of scattering planes, N is the total number of scatters and $z = 0$ represents the top surface layer. Using this formalism, we obtain

$$S(s) = M(s) = \frac{I_M(s)}{N\, f^2} = \int_0^{\infty} r\, dr\, \rho_r(r) \int_0^{2\pi} d\phi \int_0^{\infty} \rho_z(z)\, \cos(sz) dz$$

The first two integrals together amount to N_r by definition. Consequently, we can express $M(s)$ as

$$M(s) \sim \int_0^{\infty} \mathcal{L}(z)\, cos(sz)\, dz \tag{2.23}$$

where $\mathcal{L}(z) = N_r\, \rho_z(z)$ denotes the total number of scattering pairs separated by the perpendicular distance z. From this relation, we can obtain a 'layer density function' (LDF) that represents the inter-layer periodicity of the graphite planes as

$$\mathcal{L}(z) = \int_0^{\infty} M(s)\, \cos(sz)\, ds \tag{2.24}$$

The LDF curve $\mathcal{L}(z)$ represents the probability of finding two graphite planes separated by distance z and is thus a measure of the inter-layer separation along the

c-axis. Inherent to this formalism is the assumption that every graphite layer is identical, which, while valid in the ground state, may not always be true in the excited state where the lattice undergoes structural change. Nevertheless, as long as the lattice distortion along the c-axis is not significant and each scatterer retains allegiance to its original parent layer, this formalism can be used to ascertain the inter-layer structural dynamics in graphite.

Following this formalism, the data extraction from the graphite diffraction patterns proceeds in a similar fashion as before and is illustrated in Fig. 2.8. After fitting the diffraction pattern taking into account the geometrical experimental parameters as described earlier , we extract the intensity profile along the (00) rod and proceed with identical background normalization procedures as before. However, difference arises in the final step, where the $S(s)$ is defined differently for graphite $[S(s) = M(s)]$ as compared to UEnC $[S(s) = sM(s)]$ and a cosine Fourier transform of $S(s)$ [Eqn. 2.24] is performed as opposed to a sine transform in UEnC. This procedure yields the layer density function (LDF) curve $\mathcal{L}(z)$ which represents the periodicity of the graphite lattice along the $c-$ axis. The LDF obtained from the ground state diffraction pattern of graphite is shown in Fig. 2.8(c) and exhibits a strong peak at 3.35 Å and weaker peaks at its multiples representative of well-established inter-layer separation in graphite, thus illustrating the validity of the data reduction scheme. This primary LDF peak will be subsequently used in the UEC investigations to monitor the inter-layer expansion and contraction of photoexcited graphite layers.

Chapter 3

Experimental Apparatus - Design & Development

The past two decades have seen significant development of ultrafast electron diffraction (UED) systems. Early development of time-resolved electron diffraction was carried out inside a transmission electron microscope (TEM) in 1970s and 1980s employing stroboscopic methods such as repetitive beam blanking [127] and pulsed cathode TEM [128]. Mourou and Williamson pioneered the use of pulsed-laser generated electron packets inside a modified streak camera in the early 1980s to record electron diffraction patterns from a thin Al foil from a 100 ps electron source [129], which was subsequently improved to 20 ps [130]. The concept of replacing the optical probe in femtochemistry experiments by an ultrashort electron pulse was proposed by Ahmed Zewail's group at Caltech [131] in 1991 and demonstrated the following year [132]. Around the same time Ewbank *et al.* modified existing gas-phase electron diffraction setup with a pulsed laser generated electron source and a linear diode array detector and recorded changes in total scattered intensities from laser-generated transient species of various molecules with $\sim$ 20 ns time resolution [133]. The first ultrafast electron diffraction experiments was reported in the gas-phase by Williamson

et al. where the photoinduced dissociation of diiodomethane (CH_2I_2) was observed in real time [134]. More recently, independent development of gas phase UED have also been employed [135, 136]. These pioneering results were achieved on the back of several technical and theoretical advancements during the intervening years [137–140] and ultimately reached a robust stage and fruition of applications [111, 141]. While initial UED systems focused on gas-phase reactions in molecular species, the recently developed systems have aimed at studying more complex systems including surfaces, adsorbates and surface grown solids. The development of ultrafast electron crystallography (UEC) [113, 142] extends UED into these new areas [18, 21, 143–145]. Other developments have included the design of improved pulsed electron sources to reduce space-charge broadening of electron packets [146, 147] and the single-shot limit has been reached [148–150]. Recently, the laser-generated pulsed electron source utilized in UEC and UED has been coupled with a transmission electron microscope (TEM) in the development of ultrafast electron microscopy (UEM) [114]. The rather long electron drift region in a TEM column where the focusing and imaging optics are placed accentuates the space-charge effect that degrades the spatio-temporal resolution of the pulsed electron beam. The UEM developers opt to operate in the single electron mode with high pulse repetition rate ($\sim$ 100 MHz) to eliminate this space charge broadening, while a parallel development of dynamic transmission electron microscope (DTEM) [115, 151] focuses on single-shot investigation of material processes on the nm-ns scales. An exhaustive account of the development of UED, UEC and UEM systems from their inception to current capabilities can be found in Refs. [28, 111, 112, 152].

Building on these advancements emanating from Caltech, we here at MSU have developed over the last five years a UED system focused on investigations of transient structural dynamics in nanocrystals [126] and condensed systems [153] near interfaces [154], attaining spatiotemporal resolution of ($\sim$ 0.01 Å, $\leq$ 1 ps). The conceptual lay-

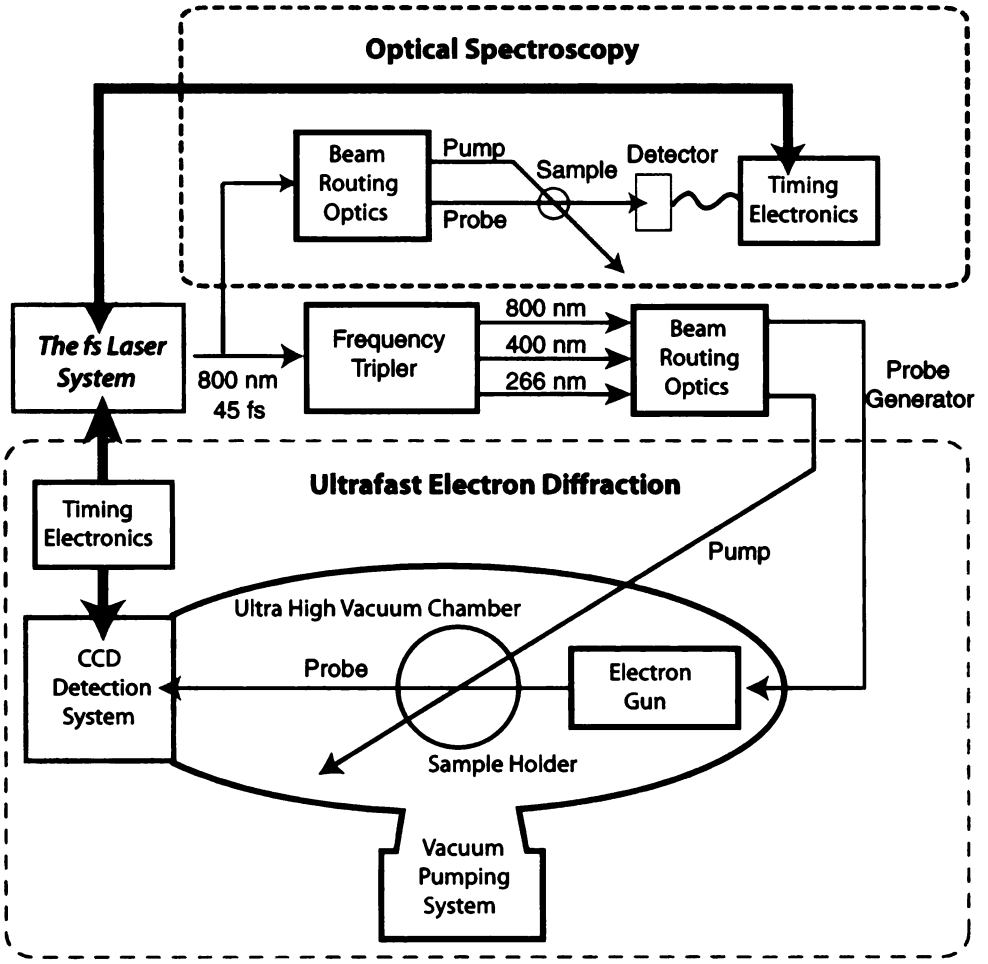

Figure 3.1: Global layout of various sub-systems comprising the UEC Lab

out of the laboratory is shown in Fig. 3.1 and is a confluence of various subsystems acting in unison. The UEC system is driven by an amplified Ti:Sapphire femtosecond laser system (*Spectra Physics, 'Spitfire'*) generating 45 fs ultrashort laser pulse centered at 800 nm with 2.5 mJ per pulse and operating at a 1kHz pulse repetition rate. This primary laser pulse is fed into a frequency tripler (*Minioptic Technologies*) that generates ultrafast pulses of higher harmonics i.e. 400 nm and 266 nm through non-linear frequency upconversion in a β-Barium Borate (BBO) crystal. Any of these three wavelengths may be utilized as the pump pulse.

The experimental setup is composed of 2 stations - one for diffraction investigations and another for optical spectroscopy. Driven by the same femtosecond laser system, the two stations operate independent of each other, allowing diffraction and spectroscopic experiments to be conducted simultaneously.

For diffraction experiments, the chosen pump and probe pulses are suitably routed through a combination of mirrors, lenses and other optical assemblies towards the experimental station, inside an ultrahigh vacuum (UHV) chamber. The pump beam is focused onto the sample placed at the center of the UHV chamber. A pulsed electron source is generated through photoemission from a semi-transparent photocathode, accelerated to 30 keV, collimated and focused onto the sample. The probe is allowed to scatter from the sample and the signal collected at the opposite end of the UHV chamber using an intensified CCD camera system that is capable of single-electron detection.

For the optical spectroscopy experiment station, a small fraction of the primary laser is split off and directed into the routing optics, where it is further split into the pump and probe pulses. The pump and probe are subsequently directed onto the sample with the pump pulse being routed through a dedicated translational delay stage to adjust the pump-probe delay. The sample can be positioned either perpendicular to the probe beam for reflection/transmission experiments or in a grazing

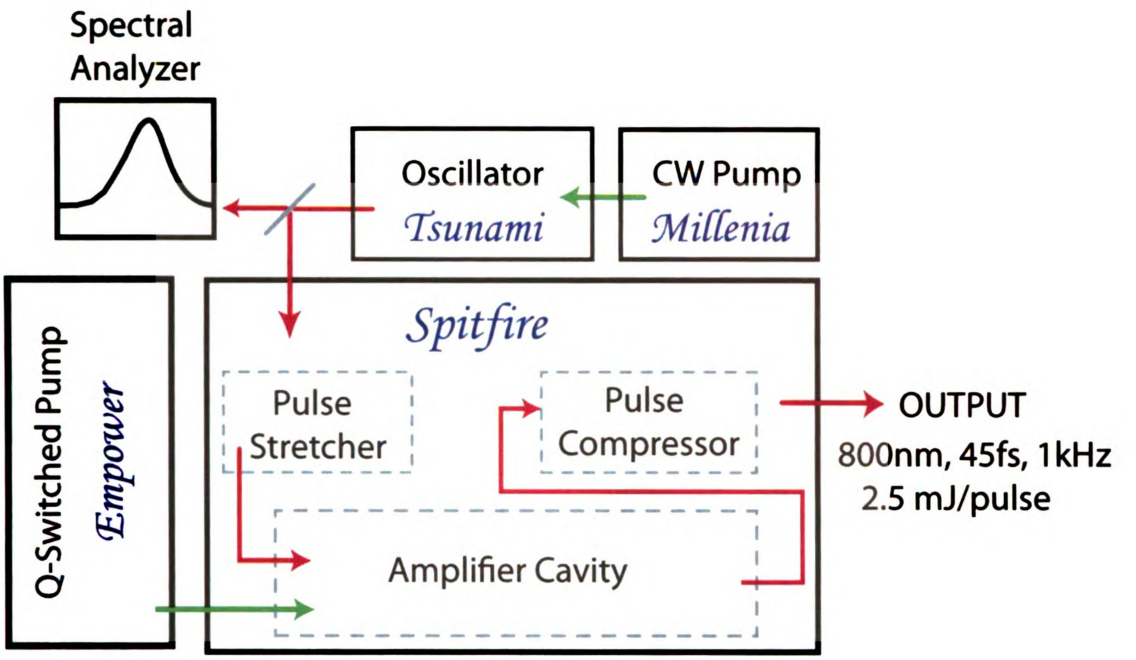

Figure 3.2: Conceptual construction of an ultrafast laser system utilizing regenerative chirped pulse amplification, similar to the system in use in the MSU UED lab.

incidence geometry for optical probing of near-surface electron dynamics.

In the following sections, we shall discuss the design, construction and performance of these various sub-systems in some detail.

3.1 The Laser System

The amplified laser system (*Spectra Physics, Spitfire*) is a *chirped pulse amplification system* consisting of 4 separate sub-units illustrated in Fig. 3.2 that act together to generate the final amplified pulsed laser output. An excellent introduction to principles of femtosecond pulse generation and their applications can be found in Ref. [155]. The system is described here briefly.

The creation of high power fs laser pulses can be separated in two stages - pulse generation and amplification. Initially, low-power ($\sim$ nJ/pulse) seed fs laser pulses are

generated within an oscillator cavity (*Tsunami*) that consists of a Titanium doped Sapphire (Ti:S) crystal as the gain medium pumped by a continuous wave (CW) diode-pumped Nd:YVO_4 laser (*Millenia*). The Nd:YVO_4 gain medium in Millenia lases at 1024 nm that is frequency upconverted to 512 nm in a non-critically phase matched Lanthanum Triborate (LBO) crystal in order to match the absorption spectrum of Ti:S in the Tsunami. Femtosecond pulses are generated within Tsunami by active modelocking to produce 45 fs laser pulses with 200 mW average power at a pulse repetition rate of 80 MHz. This corresponds to roughly 2 nJ/pulse. These seed pulses then enter the Spitfire where they are first stretched in time using a 4-pass stretcher grating. This is done to avoid non-linear effects such as self-focusing that can set in at high laser peak-power and possibly damage the optical components. The stretched pulse is then allowed to enter the amplifier cavity consisting of a Ti:S gain medium that is pumped by a Q-switched Nd:YLF laser (*Empower*) that provides $\sim$ 15 W pulsed output at 1 kHz repetition rate. As in the case of Millenia, since Nd:YLF lases at 1054 nm, the output is upconverted to 527 nm in an LBO crystal to once match Ti:S absorption peak. This intense 15 W laser pulse sets up the population inversion in the Ti:S crystal, following which, the seed fs laser pulses from the Tsunami are allowed to enter the amplifier cavity. The seed laser picks up gain each time it passes through the pumped Ti:S gain medium and builds up in strength over multiple cavity round trips. Once the population inversion in Ti:S has been completely consumed and no further amplification is possible, the amplified pulse is directed out of the cavity into a pulse compressor where it is compressed back to fs duration. The final pulse train exiting the system posses the following characteristics: 45 fs, 800 nm center wavelength, 2.5 mJ/pulse and 1 kHz pulse repetition rate.

3.2 The Ultra High Vacuum Chamber

The UHV chamber at MSU is equipped with a diverse set of experimental and sample characterization tools. The vertical layout of the chamber can be separated into levels 1, 2 and 3, with level 1 being the topmost section. The chamber is equipped with a commercial XYZ manipulator mounted on top of a differentially pumped rotatory feedthrough system that allows rotational motion of the sample manipulator about the $Z-$ axis ($\theta-$direction), while still preserving the vacuum within the chamber. The XYZ directions are controlled by stepper motors (*Anaheim Automation*, 23L series), allowing accurate sample positioning to within $\sim$ 10 μm, while the θ axis is driven by a worm/gear assembly. All 4 axes are computer controlled (*National Instruments*, MID-760x series).

3.2.1 UHV Chamber Instrumentation

Level 1 contains an Argon sputtering gun for sample cleaning, a quadrupole mass spectrometer (QMS) to monitor the residual gasses present inside the chamber and a baking lamp used to de-gas the chamber of water and other accumulated contaminants. Additionally two diode lasers are also mounted outside the chamber, aimed at the experimental location in level 2 through Quartz viewports. These 2 non-collinear laser beams are used during the pump-probe alignment procedure as explained in Sec. 3.5.

Level 2 is where the UEC experiment is conducted and houses the pulsed electron gun and the intensified CCD camera at diametrically opposite ends. An optical camera is mounted outside the chamber near-perpendicular to the probe beam direction so as to afford a clear view of the sample surface. This camera is useful during pump-probe alignment procedures and in calibration. In addition, this level is also equipped with a molecular doser system capable of dosing the sample with adsorbates such as

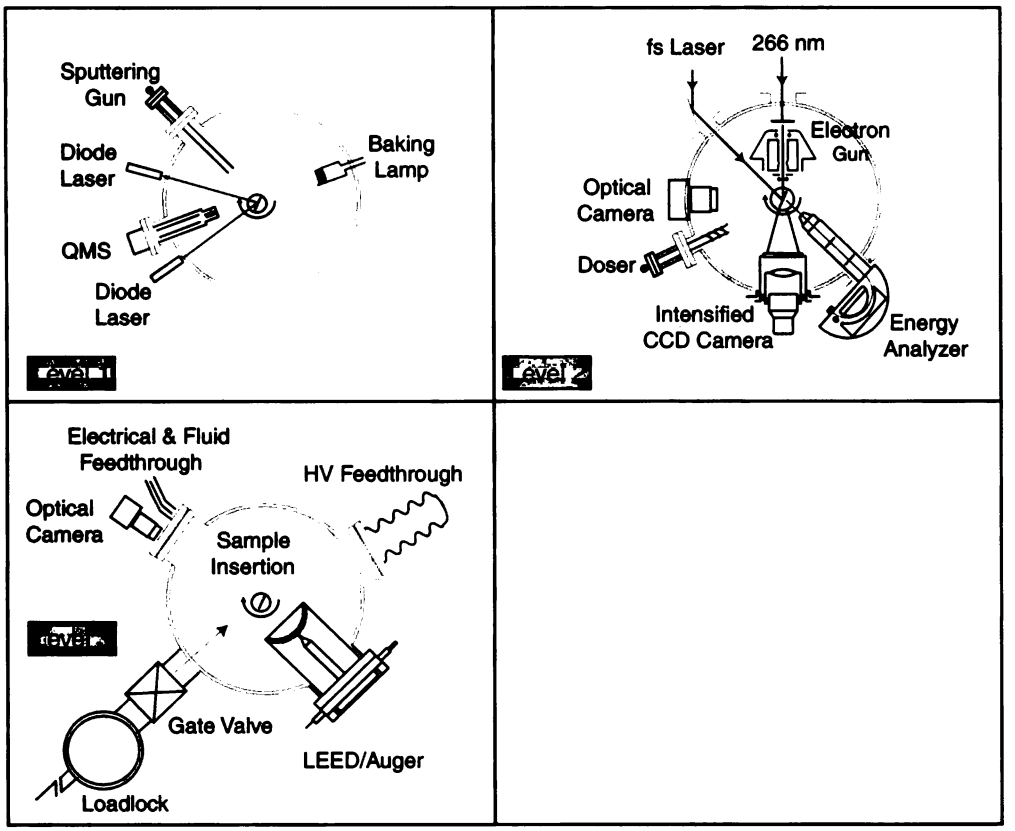

Figure 3.3: Details of experimental and sample characterization tools incorporated into the UED chamber at MSU, broken down by each level. The UED experiment is carried out at level 2.

water and organic molecules. The doser is a custom home-built system, the details of which can be found in Ref. [156]. The level also contains a hemispherical electron energy analyzer, that can be utilized to observe photoemission spectra from excited samples.

Level 3 contains the sample-transfer system that permits insertion and removal of samples from the chamber, without the need to vent the system to air. The sample insertion proceeds through a load-lock system that is isolated from the main chamber by a mechanical gate valve. It is pumped by a separate turbo-molecular pump allowing pumping and venting of the load-lock independent of the chamber. An optical camera mounted at this level is aimed at the sample insertion location so as to

provide live-feedback of the sample insertion process. The level also contains a LEED / Auger setup to examine sample surface quality, a high voltage feedthrough providing the 30 kV acceleration voltage for the electron gun, other electrical feedthroughs providing the electron beam deflector voltages and current for the magnetic lens focusing the electron pulse along with a fluid feedthrough for circulating water that cools the magnetic lens within the electron gun.

3.2.2 Chamber Pumping Schematics

Studies involving surfaces and interfaces generally require extremely clean UHV surroundings due to the high reactivity of surfaces. In addition, the presence of high acceleration field ($\approx$ 6-7 MV/m) in the electron gun also mandates the presence of a good vacuum. To achieve and maintain a high quality of vacuum, the UHV chamber is served by a turbo molecular pump, backed by a dry scroll pump. The pumping scheme of the entire UHV chamber and associated extensions is illustrated in Fig. 3.4.

The roughing pump is an oil-free scroll pump (*BOC Edwards, XDS35*) with a pumping speed of 35 m^3/hr and a base pressure of $\approx$ 7.5 mTorr, that can evacuate the chamber from 1 atm to mTorr pressures within a few minutes. Once this base pressure is attained, turbo molecular pump (*Pfeiffer Vacuum, TMH 065*) operating at 1000 Hz takes over, attaining typical chamber pressures of $\sim 1 \times 10^{-8}$ Torr. Further reduction in pressure is achieved through the use of ion-pump, resulting in chamber base pressure of $\leq 1 \times 10^{-9}$ Torr, though lower pressures of 10^{-10} Torr can be attained following extensive baking. All vacuum pumps employed here are oil-free in order to eliminate any potential hazard that could be inflicted on the chamber by an accident oil back stream.

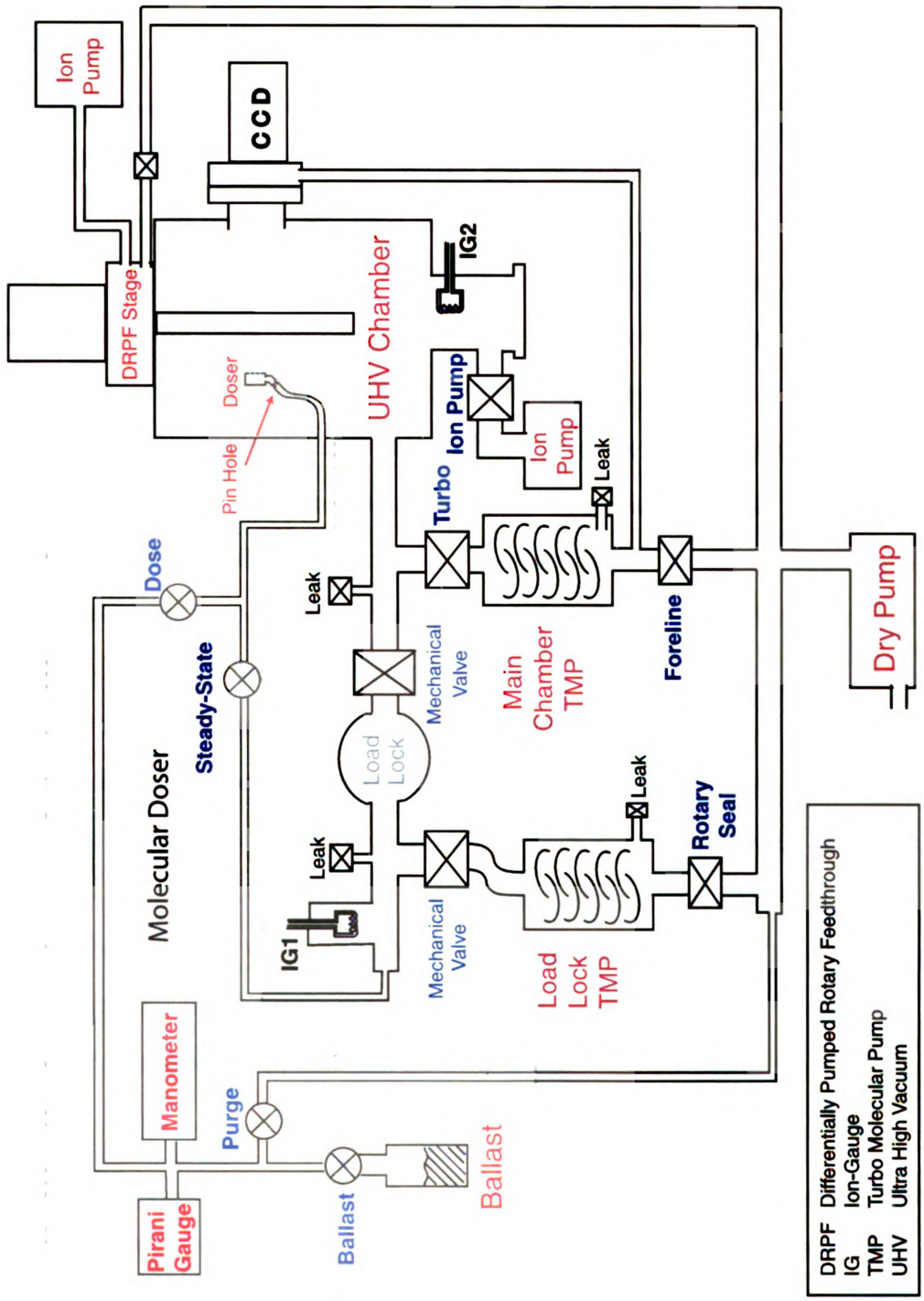

Figure 3.4: Pumping schematics for the UHV chamber. The actual components inside the chamber, such as the electron gun, the sample holder and others have been omitted for sake of clarity. For details of the molecular doser, see Ref. [156]

3.3 Proximity Coupled Pulsed Electron Gun

The construction of the ultrafast pulsed electron source employed here in the UED lab is shown in Fig. 3.5. Ultrafast electron packets are generated by impinging an fs laser (typically 266 nm, 4.6 eV) on a semi-transparent thin film ($\sim$ 40 nm) of silver (Work function $\sim$ 4.4 eV) that is thermally evaporated onto a transparent sapphire substrate. Instantaneous photoelectric effect from the silver film generates an electron pulse that preserves the ultrashort time duration of the incident laser pulse. This electron packet is accelerated to 30 kV within a short extraction distance of $\sim$ 4 mm to the anode and directed into the central bore of a magnetic pole piece through a small beam limiting 100 μm aperture. A fine Au mesh (1500 mesh) is employed just prior to the aperture to effectively screen the internal bore of the lens from the high extraction field. The magnetic lens pole piece is made of soft-iron with solenoidal current carrying coils in its interior. The pole piece contains a small break in its interior mid-section where the magnetic field lines, which normally remain confined within the soft-iron, penetrate into the central bore while jumping across the break. It is in this region that the electron pulse is spatially focused to smaller sizes. The focused electron packet exits the pole piece through a final $\sim 50 - 200$ μm aperture, beyond which, biased deflector rods ($\sim$ 1-2 kV) placed immediately outside the pole piece deflect the electron packet and guide it towards the sample at the center of the chamber.

The main challenge in developing a short-pulse electron gun is in overcoming the inherent repulsion between the electrons. This so-called space-charge effect tends to broaden the temporal resolution of the electron packet in the drift region as it propagates to the sample. Several schemes have been proposed to overcome this limitation including the use of short flight distance gun [146], use of high acceleration voltage to reduce the drift time [147], radio-frequency bunching of electron packets

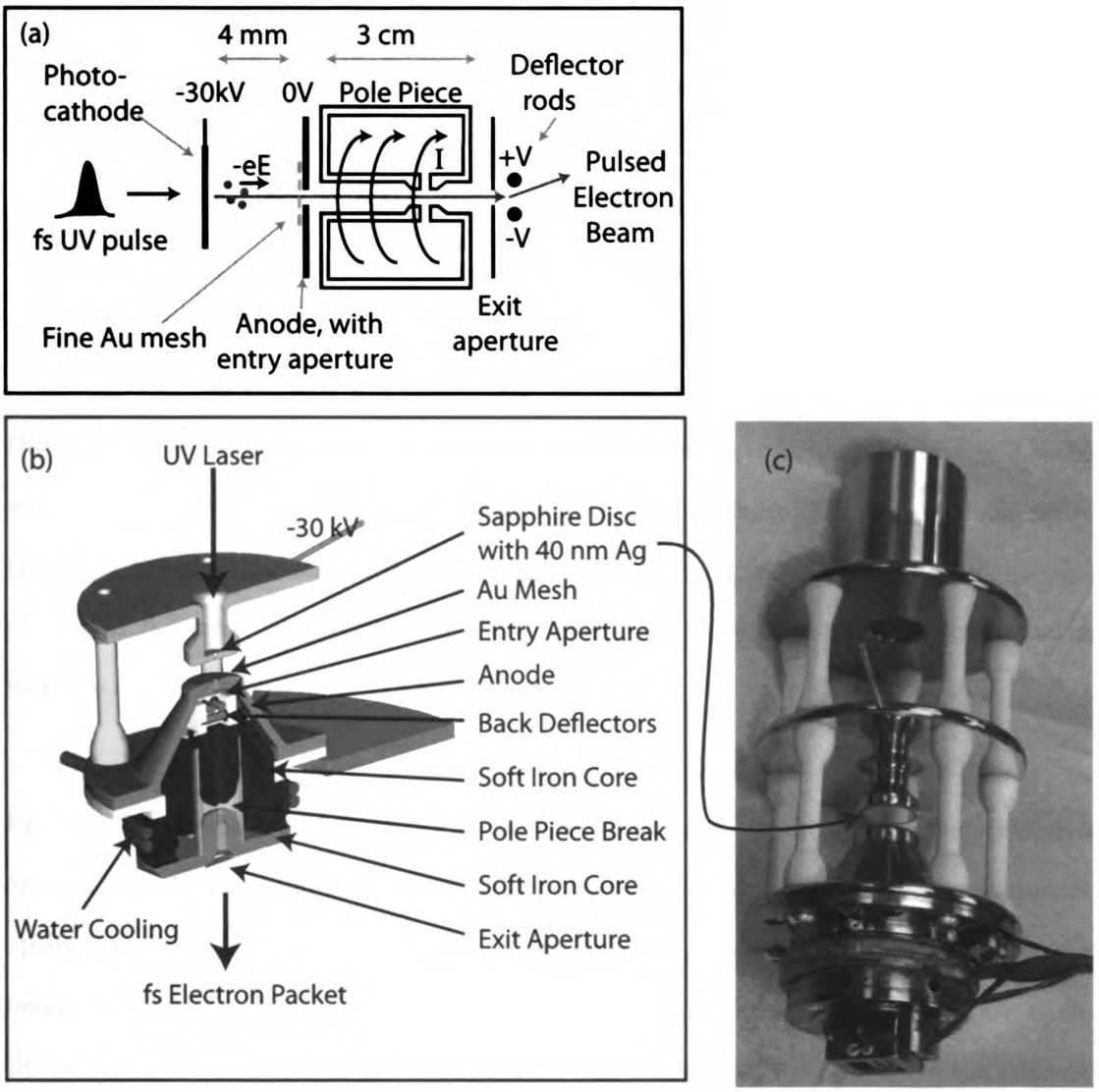

Figure 3.5: Design of the proximity coupled fs electron gun. (a) Conceptual layout of the gun. (b) Cross section CAD drawing of the optimized fs gun design currently in use. (c) Photograph of the actual electron gun, fully assembled just prior to installation within the UHV chamber.

[157, 158], electron-pulse self compression [159], and operation in the single-electron mode [160] where the space charge effect is eliminated completely. Here, we have resorted to the use of a short flight distance gun by designing a miniature gun in which the distance from photocathode to sample is $\leq$ 5 cm. Effort has been expended on careful optimization of the break in the pole-piece where the focusing action occurs to achieve strong focusing. Field calculations were performed using finite element numerical methods (*Field Precision, 'EMP suite'*) for various pole-piece geometries, paying particular attention to optimization of central bore diameter and design of the pole-piece break. the angles defining the central break were systematically varied. Focusing effect of the lens was quantified based on single electron trajectory tracking through these simulated fields. The final optimal geometry is shown in Fig 3.5 (b) which was observed in the simulations to focus an initially 300 μm electron pulse (prior to entering the lens) down to $\leq 10\mu$m at the sample position at lens currents of $>$ 300 A·turns. Figure 3.5 (c) shows the electron gun assembled just prior to installation inside the UHV chamber.

The characteristics of the electron packet generated by this source are detailed in Figure 3.6 and compared to those of the first generation electron gun. The first generation gun, also designed here at MSU consisted of two separate, smaller pole pieces optimized for 15 keV electron pulses. Consequently, using this lens to focus 30 keV beams resulted in larger electron probe size despite increased lens currents. Additionally, the increased currents were close to the upper operation limit of the current carrying wires (Kapton coated Cu wire, *Accu Glass*, 100680), with the lens requiring significant water cooling and increased wait times between diffraction exposures to prevent lens overheating. The new gun reported here aimed to overcome these limitations. A knife edge scan of the focused electron packet at the sample location yielded a minimum electron probe FWHM of $\sim$ 5 μm with the operating at current set to 322 A·turns and proper optimization to define the beam [see Fig. 3.6(b)]. This agrees

(a)	Gen-I	Gen-II
Current Per Turn	4.2 A	2.3A
# Turns	50 x 2	140
Beam Size	40 μm	5 μm
Coolant Temperature	-15 °C	5 °C
Wait time between exposures	15 - 20 s	0 - 5 s
Gun operation temperature	60 °C	12 °C

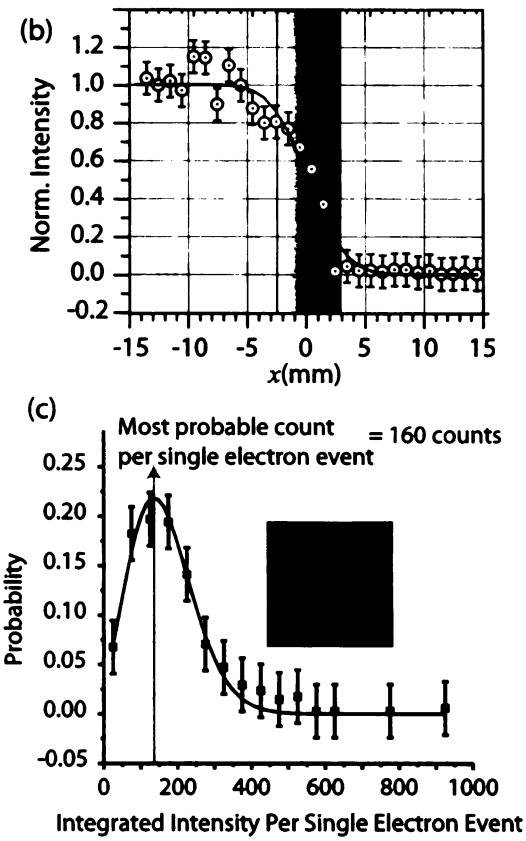

Figure 3.6: Characterization of the proximity coupled electron gun. (a) Comparison of 1^{st} and 2^{nd} generation electron gun performances. (b) Knife edge scan of the electron beam-size (2^{nd}-gen gun) at sample location showing $\sim$ 5μm FWHM. (c) Estimation of detector (CCD) response to a single electron event. Inset is a CCD image acquired at low-light levels showing 'blips' representing isolated single electron events.

well with the capability predicted from the earlier simulations. This reduction in beam size is important from an experimental point of view as it significantly reduces the detrimental effects of velocity mismatch [159] that can lead to the reduction in the temporal resolution of the system. Experiments are routinely performed with nominal electron pulse diameters of $\sim 10 - 20$ μm. Furthermore, the performance of this new gun as compared to the previous 1^{st} generation gun is also significantly improved in all aspects, as evident from Fig. 3.6(a).

We also estimated the number of electrons generated per electron packet. This

was done by operating the gun in a single electron mode by reducing the UV laser intensity to extremely low levels. This enabled the detection of isolated single electron events at the CCD. Measuring the detector response over multitude of such recorded events allowed us to determine the average detector response per single electron event. Based on this estimate, we obtained a maximum probe pulse intensity of 10^3 e^- per pulse, though normal operating conditions range in the 10^2-10^3 range. While this is not sufficient for single shot diffraction acquisition, which typically requires $10^5 - 10^6$ electrons per pulse, it is sufficient for multi-shot diffraction investigations. The low electron count ensures that the probe does not significantly perturb the system and the prospect of radiation damage to the sample is minimal. Furthermore, multi-shot probing also averages over statistical fluctuations that might be present in reversible processes. Most importantly, operation in this low electron density regime significantly reduces the effect of space charge broadening of the pulse, allowing the electron pulses to remain within the sub-ps regime despite the rather long 5 ns drift duration required for the 30 keV electrons ($v_e \sim 10^7$ m/s) to reach the sample (~5 cm away from photocathode) [146].

3.4 5-Axis Cryogenic Sample Holder

The sample holder for the UED system was designed with the following goals.

1. **Atm-UHV sample transfer capability** allowing quick, efficient transfer of samples in and out of the UHV chamber, without a need to vent the UHV system to air. This is essential to maintain and preserve UHV conditions and to the long term performance of the system.

2. **Low temperature capability** to facilitate diffraction experiments at low temperatures (< 50 K), opening the doors to investigations of exotic and complex

systems such as high-T_C superconductors, charge density wave materials and dosed adsorbates.

3. **In-plane sample rotation capability** to allow rotational control over the sample's azimuthal ϕ orientation, about the sample's surface normal. This is useful to enable probing the sample along the symmetric directions specified by its zone-axes.

4. **Transport experiments capability** to enable *in situ* electrical transport experiments by bridging the sample of interest across the two electrically insulated halves of the sample holder.

3.4.1 Overall Design

The sample holder is designed as an extension to the cold-finger tip of a commercially purchased closed-cycle helium cryostat (*APD Cryogenics, DE-202*), as shown in Fig. 3.7. The tip of the cryostat was benchmarked to attain 4K. A rather long extension ($\sim$ 12") was necessitated by the need for the sample to access both levels 2 (UED experiment) and 3 (sample transfer). The transverse width of the extension [along the probing electron beam direction, see panel (b)] was set not to exceed 1" in order to position the sample as close as possible to the electron gun and mitigate space-charge broadening of the electron pulse. The cold finger extension, $\approx$ 12" long was fabricated entirely out of oxygen free high conductivity (OFHC) copper as a single piece. A rigid cuboid framework that serves as a housing for the sample docking station was machined separately (material: OFHC) and silver soldered onto the end of the cold-finger extension. The use of silver solder to fuse these two parts ensures good thermal contact between the pieces and minimal thermal resistance at the junction allowing the heat from the docking station to be easily transported to the cryostat for rejection. Furthermore, as the large surface area of such an extended piece can

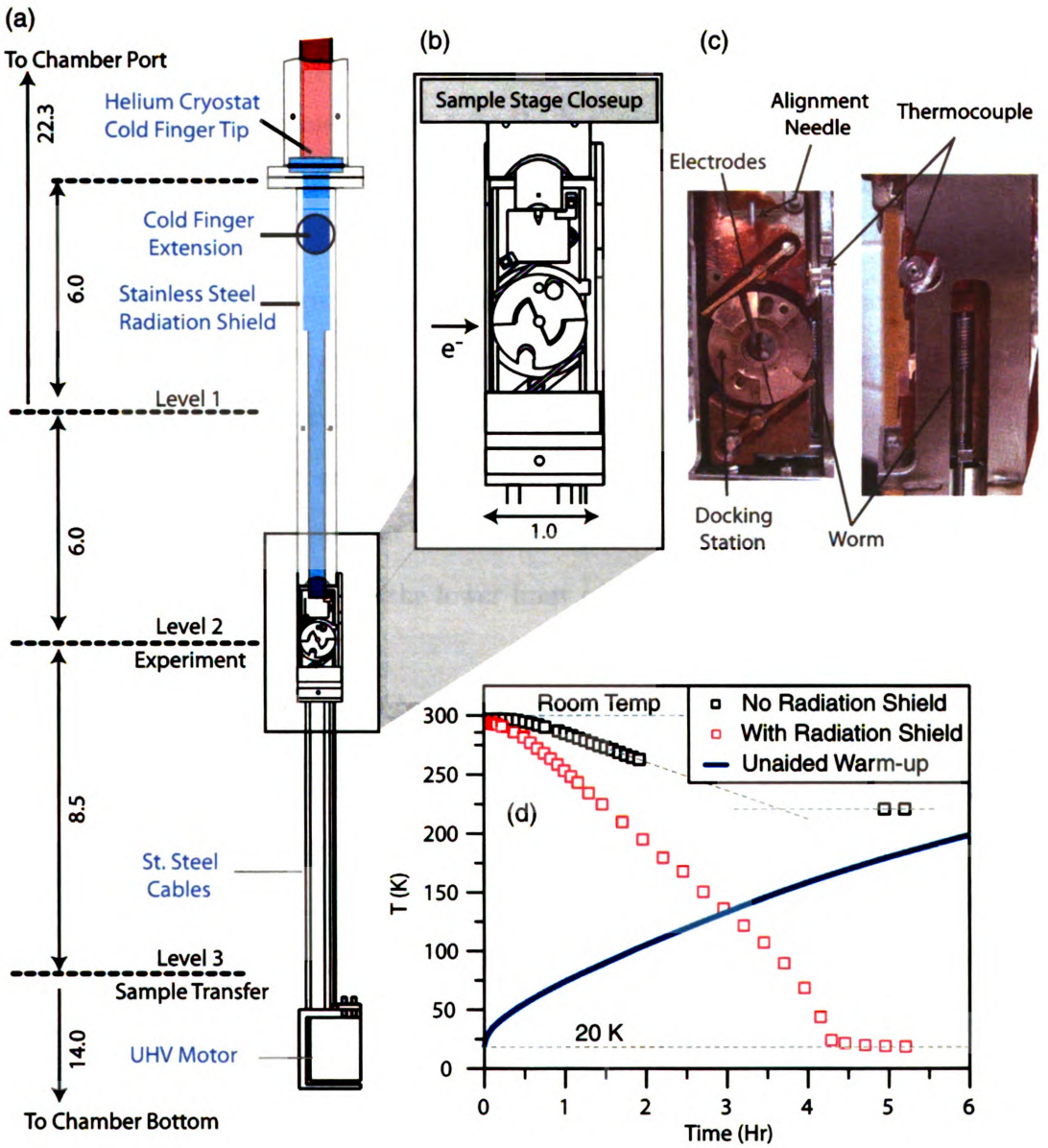

Figure 3.7: (a) Overview of the cryogenic sample holder, with sample transfer and sample-plane ϕ rotation capability. All dimensions shown are in inches. (b) Close-up of the sample stage on which the sample is mounted and ferried in and out of the chamber. (c) Front & side-view photographs of the docking station. (d) Measure of low temperatures attained by the sample stage with and without the radiation shield. Solid line represents the time taken for the sample stage to warm up once the cryostat has been switched off.

act as a source of significant heat gain from the ambient through radiation heating, the entire extension was enclosed in a stainless steel radiation shield, with only the area near the sample exposed to the ambient. The temperature of the system was monitored with a Chromel-Au/Fe type thermocouple capable of measuring down to $\sim$ 2 K, which was mounted directly onto the side of the copper framework as shown in Fig. 3.7(c).

This setup so constructed, was able to reach a low base-temperature of 19 K as shown in Fig. 3.7(c). When the cryostat was switched off and the system left to recover on its own, the temperature rose rapidly to 50 K initially, followed by a much slower heating rate, indicating good thermal insulation of the system. The importance of the radiation shield is apparent from the temperature curve obtained in the absence of the radiation shield, where the lower limit of temperature barely reached 225 K.

3.4.2 Sample Stage Construction

The sample holder can be thought of as consisting of two parts - a *docking station* that is housed inside a recess within the cuboidal Cu framework referred to earlier that remains permanently inside the UHV chamber, and a *sample stage* on which the sample is mounted and ferried in and out of the chamber through a long transfer arm. The sample stage is designed to dock on to the station, thus allowing sample transfer.

To enable rotational capability, the docking stage is mounted directly on top of the gear in a *sandwich*-like construction, as shown in Fig. 3.8. 24 ball-bearings (Be-Cu, 0.078" diameter) sit around the gear's circumference in between the gear surface and the walls of the Cu framework allowing for smooth rotation. The 'base-plate' seals the ball-bearings in their cavity.

To enable *in situ* transport experiments, the top half of the sandwich is broken into two electrically insulated halves, which are separated from the underlying components

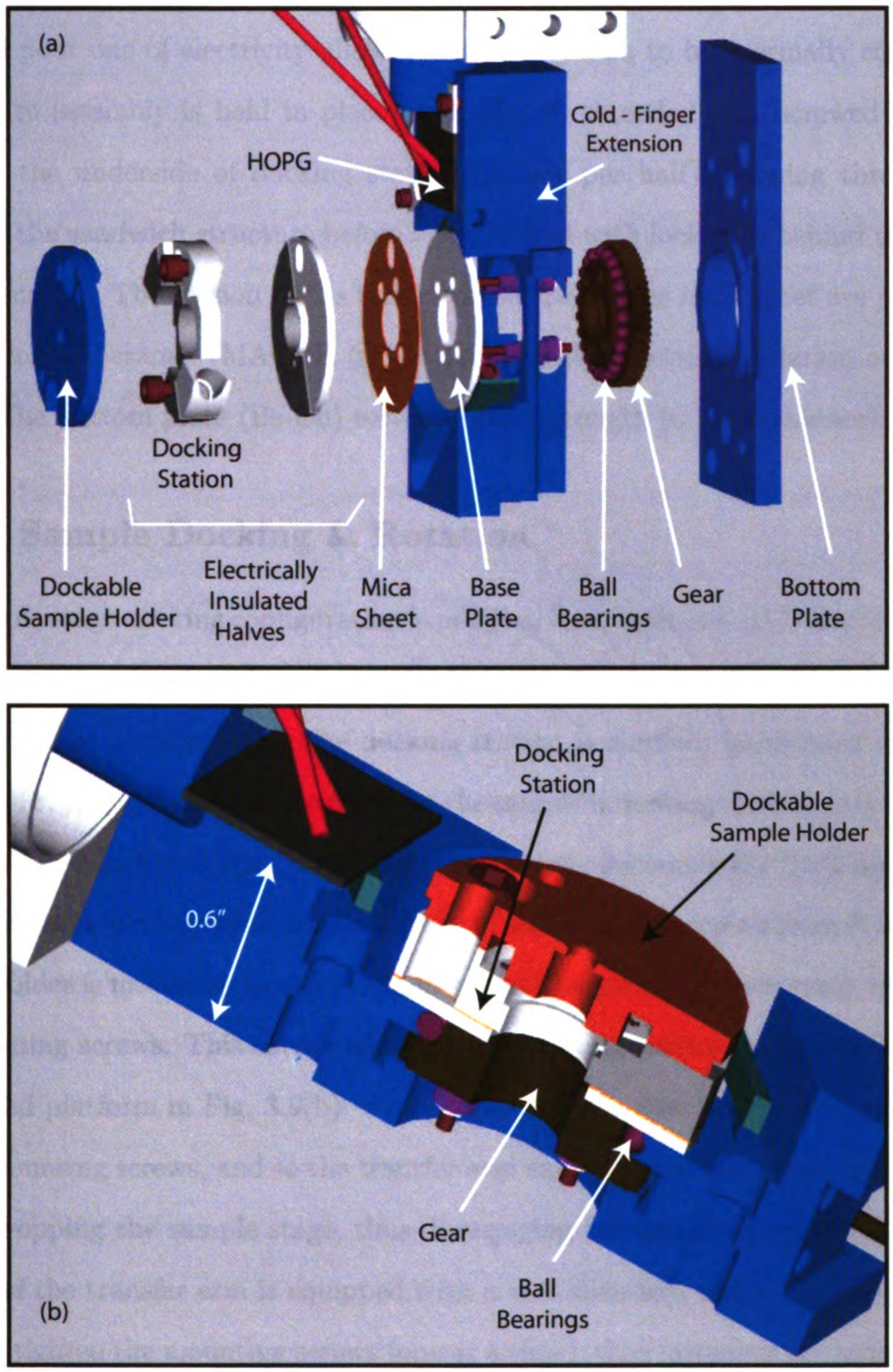

Figure 3.8: Construction of the dockable sample holder. (a) An exploded view of the docking station, showing the sandwich style construction to allow rotation. See Sec. 3.4.2 for detailed explanation of the features. (b) Transverse cross-section of the assembly, showing the location of the ball-bearings to enable smooth rotation of the entire station relative to the cold-finger extension.

(at ground potential) by a 75 μm thick mica sheet. Mica being a good conductor of heat and poor one of electricity allows the entire system to be thermally connected. This entire assembly is held in place by 4 #00-90 threaded rods screwed into tap holes on the underside of docking station (2 rods per half), running through the length of the sandwich structure before being bolted with lock nuts behind the gear's bottom surface. The section of the threaded rods below the mica sheet are protected by machinable ceramic (MACOR ®) to preserve the electrical isolation of the top halves. The bottom plate (Be-Cu) serves to lend strength to the framework.

3.4.3 Sample Docking & Rotation

The sample stage docking configuration is adapted from reference [161] and illustrated in Fig. 3.9. The docking stage is provided with a #4-40 tapped hole which can be engaged by the transfer arm. The docking station is carefully positioned at level 3 using the (x, y, z, θ) motion control so that the sample mounting screws enter the holes marked A & B in Fig. 3.9(a). Once the sample stage is completely flush against the docking station (evident from the emergence of the mounting screws from A & B), the sample holder is moved up in z, so as to move the sample stage downwards relative to the mounting screws. This causes the head of mounting screws to position on top of the shaded platform in Fig. 3.9(b). The sample stage is now loosely held in position by the mounting screws, and so the transfer arm can be safely unscrewed without any fear of dropping the sample stage, thus disengaging the arm from the sample stage. The tip of the transfer arm is equipped with a # 2 allen-key, which can now be used to firmly tighten the mounting screws (one at a time), thus fastening the sample stage firmly onto the docking station. The entire process is monitored by a video camera mounted on level 3 alluded to in section 3.2, providing the user with live feedback to carefully control the process. The docking process is relatively straightforward and can be accomplished typically within in a few minutes. Dismounting the sample is

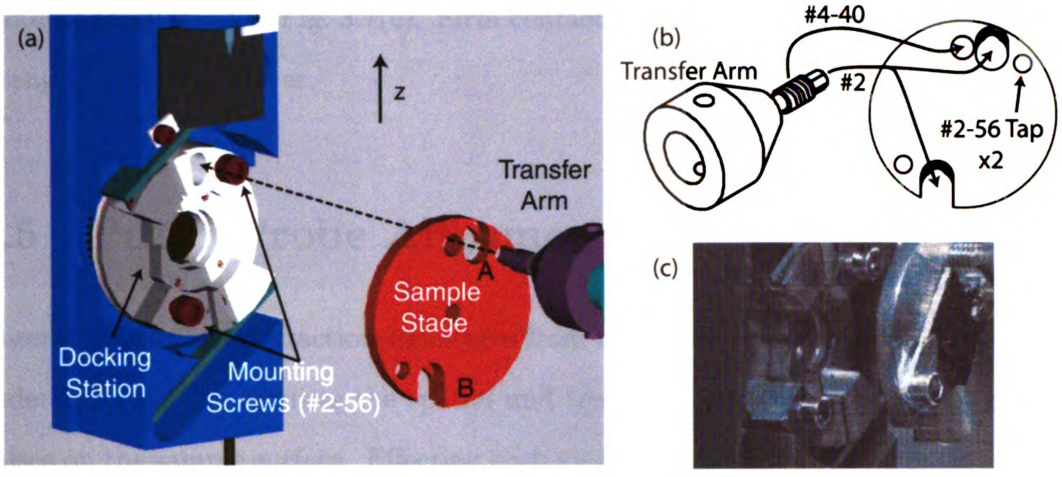

Figure 3.9: Sample docking mechanism. (a, b) The docking stage, engaged by the transfer arm, is hooked onto the docking station. The mounting screws prevent rotation of the system while the transfer arm is disengaged by unscrewing. The transfer arm tip, can be then used to tighten the mounting screws. (c) A still picture acquired from the video camera monitoring of the sample docking process.

simply the reverse of the mounting steps described here.

To enable the sample rotation, the gear on which the docking station is mounted is driven by a worm assembly attached to the shaft of a specialized UHV stepper motor (*MDC Vacuum*, Model # SM13-UHV). Since the motor can be a significant source of heat, it is displaced far away from the sample holder by hanging it from the bottom of the radiation shield by means of stainless steel (SS) cables, as illustrated in Fig. 3.7(a). The motor shaft is connected to a thin SS rod (0.063" diameter) to whose end, we attach worm that engages the gear, as seen in Fig. 3.7(c). The small diameter of the rod ensures it serves as a thermal bottleneck, thus preventing any significant heat transfer from the motor to the sample holder. The two ends of the worm are held in place by a firm wall at one end, and a spring-loaded support at the other, seen in Fig. 3.7(c)

Finally, the electrical contacts to the two insulated halves of the docking station are provided by a cantilever type electrode machined from Be-Cu, that maintains tangential contact with the sample holder even as the sample holder rotates. These

contacts are marked in Fig. 3.7(c). Firm contact is established by the inherent tensile strength of the cantilever.

3.5 Pump-Probe Alignment

Observing transient diffraction signatures from the photoexcited region of the sample under investigation requires the spatial and temporal overlap of the pump & probe pulses on the sample surface. Effecting such an overlap between the *invisible* electron pulse and the pump laser, both of which are a few hundred μm in size at a point inside the UHV chamber that is out of physical reach is a delicate task and requires some elaboration. To facilitate this task with relative ease, the UHV chamber is specifically equipped with 4 utilities: an optical video camera and, two non-collinear diode lasers operating in the visible light spectrum [see Fig. 3.3(b, c)] and a sharp-tipped needle suitably mounted adjacent to the sample [Fig. 3.7(b)]. The sequence of steps involved in the aligning the pump with the probe is illustrated in Fig. 3.10 and can be broken down into 2 steps - a *coarse* alignment, followed by a *fine* adjustment of the pump relative to the probe.

The optical camera used to monitor the alignment procedure is mounted outside the UHV chamber and aimed at the area immediately outside the electron gun's exit aperture, where the UEC experiment is conducted. Figure 3.10 (a) shows the view seen by the camera showing the exit port of the electron gun and the sample positioned adjacent to it. The horizontal dotted line drawn across the central axis of the gun represented the approximate propagation trajectory of the electron beam, projected onto the sample plane. The sample is positioned suitably close to the electron gun's exit port, following which, the y value of the sample manipulator is fixed and not altered.

The sample stage is moved in x and z directions so as to intercept the sharp tip

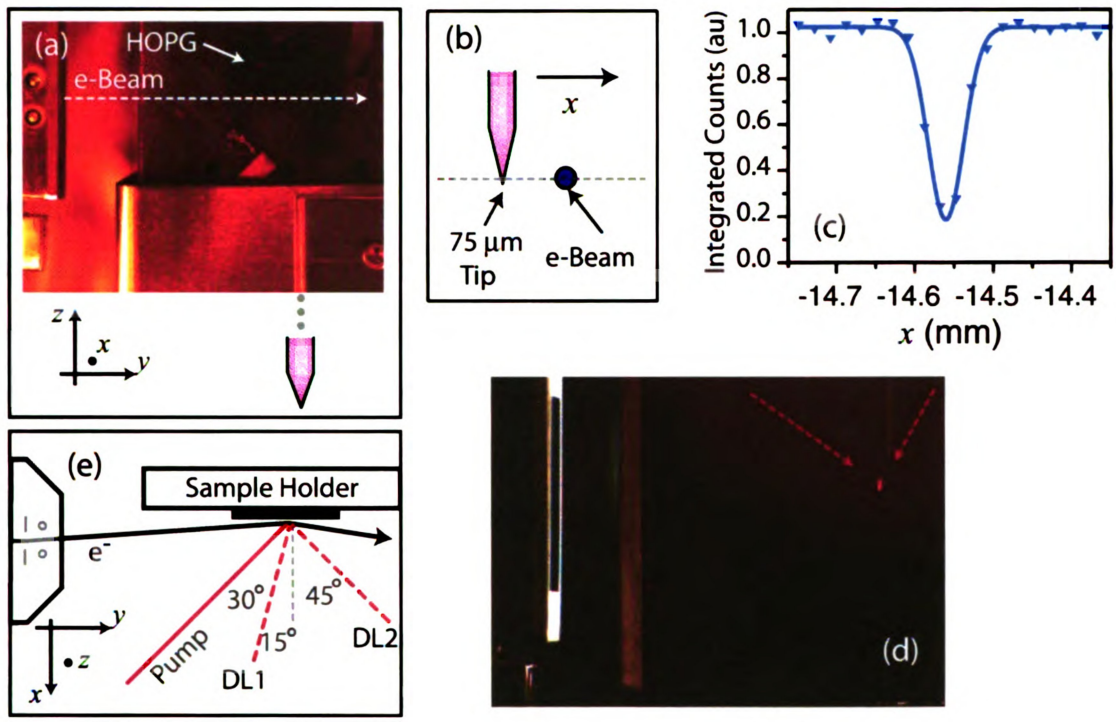

Figure 3.10: Coarse pump-probe alignment procedures. (a) View of the sample surface seen b the optical camera mounted outside the chamber. See Fig. 3.3(b). (b) Cartoon depicting the method adopted to intercept the electron beam with the sharp tip (diameter$\sim$ 75 μm) of an *in situ* mounted needle. (c) Plot of normalized integrated intensities of the electron beam as the needle cuts across its path. The inset show the appearance of the electron beam on the CCD at two representative needle locations as marked. The electron beam is clearly seen to be occluded by the needle tip at $x \sim$ -14.56 mm. (d) Directing the 2 non-collinear diode laser beams to intersect on the needle tip while the needle tip intercepts the electron pulse path in the chamber. (e) Overlapping the pump laser with the probing electron beam on the sample surface while using the intersection of the two diode lasers (DL1 & DL2) as guides.

of the installed needle with the electron beam, as illustrated in Figs. 3.10 (b) & (c). This is done by repeatedly scanning the needle across the electron beam and monitoring the occlusion of the electron beam on the CCD. When the electron beam intensity falls to roughly half the original intensity, the electron beam is occluded by the sharp tip of the needle, and the two diode lasers are directed onto the needle tip [See Fig. 3.10(d)]. The point of intersection of these two diode lasers now marks a unique location in free space through which the electron beam passes through.

The next step is to bring the pump laser also to this same point defined by the diode laser intersection. We avoid exposing the needle tip to the focused pump laser spot so as to not accidentally damage the sharp needle tip. Instead, we move the sample manipulator in x and z so as to bring a flat metallic surface such as that of the sample stage in view. The IR pump laser becomes visible on such metallic surfaces on account of fluorescence, as do the 2 diode lasers. All three are visible from the camera. The sample manipulator is moved in x direction so as to bring the 2 diode laser spots on the surface to overlap with each other. Then, the pump laser is adjusted so as to coincide with the two diode lasers, as illustrated in Fig. 3.10(e). This ensures that the pump laser is positioned close to the electron beam, though it may still not be perfectly aligned. The final alignment is executed on the sample surface directly by attempting to maximize the pump-induced change in the diffraction pattern.

We use a reference sample of graphite permanently installed inside the chamber to bring the pump laser into exact alignment with the electron pulse i.e. have pump and probe co-centric on the sample surface. We bring the reference graphite sample to the experimental level and alter the x such that the two diode lasers overlap on the graphite surface. Our prior coarse alignment procedure ensures that the laser and electron beam would be in close proximity to each other on the graphite surface. We scan the excitation laser in both 2DY and 2DX direction as illustrated in Fig. 3.11(a) by moving the focusing lens that is controlled by stepper motors. We monitor the diffraction pattern at some fixed delay which is known to be beyond the time-zero. If the approximate position of time-zero is not known beforehand, it is advisable to perform a full pump-probe delay scan first. Even though the pump and probe may not be perfectly aligned, if the coarse alignment is performed carefully, some degree of alignment is expected and some change will be detectable in the diffraction patterns using which time-zero may be ascertained. Thereafter, optimal overlap of pump and probe is performed by maximizing the changes in diffraction maxima at a fixed

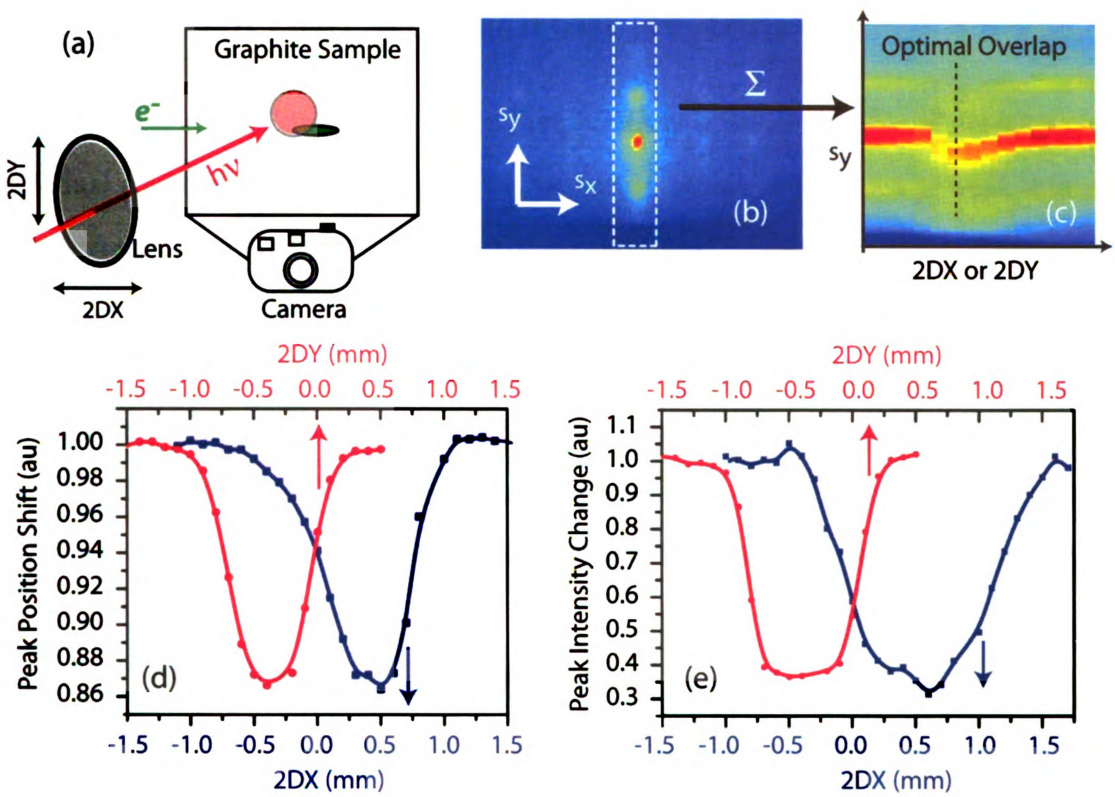

Figure 3.11: Fine pump-probe alignment procedures. (a) Raster scan pump laser (red spot) across the surface region probed by the electron pulse (green spot) by moving the focusing lens mounted on stepper-motor controlled stage. (b) Graphite diffraction pattern. We acquire diffraction pattern at a fixed pump-probe delay for a sequence of 2DY and 2DX lens positions. In each pattern, we integrate the intensity along s_x direction within the central streak region specified by the dashed box to produce a 1D curve, which are all then stacked in sequence to form a 2D map image shown in (c) that visualizes the change in diffraction pattern. The location of maximum change defines optimal pump-probe overlap. (d, e) The variation in intensity and position of the brightest Bragg spot seen in (b) as a function of 2DX and 2DY position. Both plots suggest an optimal overlap of pump and probe at (2DX, 2DY)=(-0.4, 0.5)

positive time-delay in both position as well as intensity, as illustrated in Fig. 3.11. Following this, the pump and probe are perfectly aligned.

3.6 Diffraction Acquisition System

The diffraction acquisition system is a highly sensitive device capable of detecting individual electron events (*single electron detection*), allowing detection of weak diffraction signals. This high degree of sensitivity is obtained by using a Peltier cooled CCD camera (Princeton Instruments, PI-SCX-1300) operating at -35° C (to reduce thermal noise), whose front end is coupled to an *image intensifier* that acts as an electron multiplier in order to amplify weak diffraction signals. The construction of the system is shown in Fig. 3.12. There are several stages through which the signal represented by the incident electron proceeds to achieve amplification, and eventual detection.

3.6.1 Intensified CCD Camera

At the front end of the image intensifier is a 60 nm aluminum layer that serves to block any light from entering the detection system while allowing the electrons to pass through. The penetration depth of visible light in Al ranges from 7-15 nm [162], while that for 30 keV electrons is of the order of several μm [163]. Thus most of the ambient light and any reflected laser light that may be present in the chamber is blocked by this layer. The electrons penetrate the layer, losing about 3 keV energy in the process and strike a phosphor screen behind, stimulating fluorescence in the visible region. These light photons are collected by a 2:1 tapered fiber optic assembly and transported to the image intensifier where signal amplification occurs.

The light photons are reconverted back into electrons at the front end of the image intensifier by allowing them to impinge on a photocathode. The photoelectrons so generated are then accelerated and closely focused within a short distance by 10 to

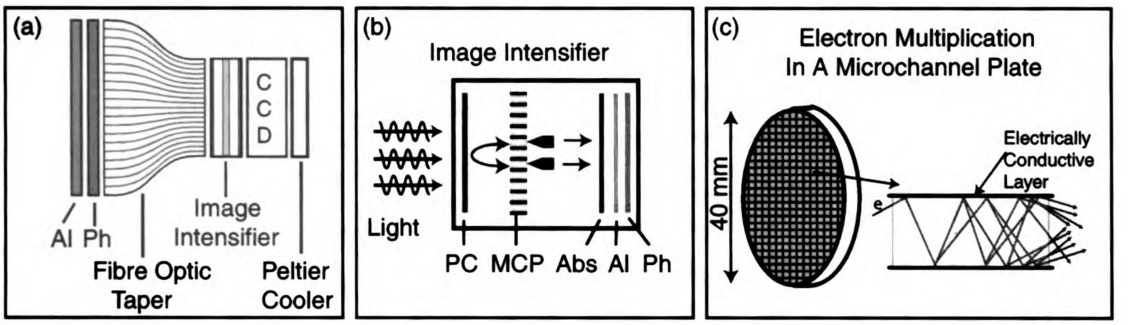

Figure 3.12: Construction of the *Intensified* CCD detector, capable of single electron detection. (a) The Intensified CCD camera (b) Image Intensifier (c) Electron multiplication in a Microchannel plate array.

15 kV and enter the *micro channel plate* (MCP) assembly. The operation of MCP is analogous to that of a photomultiplier tube; electron amplification is achieved by generation of multitude of secondary electrons each time an electrons strikes the electrically conductive boundary layer. These amplified electrons then strike another phosphor screen to convert the electrons back into light, which may then be detected by the CCD. The phosphor screen has a dual-layer protection against signal corruption by spurious light. A special absorptive layer absorbs any of the light that might leak through the semi-transparent photocathode, while the aluminium reflection layer seeks to block any light generated near the phosphor screen from returning to the photocathode. Each MCP can provide an amplification of up to 1000 e/e, and an image intensifier can have upto 3 MCPs between the photocathode and the phosphor screen, thus allowing a gain of upto 10^9. Finally, the amplified signal, in the form of light photons is incident on the CCD screen, where it is detected in the usual way.

The use of image intensifier allows one to control the amplification/gain of the detection system by increasing the bias voltage between the MCPs. As a result, even weak diffraction signals can be enhanced by increasing the gain of the system suitably. However, in order to avoid over exposure of the CCD and prevent accumulation of noise during the period in between two electron pulses, it is prudent to implement time-gated data acquisition, in which the image intensifier switched just in time to

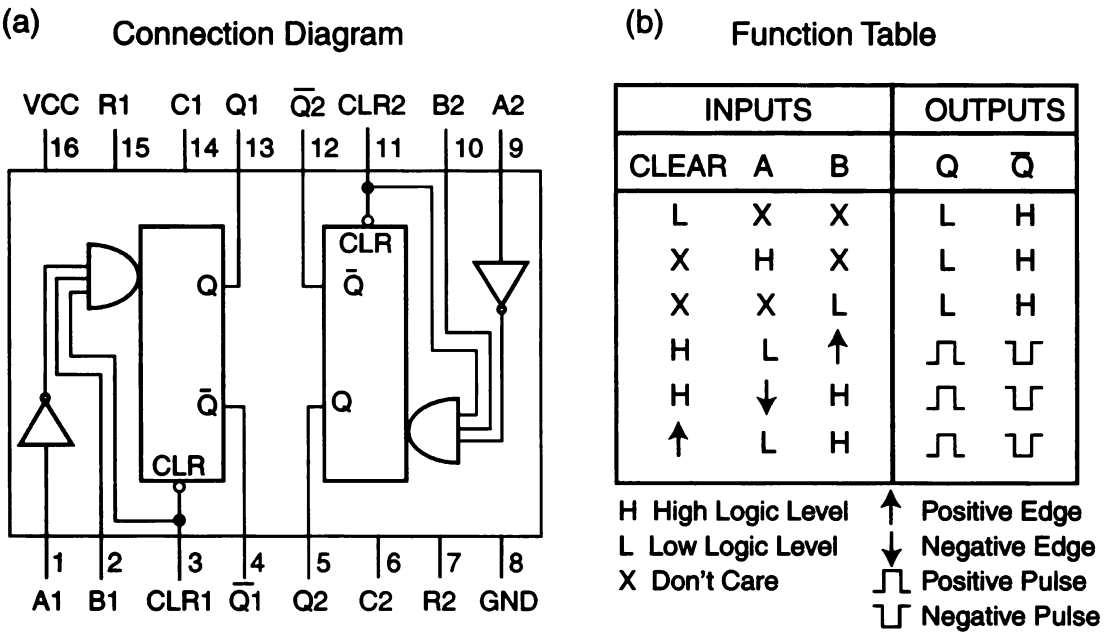

Figure 3.13: Operation Principle Of The IC LS123. (a) Connection Diagram. (b) Function Table. [Source: Fairchild Semiconductors DM74LS123 Data sheet]

record the arrival of the electron pulse.

3.6.2 Time-Gated Data Acquisition

The synchronization of diffraction acquisition with the arrival of electron pulses at the CCD is controlled by a the 1 kHz clocking pulse produced by the fs laser system's timing electronics. This master clock is a 1kHz 5V digital signal that corresponds to the generation of ultrafast laser pulses in the cavity. Owing to the finite time delay between the creation of the laser pulse and the arrival of the electron pulse at the CCD, timing the image intensifier to turn on precisely with the arrival of electron pulse at the CCD requires a control over the delay and width of the gating pulse, relative to master clock. This is achieved using an IC LS123, which is a dual, retrigerrable monostable multivibrator. The multivibrator generates a digital pulse every time it is triggered, as illustrated in Fig. 3.13. The duration of the pulse is determined by the time constant of an RC circuit at its output. The implementation of the delay-generator circuit

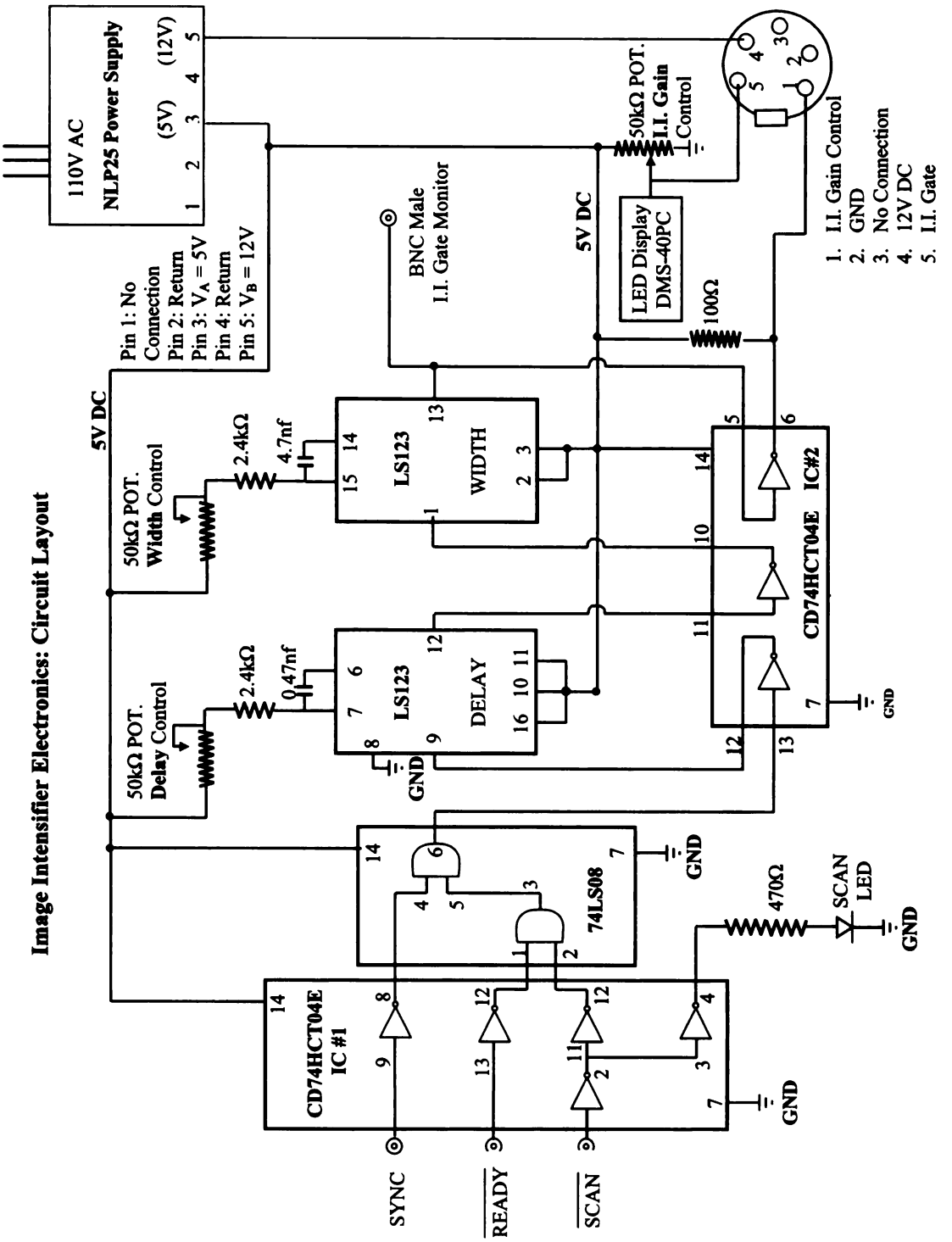

Figure 3.14: Circuit layout of the timing generator For Time-Gated Diffraction Acquisition

using the LS123 is shown in Fig. 3.14 where the two multivibrators are connected in a 'master-slave' fashion. The 1kHz clock from the laser, represented by the *SYNC* line drives the master multivibrator, whose Q output acts as the clock for the 'slave' multivibrator. Both, master and slave have their B and *Clear* signal held high, and so trigger on a negative edges [See Fig. 3.13(b)]. Thus, when the *SYNC* signal goes low, the master multivibrator generates a pulse, whose duration is determined by R1, C1. The falling edge of this pulse triggers the slave multivibrator, which in turn generates its own pulse of duration specified by R2,C2. The $\overline{Q}$-output of this slave is used as the 'Gate' signal over whose duration the image intensifier remains active. It is apparent from this that the master multivibrator controls the 'Delay' of the gate-pulse relative to the laser's clocking pulse, while the slave multivibrator controls the pulse-width. The use of a variable 50kΩ potentiometers in the RC circuits of the multivibrators allow the delay and width of the gate signal to be varied continuously.

3.7 Optical Experiment Station

The instruments described so far were all involved in diffraction experiments conducted in this lab. In addition to this, we have also established an optical experiment station capable of conducting transient reflection and transmission experiments on any sample of interest. Such optical investigations provide insights into the initial electronic dynamics on the fs scale and augment the insights gained from diffraction studies of the same system. The layout of the optical experimental setup is shown in Fig. 3.15.

A small fraction ($\approx$ 200 mW) is tapped out from the primary 800 nm laser using a 90/10 beam splitter and routed into the optics area where it is further split by a second 90/10 splitter to form the pump (90%) and probe (10%). The pump beam is directed through a translational delay stage and subsequently focused onto the sample

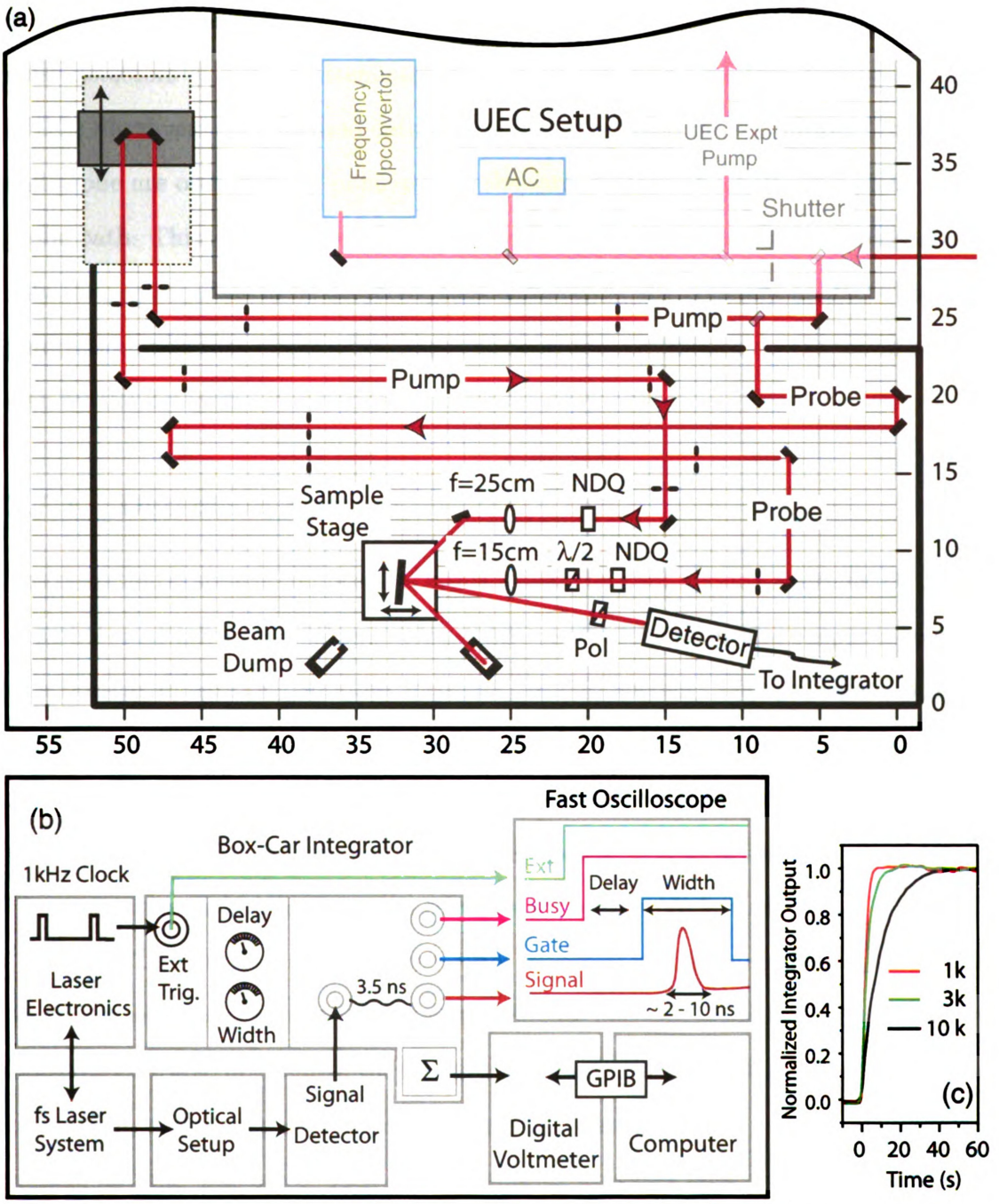

Figure 3.15: Optical experiment station. (a) Optic table layout of components. The numbers along axis are inch markers, used to approximately locate each component. (b) Box diagram outlining the detection system; Time-gated data acquisition and exponential averaging of data performed by a box-car integrator. (c) Response time of the integrator over which the average output settles to a new value when the input signal changes. 10k sample averaging provides best S/N but requires longer sampling periods to reach true average value.

at a 45° incidence angle. The probe pulse $\approx$ 10 mW which is still quite strong for most detectors is further attenuated to $\sim$ 1-10 μW using neutral density quotient (NDQ) filters and then focused onto the sample at near-normal condition. The pump and probe are orthogonally polarized by the introduction of a half-wave plate in the probe path. This, combined with a polarizer in front of the detector selectively allows only the probe pulses to be detected, thus eliminating any coherent artifacts between pump and probe that might arise near time-zero, and also minimizes the pump-scatter seen by the detector.

3.7.1 Detection System

The detection system is composed of either a fast PIN photodiode (*Thorlabs*, DET10A) or a photomultiplier tube (*Hamamatsu*, R928) as the detector whose output is coupled to a box-car integrator (*Stanford Research*, SR250) system. We opted for a box-car integrator (BCI) system over a phase-sensitive detection scheme due to the low duty cycle of the signal. The detector response to the fs laser pulse typically lasts for $\sim$ ns, while the laser pulses are separated by 1 ms leading to a signal duty cycle of 10^{-6}. Phase-sensitive or lock-in detection schemes are unsuitable in such limits.

The BCI generates a synchronized 'Gate' signal of user specified width, which can be positioned precisely over the detector response corresponding to the probe pulse. Once the gate is so positioned, the integrator sums up the detector response within the gate width, and averages the signal over multiple laser shots to produce an averaged voltage output. The use of such gated averaging prevents noise accumulation within the detector in between laser pulses and thus aids in increasing the signal to noise (S/N) ratio.

The BCI is triggered externally by the 1kHz clock of the laser system to ensure zero jitter between the probe pulse and the gate. In order to accurately position the gate over the signal, the integrator provides 3 outputs: (a) an internally delayed

(3.5ns) 'Signal Out', (b) 'Gate' and (c) 'Busy'. These are fed into a 300 MHz fast oscilloscope by means of *equal length* co-axial BNC cables and the oscilloscope is set to trigger externally by the Busy signal. The Gate can now be positioned over the Signal Out by adjusting the 'Delay' and 'Width' controls of the integrator shown in Fig. 3.15(b). Once this is achieved, the integrator integrates the signal within the gate period and calculates an *exponential moving average* (EMA) of the stream of data signal arriving from the detector. EMA is essentially a weighted average of N samples, with maximum weight alloted to the most recent sample and exponentially decreasing weights to older samples. To clarify terminology, setting the integrator averaging to $N = 10$k samples implies that the output will reach 66.67% of its true average value in 10,000 samples (i.e. in 10 s, given the laser's 1kHz pulse repetition rate). To reach within 99.9% of the true value, one needs to average longer, typically 60 s, as evident from Fig. 3.15(c). The effect of this averaging option is evident in Fig. 3.16 where we have plotted the BCI average output when the probe laser pulse is incident directly on the detector. With photomultiplier tube (PMT) as the detector, and no averaging option ($N = 1$) selected, the data shows large fractional spread of $\sigma \approx \pm 10^{-1}$. This spread reduces to $\leq 10^{-3}$ when 10k sample averaging is selected. This reduction agrees well with the $\sqrt{N}$ scaling expected from a shot-noise limited setup. Curiously though, similar scaling is not seen while using the photodiode (PD) as the detector, where no improvement in S/N is seen going from 300 samples to 10k samples. This indicates that the noise while using a PD may be limited by the detector noise, and not by statistical shot-noise as in the case of PMT. As a result, the choice of detector is an important aspect of the detection system, which is discussed further in Sec. 3.7.3.

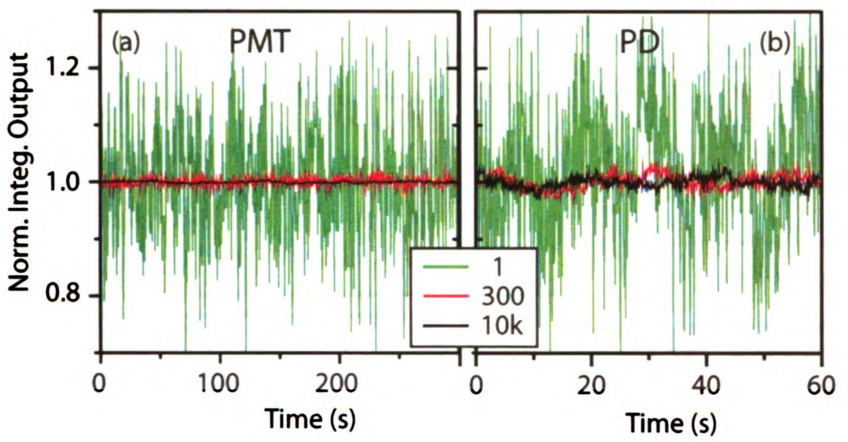

(c)

N	σ (%)	
	PMT	PD
1	12.5	12.8
300	0.6	1.3
10k	0.1	1.0

Figure 3.16: Effect of exponential moving average (EMA) option of the box-car integrator. Fluctuation in averaged integrator output for 3 different EMA options while using (a) Photomultiplier tube (PMT) with control gain set to 1.0 V and (b) Photodiode (PD) to probe the unperturbed ground state of HOPG. (c) Standard deviation of data in (a) and (b) expressed in % Note: The data was acquired at the rate of 1 sample per ms using a DAQ board (*National Instruments*), though (a) and (b) plot only selected data points 500 ms apart. The numbers in (c) are estimated based on the complete data.

3.7.2 Optical Pump-Probe Alignment

Effecting a pump-probe overlap with the optical set up requires careful considerations. In most optical setups, overlap is typically achieved through the use of second harmonic generation in a non-linear crystal such as $\beta-$Barium Borate (BBO). In such a setup, the pump & probe are allowed to spatially overlap inside a thin BBO crystal. Temporal overlap is established by scanning the relative delay between the pump & probe while looking for the second harmonic output, which occurs only when the two pulses arrive at the BBO crystal simultaneously. Here, we have used a different approach. Typically, transient optical responses are extremely fast and often decay completely on a timescale of $\sim$ 1-5 ps. Thus, a precise determination of time-zero requires scanning the translation stage at $\sim$ 100 fs resolution. However, if time-zero is not known in advance, it is impractical to carry out such a fine scan over a range of several ns; the determination of an approximate time-zero is an essential first step.

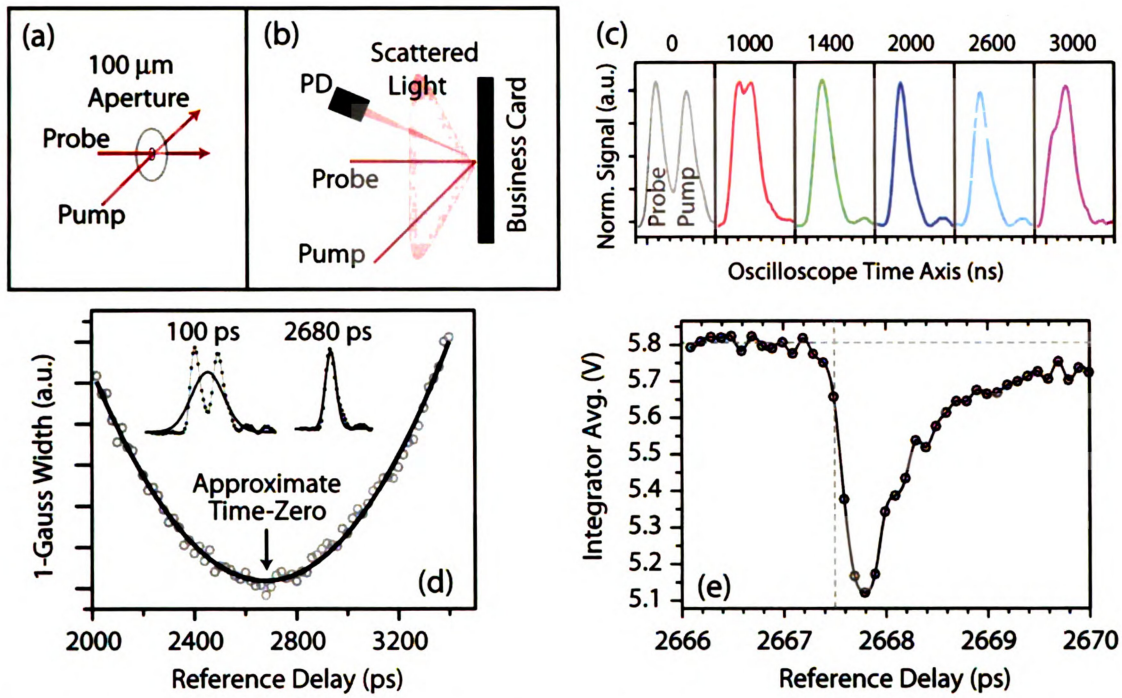

Figure 3.17: Overlapping pump & probe pulses. (a) Align pump and probe lasers through a 100μm aperture. (b) Detect using photodiode (PD), the simultaneous pump and probe scatter from a business card placed at the experimental position. (c) Evolution of PD response in (b) as the translational delay stage is scanned, showing the merging of pump & probe signals. The numbers (in ps) indicate delay stage position. (d) Width of the 1-Gaussian fit to the oscilloscope traces (points) along with a quadratic polynomial fit (solid line). The insets shows the signal profile and the fitted Gaussian curve at two select time points. (e) Determining time-zero with fs resolution based on monitoring *in situ* pump-probe change in reflectivity signal from graphite. Time-zero is clearly established as 2667.5 $\pm$ 0.1 ps

The pump & probe are first spatially overlapped by mounting a small 100 μm Pt:Ir aperture (*Ted Pella*) at the experiment location and directing the pump and probe laser beams through the aperture, as illustrated in Fig. 3.17(a). Overlap is optimized by maximizing the intensity of the lasers transmitted through the aperture. The plane of the aperture now defines the experimental location where pump & probe are spatially overlapped. Next, to obtain an approximate time-zero, the aperture is replaced by an ordinary business card that scatters incident light from both pump & probe in all directions. The scattered light is detected by a PD placed away from

the specular reflection directions of both pump & probe, and the signal fed into a fast 300 MHz oscilloscope. The PD signal shows two distinct peaks, each arising from the detector's response to scattered pump and probe respectively. The pump & probe intensities are adjusted (typically by reducing the size of iris in their respective paths) to make both peaks roughly equal in strength. As the translation stage is scanned and the pump-probe delay altered, the two peaks begin to merge, as seen in Fig. 3.17(c). A sequence of such traces is obtained for different pump-probe delay, and each trace fitted with a single Gaussian profile. Clearly, the trace for which the 1-Gaussian width is the least corresponds to a perfect overlap in time of the detector's response to pump & probe, and hence indicates temporal overlap of the two pulses at the business card. As shown in Fig. 3.17(d), this minimum width condition yields an approximate estimate of time-zero which can be reliably trusted to within $\pm$ 25 ps.

Finally, precise determination of time-zero with fs resolution is obtained by monitoring the *in situ* sample response. The business card is replaced by a graphite sample while taking care to translate the graphite sample surface onto the plane of pump-probe overlap. The detector (photodiode) is positioned so as to intercept the specularly reflected probe signal, and the response fed into the detection system. Employing nominal pump fluence of $\approx$ 20 - 30 mJ/cm^2, ensures strong reflectivity response. Time-zero is precisely determined following a pump-probe reflectivity scan with 100 fs time step spanning the time-window around the approximate time-zero obtained earlier. Such an fs response in the reflectivity signal from photoexcited HOPG is shown in Fig. 3.17(e), identifying time-zero clearly.

3.7.3 Choice Of Detector: Photodiode Or PMT?

As mentioned earlier, choosing the appropriate detector is an important aspect of the system design. The $\sqrt{N}$ scaling of averaged signal from PMT seen in Fig. 3.16

suggests the noise to be limited by the statistical shot-noise, whereas that from PD is instrument limited. On the flip side however, PMT is an extremely sensitive device with an internal gain of $\sim 10^5 - 10^7$, and consequently operable only in very low light conditions. To reduce any ambient light which can significantly affect PMT signals, the PMT is housed inside a light-tight box (*Thorlabs*, PXT-1) and a 30 μm aperture limits the light incident on the photocathode. Indeed, for the data presented in Fig. 3.16, the PMT photocathode was exposed to light levels 4 orders of magnitude lower than that incident on the photodiode. Such low light levels are necessary to prevent the PMT from getting saturated with light photons and preserve its high sensitivity.

The effect of PMT saturation on the measured signal is illustrated in Fig. 3.18. Panel (a) shows the fs pump-probe dynamics obtained from graphite excited at $F = 5$ mJ/cm^2 using a photodiode as detector and extremely low probe power levels [1]. We observe a maximum change in reflectivity of 7% at $t = 400$ fs. We subsequently swapped the photodiode with a PMT, without changing any optics upstream and monitored the maximum reflectivity change at $t = 400$ fs as a function of the PMT internal gain. We observe that the PMT is insensitive to the pump-induced transient reflectivity change at high gain and the true dR/R is obtained only at extremely low gain settings. This is indication that even at such low light levels, the PMT anode is getting saturated.

We benchmark the performance of our PMT based on a low power CW He-Ne laser source with average power of $\approx$ 1 mW. The gain curve obtained is shown in Fig. 3.18(c) and found to agree excellently with the manufacturer supplied data sheet over light levels spanning several orders of magnitude. However, when the same is performed using the fs probe pulse, the relative gain agrees well with the data sheet only for the lowest light levels, and shows deviation from the typical gain curve, indicating

[1]NDQ 300 filter (% transmission = 10^{-3}) was used in the probe path

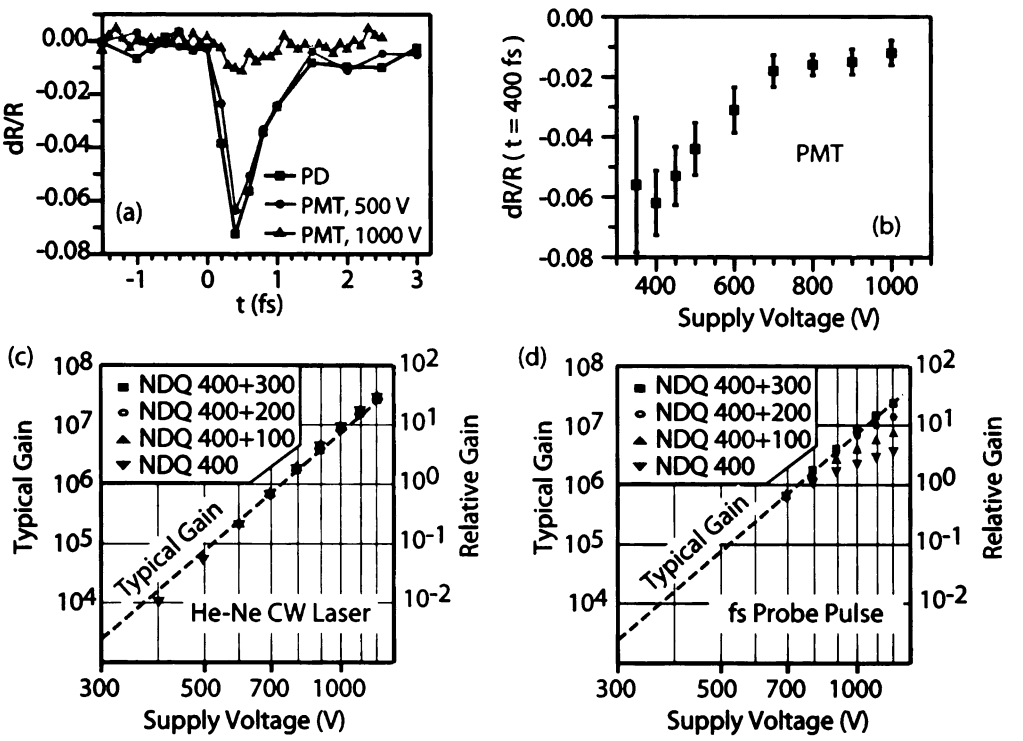

Figure 3.18: (a) Pump-probe dynamics from graphite excited at $F = 5$ mJ/cm^2 using photodiode (PD) and PMT as detectors. At high gain, the PMT saturates, and is insensitive to the pump-induced reflectivity drop. (b) Maximum dR/R measured at $t = 400$ fs while varying the PMT's internal gain via the supply voltage. (c) The PMTs gain curve while using a CW He-Ne Laser (1 mW average power). Data points (right axis) represent the gain obtained at different supply voltage relative to that at 700 V, while the dashed line represents typical gain (left axis) provided by manufacturer. (d) The same as (c), except using the fs probe laser pulse now. Deviation from the linear behavior is seen even at the lowest of light levels.

saturation. Based on the PMTs anode saturation current of 100 μA, photocathode quantum efficiency of 3% at $\lambda = 800$ nm and an anode sensitivity of 7.4×10^5 A/W, we determine an average saturation threshold for the PMT (when operating under the CW mode) as 18 photons / ns. By contrast, for the fs laser pulse, even a very weak probe of 1 mW average power corresponds to 10^{10} photons per pulse. The insertion of NDQ 400+300 filter reduces the intensity by 7 orders of magnitude to $\sim 10^3$ photons per pulse. Further reduction is achieved by the 30 μm aperture in front of the PMT. Consequently, the PMT remains in the linear regime only at the

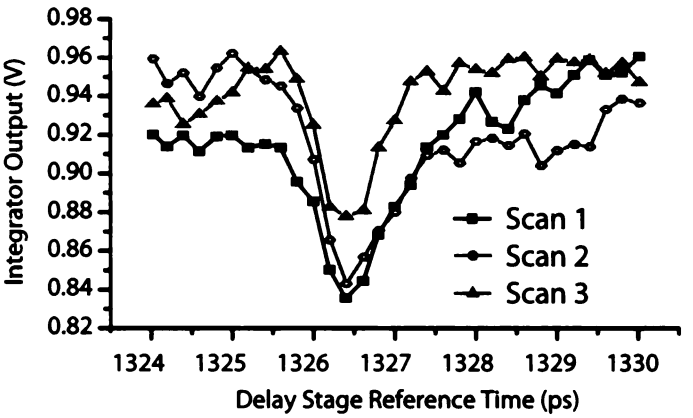

Figure 3.19: Baseline drift of signal. 3 delay scans, acquired in rapid succession show the shift of the reference baseline during the data acquisition. Each scan is composed of 31 time-points and requires about 5 minutes to complete.

very lowest of light levels and gain settings. From these results, it is clear that a PMT, while extremely sensitive, is not the ideal choice for reflectivity and/or transmission experiments where the light levels are quite high. PMT would be better suited to low-light applications such as photon counting experiments. All optical experiments reported in Ch. 4 are obtained using a photodiode as the detector.

Another problem in accurate detection of transient reflection or absorption signals is the low-frequency signal drift that occurs due to modulation of the source signal i.e. the laser. This signal drift is illustrated in Fig. 3.19 that shows 3 delay scans obtained consecutively in rapid succession. As is evident from the figure, the base-line signal is constantly drifting during the scan, and needs to be corrected for in order to accurately determine the fractional change in signal R $\Delta R/R_0$. Normally, such low frequency drift can be eliminated by normalizing the detected signal against a second reference probe signal scattering from an unperturbed area of the sample. However, this would requires the use of 2 box-car integrators, which was unavailable. As a result, data is acquired by moving the delay stage back to negative times after every positive time point and the fractional change $\delta R/R_0$ calculated. Since no significant improvement in S/N is obtained for photodiode beyond 300 sample averaging, we set

this as the sample averaging option in the BCI and consequently adopt a 5 s wait time after delay stage motion at each time-point to allow the output to settle to its true value [see Fig. 3.15(c)] before readout though the GPIB interface. Thus, every positive time point and corresponding reference data at negative time is recorded $5-10$ s apart, during which time, the laser does not drift significantly. This fractional measure $\delta R/R_0$ is averaged over many scans to improve the S/N. Tests have shown that no significant S/N improvements are obtained beyond $30-40$ scans.

Chapter 4

Ultrafast Dynamics Of Graphite At Near-IR Photoexcitation

There is a growing interest in displacing atoms in materials by photo-excitations [14], as evident from the introduction to electronically induced structure transformations in Ch. 1. Observations of transient structures thus formed offer a glimpse into the transformation pathways between different structures and into the nature of bonding in solids. Study of such processes allow us to explore novel structural configurations of materials that might otherwise be unfeasible under thermodynamic conditions. Carbon, in particular, with its propensity to form a wide range of bonding networks (sp, sp^2, sp^3) is ideal to study the dynamics of bond formation and rupture. Of particular interest is the conversion of graphite to diamond [1, 2], which is believed to involve the rhombohedral phase of graphite as an intermediate state [71, 72]. While pioneering ultrafast optical studies of graphite have provided evidence for photo-induced melting [164, 165] and generation of coherent phonons [80, 166] in graphite, the direct determination of lattice structural dynamics from optical data proves difficult, especially in the far-from-equilibrium regime. X-ray diffraction has been successful in observing ultrafast structural changes in semiconductors [27], though a direct observation of

atomic motion in nanostructures with low atomic number, such as carbon, has not yet been achieved. Here, we employ ultrafast electron crystallography (UEC) to study photoinduced structural dynamics in graphite. UEC on account of its enhanced scattering cross-section (five orders of magnitude greater than X-rays) is well-suited for this study. Combined with the advanced schemes to achieve femtosecond temporal resolution in table-top setups [28, 112, 126, 167], UEC offers a new window into the realm of photo-excited structural dynamics, with surface sensitivity down to ≈ 1 nm [28, 126, 168].

4.1 Experimental Details

UEC investigations of graphite were carried out using highly oriented (ordered) pyrolytic graphite or HOPG, which is composed of micro-crystals of graphite with grain size ranging from $1 - 10$ μm, all of whose c-axis are oriented parallel to each other. The angular spread of the c-axis between the different grains is $0.4^\circ \pm 0.1^\circ$, indicating the high degree of order along the c-axis. Thus, HOPG serves as an excellent candidate to study the *inter-planar* dynamics in graphite.

Freshly cleaved samples of HOPG (*SPI supplies*, ZYA Grade) were placed inside the UHV chamber through the load lock system at room temperature. The sample was photoexcited by an 800 nm ultrashort laser pulse (45-fs) with p-polarization, operating at a 1 kHz repetition rate. The pump laser was marginally focused ($\approx$ 600 μm diameter) onto the sample at $\approx 45^\circ$ relative to the HOPG c-axis. Prior to carrying out structural investigations, we determined the threshold for photoinduced degradation of HOPG surface. Permanent structural damage was evident on the sample surface upon multi-shot exposure at $F = 120$ mJ/cm^2 indicating irreversible structure change, arising from ablation and/or melting of graphite surface. This *in situ* determined damage threshold agrees well with values determined in prior optical

studies [165]. Subsequent UEC investigations were carried out in the fluence range $0.5 < F < 90$ mJ/cm^2, below the optical damage threshold.

The photo-generated 30 keV electron beam (wavelength $\lambda_e = 0.069$ Å), was focused using the proximity coupled electron gun down to $\approx 10 - 20$ μm, and directed onto the sample at grazing incidence of 2.4° to serve as the probe. The pump and probe were aligned on the sample surface using procedures outlined earlier in Sec. 3.5.

4.2 Ground State Characterization

The electron diffraction pattern from the ground state of HOPG was recorded by physically blocking the pump-laser from entering the UHV chamber, and is shown in Fig. 4.1(a). The pattern is dominated by diffraction maxima along the central (00) rod along with weaker reflections on the side streaks. The indexing scheme for the diffraction pattern is shown in Fig. 4.1(b). The (00) rod is dominated by even ordered maxima such as (006), (008) and (00 10); the odd order peaks of type (001), (003), (005) are kinematically forbidden as each unit cell contains 2 graphite layers which interfere destructively along these scattering directions. Similarly, the even order peaks on the (10) and ($\bar{1}$0) are also forbidden (see Appendix A). The maxima visible in the diffraction pattern represent the intersection of the Ewald sphere with the periodic modulations imposed upon the reciprocal lattice rods due to interference among the finite graphite layers that participate in scattering. The weaker side streaks on either side of the (00) rod represent Ewald sphere intersections with the rods adjacent to (00), which can vary with the choice of zone-axis. In graphite, the two characteristic zone-axes that give rise to strong diffraction patterns are the (10) and (11) zone-axes as shown in Fig. 4.1(c). We see the presence of both (10) and (11) rods in the diffraction pattern suggesting that the electron beam probes multiple zone-axes. This is indeed plausible as HOPG is composed of ≈ 10 μm graphite flakes

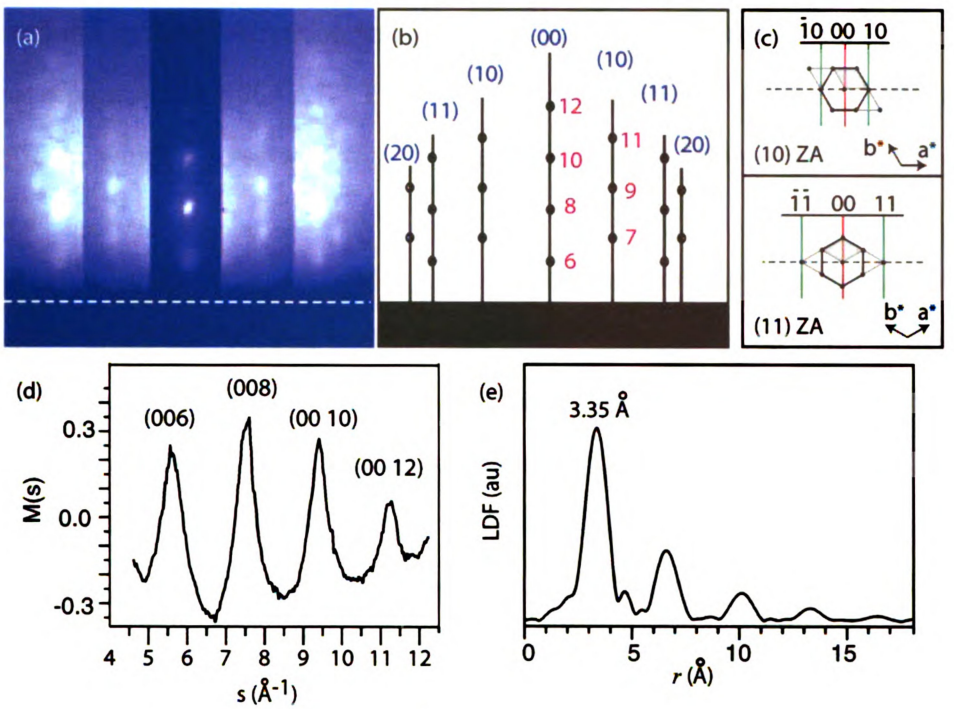

Figure 4.1: Ground state UEC characterization of HOPG. (a) Raw diffraction pattern from graphite and (b) the corresponding maxima indexing scheme. The (00) and (10) rods in (a) are digitally attenuated to reduce contrast and simultaneously view all diffraction maxima. (c) The two characteristic zone axis (ZA) in graphite basal plane giving rise to strong diffraction maxima. Dashed line represents the Ewald sphere. (d) Ground state structure function $M(s)$ obtained from (00) rod in (a). (e) Layer density function (LDF) obtained from the Fourier transform of M(s). Peaks at multiples of 3.35 Å represent inter-layer spacings in graphite.

arranged in a random mosaic spread in the basal plane. Given that the electron beam footprint on the sample surface at such grazing incidence is ≈ 200 μm, it is expected to sample many different flakes, thus allowing for the simultaneous presence of both (10) and (11) rods.

In order to extract the lattice parameters, we fit this ground state diffraction pattern, taking into account the specifics of the scattering geometry such as electron beam incidence angle, sample-to-camera distance, location of the unscattered direct beam on the camera plane, and crystal orientation. We then measured the momentum transfer vector (s_x, s_y, s_z) associated with each diffraction maxima and found the

reflections along the c^* direction to be equally spaced. Adjacent maxima on any one rod were separated by 1.868 $\text{Å}^{-1} \pm 0.04$ Å^{-1} corresponding to a c- axis repeat of 6.72 Å ± 0.01 Å, which agrees well with the established graphite c-axis lattice constant [169].

To enable quantitative estimates of $c-$axis dynamics, we extract the intensity distribution along the (00) rod to determine the structure function $M(s)$ as described in Sec. 2.2.2 and shown in Fig. 4.1(d). Fourier transform of $M(s)$ yields the layer density function (LDF) shown in Fig. 4.1(e) revealing a primary peak at 3.35 Å and less pronounced peaks at 6.7 Å and $\approx$ 10 Å, which are in good agreement with the inter-layer distances in bulk graphite [169]. The decay of higher order LDF peaks suggest a probing depth of $\approx$ 1 nm, which is consistent with the $\approx$ 100 nm penetration depth expected for 30 keV electrons within bulk graphite; the reduced penetration depth accounted for by the grazing incidence ($\theta_i = 2.4^\circ$). The use of full spectrum $M(s)$ to monitor the inter-layer dynamics as opposed to monitoring the dynamics of one or two isolated diffraction maxima is extremely important. It will soon be shown that extracting lattice dynamics by tracking isolated Bragg peaks is fraught with danger as the peak positions are susceptible to photoinduced surface charging artifacts.

4.2.1 Why Surface Diffraction is not RHEED

At this point, we briefly digress to address an important difference between the diffraction patterns obtained here in the UEC setup from those obtained in reflection high energy electron diffraction (RHEED) setups. RHEED is a surface sensitive probe [119] also involving diffraction of electrons incident on surfaces at glancing angles (as in UEC), and typically used in molecular beam epitaxy systems as an *in situ* measure of surface quality during film growth [170]. However, unlike UEC, RHEED patterns are used to study the surface order, and not order along the c-axis of the structure.

The difference arises due to the nature of surfaces the two techniques probe.

In RHEED, the surfaces studied are 'grown' under controlled conditions and often nearly flat and pristine with little or no mosaic patterns, thus possessing a large lattice persistence length $L_a \gg a^*$ along the lateral surface direction. As a result, the lateral width of the reciprocal lattice rods along the $s_{||}$ direction [Fig. 4.2(a)] is extremely narrow; for any given electron incidence angle, the Ewald sphere intersects typically with only one maxima on the (00) rod, giving rise to a specular diffraction maxima satisfying the condition $\theta_i = \theta_o = \theta_{Sc}/2$ as shown in Fig. 4.2(a). The other non-specular maxima along the $s_{\perp}$ direction arise not from the (00) rod, but from modulations on adjacent rods. Thus, the periodicity along the vertical direction in the RHEED pattern is not related to the c-axis lattice order. Furthermore, as the crystal is rocked relative to the electron beam (thus altering θ_i), the Ewald sphere first goes out-of-phase with respect to the reciprocal rod leading to vanishing of the diffraction maxima. Upon further rocking, the Ewald sphere comes in-phase again and the next higher order maxima appears at a larger s value. By gating the diffraction around the (00) rod and plotting the diffraction intensity profile along the $s_{\perp}$ direction as a function of incidence angle θ_i, a RHEED rocking curve would be similar to that shown in Fig. 4.2(c) with discrete spots along the $\theta_{Sc} = 2\theta_i$.

In contrast, surfaces such as HOPG do not posses long range lattice persistence lengths ($L_a \geq a^*$). The surfaces are typically quite rough, composed of stepped terraces and randomly oriented islands. The diffraction from such surfaces is more akin to transmission rather than reflection as illustrated in Fig. 4.2(b). Furthermore, the reduced lattice persistence along the surface direction causes the reciprocal lattice rods to be stretched out along the $s_{||}$ direction, permitting the simultaneous intersection of Ewald sphere with more than one modulation on the (00) rod, resulting in multiple maxima along the central streak region. Since these peaks arise from the same rod, they are representative of the c-axis lattice repeat. Unlike the specular

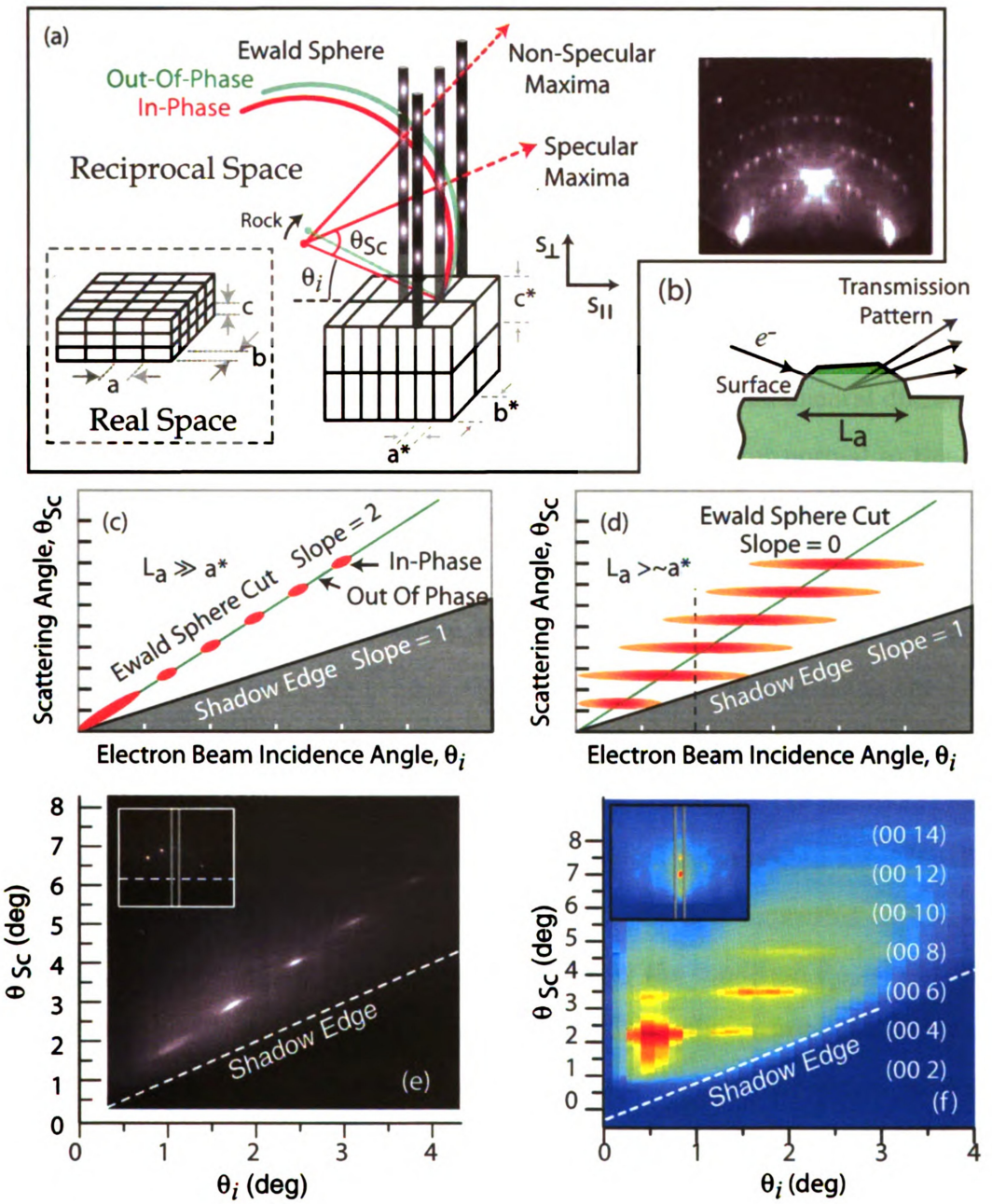

Figure 4.2: Surface Diffraction vs. RHEED. (a) Ewald sphere construction in a RHEED geometry. Inset shows an Si-111 RHEED pattern from Ref. [121]. (b) Surface diffraction from a rough surface. (c) Rocking curve expected from flat, pristine surfaces studied in RHEED and (d) from surface diffraction off rough surfaces, such as this study. (e) Rocking curve 'map' of the (00) rod for surface diffraction from Si-111 surface and (f) HOPG surface, both obtained using the UEC setup. Insets show the gating of the (00) rod.

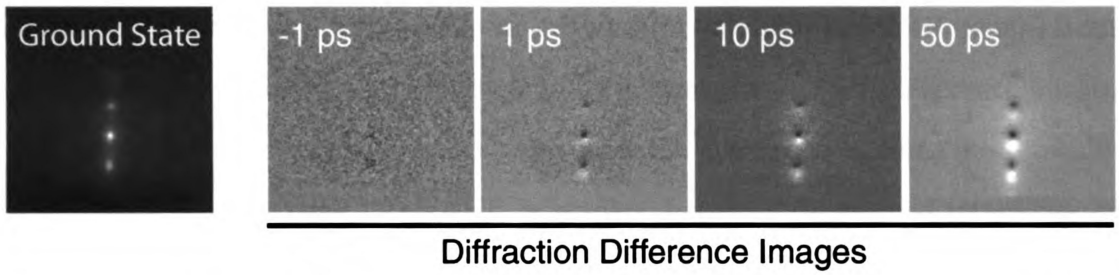

Figure 4.3: Diffraction difference images from HOPG at various pump-probe time delays as labeled, along with the ground state diffraction pattern used as reference.

condition in RHEED, these maxima are characterized by the fundamental diffraction condition $\mathbf{s} = \mathbf{G}$, where $\mathbf{G}$ represents the reciprocal lattice vector normal to the surface. This essentially translates to the condition $\theta_{Sc} = constant$, which manifests as horizontal streaks in the rocking curve, as shown in Fig. 4.2(d).

In light of this distinction between RHEED and surface diffraction evidenced through the rocking curve, we present the rocking curves obtained using the UEC setup from a flat Si-111 surface and the HOPG surface in Fig. 4.2(e, f) respectively; the gating of (00) rod shown in the inset. The rocking curve from the flat Si-111 sample displays the discrete peaks along a line with slope 2, as expected for a RHEED geometry. However, the HOPG rocking curve shows maxima appearing as horizontal streaks, illustrating that they are characterized by the condition $\theta_{Sc} = constant$ expected from rough surfaces. Consequently, these diffraction maxima are representative of the c-axis repeat and can be robustly used to monitor the c-axis dynamics in graphite.

4.3 Time-Resolved Raw Diffraction Data

Having characterized the ground state, we now allow the pump laser to photoexcite the graphite sample, and record the diffraction pattern as a function of pump probe delay. Figure 4.3 shows the diffraction difference images obtained by subtracting the

diffraction patterns at positive delay times (when probe arrives after the pump) from those at negative time when graphite is in its ground state. These difference images show an instantaneous change at $t = 0$ ps, with the diffraction maxima seen to shift towards the shadow edge. This shift is evident from the diminished intensities of the maxima at their original location with corresponding enhancement just beneath. Figure 4.4(a) shows the time-evolution map of the (00) rod, for a range of irradiated fluences, with the horizontal direction representing time. All maxima are seen to impulsively shift at t_0 with lower order maxima exhibiting larger shifts. The maxima are also broadened with their intensities diminished, and they relax back to the original ground state conditions at long times.

To quantify these dynamics, we fit the peak profile at each time-point with a Gaussian curve and trace the evolution of the peak centre. The evolution of the (006) maxima is shown in Fig. 4.4(b), where the magnitude of maximum shift is seen to increase monotonically with irradiated fluence. At the highest fluence of $F = 90$ mJ/cm^2, the shift is almost instantaneous, with a transition time of ≈ 500 fs, illustrating the sub-ps time resolution of the apparatus. Ordinarily, such a shift of the (006) maxima along the $-c^*$ direction would suggest a corresponding c-axis lattice expansion occurring on sub-ps time scales for the highest fluence. This is rather surprising since any large scale rearrangement of the lattice is expected to proceed on the phonon time scales of 1 - 10 ps. Furthermore, the maximum shift of $ds = -0.7$ Å^{-1} in (006) ($s_0 = 5.61$ Å^{-1}) at a moderate fluence of $F = 40$ mJ/cm^2 would correspond to a lattice expansion of $dc/c = -ds/s = 12.5\%$ which is an exorbitantly large amplitude. Atomic motions of such large amplitude occurring over macroscopic lengths scales would likely cause the system to melt, which is not observed here.

A closer examination of the data reveals that these observed shifts in the diffraction maxima do not arise purely from structural change. Figure 4.4(c) shows the photoinduced shift of the maxima on the (00) rod at an exemplary fluence of $F = 21$

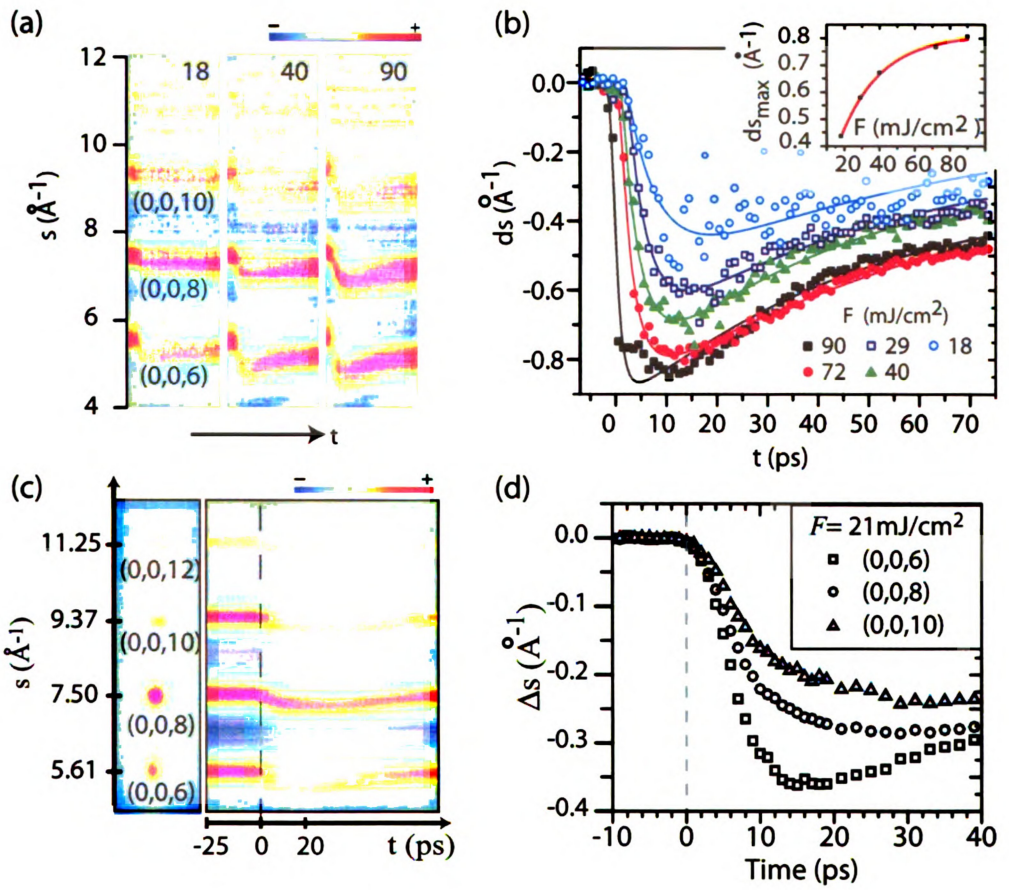

Figure 4.4: Raw data from UEC investigation of HOPG. (a) Diffraction evolution maps from the central streak in the HOPG diffraction pattern for 3 fluences of 18, 40 and 90 mJ/cm^2. Horizontal axis represents pump-probe delay time. (b) Shift of the (006) maxima for various excitation fluences. The inset plots the maximum shift observed at different fluence. (c) Diffraction evolution map for $F = 21$ mJ/cm^2. (b) Center-position of maxima, tracked from (c)

mJ/cm^2 which are traced as before and shown in panel (d). All three maxima shift abruptly at $t = 0$ ps, with (006) exhibiting the most shift while the maxima at larger s displaying progressively lesser shifts. Such a behavior is incompatible with structural change, in which, a change of lattice spacing d will result in a proportional change in scattering angle i.e. $(\delta d)/d = (\delta\theta_{Sc})/\theta_{Sc}$. In other words, a lattice structural change will cause the diffraction maxima at larger s (or equivalently, larger θ_{Sc}) to shift a greater extent than those at smaller s. However, what we observe here in the

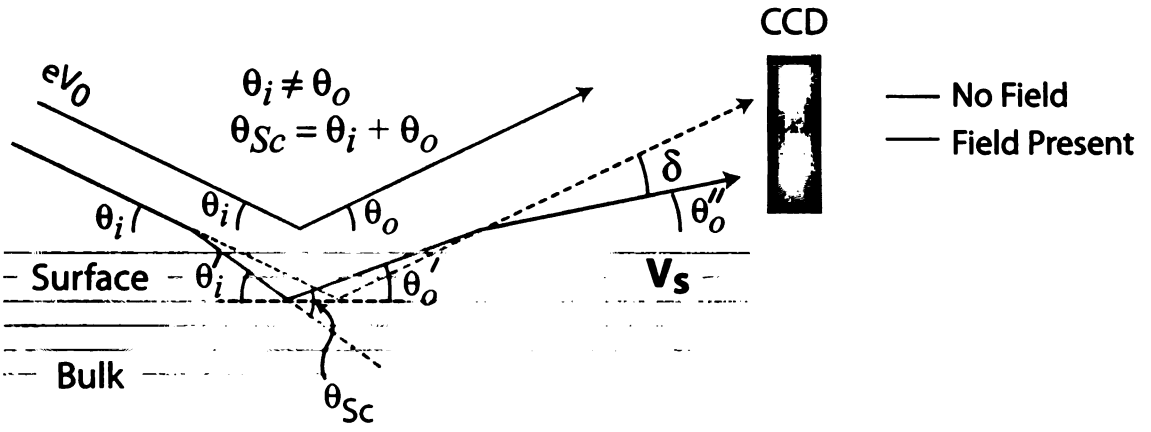

Figure 4.5: Cartoon depicting the Coulomb refraction of a grazing incidence electron beam as it interrogates a sub-surface region where a laser-induced transient surface voltage V_S exists. The refraction shift is exaggerated here for clarity. Adapted from Ref. [156]

experiment is the *exact* converse, thus discounting structural change as the cause of these observed shifts.

4.4 Coulomb Refraction

The observed shift of the diffraction maxima can be satisfactorily explained by the following *thought experiment* in which we assume the creation of an interfacial field near the graphite surface as illustrated in Fig. 4.5. Let us first consider the scattering in the ground state. The electrons, incident on the sample surface at a grazing angle penetrate beneath the surface (typically a few nm) and scatter from the various layers within the probe depth, generating diffraction maxima on the CCD. The scattering angle is determined by the fundamental diffraction condition $\mathbf{s} = \mathbf{G}$, which depends on the inter-layer distance d. Now, if we 'switch on' an interfacial field E aligned along the surface normal, the electrons will respond to this additional electrical field as they propagate within the sub-surface region. The additional momentum kick along the surface normal direction imparted by E will bend, or 'refract' the electrons

downwards, thus increasing incidence angle seen by the sub-surface lattice planes. Since the scattering angle needs to be conserved, the scattered electrons will exit the sample at a lower exit angle θ_o'', which will manifest on the CCD screen as a shift of the Bragg reflections downwards, i.e. towards the shadow edge.

Such refraction effects were observed by the earliest electron diffractionists [171] who observed the diffraction maxima from thin films to occur at scattering angles different from those predicted by the Bragg law. Refraction effects were also observed in gas-phase electron diffraction patterns from MgO and CdO smoke where several Debye-Scherrer rings were observed to occur as doublets [172]. These effects were attributed to the electron beam being refracted by the average inner potential of the lattice [173], and are now a well studied effect in surface electron diffraction [120]. However, until recent work done in this lab [154, 156] this issue and its associated implications had not been addressed within the field of time-resolved electron diffraction, which often utilizes a surface diffraction geometry.

One of the telltale signs of refraction effects in UEC experiments is the magnitude of peak-shift that is observed for different diffraction maxima - the maxima at low s suffer greater deflection on account of their smaller scattering angle. This is apparent if we consider the motion of charged particles while crossing from vacuum into the crystal (where the interfacial field exists). The charged particle will undergo a 'refraction' at the interface analogous to optical refraction, with the refractive index n taking the form

$$n = \sqrt{\frac{V_0 + V_s}{V_0}} \tag{4.1}$$

where V_0 denotes the energy of incident electrons in eV and $V_s = E \cdot l$ denotes the interfacial potential sampled by the electron within its probe-depth l. If θ_o' denotes the 'take-off' angle of any scattered electron inside the crystal [Fig. 4.5], we can relate it to the final exit angle θ_o'' via 'Snell's law' as $\cos\theta_0'' = n\cos\theta_o'$. Since $n > 1$, lower

order maxima characterized by smaller θ_O' will be deflected by a greater amount by the interfacial field.

This thought experiment provides convincing arguments supporting the view that the shift of the diffraction maxima observed in graphite is a consequence of the creation of a *transient surface voltage* (TSV) within the near-surface layers in graphite. To compute the overall TSV-induced shift of any diffraction maxima, it is essential to consider the deflections introduced both before and after the scattering event as the electron propagates within the field region. Using simple kinematic arguments [156] one can arrive at the expression relating the interfacial potential V_S to the angular shift δ of the diffraction maxima as

$$\frac{V_S}{V_0} = \frac{(\theta_0\delta - \theta_i\theta_0 + \delta^2/2)^2 - \theta_i^2(\theta_0 + \delta)^2}{(\theta_i + \theta_0)^2} \tag{4.2}$$

This derivation is based on the concept of conserving the total scattering angle $\theta_{SC} = \theta_i + \theta_O$ under the influence of the Coulomb refraction effect - an approach validated by the earlier discussion on the origin of these diffraction maxima in Sec. 4.2.1. θ_i and V_0 are fixed experimental parameters in Eqn. 4.2, while θ_O and δ are experimentally measurable quantities. Knowledge of these parameters allows us to measure V_S - an approach that has been employed successfully to investigate the interfacial charging dynamics of photoexcited Silicon surfaces [156]. The robustness of this approach has been verified by the fact that the TSV generated from different diffraction maxima all yield the same value despite the angular shift dynamics for each maxima being different from each other [154]. However, this formalism is applicable as is, only under low absorption conditions where there are no significant structural alterations and the entire shift of the maxima can be safely attributed to the interfacial field. For the study reported here, HOPG absorbs strongly at 800 nm (absorption coefficient $\alpha^{-1} \approx 30$ nm) compared to Silicon ($\alpha^{-1} \approx 1$ μm) and the pump fluence ranges

up to 90 mJ/cm^2, which is within 75% of the damage (melting) threshold. Hence, the field dependent shift of the diffraction maxima are expected to be convoluted with those arising from structural changes that are inevitable at such high fluences. Deconvolution of these two effects is essential before further analysis of the data.

4.5 Fourier Phasing Technique

Deconvolution of the TSV-induced and structure-induced shift is achieved here through a computational scheme that takes advantage of the cosine Fourier relationship between the real and reciprocal space periodicity [110]. Referring to the earlier discussion on data reduction procedures in Sec. 2.2.2 we know that the real space LDF and reciprocal space $M(s)$ in graphite are related by a cosine Fourier transform (Eqn. 2.24). The creation of an interfacial field however imparts an $s-$dependent 'phase' shift to the $M(s)$ which destroys this cosine symmetry. Consequently, the reverse Fourier transform curve of the LDF will no longer be 'in-step' with the original $M(s)$ due to the TSV induced phase shift. To correct for this, we compute a high resolution LDF* curve as a Fourier transform of a new $M^*(s)$ curve that is obtained by 'stitching' together the original $M(s)$ with the inverse transform of LDF augmented with zero-padding at larger s to attain better resolution. If the two stitched curves do not match smoothly in periodicity, the peaks in LDF* become asymmetric.

The Fourier phasing scheme is an iterative procedure whose goal is to minimize this asymmetry in the LDF* by correcting for the TSV induced phase shift. Since structural changes may also lead to asymmetry of the LDF peak, we use the low-resolution LDF as a guide to try and match LDF* as best possible with LDF, so as to not over-correct. The procedure starts with an 'assumed' V_S, from which an s-dependent phase shift $\delta(s)$ is calculated using Eqn. 4.2. The reverse phase shift $-\delta(s)$ is applied to the $M(s)$ and the corresponding LDF and LDF* are computed. The cost

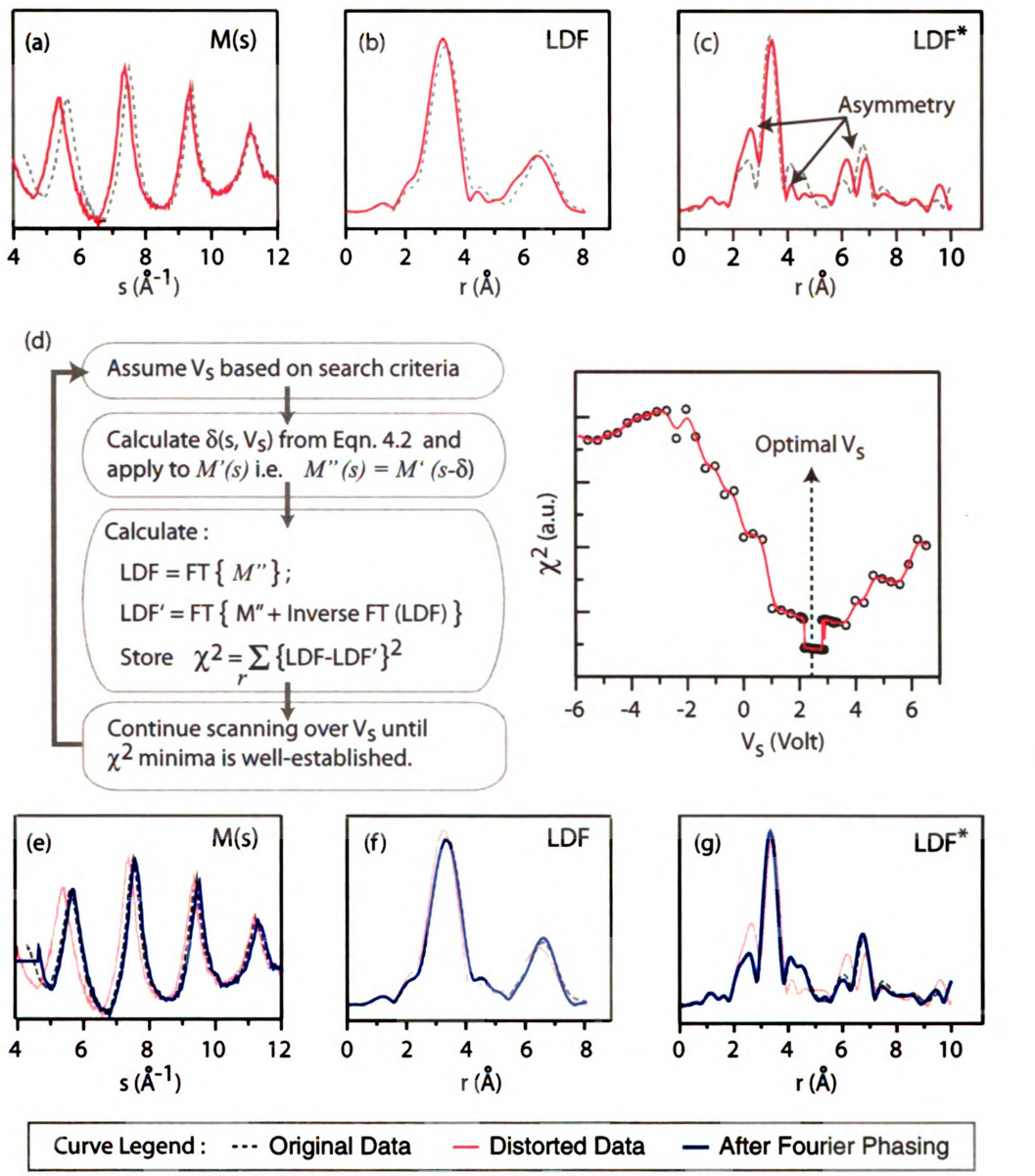

Figure 4.6: Demonstration of the Fourier phasing technique to correct TSV induced effects in diffraction patterns. (a) HOPG ground state structure function $M(s)$ and the distorted (see text) $M'(s)$ curve. (b) LDF curves and (c) high-resolution LDF * curves obtained from Fourier transform of curves in (a). Asymmetry in LDF* obtained from M' is apparent. (d) The Fourier phasing algorithm along with the plot of χ^2 used to correct the TSV-effect introduced within $M'(s)$. (e) The 'phase-corrected' $M''(s)$ compared with $M(s)$ and $M'(s)$. (f) The LDF curves and (g) LDF* curves corresponding to the $M(s)$ curves in (e). The Fourier phasing algorithm recovered the original M(s) from the shifted $M'(s)$.

function χ^2 for the minimization procedure is crafted as the square-deviation between LDF and LDF* within a user specified r-range. By scanning V_S over a wide range of values that is tunable based on the V_S 'search step size' the procedure attempts to seek the optimal V_S at which LDF* asymmetry is minimum.

The result of such a procedure is illustrated in Fig. 4.6. Using the HOPG ground state $M(s)$ as the starting curve, we intentionally impart an ad-hoc non-linear scaling function $s' = s(1 - 8/s)$ on the abscissa and shift $M'(s) = M(s')$ as shown in panel (a). This abscissa scaling function is designed to produce larger shifts at lower s values as would be expected in the case of TSV. Furthermore, using such a scaling function that is unrelated to Eqn. 4.2 used in the 'correction scheme' allows us to demonstrate the 'robustness' of the correction scheme. The asymmetry introduced in the LDF and LDF* is apparent in panels (b) & (c). We now process this M' through the Fourier phasing algorithm outlined in panel (c) and minimize the asymmetry between LDF and LDF* for various assumed V_S values. The final result based on minimized asymmetry is shown in panels (d, e) where both LDF and LDF* recover their original asymmetry and the corrected M'' and M are nearly overlapped.

Such a Fourier phasing scheme is applied to all the transient $M(s)$ curves obtained from the UEC data to generate the corrected $M(s)$ at each time-point. The necessary phase correction required at each time step is a measure of the magnitude of transient surface voltage $V_S(t)$ and the phase-corrected $M(s)$ reveal the true underlying structural change in HOPG.

4.6 HOPG Structural Dynamics

4.6.1 Low Fluence Response

We first examine the photo-induced structure dynamics in HOPG at the near equilibrium regime i.e. low fluences of $0.5 \leq F \leq 21$ mJ/cm^2, where the lattice is not

drastically perturbed. We monitor the laser-induced temperature rise within the crystal by monitoring the intensities of the diffraction maxima. It is well known that random thermal vibrations of atoms about their 'perfect' (T = 0 K) lattice sites diminish the intensity of the diffraction spectra by the Debye-Waller factor e^{-2M}, where $2M = -s^2 \bar{u}_{\perp}^2$ where $\bar{u}_{\perp}^2$ is the mean-square displacement (MSD) of the atoms perpendicular to the set of diffracting planes, characterized by the momentum transfer value s. Here, we measure the time averaged MSD $\langle \Delta \bar{u}_c^2 \rangle$ perpendicular to the basal planes from the reduction in intensities of the diffraction maxima along the (00) rod as

$$ln\left(\frac{I(s,\,t)}{I(s,\,t<0)}\right) = -s^2 \langle \Delta \bar{u}_c^2 \rangle \tag{4.3}$$

The measured increase in $\langle \Delta \bar{u}_c^2 \rangle$ can then be related to a rise in lattice temperature. Here, we monitor the integrated intensity of the (006), (008) and (00 10) maxima as shown in Fig. 4.7(a). The intensity of higher s (00 10) peak drops proportionally greater than the lower s (006) peak in accordance with the s^2 dependence expected from a Debye-Waller loss. This is more apparent in panel (b) where the $\langle \Delta \bar{u}_c^2 \rangle$ is plotted that takes into account the s^2 dependence. The $\langle \Delta \bar{u}_c^2 \rangle$ estimated from all 3 maxima rise within a common timescale of 8 ± 1 ps, indicative of increased thermal motion perpendicular to the basal planes. We also measured the MSD within the basal plane $\langle \bar{u}_{a,\,b}^2 \rangle$ using the transmission diffraction geometry to probe the in-plane lattice dynamics for comparison [See Sec. 5.3].

Recent optical studies have associated near-infrared optical excitations in graphite with a femtosecond generation of coherent E_{2g} phonons [80, 166] that produce an interlayer shearing motion, which have been shown to couple strongly to the electronic excitation of the graphitic π system [81]. The 8 ps timescale for increased interlayer thermal vibration is thus a direct measure of the phonon-phonon interactions in HOPG, and is in good agreement with reports of hot phonon relaxation times in

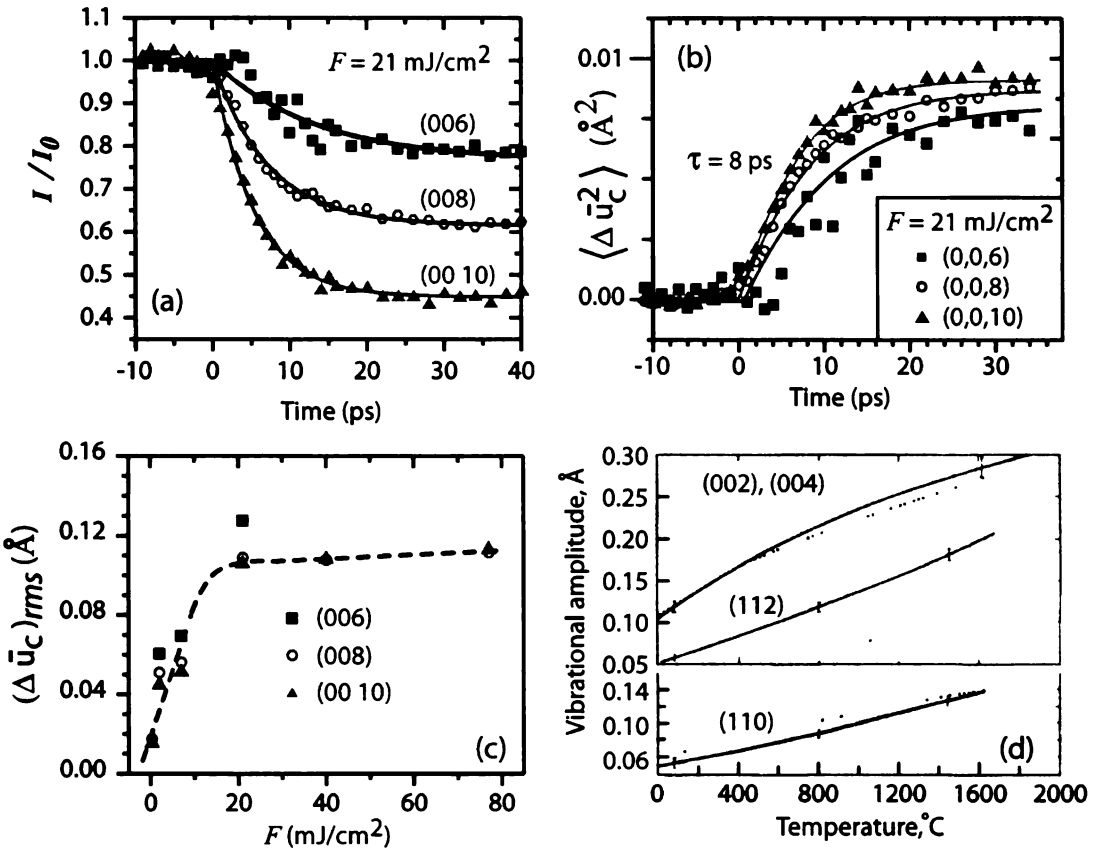

Figure 4.7: Low fluence response of HOPG: Debye-Waller analysis. (a) Decay of diffraction intensities for $F = 21$ mJ/cm^2. (b) Mean-square amplitude of vibration $\langle \Delta \bar{u}_c^2 \rangle$ estimated from (a) via the Debye-Waller relation Eqn. 4.3 (c) Experimentally measured mean-square vibration amplitudes from different maxima on the (00) rod for a range of excitation fluences. Dashed line only a guide to the eye. (d) Experimental measure of temperature dependent vibrational amplitudes in graphite using X-ray scattering corrected for thermal diffuse scattering - from Ref. [174]

graphite [81].

The measured root-mean square (rms) vibration amplitude for a range of excitation fluences is plotted in Fig. 4.7(c) and indicates a linear rise in the low fluence regime. The $(\bar{u}_c)_{rms}$ measured from different maxima for any given fluence yield similar values though the relatively larger deviation of (006) peak might be on account of surface scattering effects that may not be completely subtracted out during the empirical data reduction procedure. Comparing our data to a theoretical model of temperature dependent vibration amplitudes in graphite benchmarked with X-ray

scattering studies [174] shown in Fig. 4.7(d), we estimate a temperature rise of $\approx$ 800 K at $F = 21$ mJ/cm^2. This measure is in reasonable agreement with temperature estimates in previous optical studies that relied on HOPG's heat capacity and optical absorbance [165].

4.6.2 High Fluence Response

As we enter the far-from-equilibrium regime by increasing the excitation fluence beyond 21 mJ/cm^2, the amplitude of atomic vibrations are found to saturate, as seen in Fig. 4.7(c). This is rather surprising, for one would expect a monotonic increase in the thermal motion as graphite approaches its melting threshold at 130 mJ/cm^2 [165]. We examine the amount of surface voltage generated at these fluence. The time-dependent surface voltage $V_S(t)$ measured during the Fourier phasing correction scheme is plotted in Fig. 4.8(a) for three fluences. All 3 datasets exhibit a rapid rise following photoexcitation in $\approx$ 10 ps, followed by a slow recovery. The magnitude of maximum V_S generated at different fluence shown in Fig. 4.8(b) rises linearly. This is in contrast to the thermal response which saturates above $F = 21$ mJ/cm^2.

We believe that the key effect of the optical excitation is the depopulation of electronic states, causing re-bonding and redistribution of charges at the surface. This charge redistribution gives rise to a near-surface dipole field which induces a collective shift of the electron diffraction pattern. The linear rise of V_S indicates that the surface charging is mainly driven by the non-equilibrium diffusion of photogenerated carriers rather than multiphoton ionization or internal thermionic emission. We model the decay of this transient surface potential to be caused by the recombination of surface charges denoted by $\sigma(t)$ following a simple rate equation

$$\frac{d\sigma}{dt} = \frac{\sigma(t)}{\tau_r}$$

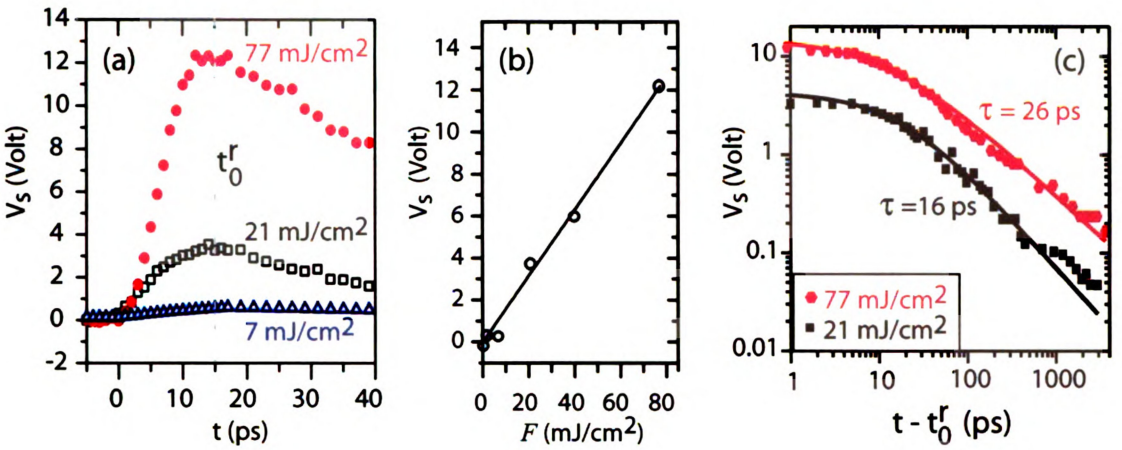

Figure 4.8: Charging dynamics near photoexcited HOPG surface (a) The transient surface voltage V_S measured in the case of 3 excitation fluences, as labeled (b) Maximum V_S as function of excitation fluence showing linear trend. (c) Log-log plot of the V_S relaxation dynamics (dots) with fit to a drift-diffusion model (lines) demonstrating power-lay decay of V_S with exponent $\sim$ -1.

with the space-charge recombination time $\tau_r = l_{e-h}/(\mu E)$ dependent on the transient field $E(t) = \sigma(t)/2\epsilon$. Here, l_{e-h} denotes the electron-hole recombination length and μ their mobility. This leads to the solution $\sigma(t) = \sigma_0/\{1 + t/\tau_c\}$, with $\tau_c = l_{e-h}/(\mu E)$. Hence, $\sigma(t)$ and consequently V_S, exhibits a power-law exponent of -1. We fit the decay of the V_S in Fig. 4.8(c) to the drift diffusion model and obtain recombination times τ_c = 16 and 26 ps for F = 21 and 77 mJ/cm^2 respectively. Thus, the photogenerated charges near the surface typically decay on the timescale of $\approx$ 20 ps.

4.6.3 Observation Of Transient sp^3-Bonds in Graphite

To examine the effect of optical excitations on the atomic structure at these elevated fluences, we monitored the interlayer separation by tracking the temporal evolution of the primary 3.35 Å LDF peak, as shown in Fig. 4.9(a, b). Contrary to an expected thermal expansion of the graphite layers on account of laser heating, we observe the interlayer separation to contract rapidly. The rate and magnitude of

contraction increase with the fluence followed by eventual relaxation to the ground state values. At elevated fluence $F \geq 21$ mJ/cm^2, the relaxation overshoots and a slight expansion is observed. At the highest fluence of $F = 90$ mJ/cm^2, a pronounced expansion of ≈ 0.1 Å is observed, suggesting significant heating of the lattice. Based on graphite's coefficient of thermal expansion along the c-axis $\alpha_C = 2.7 \times 10^{-5}$ [175, 176], we obtain a lattice temperature rise of $\approx$ 1,100 K. Notice however that the expansion has not yet saturated and the lattice is likely to heat up to much higher temperatures at this fluence that approaches the sample damage threshold. Figure 4.9 (c) plots the observed maximum values for interlayer contraction and expansions. The contraction is found to rapidly increase as the fluence increases, whereas the expansion remains nearly stationary for $F \leq 80$ mJ/cm^2. This suggests that the effects of layer compression might persist on several 100 ps timescales, thus preventing significant expansion associated with lattice heating.

Figure 4.9(d) plots the change in the interlayer spacing Δd along with the transient surface voltage V_S at $F = 77$ mJ/cm^2 and the two curves are found to correlate well. Notably, V_S is observed to rapidly relax back to $\approx$ -2 V within 100 ps, followed by a slow relaxation back to ground state. This supports our earlier conjecture about the long-time persistence of V_S and associated contraction effects. We measure a maximum value of $V_S \approx 12$ V to correspond to an interlayer contraction of $\approx 6\%$. Assuming an electron probe depth of 1 nm, $V_S = 12$ V amounts to an internal field of $E \approx 1.2$ V/ Å, which is the source of Coulombic stress that drives the layer contraction. Using this value of E and relative permeability $\epsilon_r = 10$ for graphite, we estimate a maximum electrostatic energy density stored within the system as $U_e = \epsilon_r \epsilon_0 E^2/2 = 0.2$ eV/atom. This is close to the ≈ 0.3 eV/atom activation barrier for graphite-to-diamond transformation calculated from DFT [1, 71].

To further elucidate the structural evolution, we examined closely the diffraction spectra. Figure 4.10 (a) shows time evolution of $M(s)$ and the corresponding LDF

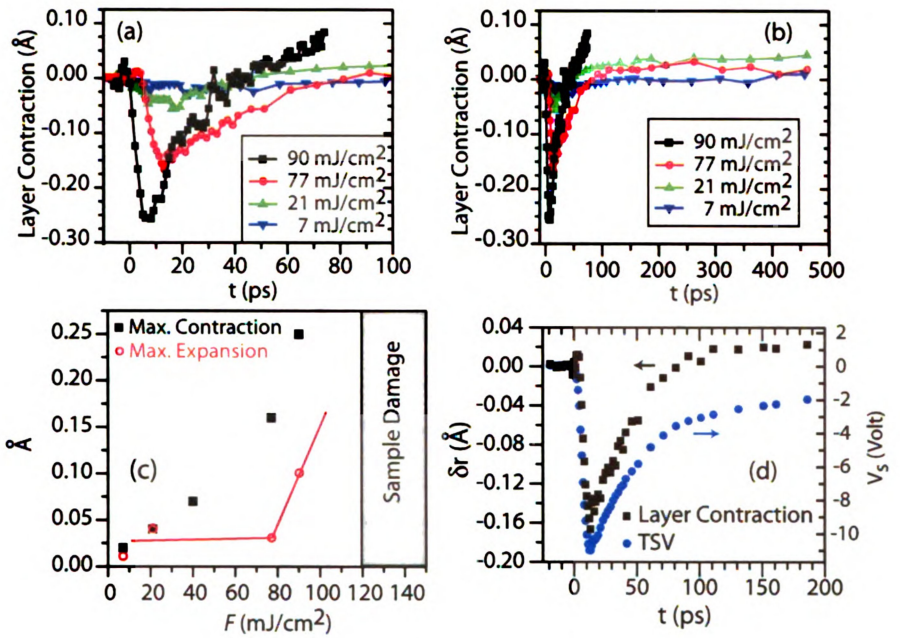

Figure 4.9: Interlayer structural dynamics in graphite. (a) Contraction of primary LDF peak at various fluences for short times and (b) for long times. (c) The maximum contraction of LDF peak at short times, and maximum expansion (overshoot) at longer times. (d) Correlation of the measured TSV with inter-layer contraction at $F = 77$ mJ/cm^2.

curves at $F = 77$ mJ/cm^2, just below the damage threshold. Starting at ≈ 6 ps, as V_S rises beyond 4 V, we observe the onset of peak shouldering and broadening in the $M(s)$ curve and appearance of a new peak at $c \approx 1.9$ Å in the LDF curve. Concurrent with this, we also observe a drastic change of relative intensities of the (00 2l) maxima in $M(s)$ between maxima with even l and odd l. The observed higher intensity of the (00 12) peak relative to(00 10) in Fig. 4.10(b) cannot be explained by thermal vibrations which would produce a monotonic decrease and instead suggests a structural change. Given that the interlayer separation in diamond is 2.05 Å $\leq$ 3.35 Å, the diminishing of even order peaks is akin to the near doubling of lattice constant along the c-axis. Based on this and the observation of a well-defined interlayer bond at $c \approx 1.9$ Å, we conclude that the transient structure generated here is consistent with sp^3 bonding. We find the transient sp^3-like structure, associated with the relative

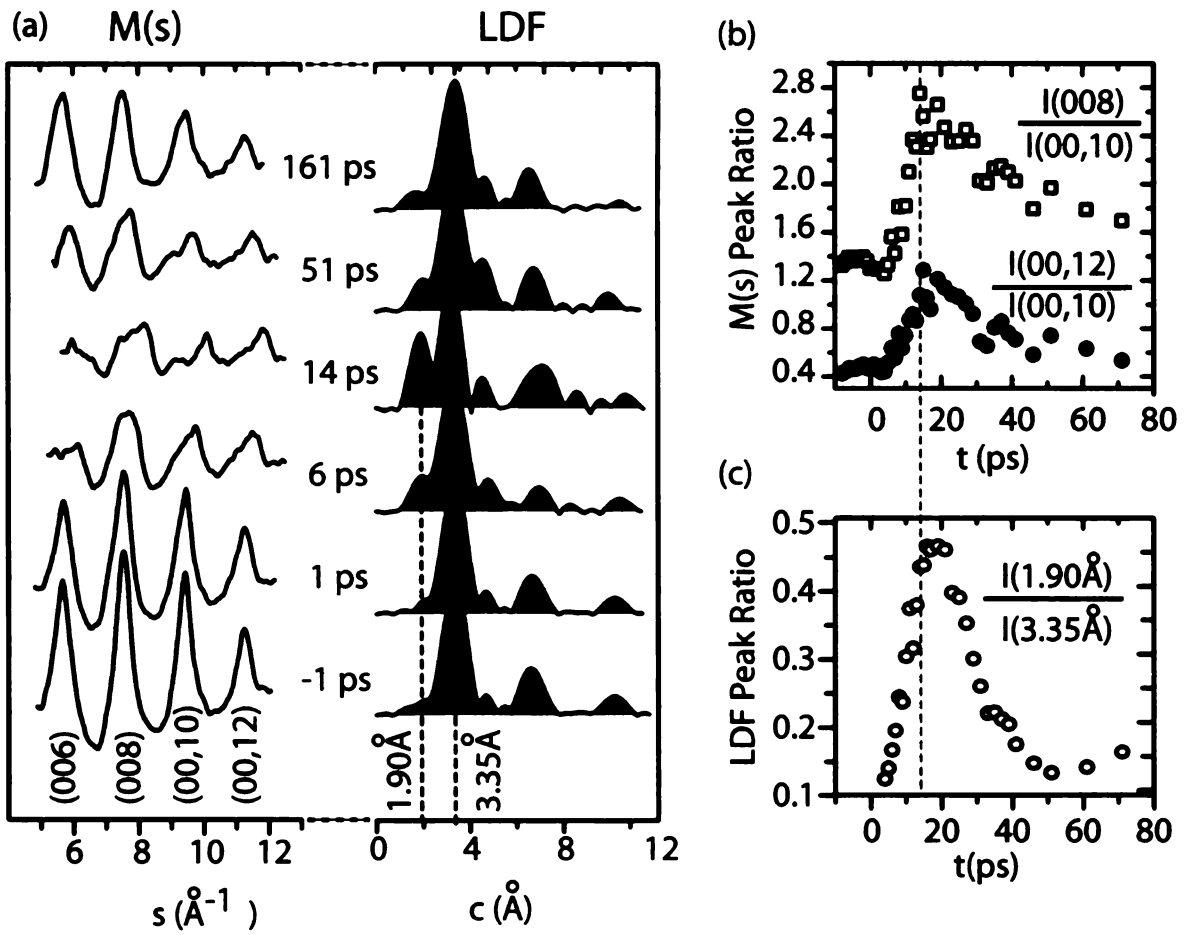

Figure 4.10: Signature of sp^3-like bonding in HOPG. (a) Molecular interference pattern $M(s)$ and the corresponding LDF curves at selected time stances following strong photo-excitation. The transient peak at 1.9 Å in the LDF indicates formation of an interlayer bond. (b) Ratio of peak intensities obtained from the diffraction patterns. The enhancement of the (00 12) with respect to the (00 10) peak cannot be explained by thermal vibrations and indicates a transient structure consistent with sp^3 bonding. (c) Ratio of peak intensities at $R = 1.9$ Å and 3.35 Å in the LDF.

intensity of the $c \approx 1.9$ Å peak in the LDF curve, to reach a maximum fraction of 47% at 14 ps, as seen in Fig. 4.10(c). Similar $sp^2 - sp^3$ hybrid structures have also been identified in pressure-driven pathways of graphite-to-diamond transition [70], in which 50% of the bonds in graphite were observed to transform into sp^3-like nature leading to the formation of superhard graphite. Complete diamond formation was not evidenced as the structure returned to its ground state configuration upon the release of pressure. Similarly, in this UEC study, the transient structure recovers its sp^2 character by 45 ps, but remains hot even after 3 ns with an average value $(\Delta\bar{u}_{\perp})_{rms} = 0.09$ Å, corresponding to a lattice temperature $T \approx 700$ K.

4.6.4 Density Functional Theory Calculations

To clarify the origin of the structural changes, we studied the effect of laser pulses on the electronic structure and bonding in hexagonal graphite using *ab initio* DFT calculations in the local density approximation (LDA). While much of the basic physics underlying photo-induced structural changes can be understood in the bulk structure, we also considered graphite slabs for quantitative predictions. The total energy was determined using the ABINIT plane-wave code [177] with a 64 Ry energy cutoff, Troullier-Martins pseudopotentials, and the Ceperley-Alder form of the exchange-correlation functional. The Brillouin zone of the 4−atom bulk unit cell was sampled using a fine mesh of 24×24×12 k-points that included the $K - H$ line at the Brillouin zone edge, close to the Fermi surface. This approach correctly reproduced the observed [169] in-layer bond length $d_{CC} = 1.42$ Å and the interlayer spacing $d_0 = 3.34$ Å in the bulk system at $T = 0$, shown schematically in Fig. 4.11(a). The electronic density of states of graphite near the Fermi level is shown in Fig. 4.11(b), and the total charge density is depicted in Fig. 4.11(c) in a plane normal to the layers. In the following, we will study the effect of two types of photo-induced electronic excitations on the structure.

First, we will consider the thermalization of the initial nonequilibrium population of electronic states in the laser-irradiated target over a sub-picosecond time scale [178] to that of a very hot electron gas [58]. The electronic temperature (T_e) is probably lower than the limiting value $k_B T_e \approx h\nu = 1.55$ eV and depends on the laser fluence. For the sake of illustration, we compare the Fermi-Dirac distribution in graphite at $k_B T_e = 0$ and $k_B T_e = 1.0$ eV in Fig. 4.11(b), indicating the electronic excitations in the $\pi - \pi^*$ manifold of the hot electron gas. Populating initially empty conduction states by valence electrons leads to a change in the total electron density $\Delta\rho(\mathbf{r}) = \rho(\mathbf{r}; k_B T_e) - \rho(\mathbf{r}; 0)$, which is depicted in Fig. 4.11(d) for $k_B T_e = 1.0$ eV.

As stipulated by DFT, changes in the charge density modify the force field in the system. Our results in Fig. 4.11(d) suggest an increased population of C$2p_z$ orbitals that may hybridize to $pp\sigma$ bonding states connecting neighboring layers, increasing their attraction. The depopulation of in-layer bonding states, on the other hand, should cause an in-layer expansion. To obtain a quantitative estimate of photo-induced structural changes, we performed a set of global structure optimization calculations of graphite with electrons subject to effective temperatures in the range 0 eV$< k_B T <$ 1.55 eV. We used a stringent convergence criterion, requiring that all stress components lie below 5.0×10^{-7} Ha/a_0^3 and that no force exceeds 5.0×10^{-5} Ha/a_0. In bulk graphite, we indeed found that nonzero electronic temperature leads to a maximum interlayer contraction $\Delta d/d_0 = -1\%$ and in-layer expansion $\Delta r_{CC}/r_{CC} = +1\%$ for $k_B T_e \approx 1.0$ eV. In the slab geometry, we obtained a slightly larger interlayer contraction of up to $\Delta d/d_0 = -1.5\%$.

To further take into account the effect of Coulomb stress induced by the laser pulse, we represent the charge separation in the electronic ground state, corresponding to the observed internal field of $\approx$1.2 V/Å. To model this system, we immersed three-layer graphite slabs, separated by 30 Å, in a uniform electric field and adjusted its strength to reproduce the observed field value. With the polarized charge distribution frozen

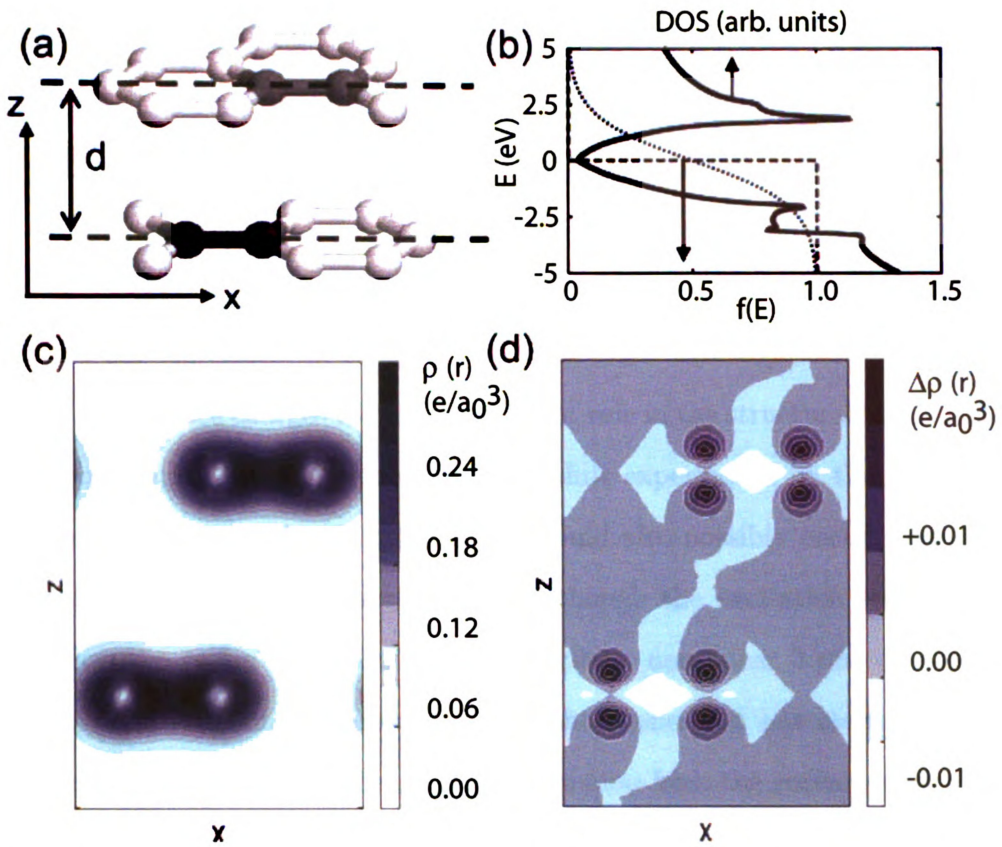

Figure 4.11: Electronic structure changes during photo-excitations in graphite. (a) Schematic view of the structure. (b) Electronic density of states (solid line) and the Fermi-Dirac distribution of graphite at $T = 0$ (dashed line) and $k_BT = 1.0$ eV (dotted line). (c) Total pseudo-charge density $\rho(\mathbf{r})$ and (d) change in the pseudo-charge density $\Delta\rho(\mathbf{r})$ due to an electronic temperature increase to $k_BT = 1.0$ eV. The plane used in (c) and (d) intersects the graphene layers along the dashed lines in (a).

in, the external electric field was switched off. Then, the internal field was only due to the polarized charge distribution. The slab calculations were performed using the SIESTA code [179] with double-polarized triple-ζ local basis and a fine 24×24 k-point mesh. The charge density was obtained on a real-space grid with a mesh cutoff energy of 250 Ry. From total energy calculations at different interlayer separations, we found that charge density redistribution associated with the internal field may further reduce the interlayer separation by $2-3\%$. Combined with the contraction induced by the initial non-equilibrium electron heating, we thus can explain the observed contraction

of the topmost interlayer separation by up to ≈5%.

4.7 Role Of Surface Charge: Photoemission Imaging Study

One of the key experimental observation in the UEC investigations of HOPG that identified sub-surface charges to play a dominant role in the structural transformation was the observation of a Coulomb refraction shift experienced by the probing electron beam. However, such refraction effects could also possibly occur from electron emission from a photoexcited surface. Even though the excitation laser (1.55 eV) is well below the ≈ 5 eV work function of graphite, non-linear 3 photon absorption processes and thermionic emission from the photogenerated hot electron gas could contribute to a vacuum space charge (VSC) emission from the surface, thus affecting the UEC data. To quantify the amount of such VSC emission from the photoexcited graphite surface and study its contribution to the observed refraction effects on UEC data, we developed a novel technique to directly image and track the spatiotemporal evolution of the photo-emitted electron bunch generated over a femtosecond laser excited surface. The method possesses sufficient sensitivity to image electron bunches as small as 10^{10} e/cm^3 and permits quantitative measurement of the instantaneous electron bunch density distribution and its translational and expansion velocities in the picosecond and micrometer regime.

Besides the obvious relevance to this study, understanding the mechanisms of VSC emission [180–182] and surface charge formation is also central to the development of pulsed laser driven electron technologies such as time-resolved photoemission [180, 181, 183], scanning probe microscopy [184, 185], electron diffraction [28, 110–112, 167, 186], and microscopy [114, 151]. While the vacuum space charge has been studied both theoretically [146, 187–189] and experimentally [111, 180, 181, 190], the role

of subsurface electron dynamics within the materials and the nature of the early development of VSC remain topics of high interest. Transient vacuum electric fields established by generation of VSC have been investigated based on the influence of the field on a pulsed electron beam [191, 192]. The method employed here differs from these techniques in that it allows a direct ultrafast imaging of the evolution of the photoemitted electrons.

4.7.1 The Point-Projection Imaging Technique

The experiment is based on a novel probing geometry derived from conventional pump-probe UED geometry, as illustrated in Fig. 4.12. Instead of overlapping the pump & probe spatially on the sample as UED experiments demand, we intentionally displace the pump laser laterally by a distance x_0 relative to spot P that is being probed by the electron pulse. We shall refer to this distance x_0 as the offset distance. The incident electron beam now scatters from an unperturbed region of the sample, generating a stream of forward scattered electrons. The pump-laser on the other hand, lands at point G and generates the VSC cloud that is ejected into the vacuum depicted as a disc in Fig. 4.12. The forward scattered electrons originating at P are intercepted by the VSC cloud over point G leading to a reduction in the signal intensity at the CCD, that is best viewed as a dark shadow in diffraction difference images. The typical values of $x_0 \approx 2 - 4$ mm are much larger than the dimension of the electron beam footprint on the sample (≈ 200 μm), allowing us to treat P as a point-source. This forms a projection imaging geometry where the shadow cast on the CCD is an image of the VSC cloud, with the shadow's darkness being a measure of the electron density within the VSC cloud. Given that the sample-to-camera distance L of our UHV chamber is 150 mm, this projection imaging geometry yields a magnification of $L/x_0 \approx 75$.

The temporal evolution of the VSC cloud is tracked in the usual way by adjusting

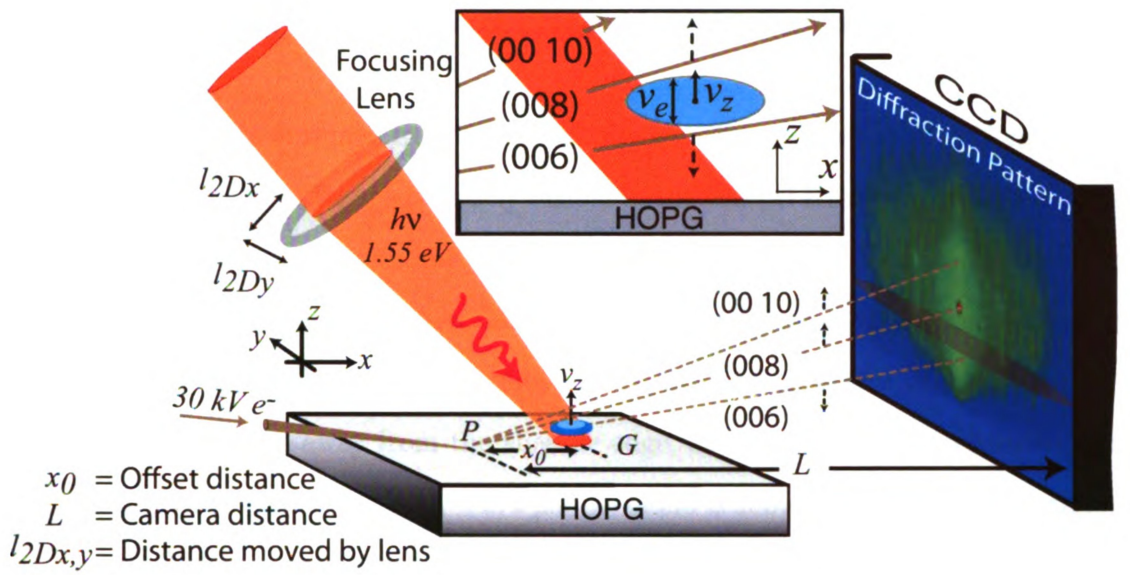

Figure 4.12: Schematics of the electron point-projection imaging technique. Typical values are $x_0 \approx 1$ - 4 mm, $L \approx 150$ mm. The dashed arrows illustrate the effect of the photo-emitted electron bunch on the coherently scattered electrons constituting the diffraction maxima.

the relative pump-probe delay and capturing the shadow images at different times relative to the initial VSC cloud creation instance. From these shadow images we can extract the cloud's propagation velocity v_z, expansion velocity v_e and the charge density within the cloud. Such quantitative analysis requires accurate control over the offset distance. To achieve this, we first obtain perfect pump-probe overlap at point P as described earlier in Sec. 3.5. Thereafter, the laser is shifted relative to the electron probing spot by moving the focusing lens mounted on a stepper motor controlled stage, as illustrated in Fig. 4.12. This allows accurate positioning of the laser relative to P. A high magnification camera mounted outside the chamber with a clear view of the sample surface records the motion of the laser spot as it traverses across the surface. Accurate calibration of x_0 is obtained by using the known length of the HOPG sample (1 cm) as an *in situ* scale bar.

4.7.2 Imaging VSC Cloud Over HOPG Surface

The shadow images obtained from an HOPG surface photoexcited at $F = 75$ mJ/cm^2 is shown in Fig. 4.13. Change is clearly visible in the central streak region at $t = 2$ ps as a shift of the diffraction maxima towards the right, away from the shadow edge. By $t = 7$ ps, we see the emergence of a thin dark strip near the shadow edge representing the VSC cloud. The cloud rapidly builds in strength and is clearly visible by $t = 17$ ps. It steadily moves away from the shadow edge, accompanied by an expansion in width along the z-direction. By $t \approx 272$ ps, the cloud is sufficiently diffuse and cannot be discerned clearly any longer. However, the effect of the cloud is still apparent in the shift of the maxima.

Focusing on the behavior of the three maxima momentarily, they all are observed to instantaneously shift to the right at time-zero when the VSC cloud is generated. However, the deflection of each maxima reverses sign as the VSC cloud crosses the maxima. This is apparent in the panels from t =72 - 172 ps. At 72 ps, the VSC shadow is located in-between (006) and (008). Consequently, the (006) maxima is shifted to the left, whereas (008) and (00 10) remain shifted to the right. As the cloud crosses (008) around $t = 122$ ps and (00 10) around $t = 172$ ps, the shift of these maxima reverse.

This effect is prominently illustrated in Fig. 4.14. Diffraction evolution maps are generated from two regions within the shadow images - one along the region in-between (00) and (10) rod where there are no diffraction maxima, and one along the (00) rod that include the (00 $2l$) maxima. The map from the former in panel (b) shows a dark streak representing the generation, evolution and propagation of the VSC cloud with time on abscissa. Contrast this with panel (c) that is obtained from the central (00) rod. The three diffraction maxima appear as horizontal stripes prior to the creation of the VSC cloud. They exhibit a slight shift at the instant of VSC

Figure 4.13: Shadow images obtained from a photoexcited HOPG surface (using offset distance $x_0 = 2.4$ mm), illustrating the creation, emergence and evolution of vacuum space charge (VSC). The numbers indicate the pump-probe delay in ps.

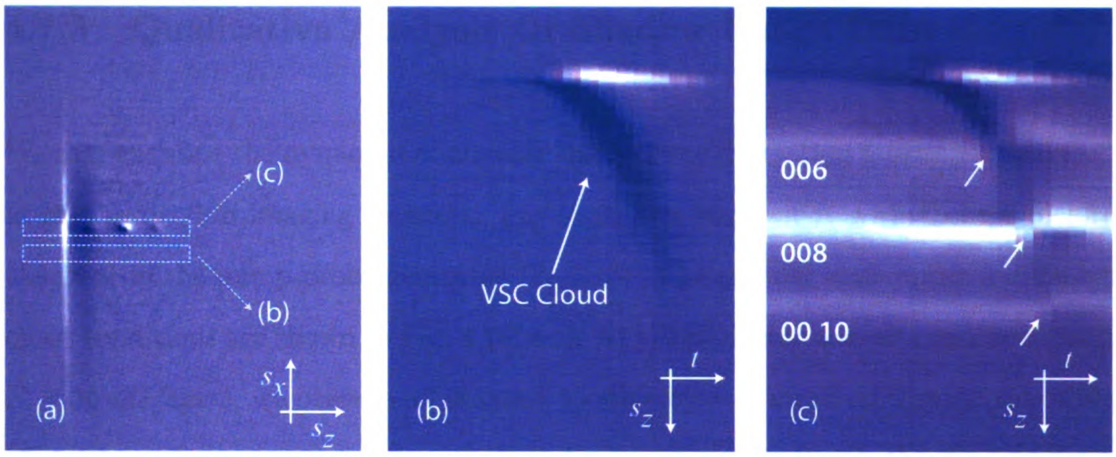

Figure 4.14: Time-evolution map of VSC Cloud at $F = 75$ mJ/cm^2. (a) Typical shadow image obtained. Dashed boxes indicate the regions chosen to create the diffraction evolution map shown in panels (b) and (c) as labeled. (b) The dark streak in panels (b) and (c) represents the propagation trajectory of VSC cloud with time on abscissa. The maxima show a clear shift as each is crossed by the VSC at separate time instances marked by the arrows in (c).

creation, followed by a pronounced and abrupt reversal in their position as the VSC cloud intersects with the stripe, clearly demonstrating the effect of the VSC cloud on the maxima.

This behavior of diffraction maxima is evident from the inset to Fig. 4.12. Each maximum is produced by electrons scattered along a well defined directions emanating from P, which we shall refer to as 'Bragg rays'. Initially, when the VSC cloud is close to the HOPG surface, it lies below all the Bragg rays, thus deflecting them away from the surface. As the VSC cloud reaches the height of each of each Bragg ray above the sample surface, the field direction reverses, leading to the reversal in the shift of maxima on the CCD. For a given offset distance, the height of the Bragg rays above the surface is known. Consequently, measuring the time required for the reversal of shift allows us to determine the propagation velocity of VSC cloud.

4.7.3 Qualitative Analysis Of Shadow Image Data

We first examine the dynamics of angular shifts of the diffraction maxima introduced in this projection imaging geometry ($x_0 \neq 0$) and contrast it with those typically observed in the pump-probe geometry ($x_0 = 0$). The angular shift under 3 different offset conditions are shown in Fig. 4.15(a-c). At the perfectly aligned condition (with $F = 35$ mJ/cm^2), we observe all maxima to shift by ~ 6 mrad on a rapid timescale of ≤ 10 ps. In contrast, for the off-aligned cases in panels (b, c), the dynamics are observed to be much slower, occurring on several 100 ps timescale. Furthermore, the magnitude of angular shift is an order of magnitude smaller, even though the applied fluence is larger as compared to the perfectly aligned case. Interestingly, the dynamics of all 3 maxima coincide in the case of $x_0 < 0$ [panel (c)] but are separated when $x_0 > 0$ [panel (b)]. This behavior is evident from the inset cartoons in the two panels depicting the probing geometry. For $x_0 < 0$, the VSC cloud interacts with the probing electron beam prior to surface incidence. Consequently, all scattered Bragg rays are deflected by the same amount. For $x_0 > 0$, this is not the case and the VSC cloud interacts with the scattered Bragg rays individually, thus leading to the separation in the dynamics. Furthermore, we also observe a shift in time-zero for the mis-aligned experiment relative to the aligned experiment, which is expected since the time-zero is defined by the location in space where the pump laser and probing electron pulse arrive simultaneously.

Another feature that distinguishes effect of VSC from that of sub-surface charge dynamics is the observed drop in integrated intensities of the diffraction maxima. As evident from Fig. 4.15(d-e), the intensity of the three maxima reach their respective minimum at different times that correspond well with the time instant of their respective angular shift reversal. This clearly suggests that the intensity drop results from the VSC cloud crossing scattered electrons constituting the maxima. More impor-

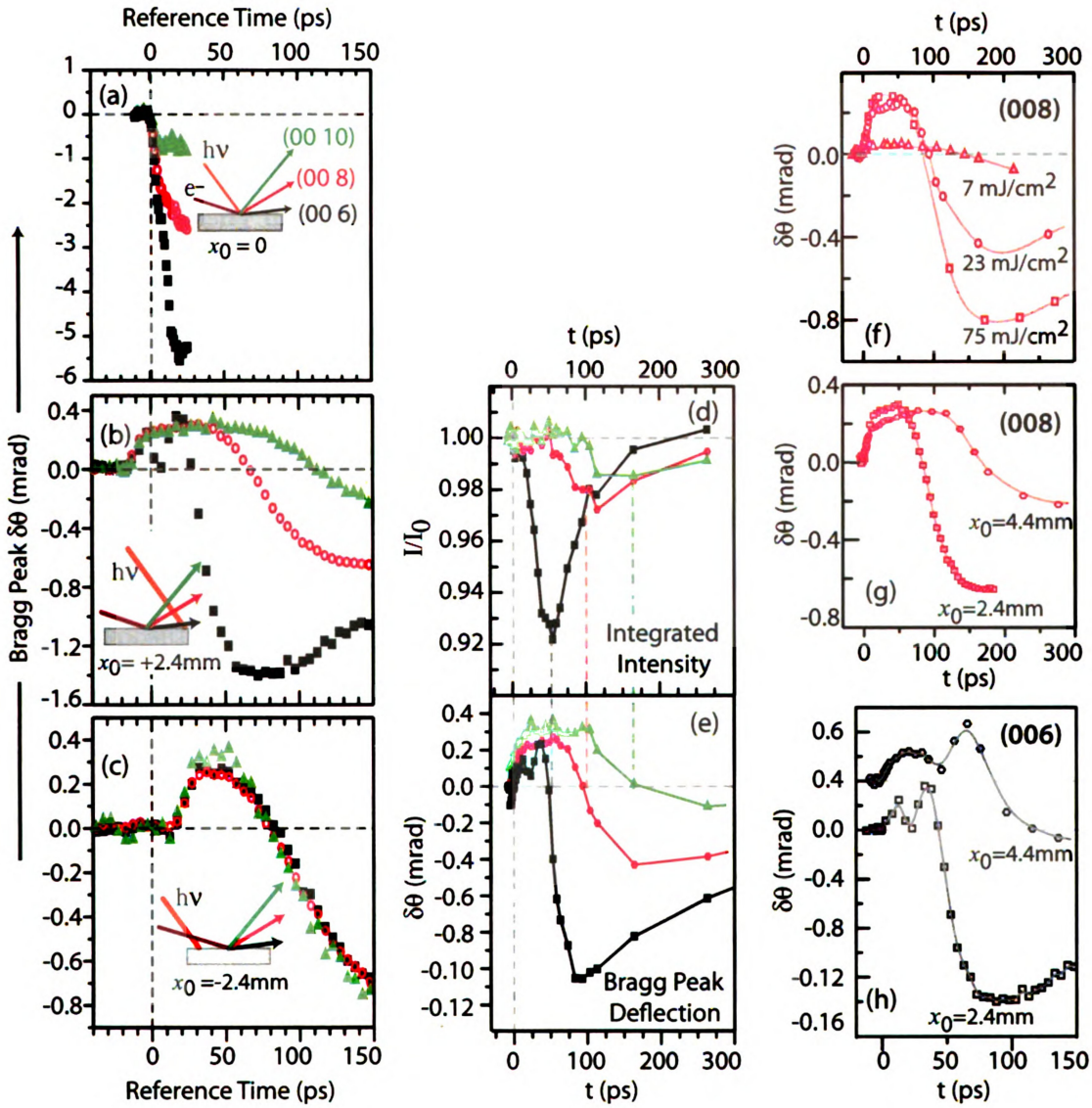

Figure 4.15: Qualitative analysis of VSC induced changes in diffraction pattern. (a-c) Angular shift of (00 $2l$) diffraction maxima at $F = 35$ mJ/cm^2 in (a) and $F = 56$ mJ/cm^2 in (b, c) for different offset distances x_0, as illustrated by the inset cartoons. (d) Dynamics of integrated intensity and (e) angular shift of the diffraction maxima, with $F = 23$ mJ/cm^2 and $x_0 = 2.4$ mm. (f) Angular shift of (008) maxima at different excitation fluence while holding $x_0 = 2.4$ mm constant and (g) the same at different x_0 while holding $F = 56$ mJ/cm^2 constant. (h) Angular shift of (006) maxima at 2 different fluences, showing a unique double-hump feature that is as yet unexplained. The two curves are vertically offset for clarity; dashed lines represent respective zero-level.

tantly, the lower-order (006) peak drops the most in intensity, since the VSC cloud is dense near the surface and becomes more dilute by the time it reaches the heights required to intercept the (008) and (00 10) Bragg rays. This is exactly opposite to what is seen in the case of perfectly aligned pump-probe data discussed earlier in Sec. 4.6.1 where the intensity drop followed the s^2 dependence set forth by the Debye-Waller relation.

Finally, Fig. 4.15(f-h) illustrate some salient features of VSC induced dynamics. Figure 4.15(f) shows the effect of increasing the photoexcitation fluence on the degree of angular shift produced for the (008) peak. The initial positive shift appears to be largely fluence independent, at least beyond F=20 mJ/cm^2, though the reversed down swing shows some fluence dependence. This is possibly due to the fact that during the stage of positive shift, when the VSC cloud is below the maxima, the effect of VSC electrons is compensated for by the corresponding image charges and holes within the HOPG surface, thus leading to a very weak fluence independent shift. Only at very low fluences (F = 7 mJ/cm^2), where the screening may not efficient is any variation observed. However, as the VSC cloud rises above the maxima, the probing electron beam experiences the combined field from charges both above and below, leading to the observed effect. Increasing x_0 leads to slower and weaker dynamics as seen in Fig. 4.15(g), which is to be expected. Finally, a note on the curious behavior of the (006) peak shift seen in Fig.4.15(h). The peak shift exhibits a unique double-hump feature, that is as yet unexplainable based on the scenario constructed so far. The behavior is robust, occurring at all excitation fluences and various offset distances. It also exhibits similar dependence on the offset distance as the (008) maxima in panel (g). These could possibly arise from strong recoil effects arising from interaction between the (006) ray and the dense VSC cloud or a systematic near-surface artifact. Further experiments are required to clarify the role of this behavior.

4.7.4 Quantitative Analysis: VSC Cloud Dynamics

Proceeding to the quantitative analysis of this VSC imaging data, the shadow images offer two complementary methods to extract information regarding the dynamics of VSC cloud over the HOPG surface. One involves the analysis of the shadow pattern directly, while the other utilizes the information content within the peak deflections.

To analyze the shadow images, we obtain a line-scan profile of the VSC cloud from the shadow images as illustrated in Fig. 4.16. The cross-sectional line scans obtained along the dashed lines shown in the figure consist of a strong peak near the shadow edge, followed by a broad depletion profile. The strong peak is caused by enhanced surface scattering and bending of near-surface electrons that results in electron accumulation near the shadow edge. The depletion profile represents the VSC cloud and is modeled as a Gaussian evolving in space over time. To extract the spatiotemporal dynamics of the electron bunch, we need to relate the line scans extracted from the shadow images on the CCD to actual parameters of the VSC cloud. This is done by treating the intensity depletion at a point d along the z direction on the CCD screen as the integrated strength of the Gaussian cloud along probing electron's propagation direction, as illustrated in Fig. 4.16(b). This formalism, along with the accumulation peak modeled as an exponential decay yields an analytical form for the z-direction line scans as

$$I(d) = A\,exp(-d/\Delta_0) + B\frac{\Sigma_0}{\Delta_z}\left[\frac{exp\left(-\frac{(dx_0 - Lz_0)^2}{2(d^2\Delta_x^2 + L^2\Delta_z^2)}\right)}{\sqrt{\frac{1}{\Delta_x^2} + \frac{d^2}{L^2\Delta_z^2}}}\right] \tag{4.4}$$

where d is the distance on screen measured from the shadow-edge. The charge distribution $\rho(x, y, z, t)$ is modeled as a 3D Gaussian in x, y and z directions with a sheet electron density Σ_0 in the xy-plane, $1/e$ half-widths Δ_x, Δ_y, Δ_z and a CoM position

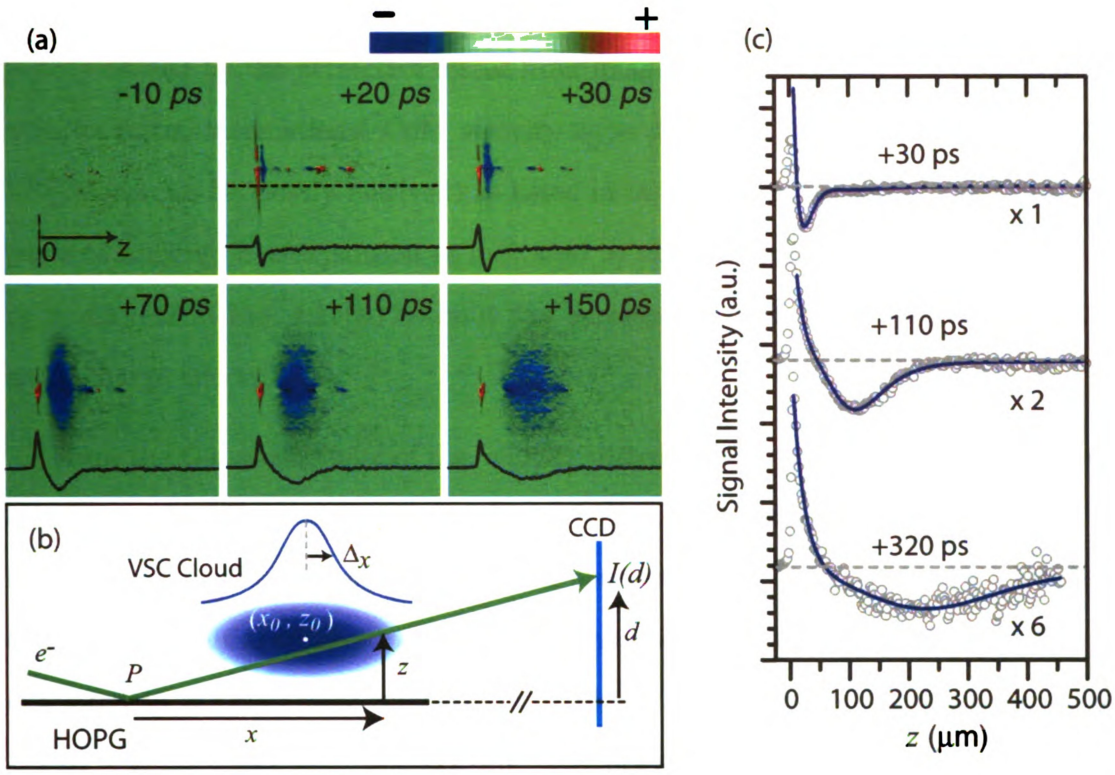

Figure 4.16: (a) Snapshot shadow images of photoemitted electron bunch obtained with x_0 = 4.3 mm. The cross-sectional line profiles (black curves) are extracted along the dashed line in the second panel. (b) Model used to construct an analytical expression for the shadow image z line scans in Eqn. 4.4. The shadow intensity on CCD is related to the integrated strength of the Gaussian VSC cloud along the probe electron propagation trajectory. (c) Fitting curves (lines) of cross-sectional line-profile data (circles) using a Gaussian model considering the projection geometry.

(x_0, y_0, z_0). By fitting the line-profile of the transverse size of the VSC cloud, we determine $\Delta_y \approx 500\ \mu m$ which remains nearly unchanged and corresponds well with the width of laser illumination on the surface. To extract the cloud dynamics along the z direction, we fit the z direction line-scans extracted from the shadow images as shown in Fig. 4.16(a) and fit the profile using Eqn. 4.4, as shown in Fig. 4.16(c). From these fits, we extract the parameters z_0 and Δ_z as a function of time, from which we can estimate instantaneous values of the cloud's propagation speed v_z and expansion speed v_e. The evolution of VSC cloud's position and width along z direction is shown in Figs. 4.17 (a, b) and summarized in Table 4.1 for fluences F =7, 23 and 56

mJ/cm^2. The results indicate the electron cloud CoM to follow a projectile-like trajectory caused by the attractive forces from image charges and holes within HOPG, with an initial translational CoM velocity $v_0 = dz_0/dt$ at earliest times (where the VSC cloud can be clearly resolved) as listed in table 4.1. Interestingly, the cloud appears to undergo free-expansion as indicated by the nearly constant expansion speed $v_e = d\Delta_z/dt$ in Fig. 4.17(b) without any acceleration that might be introduced by space-charge effects.

From the Gaussian shape of the velocity distribution and the lack of a power-law enhancement of Σ_0 over increasing F, we believe a thermionic emission scenario is best to describe the dynamical parameters observed here. For a steady-state thermal emission, the initial translational speed v_i and the expansion speed v_e of the bunch is related to the electronic temperature (T_e) at the surface via the relations: $v_i = \sqrt{k_B T_e/2\pi m_e}$, and $v_e = \sqrt{k_B T_e/m_e}$. The observation of a v_0 significantly higher than v_e in Table 4.1 suggests an electron acceleration and cooling during the initial adiabatic expansion of the cloud. This scenario is supported by the observation of an apparent shift of the *zero-of-time* extracted from the linear extrapolation of cloud expansion to intercept with the time axis [Fig. 4.17(b)], indicating a rapid decrease of v_e within 10 μm (resolution-limited) of the expansion. This cooling process converts part of the electronic enthalpy ($\Delta h = 5/2 k_B \Delta T$) to the kinetic energy of the bunch, and under such an adiabatic model we can deduce the initial electron temperature (T_i) using $1/2 m_e(v_o^2 - v_i^2) = \Delta h$. The T_i deduced from our experiment shows a saturation at high fluence, and the highest electronic temperature obtained is just above the laser pulse energy 1.55 eV (18,000 K), further confirming a thermally limited emission. During the same period, by assuming an initial cloud size of 30 nm (comparable to the laser penetration depth) and $\Sigma_0 = 2 \times 10^8$ e/cm^2, we estimate the possible heating effect arising from space-charge driven acceleration of the electrons at the expense of Coulomb self-energy to be at most 0.2 eV. Thus Coulomb explosion

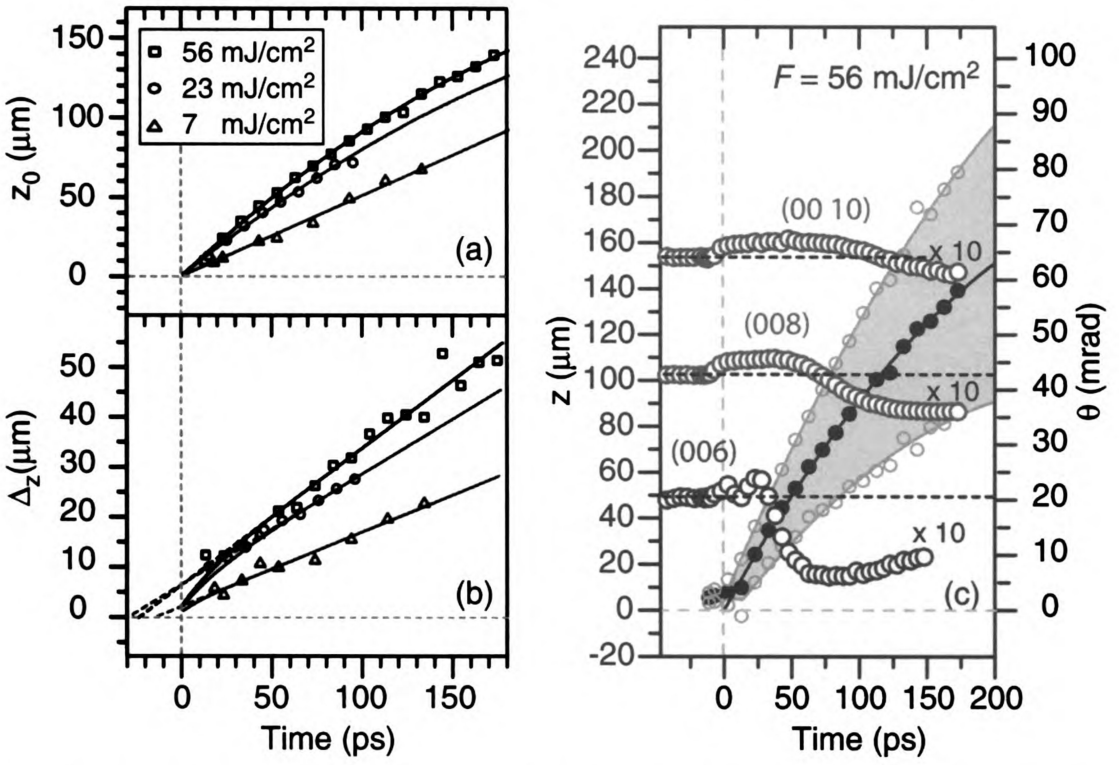

Figure 4.17: Photoemission from graphite surface: Dynamics along the z-direction, with $x_0 = 2.4$ mm. (a) Time-evolution of the electron bunch's center-of-mass (CoM) and (b) $1/e$-width. (c) Spatiotemporal evolution of the diffraction maxima and the electron bunch at $F = 56$ mJ/cm^2, showing the bunch CoM (black dots) and its spread ($1/e$-width) relative to the CoM (gray circles).

cannot provide the observed high initial CoM velocity.

In addition to the imaging, we also analyze the trajectory of the (006), (008) and (00 10) diffraction maxima in the central streak region of the diffraction pattern. The instantaneous vacuum electric field $E(z,t)$ established by the two opposing fields associated with the VSC $\rho(z,t)$ and its mirror-charges on the surface can be described by

$$E(z,t) = \frac{e}{2\epsilon_0}\left(a(z)\Sigma_0 - 2\int_z^\infty \rho(z',t)dz'\right) \tag{4.5}$$

where $a(z) \approx z/\sqrt{z^2+\Delta_x^2}$ is the proximity effect factor [191], describing the reduction in local electric field from mirror charges with a finite-sized slab, which is

[1-$a(z)$]e$\Sigma_0/(2\epsilon_0)$. The Bragg ray located at a height z_c above the surface interacts with VSC and exhibits an inversion, as shown in Fig. 4.17(c) when the CoM of the electron bunch reaches a height $z_0 = z_c - \gamma\Delta_z$, such that the local electric field at z_c, $E(z_c) = 0$. Carrying out the integration in Eqn. 4.5, we obtain the condition for Bragg ray inversion as γ = 1.6, 1.3, 1.1 for z_0 = 50 μm, 100 μm and 150 μm corresponding to the (006), (008) and (00 10) diffracted beams respectively. Inspecting the trajectories $\Delta_z(t)$ and $z_0(t)$ in Fig. 4.17(c) at the point of Bragg ray inversion, we measure $\gamma = 1.0 \pm 0.4$, 1.2 ± 0.2 and 1.2 ± 0.2, which is in good agreement with the predicted values above. The deviation in the case of (006) ray is believed to be caused by the recoil effect, which plays a more significant role here. Given this confirmation, we can reliably obtain the sheet electron density Σ_0 for the three fluences studied here (Table I), and compare them with the initial electron temperature T_i. Σ_0 scales linearly with T_i to a satisfactory degree, agreeing with the thermionic emission model proposed by Downer and coworkers [193]. The electron bunch dynamics measured here reveals that the majority of the electrons will return to the surface within 1 ns, see t_{return} in Table 4.1, with only a very small portion ($< 10^{-4}$) of the cloud remaining in vacuum beyond 3 ns.

Finally, to relate these VSC studies to our original HOPG data, we shift the the laser spot back to the aligned condition of $x_0 = 0$ without modifying any other aspect of the experiment and observe a dramatic increase in the electron refraction ($\delta\theta_{Sc}$) [154], as shown in Fig. 4.18(a). With the knowledge gained about the electron

Table 4.1: Results of fitting experimental data to the projected Gaussian model.

F	v_0 $\times 10^6$	ve $\times 10^6$	T_i $\times 10^3$	Te $\times 10^3$	Σ_0 $\times 10^8$	t_{return}
(mJ/cm^2)	m/s	m/s	K	K	e/cm^2	ps
56	1.06	0.27	19	5.0	1.93	350
23	0.91	0.22	14	3.3	1.61	400
7	0.51	0.15	4.7	1.5	0.39	820

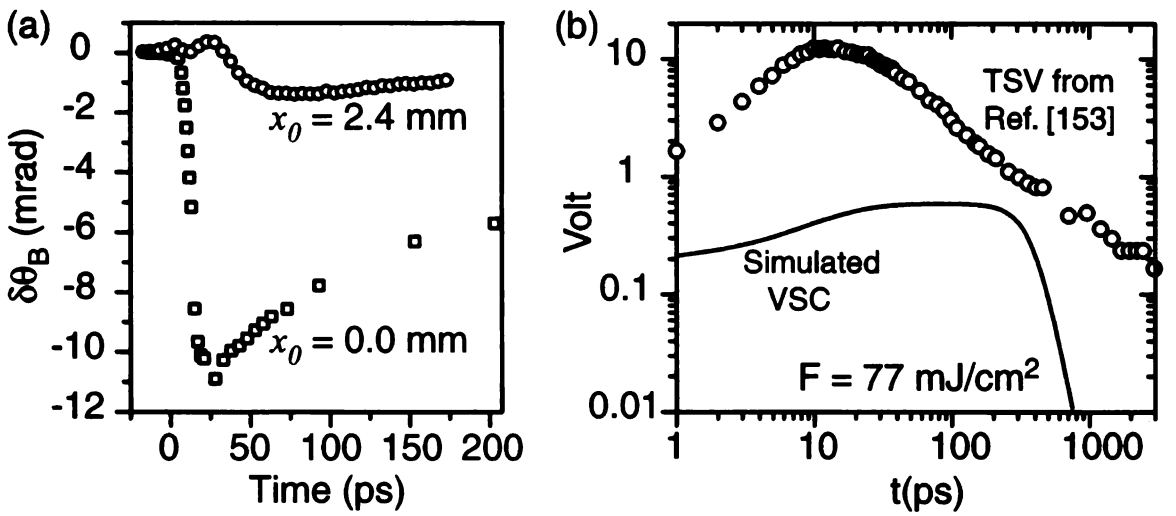

Figure 4.18: Comparison of TSV and VSC effects in UEC investigations of HOPG. (a) Shift of the (006) maxima in case of perfect pump-probe alignment ($x_0 = 0$) and projection imaging geometry with ($x_0 = 2.4$ mm). (b) Comparison of the TSV measured by the probing electron beam submerged beneath the HOPG surface in the UEC study (Ref. [153]) along with the estimated effect of VSC in that study, based on the VSC dynamics extracted here.

density within the VSC cloud and its propagation dynamics, we simulate the effect of VSC under this aligned condition. The effect of simulated VSC and the total Coulomb refraction shift measured from the original pump-probe HOPG experiment is shown in Fig. 4.18(b) and clearly indicates that VSC alone is not sufficient to explain the observed large and rapid 10 V rise in the transient surface voltage of fs-laser excited graphite surface [153]. This consequently mandates the presence of a surface dipole field that is invisible in vacuum to account for the full refraction effect. Based on the observed deflection of electrons at the aligned condition and a parallel plate capacitor model for the surface dipole field within the probe-electron depth of $\approx$ 1 nm, we deduce a ps retention of surface charge density in graphite on the order of 10^{14} e/cm^2, which is comparable to the typical surface/interface state density. The thermionic emission on a sub- to a few picosecond timescale is likely mediated by the image/interlayer states of graphite, which has a strong 3D character [194]. These states above the vacuum level can efficiently transport electrons to

vacuum and create the dipole field near the surface. Following the electron cooling, the coherent interlayer transport normal to the basal planes of graphite is essentially turned off, causing the slow decay of the surface dipole field, which plays a major role in influencing the surface structure dynamics [82, 153, 195].

4.8 Optical Investigation of HOPG

We have seen thus far the important role played by charges in the near-surface dynamics of graphite. The ultrafast carrier dynamics in graphite is by no means a new topic and has historically been investigated optically by many authors focusing on both the high-fluence regime above the melt threshold [164, 165, 196], and the low-fluence regime [197] in bulk graphite. Recent studies have focused on measuring quasi-particle lifetimes [198] as well as carrier dynamics in free standing graphite films [199, 200] and epitaxial graphene [201]. All these experiments have focused on the fs time scale of electronic excitation. To relate our results to the wider optics community, we are also in the process of obtaining time-resolved reflectivity response from the graphite sample using the setup described in Sec. 3.7

Figure 4.19 shows the transient reflectivity recorded from HOPG surface excited by p-polarized, 800 nm, 45 fs laser pulse. The reflectivity was monitored at near-normal incidence while the pump was incident on the surface at 45°. The transient decrease in reflectivity is found to rise initially with increasing fluences and saturates rather quickly beyond $F = 10$ mJ/cm^2. Fig. 4.19(e) shows the transient response at various fluence conditions with the maximum change in each curve normalized to unity. All curves lie on top of each other despite the fluence spanning a wide range, indicating a fluence independent relaxation dynamics. By fitting the 58 mJ/cm^2 data with a functional form representing exponential growth convolved with subsequent exponential decay, we obtain a relaxation time scale of $\tau \leq 1$ ps.

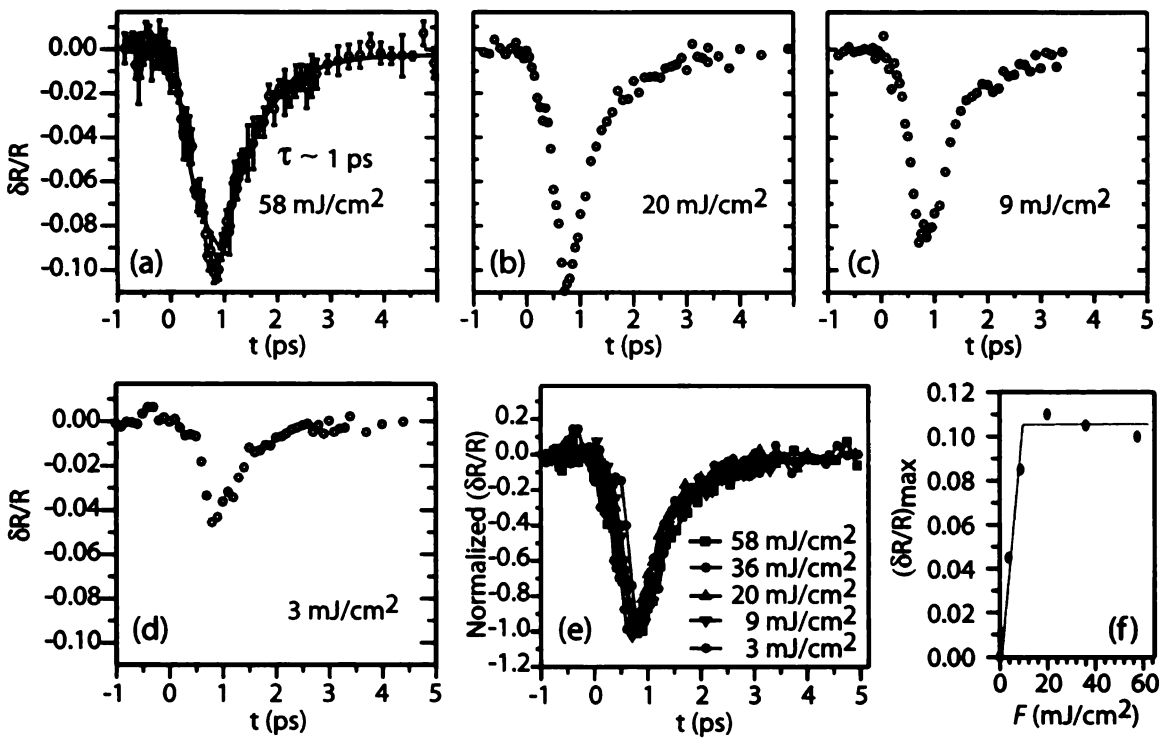

Figure 4.19: Optical reflectivity data from HOPG. (a-d) Transient reflectivity $\delta R/R$ at different fluences, as labeled. (e) Reflectivity data at various fluences with maximum change in $\delta R/R$ self-normalised to unity. The timescales of initial reflectivity drop and subsequent relaxation are largely fluence independent. (f) Maximum change in reflectivity plotted as a function of irradiated fluence, showing saturation beyond 10 mJ/cm^2.

To obtain reflectivity data with high quality S/N, we repeated the experiment at 2 fluences of 4 and 15 mJ/cm^2, averaging the data over 70 scans. The result of such long scans are shown in Fig. 4.20(a). Fitting the data as before yields a time constant for the initial reflectivity drop as 0.2 ps, while that of the relaxation exhibits a very weak fluence dependence with $\tau_2 \sim 0.5$ ps. These data are in fairly good agreement [see panel (b)] with a previous exhaustive study of carrier dynamics in graphite by Seibert *et al.* [197]. It is evident from these data that the optical reflectivity relaxes back to the ground state within 4 - 5 ps. This relaxation dynamics has been attributed in the optics study to the relaxation of electron-hole plasma created by the laser back to the band extremum. However, UEC studies have pointed towards the long-lived

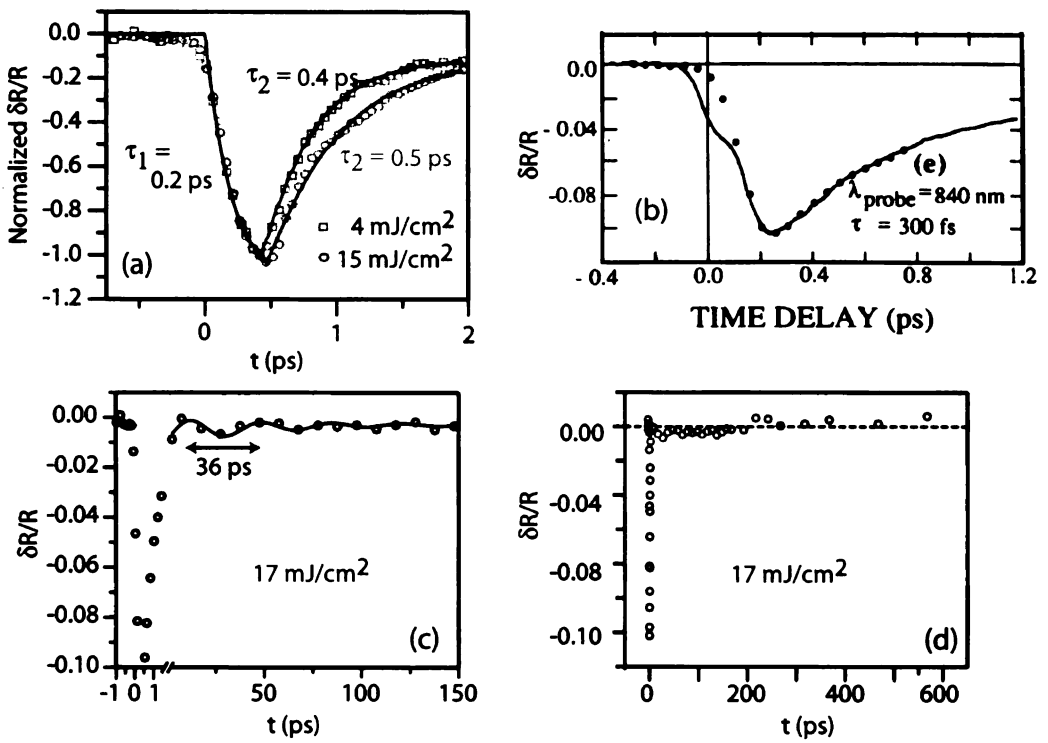

Figure 4.20: (a) Optical reflectivity data acquired with good S/N (70 scans) for 2 fluence limits with fits to convoluted growth & decay $\sim \{1 - exp(t/\tau_1)\} exp\{(t - t_1)/\tau_2\}$. (b) Transient reflectivity from HOPG at $F = 13$ mJ/cm^2 reported by Downer & co-workers [197]. (c) Long-time dynamics at $F = 17$ mJ/cm^2, showing no long-term response (note the break in the abscissa). The optical signal relaxes completely within 10 ps. A weak oscillatory signal, possibly due to acoustic waves triggered in the graphite surface layers is detected. Solid line represents fit to a decaying sine function. (d) Long time optical response from HOPG. No noteworthy dynamics are observed at these long timescales.

charges near the HOPG surface which are not reconcilable with this optics datasets. We believe that the main reason for this discrepancy between optics and UEC results is that charging dynamics is localized to within a few sub-surface layers which the normal incidence probe (optical penetration depth $\sim$ 30 nm) is not sensitive to. We have extended the optical investigation to longer timescales $\sim$ 1 ns and observed no noteworthy dynamics. Hints of a weak oscillatory signal, possibly due to acoustic oscillations of the graphite layers launched along the c axis are observed.

Based on this investigation, we conclude that optical investigations employing

near-normal incidence may not be the ideal geometry to study the structural dynamics in HOPG which are focused near the surface. A grazing incidence reflectivity experiment which might be better suited to shed some light on the near-surface electronic dynamics is currently under execution.

4.9 Summary

In conclusion, we have observed a nonthermal pathway for photo-induced structural changes in graphite through multidimensional crystallographic determination in space, time and energy. The use of electrons as a probe has revealed the photoinduced creation of hitherto unobserved surface dipole field that is invisible in vacuum but exerts significant influence in the dynamics of the surface layers. Beyond a threshold fluence of $F \approx 21$ mJ/cm^2, transient sp^3-like structure with well-defined interlayer bonds are observed, where the layer compression is driven by the Coulombic stress generated by the surface dipole field. Based on diffraction analysis of transient states generated at a fluence of $F = 77$ mJ/cm^2, nearly 50% of the probed volume is observed to be converted into an sp^3 bonding network, with an inter-layer compression of $\approx 6\%$, with the lattice being only moderately heated; though the original graphite structure is recovered at long times. *Ab initio* DFT calculations confirm that the depopulation of the bonding electrons along with the creation of a surface dipole field brought about by the fs laser can lead to a layer compression of $\approx 5\%$ similar to that observed experimentally. These structural responses in graphite arise from a strong coupling of electronic excitation to the inter-layer shearing mode (E_{2g}). Optical experiments utilizing THz [81] and Raman [202] probes have revealed that nearly 90% of the laser excitation energy is transfered to these strongly coupled optical phonons (SCOP) on a sub-ps time scale. Such layer sliding has also been identified as one of the essential precursors in a possible pressure driven pathway of graphite-diamond con-

version [73]. The 'pressure' here is generated however through an inter-layer Coulomb stress caused by the surface dipole field. Due to the small penetration depth of $\approx$ 30 nm, photoexcitation can results in a strong gradient of carrier populations among the different layers, which are preserved over timescales of several ps owing to weak inter-layer coupling [197] preventing vertical charge migration.

Such sp^3 bonded domains as reported here have since been observed in another study of graphite as well via scanning tunneling microscopy (STM) observations of the surface structure following 800 nm fs photoexcitation [82]. Long-lasting sp^3-like domains were generated in their work above a threshold fluence of 60 mJ/cm^2 with p-polarized fs laser excitation. demonstrating the electronic origin of such transformations. The authors propose the formation of interlayer charge-transfer (CT) excitons spanning neighboring layers that can self-localize and distort the lattice around themselves, thus causing buckling of the graphite 6-membered ring and inter-layer contraction [203]. When sufficient number of such CT excitons are created, conditions become favorable for the formation of sp^3 nanodomains.

While the complete pathway connecting sp^2 and sp^3 structures is likely to be complex requiring further detailed study, UEC investigations reported here have provided a first glimpse into a possible all-optical pathway for diamond formation and identified the role of interfacial charges in driving this process, thus opening up another fascinating avenue for the study of material transformations.

Chapter 5

Further investigations of Graphite-Diamond Transition

While the UEC study confirmed the creation of transient sp^3 bonds, there was no permanent formation of macro or microscopic diamond, and the lattice returned to the graphite ground state at long times ($\approx$ ns) following photoexcitation. We have attempted to explore the conditions suitable for a laser induced graphite-diamond structure transition in two types of graphitic systems - (a) bulk HOPG and (b) ultra-thin graphite nanoplatelets, which are graphite sheets as thin as 10 - 30 atomic layers. We have studied the effect of intense p-polarised fs lasers in both these samples and studied the resulting morphologies. While these efforts have not yielded conclusive evidence of permanent or long-lasting diamond formation, there are sufficient promising hints that such a path may be viable. The results reported here could serve as a launching ground for subsequent efforts targeting the search for a photoinduced pathway to diamond formation.

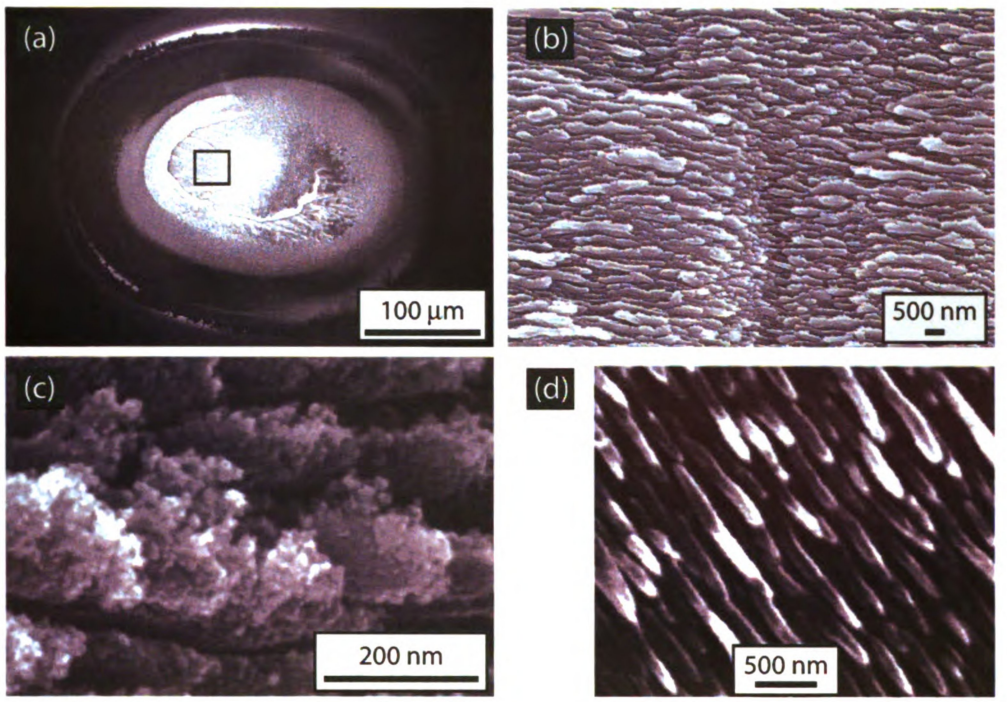

Figure 5.1: Morphology of laser-ablated graphite at F=100 mJ/cm^2. (a) Low-mag SEM image of the entire spot. (b, c) Higher magnification views of the centrally ablated area marked by a square in (a), showing creation of crystalline like nanostructures. (d) Similar result obtained by Huang & co-workers at $F = 170$ mJ/cm^2 [204].

5.1 Pulsed Laser Ablation Of HOPG

Freshly cleaved HOPG surface was exposed in air to p-polarized 800 nm fs laser at an irradiated fluence of $F = 100$ mJ/cm^2 for 10 s. The sample was subsequently imaged under the scanning electron microscope (SEM), and the images acquired are shown in Figs. 5.1 & 5.2. The central region within the laser footprint is shown in Fig. 5.1 and seen to undergo significant surface damage. We see the formation of linear striations which appear to be formed by the melting and resolidification of graphite. Such 'grating like' features have been observed by other groups as well [204] whose results are shown for comparison in Fig. 5.1(d). A closer inspection of the features generated in our work [panels (c, d)] reveals the linear striations to be decorated with smaller

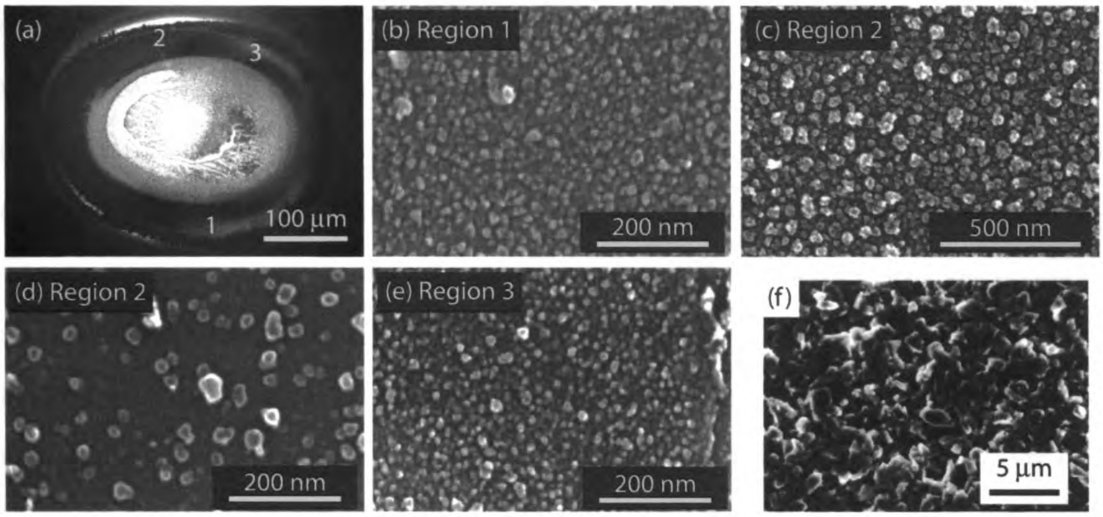

Figure 5.2: Morphology of nanostructure created from fs laser ablation (F = 100 mJ/cm^2) of graphite, in areas surrounding the central ablation spot. (a) Low-mag SEM image of the ablation spot. (b-e) Magnified views of nanostructures from different surrounding regions labeled in (a). The nanostructures exhibit regular crystalline facets suggesting the creation of sp^3 bonded diamond-like carbon structures. (f) The 'cauliflower' like texture commonly observed in ns pulsed laser diamond-like-carbon films obtained from ns pulsed laser deposition using 248 nm KrF laser [205]. The film texture produced in this study in (b-e) resembles this 'cauliflower' pattern.

structural features with well defined domains ranging over 10-20 nm. Such nanoscale features were more apparent around the edges of the ablation spot shown in Fig. 5.2. The entire surface appears to be covered in regular geometrically faceted crystal-like features. Such features were observed at different locations all around the central ablated spot, suggesting that they arise from the deposition of material ablated from the center. Furthermore, the surface morphology of these features resembles very closely that of the so-called 'cauliflower' pattern seen in diamond-like carbon films generated by pulsed laser deposition utilizing ns pulsed lasers, shown in Fig. 5.2(f). It is interesting to note however, the features created in our study are on the nanoscale, while those in the ns pulsed laser ablation study range on the μm scale.

To determine whether these nanostructures contain any sp^3 carbon in them, we obtained Raman spectra from the ablated areas. The Raman spectrum of graphite

consists of a strong G-peak at 1580 cm^{-1}, while that of diamond contains a sharp narrow peak at 1332 cm^{-1}. These peaks serve as fingerprints of the bonding structure in the material and can be used to distinguish graphite from diamond. The spectrum recorded from 4 different regions of our laser-ablated area is shown in Fig. 5.3(a, b). The spectrum from outside the ablation area agrees well with that of pristine graphite, showing a strong G-peak at 1582 cm^{-1} and the second order 2D-peak at 2719 cm^{-1} (not shown here). As we move into the ablation region, we see the emergence of a second peak near $\approx$ 1350 cm^{-1}, which abruptly increases in strength as we cross into the centrally ablated region. This is accompanied by a broad tail down extending to 1000 cm^{-1} and a drop in G-peak intensity. The reduction in G-peak indicates a reduction in perfectly ordered HOPG structure. However, the bandwidth of the new emergent peak is too broad to be unambiguously attributed to diamond (1332 cm^{-1}). This is because the Raman spectra of small graphite crystallites is known to exhibit an additional 'disorder' D-line at 1354 cm^{-1} [206] which originates from disordered graphitic structures. Since pulsed laser ablation of graphite would generate a host of carbonaceous materials, the new peak could well arise from a combination of both disordered graphite as well as nanoscale diamonds. However, the broad tail in the 1000-1300 cm^{-1} is suggestive of nanoscale diamond features - the Raman spectra of nanoscale diamond [207] and diamond nanosclusters [208] show peaks at 1140 and 1120 cm^{-1} respectively. The Raman spectra from a fully sp^3 bonded amorphous carbon network is expected to posses a strong peak at 1265 cm^{-1} [209]. These comparisons indicate that the structures generated in this study could be diamond like sp^3 bonded carbon nanostructures.

We also compare our Raman spectrum with that obtained by Meguro *et al.* from the nanodiamonds generated in their work [2] in Fig. 5.3(c) and find them to be very similar. Meguro *et al.* were able to confirm the creation of nanodiamonds based on STM measurement of I-V curves showing a 5 eV band-gap similar to that

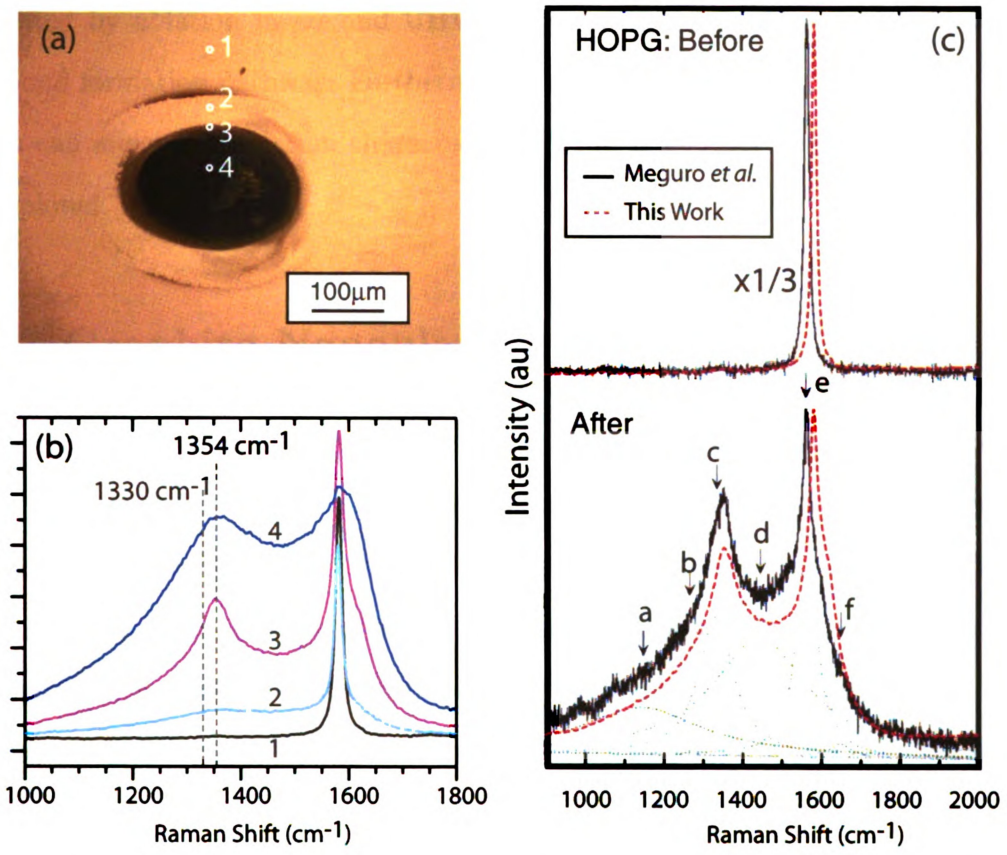

Figure 5.3: Raman spectrum from laser-ablated HOPG. (a) Optical micrograph of the laser ablated region with 4 regions labeled. (b) Raman spectrum obtained from the 4 regions labeled in (a). (c) Raman spectrum obtained from pristine HOPG and from region 4 in (a) in this study overlayed on top of that recorded by Meguro *et al.* [2]. Meguro characterized their spectrum as originating from creation of nanodiamonds.

expected from diamond. The similarity of our Raman spectra with their work is further indication of the creation of sp^3 bonded structures.

Despite strong evidence presented here for the formation of sp^3 bonded carbon from laser ablation of graphite, the evidence remains circumstantial. A conclusive test might be obtained by devising a scheme to collect the nanostructures on a TEM grid for examination by nanodiffraction and EELS. These tests could serve as unambiguous probes of the origins of nanostructures generated. It is speculated that the ablation in air could possibly enable sp^3 bond formation due to the presence of oxygen that stabilizes the dangling bonds in graphite. A comparative study of nanostructures

generated by ablation in air and UHV environments might also shed light on the sp^3 bond formation pathway. Furthermore, the role of temporal profile of the pulse, which can affect the ablation characteristics [210], is another parameter that could be explored.

5.2 Graphite Nanoplatelets

While HOPG is an excellent system to study the inter-layer dynamics of graphite, it is not ideal to study the basal plane dynamics. The signal to noise ratio of the side streaks of (10) and (11) rods observed in the UEC patterns of graphite [Sec. 4.2] is insufficient to afford investigations of basal plane dynamics in that surface probing geometry. As a result, we have attempted to perform UEC experiments in the transmission mode using ultra-thin exfoliated graphite nanoplatelets (xGNP). These samples consist of ultra-thin sheets of graphite, typically 4 - 10 nm thick (10 - 30 atomic layers) deposited on a TEM grid. The samples were prepared by an acid-exfoliation technique [211] in which bulk graphite samples are intercalated with strong acids such as nitric and sulphuric acid, and exposed to microwave radiation. The intercalated graphite undergoes exfoliation to yield these ultra-thin exfoliated graphite nanoplatelets (xGNP). These xGNPs are thin enough to allow transmission diffraction experiments in which the probing electrons are directed along the graphite *c*-axis and thus sensitive to the basal plane dynamics. xGNPs are also amenable to local structure investigations in a TEM.

5.2.1 xGNP Laser Ablation

Local structure investigation of xGNPs in a TEM to search for creation of nanodiamonds is allowed through two powerful probes - nanodiffraction and electron energy loss (EEL) spectroscopy. The nanometer sized electron probe in a TEM allows

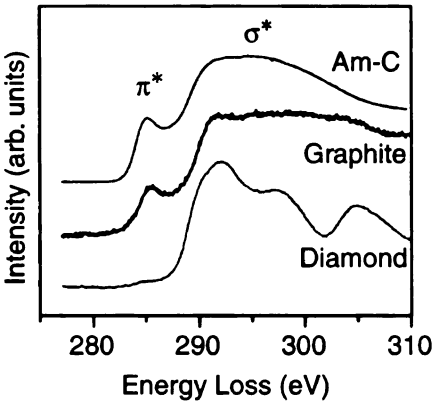

Figure 5.4: Electron energy loss spectrum acquired from 3 types of carbon - graphite, amorphous carbon and diamond. The absence of π^* peak along with the the rather sharp dip around 300 eV can be used as a fingerprint of diamond-like structures.

site-specific investigations of nanoscale features, which might be averaged over when probed by the micron sized electron pulse of the UEC system. EELS in particular offers a powerful means to distinguish between graphite and diamond bondings tructures. The EELS spectra of graphite, amorphous carbon and diamond is shown in Fig. 5.4. Graphite and amorphous carbon EELS spectra consist of a small π^* peak arising from a 1s-$\pi*$ transition. This peak is present only in π bonded structures and consequently, absent in the case of diamonds. Thus, acquiring EEL spectra from laser-ablated regions of xGNP can provide valuable information about any bonding change induced by the fs laser.

xGNPs were deposited on a TEM grid with an ultrathin lacey amorphous carbon support, as shown in Fig. 5.5(a). Diffraction patterns acquired from these samples reveal the characteristic regular hexagonal pattern in Fig. 5.5(b). The sample was subsequently ablated in air at $F = 100$ mJ/cm^2. Since the xGNP is rather fragile, laser exposure led to the complete disintegration of the sample in the center, where the laser peak intensity is quite high. Subsequent TEM examination was performed at the edge of the damaged area where the laser intensity was not high enough to cause disintegration, as shown in Fig. 5.5(c). Exhaustive search for non-graphite like

structures was performed based on site-by-site diffraction investigation. Most areas produced either a perfect graphite-like diffraction, or a diffraction pattern replete with multiple peaks that were unanalyzable. However, we observed a curious behavior as detailed in Figs. 5.5 (d-f). Panel (f) in this figure shows a small region within which diffraction patterns and EEL spectra were acquired from spots labeled as 1, 2, 3. The diffraction pattern from spot 1 agreed well with perfect graphite lattice, while that from spot 2 shown in panel (e) exhibited the creation of additional diffraction maxima (as marked by the arrows) symmetrically on either side of the central (00) location aligned along one direction. The original maxima arising from perfect graphite lattice at spot 1 completely disappeared at spot 3 (not shown) and only the new maxima remained. The diffraction patterns were fitted to theoretically simulated patterns and the 'new' maxima were measured to be distorted from the perfect position by 6%. Furthermore, the EEL spectra obtained from these three spots shown in panel (f) showed changes in the strength of π^* peak.

These changes in the diffraction pattern and EEL spectra can be attributed to the coexistence of normal and asymmetrically distorted graphite sheets in the sample, thus highlighting the difficulty in characterization of possibly novel structures. The 'new' diffraction maxima along certain direction arise from the xGNP sheets not lying flat on the TEM grid (perpendicular to the probing electron beam) but distorted along some arbitrary direction, leading to expansion of the reciprocal lattice rod along that particular direction. Such signatures were observed in unablated xGNP samples as well as shown in Fig. 5.6. Panel (a) shows a region of xGNP from which diffraction and EEL spectra was recorded. The diffraction patterns shown in panels (b-d) show the creation of 2 sets of diffraction maxima similar to that seen earlier from ablated GNP samples. The EEL spectra too showed a change in the π^* peak intensity despite the sample being composed purely of xGNPs. These results can be attributed to the relative angle between the TEM electron beam and the graphite c-axis. Since these

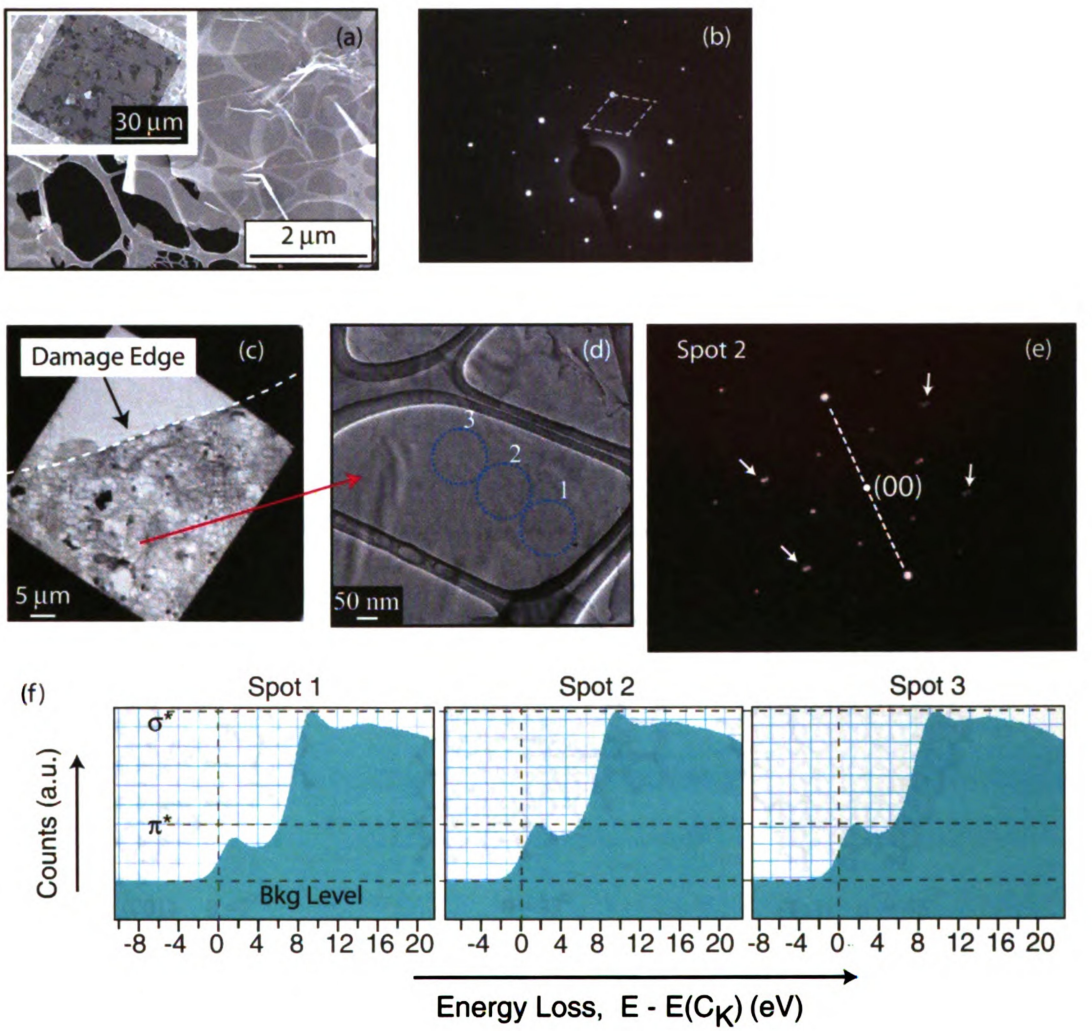

Figure 5.5: Analysis of laser-ablated xGNP sample. (a) SEM Image of xGNP sample on the lacey carbon grid. Inset shows 1 full grid covered in xGNP. (b) Diffraction pattern from a small select area ($\approx$ 100 nm) acquired in a TEM from the unablated sample. Dashed quadrilateral marks the reciprocal cell expected from the honeycomb structure of graphite layers. (c) Low-mag image of the edge of laser-induced damage. Investigations were carried out within this grid, just inside the edge. (d) A small region adjacent to the laser damage edge (as marked by the arrow emanating from (c), which showed interesting results summarized in following panels. (e) Diffraction pattern from spot 2 labeled in (d) showing the presence of new spots marked by arrows, created symmetrically on either side of the dashed line suggesting lattice contraction. The central (00) spot is digitally added for reference. (f) Normalized EEL spectra acquired from spots labeled 1, 2, 3 in (d), showing the change in intensity of the π^* peak.

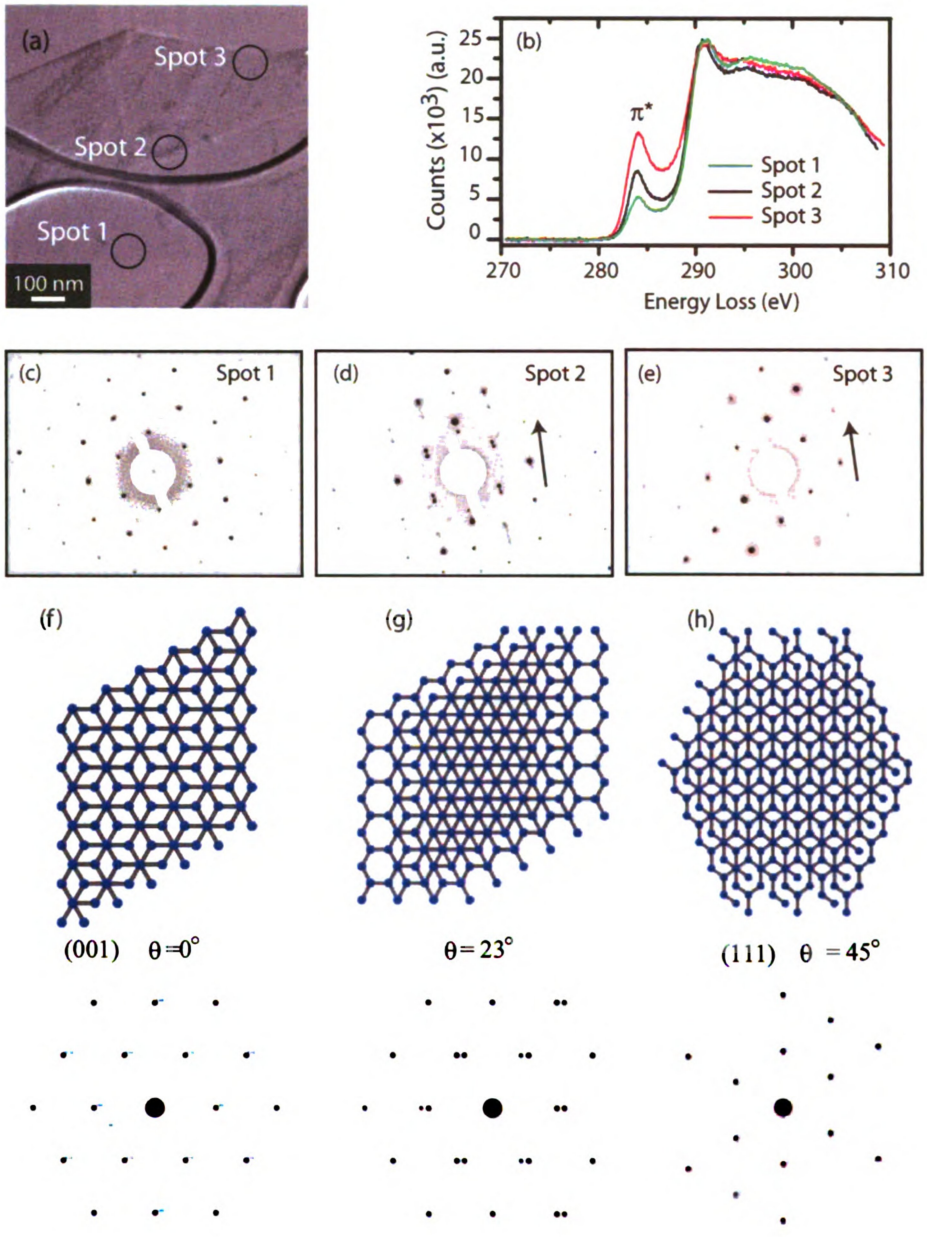

Figure 5.6: Analysis of diffraction and EELS signatures from unablated GNP. (a) High resolution TEM image of GNP, with 3 spots marked. (b) Normalized EEL spectra recorded from adjacent regions labeled in (a), showing change in the π^* peak. (c-e) Diffraction patterns recorded from spots labeled in (a). Diffraction from spot 1 agrees well with pristine graphite, whereas those from spots 2 & 3 show distortions such as creation of multiple Bragg spots and stretching of the hexagon along directions marked by the arrows, which are features similar to those seen in the ablated sample. (f-h) Simulation of TEM diffraction pattern from a perfect graphite lattice, for varying angles (θ) between the graphite's $c-$axis and the electron beam direction. Note the creation of additional spots in (g) and the stretching of the hexagon in (h).

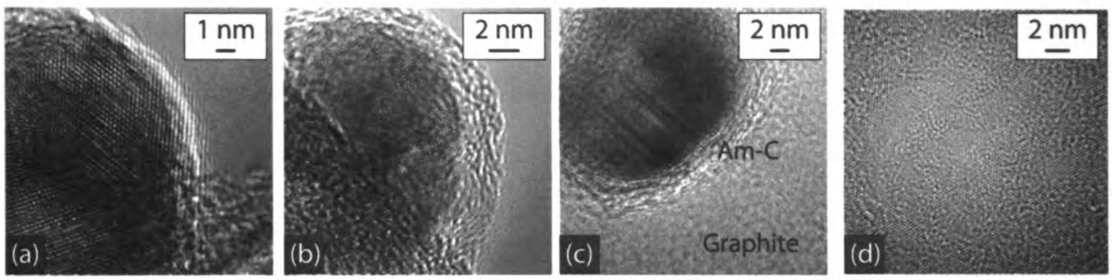

Figure 5.7: (a-c) High resolution TEM images of 3 different crystalline nanostructures with size in the 10-20 nm range observed near the laser ablated region within the xGNP samples. Each nanostructure appears to be surrounded by few layers of amorphous-carbon. (d) A high-resolution TEM image of a flat xGNP sheet, provided for comparison.

xGNPs are very thin, it is possible that they have ripples on the surface due to the folding of ultrathin graphite sheets. Also, the sheets might not be relatively flat near the edges and may stand up. This can explain the variation in the intensity of the of π^* peak in panel (b), which depends on the relative orientation of the c-axis and the electron beam. The distortion seen in the diffraction pattern can also be explain based on this misalignment. Panels (f-h) simulate the TEM diffraction pattern from a graphite lattice for various angles of electron beam incidence. At $\theta = 23^\circ$, we see the creation of maxima doublets and the stretching of the hexagon seen in (h) can be attributed to arise from the 111 plane. These investigations reveal that TEM studies of xGNP require further care to account for the ripple on the sheets. The artifacts in the EEL spectra could presumably be eliminated by acquiring spectra from the same spot at different incidence angles, though such data is very hard to acquire.

Finally, we also observed the creation of a few nanocrystals shown in Fig. 5.7. These structures are dissimilar from the surrounding xGNP substrate seen in panel (d), and appear to posses a more 3-dimensional structure. Characterization of these nanocrystal might possibly require EELS investigation in the Scanning TEM mode, which was not performed. Furthermore, the yield of such nanocrystals was extremely low - only 3 or 4 such features were observed following an exhaustive search around

the laser ablated spot. Thus, finding these structures becomes a matter of chance rendering a systematic study quite difficult.

5.3 UEC Investigations Of GNP

The disadvantage of the preceding TEM investigation lay in the fact that it is not *in situ*. Consequently relating any observed nanoscale features to the effect of laser becomes quite difficult. We also performed UEC investigations of these xGNP samples employing diffraction in the transmission mode. Figure 5.8 (a) shows the typical diffraction pattern obtained from these samples in the UEC system. Since the electron probe is $\sim 20\mu$m in size, it samples many different randomly oriented xGNPs to produce diffraction rings. The xGNP appears to be randomly oriented not only within the 2D plane as some maxima due to symmetry along c-axis are also observed. We however focus on two such maxima (100) and (220) arising purely from basal plane order. We determined the damage threshold for these samples *ex-situ* to be $F = 40$ mJ/cm^2 and consequently, probed the transient dynamics in the fluence range $5 \leq F \leq 20$ mJ/cm^2. The diffraction rings were averaged to produce 1-d diffraction curve shown in Fig. 5.8(b). Any long range lattice transformation is expected to show up as a radial breathing of these rings. However, no such effect was observed within the fluence range probed. We monitored the diffraction intensity of these rings to extract the laser-induced increase in the in-plane vibrational amplitudes. The increase in the in-plane mean-square vibration amplitude observed here is found to be significantly smaller than that observed along the c-axis in the UEC study of bulk graphite, though the timescale for hot-phonon relaxation is still measured at 8 ps, consistent with the HOPG data. The discrepancy in the intensity drops can be attributed to the greater strength of in-plane σ bonds compared to the van der Walls bonds along the c-axis. Thus large amplitude vibrations are not as easily excited

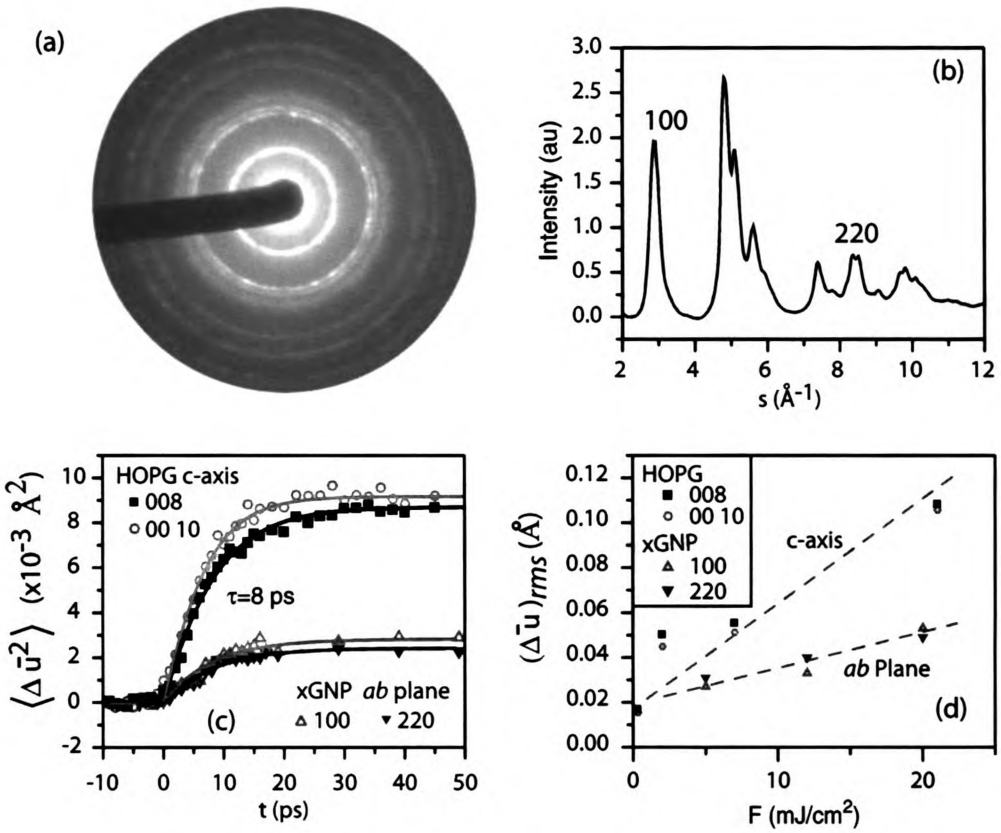

Figure 5.8: UEC investigations of exfoliated graphite nanoplatelet (xGNP) samples. (a) Ground state transmission UEC diffraction pattern. (b) 1d diffraction curve obtained from radial averaging of rings in (a) (c) Mean-square atomic vibrations within the basal plane, extracted from (100) and (220) maxima in (b) compared with that along c-axis dynamics acquired from HOPG. Fluence in both cases is $F = 20$ mJ/cm^2 (e) Comparison of rms vibrations along the basal and the c-axis. Dashed lines only a guide to the eye.

in-plane. This difference between the in-plane and c-axis vibrations agrees well with the previous X-ray diffraction analysis of equilibrium vibration amplitudes in graphite [see Fig. 4.7(d)]. The lack of significant changes in the position of the diffraction rings suggests that the graphite layer maintains its structural integrity within the fluence regime probed here.

5.4 Summary

We have listed here different attempts at evidencing the graphite-diamond transition. While the laser ablation of bulk graphite yielded some promising results, further systematic study is warranted to detail the origins of the fs-laser ablated nanostructures created therein. UEC investigations of xGNP samples is still a work in progress. While the bulk graphite showed transient sp^3 bonds to be created around $F = 77$ mJ/cm^2, the fragile nature of xGNP prevents investigation at such high pump fluences in a multi-shot setup. Further studies will be aimed at detailing the differences in the structural dynamics along the c-axis and the basal plane during this $sp^2 - sp^3$ transition.

Chapter 6

Photoinduced Fragmentation In Silver Nanocrystals

Optically induced fragmentation of nanoparticles has been characterized by explosive boiling [100] and also by Coulomb explosion [99, 102, 103] at low laser excitation thresholds near the surface plasmon resonance (SPR) [99, 101, 104]. Such low threshold fragmentation was first reported by Kamat *et al.* . who observed breakup of 40-60 nm Ag NCs and attributed the cause to NP charging based on picosecond (ps) transient bleaching and absorption signals in the plasmon band [99]. Plech *et al.* examined the melting transition of 38 nm Au NPs using time-resolved X-ray scattering and found evidence of ablation below the melting threshold within 1 ns [104]. Conversely, Yamada *et al.* showed Au NPs size reduction from 8 nm to $\sim$ 3 nm using a focused ns laser pulse and attributed it to Coulomb assisted evaporation mediated by thermionic emission [102] with estimated NC charging up to 700 $e+$ per NC. At exceedingly high fluences, Koda and coworkers have achieved size reduction of Au NPs from 20-50 nm into sub-10nm, and suggested the causes to be evaporative ejections of atoms and small clusters followed by recondensation [100]. Pulse-length dependent NPs reshaping and resizing were also reported by El-Sayed and coworkers [103], who

attributed Coulomb explosion as the main cause for fragmentation with fs excitation and a thermal mechanism with ns pulses. The rivalry between the Coulomb and thermal mechanisms is fuelled by the competing heating and charging rates of the NC, and the exact pathway of NC disintegration can be affirmed directly by imaging the transition state structures at the onset of fragmentation. Using ultrafast electron crystallography (UEC) [110], transient dynamical structures and charge states of the NCs near the SPR induced fragmentation limit were probed to elucidate these competing mechanisms as described in the remainder of this chapter.

6.1 Ultrafast Electron Nanocrystallography

One of the key steps in a successful investigation of transient structures in photoexcited nanocrystals (NCs) is the design of the sample geometry. Some of the considerations that necessitate careful control are:

1. **Reduced particle-particle interaction:** While studying an ensemble of NCs, it is important to have them widely separated from each other in order to reduce any inter-particle interactions. With SPR in particular, the reduction in particle-particle distance enhances the near-field coupling amongst the NCs leading to additional resonances at lower energies [83, 212] and can also lead to long range inter-particle interactions [213].

2. **Prevention of NC agglomeration:** Once the NCs are excited, they may gain sufficient energy to move around in their vicinity. Furthermore, with the increased energy, they may have propensity to aggregate and coalesce to form larger NCs or clusters.

3. **Reversible probing methodology:** Multi-shot exposures over several pump-probe cycles are beneficial to average out statistical fluctuations in the process

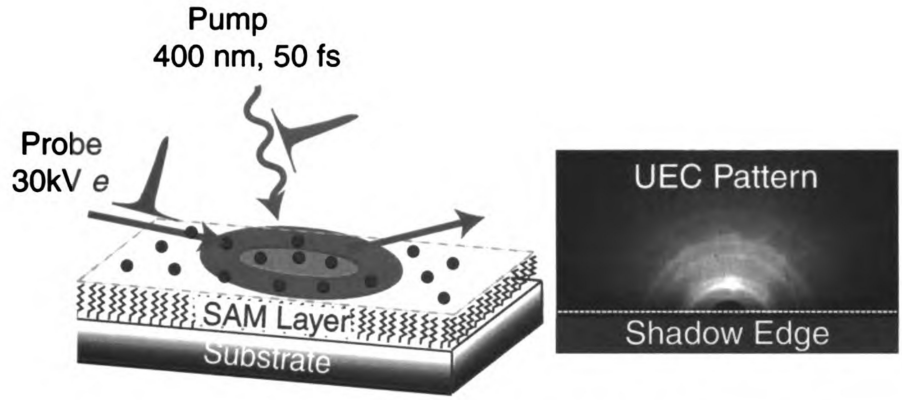

Figure 6.1: Sample geometry employed in the UEC investigation of nanopaticles.

and achieve superior S/N diffraction data with high degree of data reproducibility. This will be necessary later while employing structure refinement schemes to visualize the diffraction data. As a result, sample integrity must be preserved over multiple such pump-probe cycles.

Any controlled investigation of particle dynamics should attempt to achieve the above mentioned goals. Optical investigations do so typically by utilizing a dilute solution of NCs in water or other non-interacting liquids such as cyclohexane, toluene, *o*-xylene and chlorobenzene [99]. Such liquid samples however are untenable for most electron diffraction studies which require vacuum environments. Powder NC samples are often used in steady-state structure investigations, but are not ideal for dynamical studies due to the possibility of melting and coalescence at elevated excitation levels. Electron diffraction is possible from NCs deposited on a TEM grid with an ultrathin amorphous carbon support. However, the instability and low damage threshold of these membranes to laser excitation prevent study at even moderate fluences of 20 - 30 mJ/cm^2.

The sample geometry employed in this lab is one that attempts to addresses all concerns raised above, in which the NCs are sparsely distributed and firmly anchored to a substrate via a self-assembled monolayer (SAM) of organo-silane molecules, as

shown in Fig. 6.1. This geometry, which is compatible with UHV settings, ensures minimal inter-particle interactions and prevents any surface diffusion of the NCs. The electron beam is incident on the sample at grazing angles ($\theta_i \leq 1.5^{\circ}$) and samples an ensemble of NCs within its footprint. Given that the penetration depth of 30 keV electrons in silver NCs is ≈ 1.5 μm, at these grazing angles, the electron probes a vertical depth of ≈ 40 - 50 nm, thus ensuring that the significant fraction of the scattered signal arises from the NCs. The presence of the SAM layer further suppresses any substrate scattering which would otherwise be significant at such grazing incidence experiments, as will be soon highlighted.

By isolating NCs from their neighbors and eliminating direct contact between the NCs and the substrate, the normally irreversible phase transformations become reversible, allowing multi-shot pump-probe diffraction to map out their full course. Such implementation allows the use of a low-density electron pulse to avoid the pulse-broadening effect [214] and has high data reproducibility compared with single-shot experiments where a much higher density electron pulse is required [215].

6.1.1 Sample Preparation

The sample preparation procedure has been adapted from wet chemistry methods pioneered by Alivsatos and co-workers [216] that are now commonly employed in fabricating ordered 2D assembly of nanoparticles on substrates [217–222]. The process can be broken down into 3 major steps as described below.

1. Surface pre-treatment: Silicon wafers are cleaned by ultrasonic agitation in acetone and then in methanol to remove macroscopic contaminants. Thereafter, they are carried through a modified RCA-like process [223, 224] to throughly clean the surface of all organic and inorganic residues. This involves immersion in the following solutions for 10 min each:

1. H_2SO_4/H_2O_2 (7:3), at 90°C to remove organic residues.

2. 40% NH_4F solution in deionized (DI) water at room temperature, to remove the native oxide layer on silicon.

3. $NH_4OH/H_2O_2/H_2O$ (1:1:6) at 90°C to remove metallic contaminants and establish a fresh, thin (1-2 nm) oxide layer with hydroxyl (-OH) coating.

4. $HCl/H_2O_2/H_2O$ (1:1:5) at 90°C to remove final trace metal & ionic contaminants introduced in the steps above.

The substrate is throughly rinsed in copious amounts of DI water in between each of the above mentioned steps, which finally results in a clean, hydroxyl (-OH) terminated silicon substrate.

2. Surface functionalization: The organic molecule used in this study for surface functionalization (creation of the SAM layer) is (3-Aminopropyl)trimethoxysilane $[H_2N(CH_2)_3Si(OCH_3)_3]$ abbreviated as APTMS. Other organosilane molecules with differing alkane chain lengths may also be employed. The clean substrate is immersed for 60 min in a dilute solution ($\approx$ 9mM) of APTMS in DI water, with some acetic acid to enhance functionalization. (APTMS:Acetic Acid:DI water = 1:5:480). This is followed by a thorough rinse in DI water and drying under dry-nitrogen gas, as shown in Fig. 6.2(b-c). It is then heated to 120°C to strengthen the siloxane (Si-O) bond between the terminal silane group of the SAM and the Silicon substrate [218].

3. Nanocrystal deposition: Finally, the surface functionalized substrate is immersed in a citrate stabilized colloidal nanocrystal solution for a period of 1-2 hours to allow the NCs to anchor onto the SAM surface [Fig. 6.2(d-e)]. Immersion of the substrate in the solution protonates the terminal amine (NH_2) groups of the SAM molecules to form positively charged NH_3^+ end groups [221]. The NCs on the other

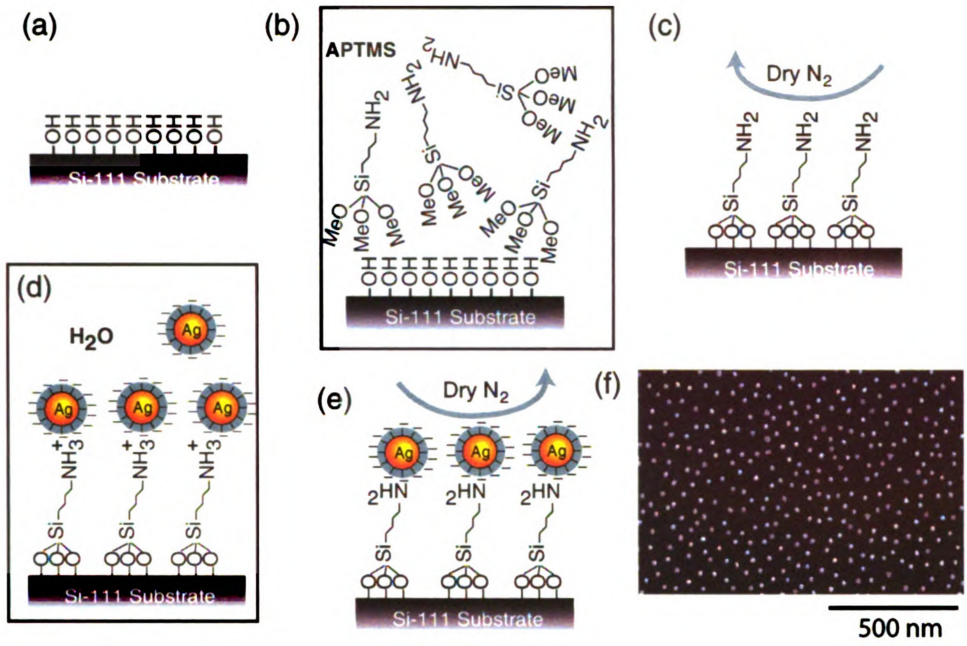

Figure 6.2: Steps to deposit colloidal nanocrystals on silicon surface. (a) Hydroxyl terminated silicon surface. (b, c) Surface functionalization (d, e) Nanocrystal deposition. (f) SEM image showing typical sample morphology obtained using 20 nm Au NCs here as example.

hand, are covered by negatively charged citrate ligands that stabilize them against agglomeration via mutual repulsion. These negatively charged ligands bind electrostatically to the protonated NH_3^+ groups of the SAM, thus immobilizing the NCs on the surface [222]. There would of course be a large number of SAM molecules underneath a single NC to help anchor the nanocrystal firmly onto the substrate. Any loosely bound nanocrystals are removed by a final rinse and dry cycle. Figure 6.2 (f) shows the typical sample morphology obtained by this procedure. The NCs (20 nm Au, in this case) are seen to be isolated and uniformly dispersed on the substrate, albeit with inter-particle distances on similar scales as the particle dimension.

The density of the NC coverage can be tuned by controlling 3 parameters during the final NC deposition step - (1) the immersion duration, (2) the pH, and (3) the concentration of ethanol in the NC colloidal solution. The deposition rate of citrate-stabilized colloidal NC on aminosilane surfaces is known to be limited by diffusion,

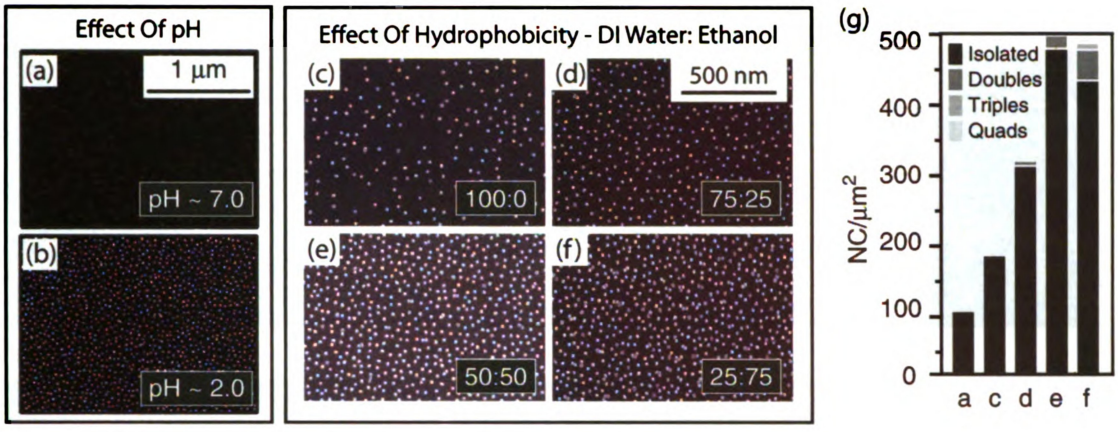

Figure 6.3: Controlling areal density of NCs on organosilane covered Si-111 substrate. (a-b) Changing pH of Ag colloidal suspension using acetic acid. (c-f) Changing hydrophobicity of Ag colloidal suspension using ethanol. (g) NC counting statistics averaged over two separate 1 μm^2 areas.

exhibiting a $t^{1/2}$ dependence [217]. Changing the pH on the other hand alters the protonation rate of the amine group [221] while an increased concentration of ethanol increases the hydrophobicity of the colloidal solution [220]. The effects of changing pH and hydrophobicity are shown in Fig. 6.3. In this case, we altered the pH using the addition of acetic acid. Lower pH and increased ethanol content leads to increased NC coverage.

6.1.2 Importance Of SAM layer

The presence of the organic aminosilane layer underneath the NC is vital in this experiment. (1) It firmly anchors the NCs at one spot, preventing agglomeration [225]. (2) It acts as a barrier preventing diffusion of NC into the underlying substrate [226]. (3) It isolates the NC from other surrounding NCs, thus preventing any fusion or agglomeration of multiple NCs that might occur at elevated temperatures as the NCs are excited far from equilibrium. This ensures that the isolated NC returns to the original configuration after each pump pulse. (4) It screens the underlying substrate from the probing electron beam, thus suppressing substrate scattering.

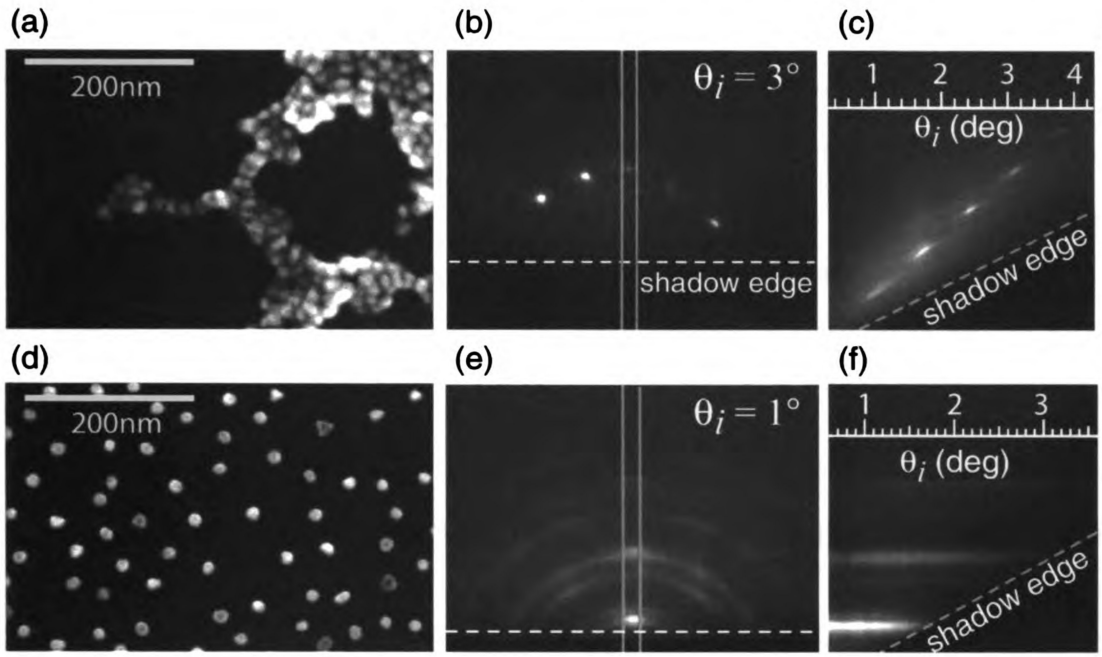

Figure 6.4: Importance of Buffer SAM layer for UEC investigations of surface supported nanoparticles. (a) Sample morphology obtained with unsuccessful or incomplete surface functionalization, with corresponding diffraction pattern (b) and rocking curve (c). (d) Ideal sample morphology, showing uniform coverage of isolated NPs, with corresponding diffraction pattern (e) and rocking curve (f).

The importance of the SAM layer is illustrated in Fig. 6.4. If the surface functionalization is unsuccessful, the NCs no longer have a firm anchor. Consequently, as the NC colloidal solution evaporates after the final NC deposition step, surface tension forces tend to drag them together to form coalesced clusters, as shown in Fig. 6.4(a). The diffraction pattern and the rocking curve from this sample is shown in Figs. 6.4(b, c) exhibit peak periodicity similar to that observed in RHEED patterns [See Sec. 4.2.1] arising from a flat surface.

In contrast, when the surface functionalization is successful, the NCs are deposited uniformly on the surface as seen in Fig. 6.4(d), using 20 nm Au NCs as an example. Most importantly, they are isolated and well-separated. The diffraction patterns from this sample consists of powder-like diffraction pattern consisting of Debye-Scherrer

rings showing no dependence on the incidence angle of the probing electron beam. This is expected as the electron beam samples an ensemble of *randomly oriented* NCs within its footprint to produce transmission diffraction patterns. Additionally, the Debye-Scherrer rings are found to be in good agreement with the fcc symmetry expected from Au, indicating that the diffraction pattern indeed arises from the surface supported NCs. The substrate signal has been effectively suppressed by the SAM layer.

6.2 Silver Nanocrystals - Ground State Characterization

Colloidal silver NCs (*Ted Pella*, 40 $\pm$ 7 nm) were dispersed *ex-situ* on a Si-111 substrate functionalized with an APTMS SAM as described in the previous section. SEM characterization of the sample showed uniform coverage, with low mean areal density of 7 NC per μm^2 [Fig. 6.5(a)]. The NCs were well separated with average inter-particle separations of $\approx$ 200 - 300 nm, far exceeding the particle dimensions, as desired.

The ground state diffraction pattern from this sample consisting of the Debye-Scherrer rings [Fig. 6.5(c)] was averaged radially to obtain the normalized 1D structure function $sM(s)$ [Fig. 6.5(d)], as described in section 2.2.1. Since the electron beam samples an ensemble of NCs, the $sM(s)$ carries information about the average structure of the NCs in reciprocal space. Fourier analysis of $sM(s)$ yielded the atom-atom pair correlation function $G(r)$, which denotes the probability of finding 2 atoms in real space separated by a distance r. For an ideal fcc structure, the atom-atom distance list can be expressed analytical by the expression $r_i = (i/2)\, a_0^2$, where a_0 is the lattice constant of the cubic fcc sturcture. We find a good agreement between the experimentally obtained $G(r)$ peaks with the theoretically predicted distance lists for

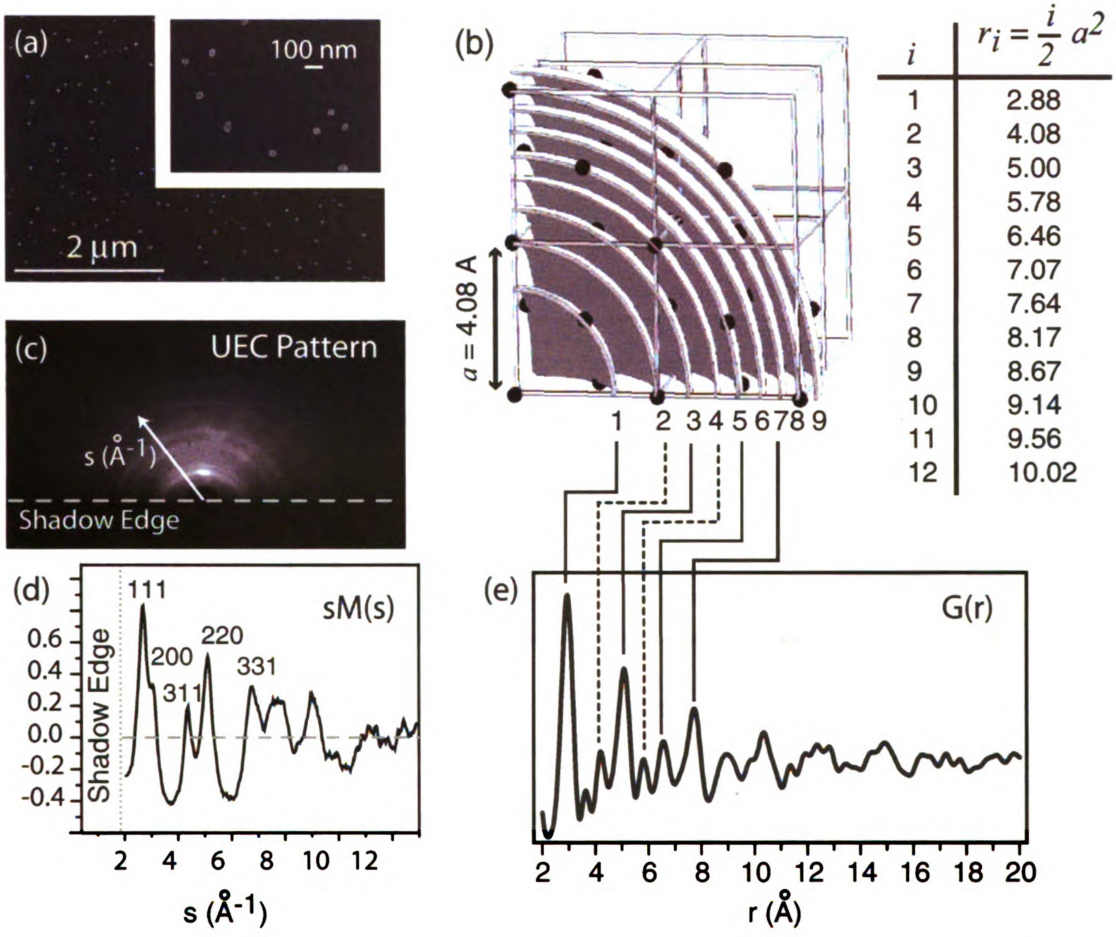

Figure 6.5: Ground state characterization of 40nm Ag NC using UEC. (a) SEM images of the Ag NC sample. (b) Theoretical distance list for fcc Ag lattice using lattice constant $a_0 = 4.08$ Å (c) UEC diffraction pattern obtained from ground state of sample in (a). (d) $sM(s)$ pattern obtained from radial averaging of diffraction pattern in (b), as described in Sec. 2.2.1. Characteristic fcc peaks are labeled. (e) Atom-atom pair correlation function $G(r)$ in the ground state, obtained through Fourier analysis of (c). The peaks agree well with theoretical predictions in (b).

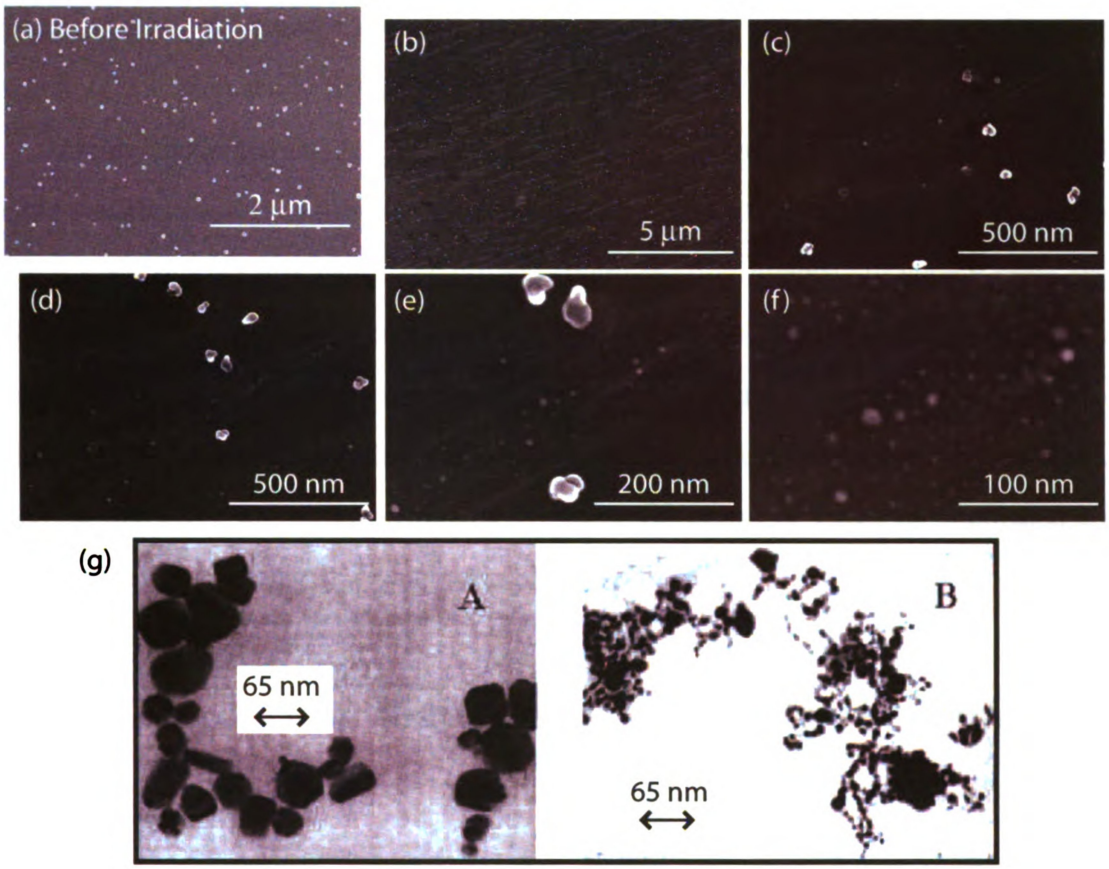

Figure 6.6: SEM Investigation of Ag NC fragmentation. (a) Sample before irradiation (b-f) Random areas of the sample within the laser footprint. Excitation at 400nm, F=30 mJ/cm^2. (g) Similar fragmentation of Ag NCs observed in the solution based study by Kamat *et al.* [99]. (A) - before; (B) after excitation by a 355 nm ps laser.

silver lattice based on the accepted fcc lattice constant of a_0 =4.08 Å [227].

The NC sample is now irradiated using the ultrafast laser pulse (50 fs, p-polarized, 45° incidence) at 400 nm, which is within the SPR bandwidth (385±40 nm), to check for traces of fragmentation. At a critical fluence F = 30 mJ/cm^2, multi-shot SPR excitation leads to fragmentation into predominantly 2 nm NCs as shown in Fig. 6.6. The fragmentation of NC seems to be accompanied by a 'trail' in these SEM images, which we speculate to be the result of damage to the underlying SAM layer. The lack of any solution environment that might facilitate explosive boiling and recondensation indicate the fragmentation mechanism to be internal to the NC. Such photoinduced

fragmentation of silver NCs have also been observed in solution based studies; the result of one such study [99] is shown in the figure.

Having confirmed the fragmentation of the NCs, we attempt to observe the transient structures and the atomic rearrangements leading to the fragmentation by probing a fresh sample just below the critical fragmentation fluence. In such a case, the NC would approach the fragmentation threshold but not posses sufficient energy to cross the activation barrier, and thus return to the ground state. This allows multi-shot probing of the reversible atomic rearrangement of the pre-fragmentation state. Sample integrity was retained during pump-probe cycles of UEC, as confirmed by SEM imaging following the conclusion of experiment.

6.3 Diffraction Signatures From Pre-Fragmented State

UEC investigation of Ag NC prefragmentation dynamics was performed at an irradiated fluence of F =17 mJ/cm^2 and the transient diffraction patterns recorded. As is in the case of graphite, structural changes within the UEC diffraction are convolved with a transient surface voltage (TSV) induced Coulomb refraction shift that is inevitable in all UEC reflection experiments. Hence, prior to analyzing the data, this refraction shift needs to be corrected. For a Debye-Scherrer diffraction pattern, structural change such as lattice expansion or contraction will induce a radial breathing of the rings with the ring center unchanged, whereas a refraction shift will induce a lateral shift of the rings in a direction normal to the surface (or shadow edge). Furthermore, the lateral shift will depend on the polar exit angle of the electron, but be independent of the azimuthal exit angle. Keeping this in view, a 2D Fourier phasing algorithm was implemented to correct for the TSV induced refraction shift directly in the 2D diffraction patterns before radial averaging. The correction procedure also

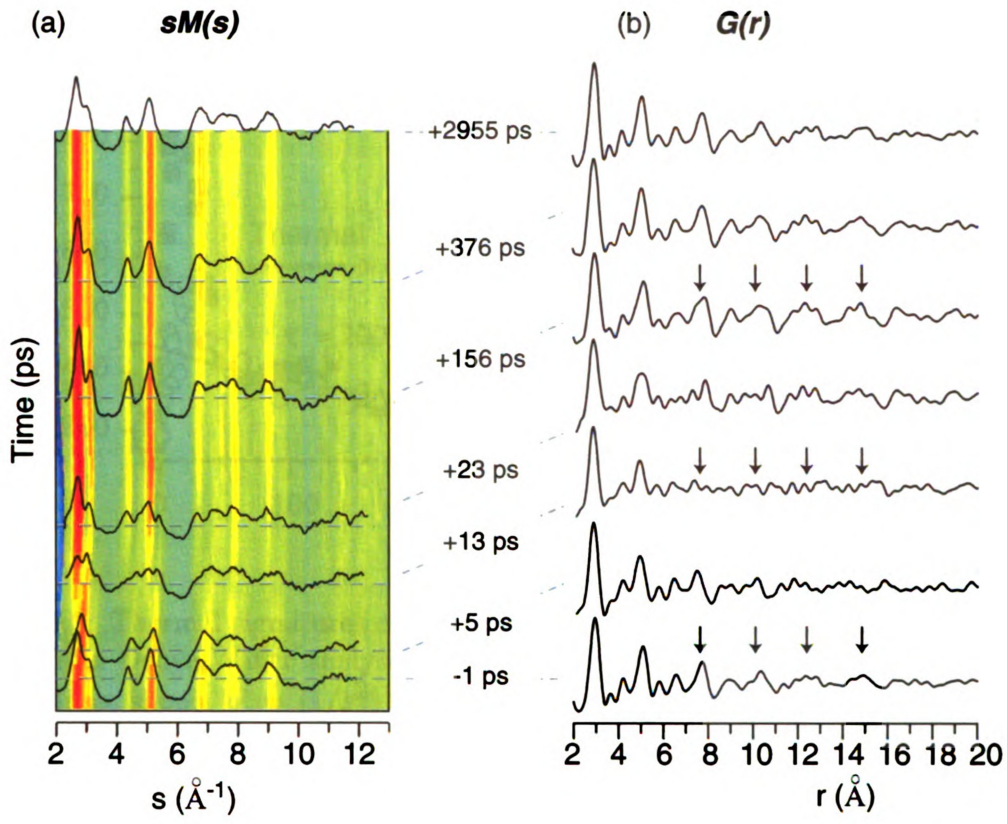

Figure 6.7: UEC Data (a) Time evolution map of the normalized structure factor $sM(s)$ of Ag NCs excited at SPR at $F = 17$ mJ/cm^2, with $sM(s)$ at select times explicitly overlayed. (b) Pair correlation function $G(r,t)$, corresponding to the select times in (a). The arrows point to the medium range order peaks, which completely dephase by $t = +13$ ps, before their eventual revival at long times.

yielded the average transient surface voltage (TSV) seen by the electron beam, which will be utilized later in determining the interfacial charging dynamics.

The TSV-corrected diffraction patterns are radially averaged to obtain $sM(s,t)$ and $G(r,t)$ which are shown in Fig. 6.7. These $sM(s,t)$ and $G(r,t)$ represent the photoinduced structural changes occurring within the NCs. The transient alteration of the $sM(s)$ in Fig. 6.7(a) reveal that by $t = +13$ ps, the initial fcc ordered diffraction maxima diminish along with a concomitant rise of diffusive scattering in between the peaks to form multiple peak like pattern, indicating a departure from the cubic fcc symmetry. The dramatic drop in the intensity of (111) peak relative to the other

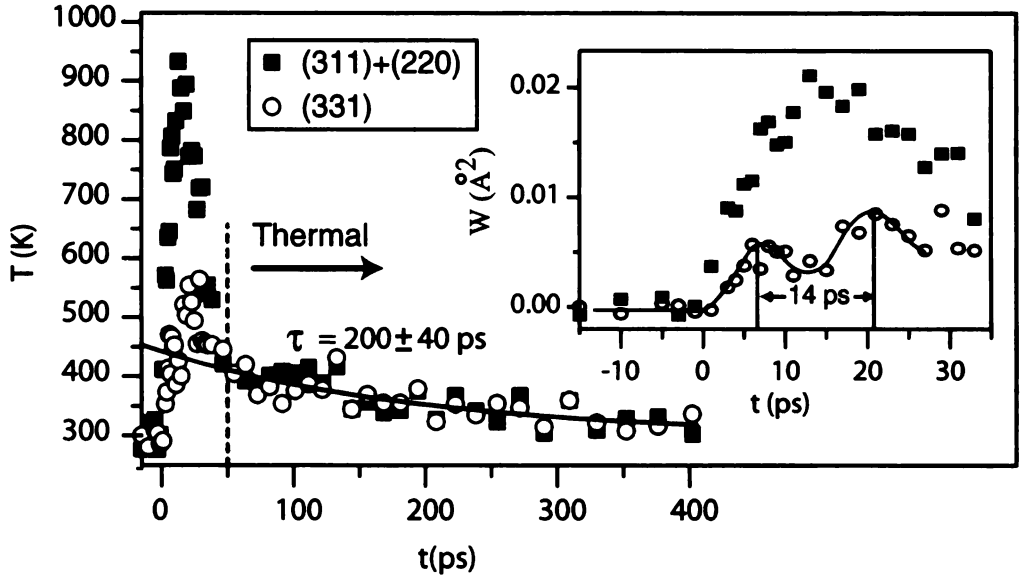

Figure 6.8: Thermal signatures of NC fragmentation process. NC temperature estimated from Debye-Waller analysis of peak intensity drop in (331) and (311)+(220) peaks. Inset shows $W = (1/s^2)\ ln\,(I/I_0)$ determined for the same two peaks, and exhibits anisotropy at short times. The oscillatory curve is drawn as a guide to the eye, representing acoustic oscillations of the NC.

peaks at larger s values is also noteworthy and will soon be examined in detail. The corresponding pair correlation functions $G(r,t)$ shown in Fig. 6.7(b) reveal a reduction in long-range order. The atom-atom correlation peaks greater than 10 Å smear out completely by $t = +13$ ps, while the short-range peaks ($r \leq 10$ Å) retain their strength. This indicates the persistence of short-range order during this pre-fragmentation process.

6.3.1 Thermal Signatures of Fragmentation

To identify the origins of this structural disorder, we first calculate from each Bragg intensity a parameter $W = (1/s^2)\ ln\,(I/I_0)$. W is closely related to the mean-square displacement of atoms $\Delta\bar{u}^2$ ($3W = \Delta\bar{u}^2$) - a tool often used in cases of quasi-equilibrium conditions to extract lattice temperature via the Debye-Waller relation [118]. In such cases, $\Delta\bar{u}^2$ is independent of the diffraction order used, as observed

earlier in the case of graphite [153]. However, we find here [inset to Fig. 6.8] that for $t < 50$ ps, the W determined from higher order (331) peak is smaller than that from the lower order (311)+(220) peaks[1] indicating the nonthermal nature of the structure disordering process. We will argue that this anisotropy in W is the manifestation of a structural change that destroys long-range coherence in the NCs and acts as a precursor to the fragmentation observed above the critical fluence. It is also interesting to note the appearance of a transient oscillatory signal of period $\approx$ 14 ps in the 331 peak, which agrees well with the timescale of the fundamental radial breathing mode oscillations measured for silver NCs [94].

At longer times ($t > 50$ ps), W shows no s-dependence, and so, we can reliably extract the lattice temperature from W by relating it to the Debye-Waller factor. Using values tabulated in literature for temperature dependence of $\bar{u}^2$ [228], we scale the experimentally obtained quantity $\Delta\bar{u}^2(t,T) = \bar{u}^2(t,T) - \bar{u}^2(t_0, 300K)$, to obtain the instantaneous temperature of the NC, as shown in Fig. 6.8. Focusing only on the data beyond $t > 50$ ps for which this Debye-Waller analysis is applicable, the temperature decays exponentially with an average time constant of $\tau = 200\pm40$ ps. We model this heat loss from the NC as an interface conductance limited thermal transport across the SAM layer into the Si bulk. Based on the bulk specific heat of silver $C_v = 232$ J/kg/K $= 8.2 \times 10^{-7}$ J/K, we obtain an interface thermal conductance of $G_T = 4.8 \times 10^{-7}$ W/K, which is in good agreement with values for single-molecule thermal conductance and average areal densities of APTMS molecule [219, 229]. Furthermore, extrapolating the temperature decay trend to earlier times, we obtain a maximum temperature rise within the NC at $t = 0$ ps of at most 450 $\pm$ 25 K, which is well below the melting threshold of silver NC.

Reverting our attention back to the short-time dynamics, we now seek to explain the observed anisotropy in the W values calculated from different Bragg peaks. To

[1]See Fig. 6.5(d) for peak indexing

show that this anisotropy is a characteristic fingerprint of the NC undergoing fragmentation, we carry out a simulation of the diffraction signatures expected from a pre-fragmented NC. Starting from a $15 \times 15 \times 15$ supercell structure for the NC, the supercell is fragmented (subdivided) into smaller units as illustrated in Fig. 6.9(a). The separation between fragments and their relative orientations are altered randomly so as to remove any inter fragment correlations. Such fragmented assemblies are generated for several fragmentation numbers, following which, the $sM(s)$ intensity from the fragmented assembly is computed for each case. The lattice temperature is maintained (at 300 K), so that any changes evident in the $sM(s)$ intensities arise solely from the fragmentation process. The W parameter extracted from these 'simulated' $sM(s)$ is shown in Fig. 6.9(c), and remarkably, exhibits the same anisotropy trend seen in the experimentally determined W [inset to Fig. 6.8]. A qualitative agreement between the scale of anisotropy seen in experiment and simulation is reached when the number of fragments exceed 100, corresponding to an individual fragment size of ≈ 2 nm, which is close to the average fragment sizes observed in the SEM image [Fig. 6.6]. Furthermore, from Fig. 6.9(b, d), the (111) & (220) peaks in both experiment and simulation show similar features such as the dramatic drop in intensity and appearance of new bifurcations in the peaks. These results indicate that the anisotropy seen in W is indeed a signature of pre-fragmentation dynamics within the NC. A similar Debye-Waller anisotropy has been observed in the non-thermal melting of InSb and calculations show that the time scale and the fluence dependence of the observed dynamics from InSb are consistent with a carrier induced disordering process. However, the calculations do not reproduce the experimentally observed anisotropy [230]. Our simulation here suggests that such anisotropy in diffraction might be a universal representation of a prefragmented state consisting of domains or nucleation pockets that destroy the long range correlation along certain preferred directions. This W-anisotropy in conjunction with the reduced temperatures of the NC

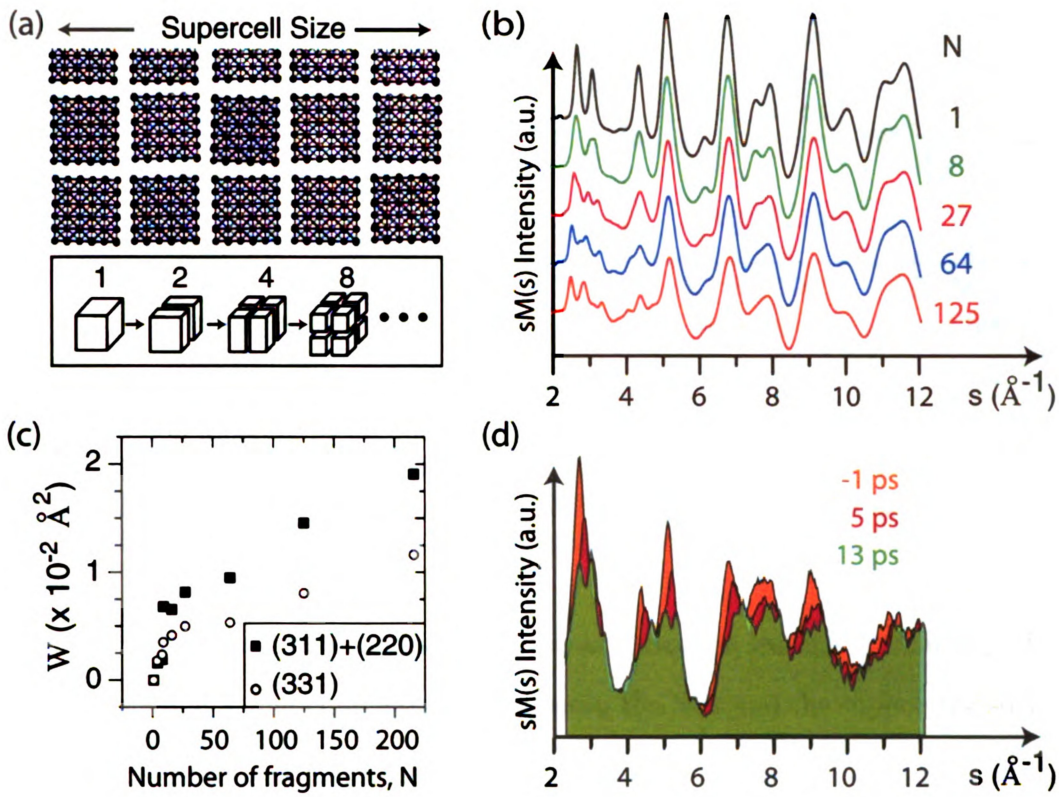

Figure 6.9: Simulation of Ag NC fragmentation and associated signatures in diffraction pattern. (a) Planar slice along the center of a Ag $15 \times 15 \times 15$ supercell, that is progressively subdivided into smaller pieces. The individual fragments are displaced from each other and oriented randomly to remove any correlation between the fragments. (b) W parameter estimated from the computed $sM(s)$ from these fragmented NC. (c) Computed $sM(s)$ from these fragmented NCs for select fragmentation degree, showing the similar dramatic drop in (111) & (220) peaks as observed in the UEC data shown in (d).

indicate that the pre-fragmentation dynamics in silver NCs can be better described by a nonthermal restructuring rather than thermal disorder.

6.3.2 Role of Charges in Fragmentation

Thus far, we have focussed on the diffraction signatures from the pre-fragmented state of Ag NC. However, it is known that charges can play a significant role in photophysics of nanoparticles and in ultrafast processes near interfaces, as evidenced in the case of graphite. To find out the role of charges and Coulombic forces in the

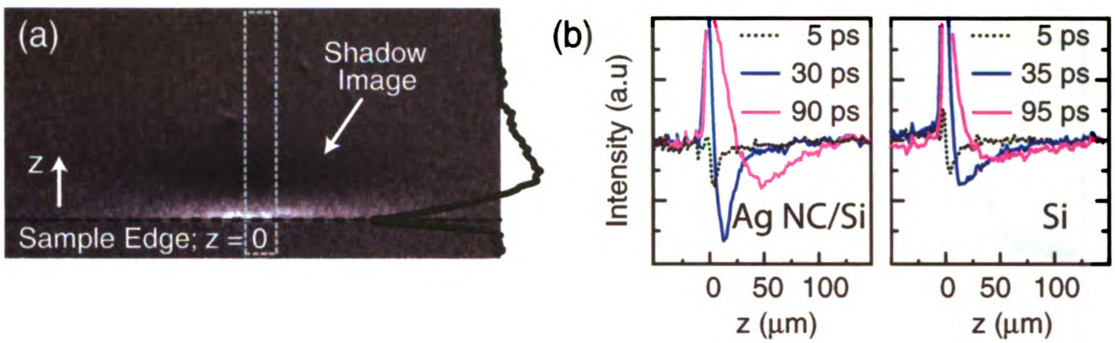

Figure 6.10: Determining photoemission (PE) yield from Ag NC sample using the point-projection imaging technique described in section 4.7.1. (a) Normalized shadow images of the PE cloud. The cloud profile is shown on the right. (b) Evolution of PE cloud profiles along z direction normal to Si-111 surface both with and without the Ag NCs. Significant enhancement of PE is seen in presence of Ag NCs.

fragmentation process, we examine two relevant processes leading to charging of the NCs: photoemission and charge transfer between the NCs and the supporting surface.

To determine the photoemission yield, we use the projection imaging method [231] as outlined earlier in section 4.7.1 to determine the fraction of charges ejected from the NCs. By analyzing the normalized shadow images of the electron cloud generated over the Ag NC sample, we extracted the density of photoemitted electrons to be 7.9×10^7 e/cm^2. This number is nearly double the value obtained from a bare Si-111 surface, as evident from Fig. 6.10(c). Such enhancement in photoemission is significant considering the NCs occupy less than 1% of the surface. Similar photoemission enhancement from Ag NCs has been observed in other studies as well and attributed to SPR assisted multiphoton processes [98].

The second source of NC charging - a charge transfer between the NC and the substrate is monitored via the strong (001) diffraction peak at $s = 2.75\text{Å}^{-1}$ arising from the ordered SAM layer underneath the Ag NC as illustrated in Fig. 6.11(a). Any interfacial charge transfer between the Ag NC and the substrate leads to the creation of a transient field at the Ag NC/SAM/Si interface, causing a Coulomb refraction shift of probing electron beam traversing the region in between. However, the Bragg

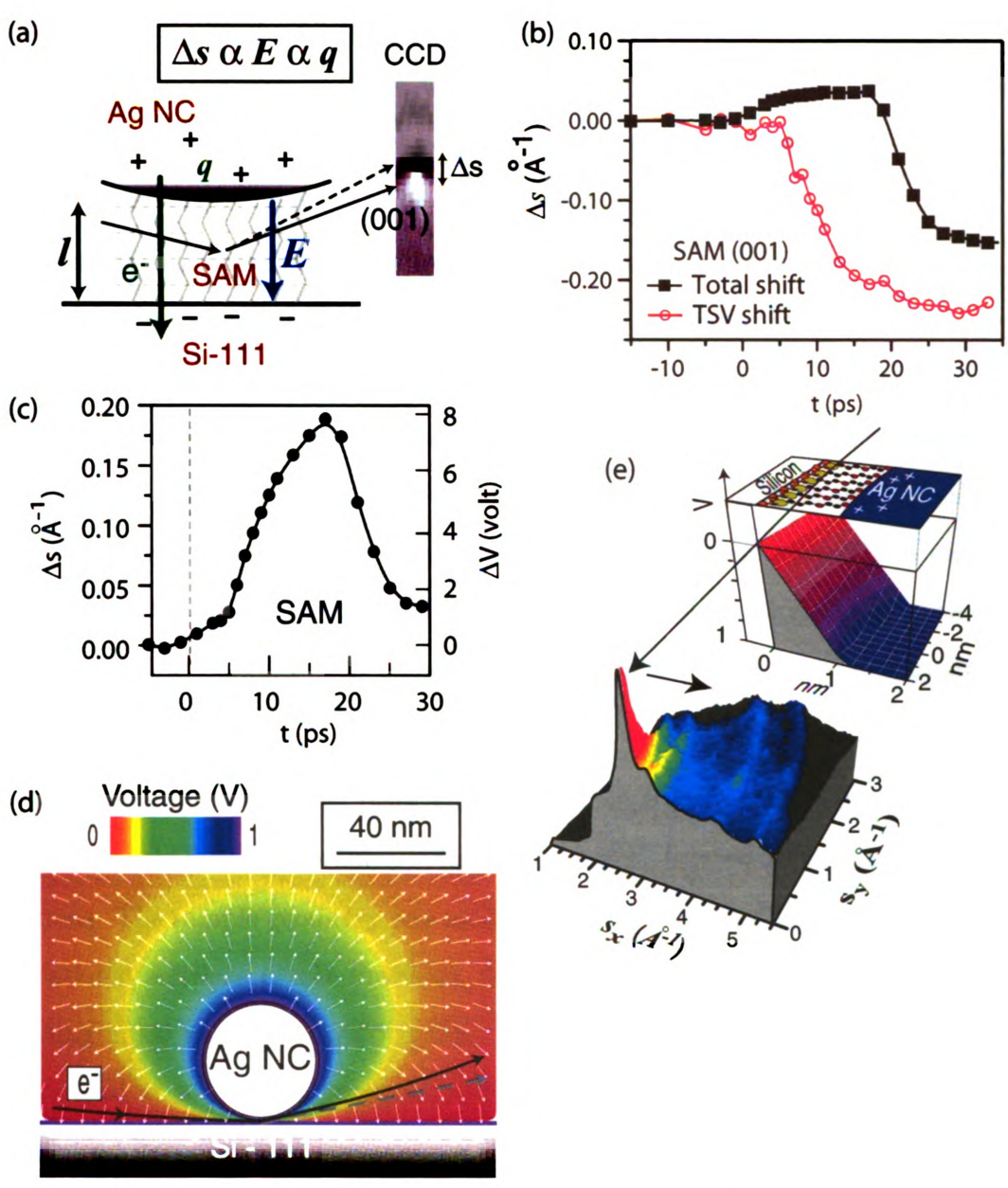

Figure 6.11: Monitoring NC charging dynamics through SAM (001) peak shift. (a) Refraction shift of SAM (001) peak due to interfacial charge transfer. (b) Total shift of the SAM (001) peak along with the TSV-induced shift deduced from Fourier phasing algorithm. Difference between the two yields the contribution to the interfacial field from the SAM layer alone. (c) The shift of the SAM peak correlated to the degree of NC charging, based on the calculations in (d, e). (d) Finite element simulations of the field generated by the NC charged to unit positive voltage. The SAM layer ≈ 1 nm is too small to be seen on this scale. (e) 2D surface plot of the interfacial voltage, and its effect on the SAM peak. Note the intensity of the SAM peak relative to the Debye-Scherrer rings from Ag.

scattered electron is also affected by the TSV induced shift that is generally present everywhere near the surface. Thus, we subtract the TSV induced shift (TSV is known from the Fourier phasing correction of the diffraction patterns) to isolate the refraction shift of the SAM (001) peak purely due to NC charging, shown in Fig. 6.11(b). The peak exhibits a positive shift away from the shadow edge, indicative of the creation of positive charges within the NC. Interestingly, the NC charging occurs through a two-step process with a short fs rise, followed by a delayed ps rise with larger amplitude. Such delayed charging is not observed in the case of Au NPs on a similar interface (See pp. 139, Fig. 6.12 in [156]) leading to the speculation that these charging dynamics are intimately linked to the SPR excitation, which in the case of Au NPs is centered closer to $\approx$ 500 nm [232]. This SPR enhanced localized charge transfer between NCs and the substrate leads to a pronounced charging of the NCs, as will be quantified soon.

To correlate this observed peak shift with NC charging, we numerically compute the electric field distribution surrounding a charged NC using finite difference field calculations. The sample geometry was modeled using the Static Field Analysis Toolkit Educational software (*Field Precision*, SATE) with a variable-size conformal mesh spanning 1,000 nm with 12,000 nodes. The 40 nm NC was treated as a metallic sphere held at a constant potential with the silicon surface grounded. The citrate passivating ligand around the nanoparticle and the SAM layer on silicon were each taken to be 1 nm long with dielectric constant of 2.5. By ray-tracing electron trajectories through the electric field solution thus obtained, we estimated a refraction shift of 0.0234 Å^{-1} to be introduced in the SAM peak per 1 V rise in NC voltage. Furthermore, numerical integration of the field energy density yielded an interfacial capacitance of C=7.5 attoFarad. Based on these results and the maximum observed s-shift of the (001) peak, we determined a maximum charging per NC of $q \approx 400$ e^+, which is significantly higher than the 0.2 e^+ estimated from the vacuum emission

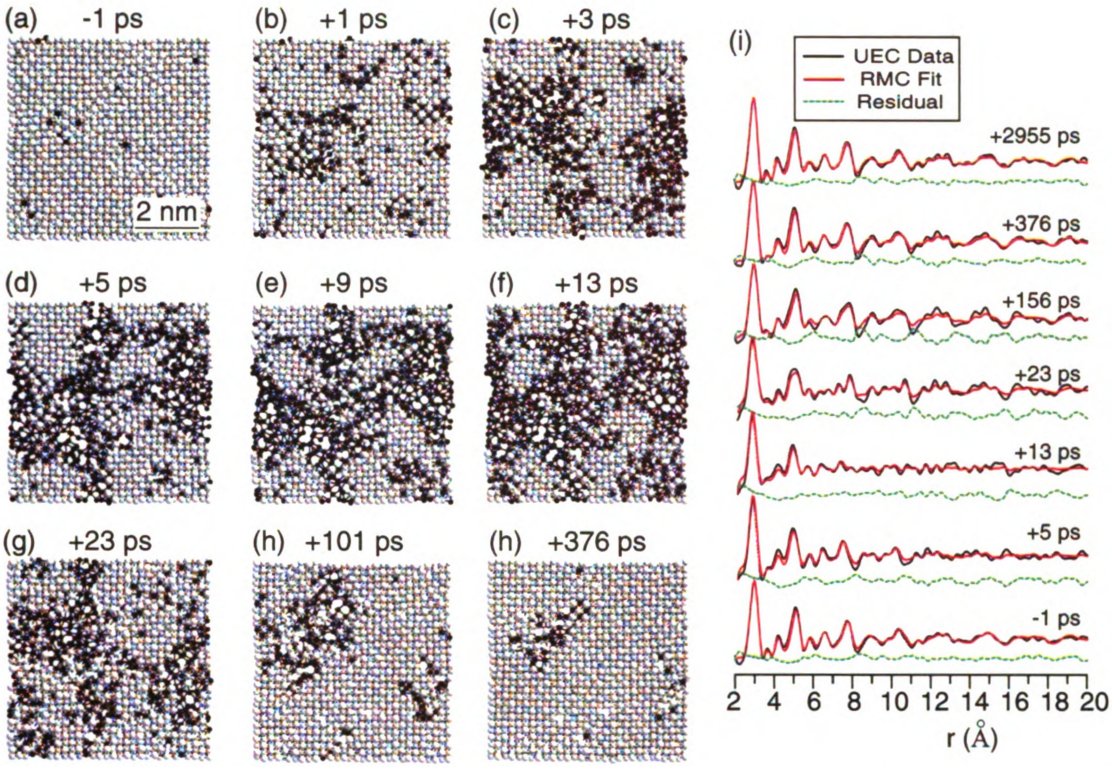

Figure 6.12: (a-h) Prefragmentation states of Ag NC at select times, determined using the PRMC structure refinement scheme described in the text. Growth of local disorder is apparent from the increase in number of undercoordinated atoms (black) (i) Final G(r) fits obtained after PRMC convergence.

measurement.

Multiply charged NCs are known to be unstable and prone to Coulomb explosion when the disruptive Coulomb force exceeds the attractive cohesive force between the atoms. This instability is parametrized within the liquid drop model by a 'fissility ratio' X defined as $X = q^2/n$, where q is the amount of charge and n is the number of atoms within the NC. Muto & co-workers [233] have determined the fissility regime required for Coulomb explosion of NCs to be within $0.3 < X < 1$. Based on our estimates of charges within the 40 nm NC, we determine a Coulomb fissility ratio of $X \approx 0.08 < 0.3$, with $n \approx 2 \times 10^6$. Thus, it appears unlikely that fragmentation of Ag NC occurs through Coulomb explosion.

6.4 Progressive Reverse Monte-Carlo Modeling

To visualize transient atomic processes associated with electronic excitation, we employ a Reverse Monte Carlo (RMC) structure refinement scheme to construct 3D structure models of the transient pre-fragmented states of the NC based on observed diffraction signatures. RMC is an iterative procedure, that seeks to minimize the difference between the diffraction pattern computed from a theoretical structure model (also called a 'supercell') and the experimentally obtained diffraction via random moves of randomly selected atoms within the supercell. The cost-function χn for the n^{th} iteration step is calculated as

$$\chi_n^2 = \sum_s \frac{\left\{I^{Cn}(s) - I^E(s)\right\}^2}{\sigma(s)^2} \tag{6.1}$$

where I denotes diffraction intensities, C and E denote 'computational' and 'experimental' respectively. σ is a control parameter defining the confidence limits desired at convergence. If $\chi n \leq \chi_{n-1}$, then the move is definitely accepted; otherwise it is accepted with a probability $exp\left(-[\chi_n^2 - \chi_{n-1}^2]/2\right)$. This finite probability of accepting 'false' moves allows RMC to wriggle out of local minima, where it would otherwise get stuck.

Here, we specifically employ the RMC++ implementation [234, 235] of the RMC algorithm using a 15 × 15 × 15 Ag supercell. At each iteration step, we attempt to fit both $sM(s)$ as well as $G(r)$ simultaneously and the cost function is defined as a sum of the cost functions for both curves. While $sM(s)$ and $G(r)$ in principle posses identical 'information' content, they are inherently weighted differently. The dominant peak positions and intensities in the $sM(s)$ represent long range order while $G(r)$ are better suited to represent the short-range order. As a result, employing both these in the fitting routine allows tight constraints on allowed moves, preventing any

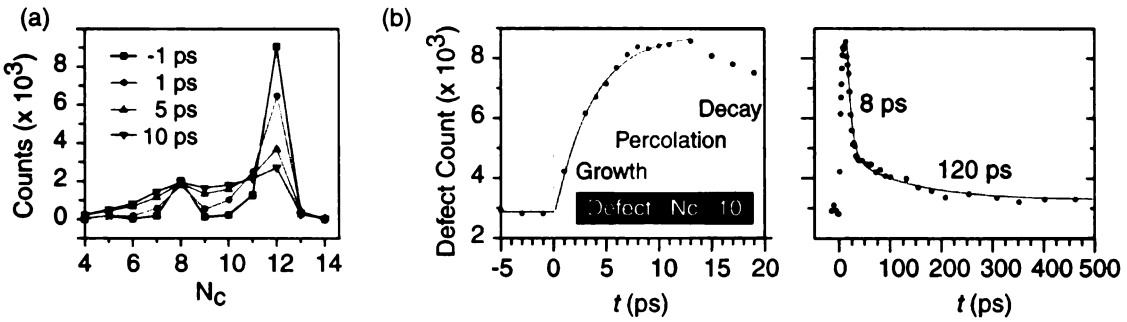

Figure 6.13: Growth and decay dynamics of defect sites in the PRMC refined supercell structure. (a) Evolution of the number of atoms with given coordination number following photoexcitation. Counts of Perfect fcc coordinated atoms ($N_C = 12$) decreases as the number of undercoordinated sites increase. (b, c) Evolution of total number of defect sites characterized by $N_C \leq 10$ showing their growth and percolation at short times, and decay at long times. Long time decay in (c) is fit to a biexponential function, with the $1/e$ timescales shown.

rapid divergence of the structure. Since RMC is a global structure solver, it is prone to yielding non-unique solutions, especially for excited states with increased disorder. Hence, an efficient implementation of RMC requires physical constraints to restrict the search space [236]. This constraint is imposed here via a progressive refinement scheme in which the RMC refined structure at time t_i serves as the starting structure for the refinement at t_{i+1}. First, we confirm that the data has sufficient signal-to-noise ratio by noting that the RMC result for ground state (t <0) retains a robust fcc structure, as shown in Fig.6.12(a). The time-intervals between frames are suitably close such that structural difference between adjacent frames are not expected to be large. Consequently,we restrict the search space by constraining the atoms to move $\leq$ 0.05 Å per atom per iteration step. This maintains the structural correlation between the frames, thereby allowing changes to be tracked progressively and reliably within a restrictive search space, without need for a global search. Convergence is typically obtained in $\leq$ 100,000 moves.

Select RMC results are depicted in Figs. 6.12 (a-h) with a planar slice cut off from the 3D supercell to expose the degradation of the pristine fcc lattice over time.

The atomic sites colored in black represent defect sites with coordination number $N_C \leq 10$, whereas the fully coordinated ones have $N_C = 12$ corresponding to the fcc structure. These defects, which are negligible in the ground state, are instantaneously seeded within the first few ps following SPR photoexcitation. They subsequently grow and percolate into strips and saturate within 10 ps. This results in the creation of fragmented nanocrystalline domains of average size $\approx$ 2 nm with a structurally ordered core surrounded by 'weak' undercoordinated periphery. This disordered state persists for nearly 15 ps before a slow recovery to fcc on a time scale of $\approx$ 100 ps. This lattice degradation is in contrast to the response of Au NCs, where PRMC refinement shows only surface melting with a structurally intact core [110].

Quantitative analysis of atomic coordination numbers from these PRMC refined structures in Fig. 6.13 show the growth and decay of undercoordinated defect sites following SPR excitation. At t = +1 ps, we see an instantaneous drop in the number of perfect 12-coordinated fcc atoms accompanied by a corresponding rise in the number of undercoordinated atoms ($N_C \leq 10$). The growth of these defect sites occurs rapidly on a timescale compatible with the 6 ps NC charging incubation period prior to charge redistribution within the Ag NCs. The slow recovery back to ground state proceeds with a biexponential rate of 8 ps and 120 ps that is commensurate with the timescale of NC discharging.

6.5 Proposed Fragmentation Pathway

Summarizing the UEC experimental observations from the pre-fragmented state of SPR excited Ag NCs:

1. Estimates of NC temperatures at $t = 0$ ps from Debye-Waller analysis is $\approx$ 450 K which is too low for thermal ablation or melting.

2. Anisotropy in diffraction intensity drop from different Bragg peaks are consis-

tent with a disordered pre-fragmented state of the NC.

3. The NC charging due to near surface charge transfer to the substrate is initially inhibited for nearly 6 ps, following which, the NC charges upto $\approx 400\ e^+$ within 10 ps.

4. Progressive Reverse Monte-Carlo refinement shows the fragmentation to be seeded by the creation of undercoordinated defect sites within 1 ps, followed by growth and percolation on the 10 ps timescale leading to the creation of nanocrystalline domains surrounded by weak undercoordinated boundaries.

5. The dynamics of defect growth and relaxation agree well with that of NC charging and discharging.

These observations are consistent with a progressive Coulomb-induced fragmentation scenario proposed by Kamat and co-workers [99]. They proposed, based on optical investigations of Ag NCs in a laser flash photolysis setup, that SPR photoexcitation led to the generation of charges within Ag NCs over ps timescales leading to eventual fragmentation. Here, we observe similar timescales for the creation of the pre-fragmented state. The initial 6 ps incubation period for charging represents the timescale for charge redistribution at NC interface which is absent at non-SPR excitations [110]. It is thus indicative of transient trapping of hot electrons at the excitation sites.

Earlier studies of fs laser induced melting in metals using optical and photoemission techniques have revealed that interband transitions [106] and thermionic emission [237] can both lead to rapid bond softening within the initial non-equilibrium time scales of core hole lifetime ($\approx$ 100 fs) and electron-phonon coupling time ($\approx$ 1 ps) [238]. In Ag, the nonlinear interband excitation involving inner valence shell ($d \rightarrow sp$) is found to be strongly coupled to the SPR dephasing pathway [97]. These excitations

can provide seeds for valence destabilization through SPR. Such a process would be inhomogeneous in nature and proceed on a phonon timescale.

The migration of charges to the interface and the accompanied rise of interfacial field seen by the electron beam is hindered as the lattice is undergoing atomic restructuring during this incubation period, which also coincides with the period of W - anisotropy (Fig. 6.8). The observed correlation between the atomic process and charge trapping suggests that local valence instabilities which cause bond softening [50] lead to structural defects and charge localization as seen in our studies.

In summary, an electronically driven, progressive fragmentation of Ag NCs is presented. We suggest that the fragmentation process is triggered by the creation of local valence instabilities, caused by redistribution of local charge density, facilitated in Ag through the strong nonlinear coupling between SPR and interband transition. When sufficient valence instabilities are instigated at a high fluence ($F \geq 17\,\mathrm{mJ/cm^2}$), the electronic states are strongly perturbed, leading to a prolonged ps lifetime of the local charge redistribution associated with valence excitation due to an insufficient dynamical screening. Such a dynamical localization feature is central to the creation and growth of the topological defects, which can persist on the phonon timescales, and could be common in nonequilibrium photoinduced structural phase transition.

Chapter 7

Conclusion

The results presented here have demonstrated the development of an ultrafast electron crystallography (UEC) system specifically aimed at studying photoinduced structural changes in nanostructures and interfaces. Robust data extraction formalisms have been developed allowing quantitative investigations of nanostructures as small as 2 nm [110, 126]. Building up on the earlier work of ultrafast diffractive voltametry [156] that is sensitive to photoinduced surface charges, a Fourier phasing algorithm is developed to correct for Coulomb refraction shifts in UEC data to reveal the underlying structural dynamics. This also yields in the process a measure of the transient surface voltage generated by the optical excitation. UEC data is combined with a progressive reverse Monte-Carlo (PRMC) scheme to enable 3D structure refinement and visualization of average atomic dynamics within an ensemble of nanostructures. Finally, on going efforts to build optical experimental capabilities to complement data acquired from the UEC system is also detailed.

Using this approach, electronically induced structure transformations have been studied in graphite (HOPG) [153] and silver nanocrystals (Ag NC) [239] by extracting from the UEC data, transient thermal, structural and charge dynamics in the non-equilibrium regime. Following near-IR p-polarized photoexcitation in graphite, a new

inter-layer distance at $\sim$ 2 Å is observed along with a reduction in the c-axis lattice constant revealing the creation of transient $sp^2 - sp^3$ hybrid structures. This transformation is observed to be driven by an inter-layer Coulomb stress generated from the creation of hitherto undetected surface dipole field, whose observation has been made possible here by the Coulomb refraction effect on the probing electrons. Vacuum emission of charges from the photoexcited graphite surface is shown to play only a minor role and hence, the refraction effects on the electron probe arise predominantly from the sub-surface charge redistribution [231]. This result strengthens the previous reports of effecting a graphite-diamond transition through electronic destabilization of the graphite lattice [1, 2, 77]. However this optically induced transformation is not long-lasting and the hybrid structure reverts back to the ground state sp^2 configuration on the $\sim$ 100 ps time scale - a structural reversal seen in another pressure induced equilibrium study as well [70]. The structural dynamics of Ag NC excited at their surface plasmon resonance (SPR) just below the SPR induced fragmentation limit are also studied, enabled by a judicious choice of sample geometry involving surface supported NCs. The anisotropic response from different diffraction maxima are shown to be consistent with a lattice fragmentation picture and the PRMC data refinement scheme reveals the pre-fragmented state of Ag NC to be seeded by the inhomogeneous creation of undercoordinated defect sites. The growth and percolation of these defect sites correlate with a slightly delayed interfacial charging dynamics indicating transient trapping of photogenerated hot electrons at the excitation sites. The creation of sufficient such defect sites at elevated excitation fluences provide the lattice with an incentive to fragment.

The underlying feature in these processes is that they are driven by electron redistribution effects arising from photogenerated hot electron populations in the system while the lattice remains relatively cold, below the melting threshold. While optical probes reveal the initial electronic excitations to proceed on the $\sim$ 100 fs

timescale, the electron redistribution occurs over longer time scales of a few ps. In both silver and graphite, this electron redistribution correlates well with the lattice restructuring dynamics, but is found to be uncorrelated in the case of photomelting of gold nanoparticles [110]. Such electronically induced processes can be identified with a larger class of photoinduced phase transitions (PIPT) [14]. It is also heartening to note that the UEC results on graphite have been replicated in other independent studies as well. Carbone *et al.* also observed the photoinduced contraction of the graphite layers in a similar UEC study [144] while Tanimura and co-workers observed the creation of isolated sp^3 nanodomains from STM investigations of photoexcited graphite surface [82]. Employing theoretical efforts to understand the process based on total energy minimization calculations, Nasu and co-workers have proposed the creation of an interlayer CT excitons that self-localize and deform the local graphite lattice leading to buckling of the 6-membered carbon ring [203] and predicted the existence of a hybrid structure termed 'Diaphite' [82]. Similar charge-trapping as proposed by Nasu in the form of a CT exciton and evidenced in the UEC study of both graphite and silver indicate the possible universality of such charge redistribution processes in electronically induced structure changes.

Looking towards the future, the creation of transient diamond-like structures in this study and the diamond-like nanodomains generated in other studies leads to the obvious question - how can permanent transformation into diamond be achieved through optical means? This is likely to form the object of future research efforts in this direction, requiring controlled exploration of novel photoexcitation schemes employing multiple shaped pulses with tunable frequencies (energy) to guide graphite and the transient intermediary structures toward the final desired structure, say diamond. Such studies would also require the excitation to be coupled to *in situ* structure probes such as UEC and UEM systems to monitor the transient species in real time. Electron spectroscopic techniques, particularly EELS would also serve

as a sensitive probe of the bond re-structuring dynamics, particularly in the graphite-diamond transition. Similarly, in the case of nanostructures, while the study reported here utilizes nearly monodisperse NCs, the effect of surface morphology of individual NC is not considered. To this effect, there is a need for an ultrafast nanoscale probe with sufficient brightness to allow investigations of non-equilibrium processes in single nanostructures. Since the electrons in such probes will be strongly confined spatially, the development would have to be coupled with electron pulse compression schemes designed to overcome the detrimental effects of the resulting space-charge effects. The transmission electron microscope offers a natural template from which to springboard the further development of UEC and UED systems as it allows the confluence of electron diffraction, spectroscopy and imaging in one system, providing a versatile probe of ultrafast processes on the nanoscale. The need for such systems has already been acknowledged, as evident from the furious pace of development of UEM at Caltech [25, 114, 160, 240–242] operating in the single-electron mode, the conception and on-going efforts to build the high-brightness ultrafast electron microscope *Spartan-1* here at MSU utilizing radio-frequency pulse compression scheme, and the development of DTEM at Lawrence Livermore National Lab [115, 243, 244]. As these systems mature, they will provide the diverse probing schemes to allow the exploration of non-equilibrium processes involving the interplay of charges and lattice from the inception on the fs time scale to eventual fruition on the ps - ns time scales.

Appendix A

Graphite Structure Factor

The graphite lattice can be mathematically represented by a hexagonal unit cell defined by the lattice repeat vectors $(\mathbf{a}, \mathbf{b}, \mathbf{c})$ with each unit cell comprised of 4 basis atoms located at $(\mathbf{u_1}, \mathbf{u_2}, \mathbf{u_3}, \mathbf{u_4})$ as shown in Fig. A.1. To calculate the structure factor $F(hkl)$ from this graphite lattice, we need to evaluate the sum $\sum exp\,(i\,\mathbf{K}\cdot\mathbf{u_i})$ over all 4 basis atoms.

Combining Fig. A.1(b) with some elementary algebra, we can deduce the lattice and basis vectors defining the graphite structure as:

$$
\begin{aligned}
a &= \sqrt{3}\, d_{C-C} \\
\mathbf{a} &= a\left(\frac{\sqrt{3}}{2},\ \frac{1}{2}\right) \\
\mathbf{b} &= a\left(\frac{\sqrt{3}}{2},\ -\frac{1}{2}\right) \\
\mathbf{c} &= (0, 0, c)
\end{aligned}
\qquad \text{and} \qquad
\begin{aligned}
\mathbf{u_1} &= -\frac{\mathbf{a}+\mathbf{b}}{3} \\
\mathbf{u_2} &= 0 \\
\mathbf{u_3} &= \frac{\mathbf{c}}{2} \\
\mathbf{u_4} &= \frac{\mathbf{a}+\mathbf{b}}{3} + \frac{\mathbf{c}}{2}
\end{aligned}
$$

Correspondingly, let the reciprocal lattice vectors be denoted by ($\mathbf{a}^*$, $\mathbf{b}^*$, $\mathbf{c}^*$), that by definition, satisfy the usual reciprocal relation i.e. $\mathbf{v}\cdot\mathbf{v}^* = 2\pi\delta_{ij}$, where $\mathbf{v}$=$\mathbf{a}$, $\mathbf{b}$, $\mathbf{c}$. Now, if $\mathbf{K} = h\mathbf{a}^* + k\mathbf{b}* + l\mathbf{c}*$ represents any arbitrary family of lattice planes,

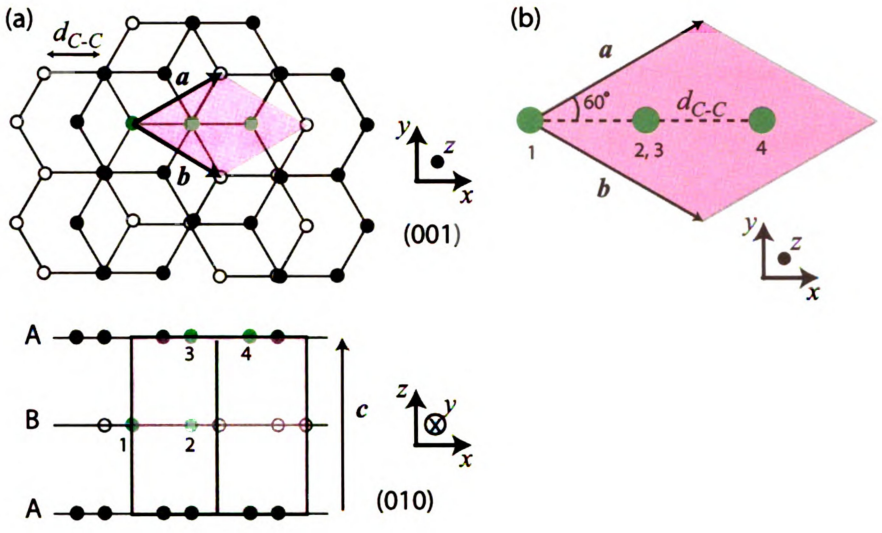

Figure A.1: Graphite Unit Cell. (a) Views along the 001 (top) and 010 (bottom) to help visualize the 3D structure of graphite, showing the $ABAB\ldots$ stacking of the individual graphene layers. The shaded pink region represents the unit cell and the green atoms labeled 1-4 are the basis atoms comprising one unit cell. (b) Magnified view of the unit-cell and the constituent basis atoms.

then by employing the above stated orthogonality we calculate the structure factor of the Bragg peaks associated with the hkl family of planes as

$$\begin{aligned} F(hkl) &= \sum_{i=1}^{4} exp(i\mathbf{K}\cdot\mathbf{u_i}) \\ &= 1 + e^{i\pi l} + e^{i2\pi\left(-\frac{h+k}{3}\right)} + e^{i2\pi\left(\frac{h+k}{3}+\frac{l}{2}\right)} \end{aligned}$$

Using this expression of $F(hkl)$ we can deduce those Bragg reflections that are kinematically forbidden.

Case 1 - (0,0) rod: Using $h = k = 0$ in the above expression for $F(hkl)$, we obtain

$$\begin{aligned} F(00l) &= 1 + e^{i\pi l} + 1 + e^{i\pi l} \\ &= 2\left(1 + e^{i\pi l}\right) = \begin{cases} 0 & \text{if } l \text{ is odd} \\ 4 & \text{if } l \text{ is even} \end{cases} \end{aligned}$$

Thus, odd order Bragg reflections on the (0,0) rod such as (001), (003), (005) and so on are *forbidden* and do not appear in the diffraction pattern. Even though the Bravais lattice allows for a Bragg maxima along these directions, the internal symmetry within the unit cell is such that the electron waves scattered from the 4 basis atoms all interfere destructively along these odd order $(00l)$ directions, thus precluding the possibility of a Bragg maxima.

Case 2 - (1,0) rod: Using $h = 1$, $k = 0$ in the above expression for S_{hkl}, we obtain

$$\begin{aligned} F(10l) &= 1 + e^{i\pi l} + e^{-i\frac{2\pi}{3}} + e^{i\frac{2\pi}{3}}\ e^{i\pi l} \\ &= \begin{cases} -\sqrt{3}\,i & \text{if } l \text{ is odd} \\ 0 & \text{if } l \text{ is even} \end{cases} \end{aligned}$$

Thus, along the (10), and by symmetry, $\bar{1}0$ rods, the even order Bragg reflections shall vanish. Furthermore, the intensity of the even order maxima along these rods that are visible is diminished from those along the (00) rod by a factor of 3/16 (since intensity is proportional to $|F(hkl)|^2$)

We can extend this calculation further to show that on the (11) rod, once again, the odd order maxima shall vanish. These results explain the ground state diffraction pattern obtained from graphite.

Case 3 - (1,1) rod: Using $h = 1$, $k = 1$ in the expression for S_{hkl}, we obtain

$$\begin{aligned} F(11l) &= 1 + e^{i\pi l} + e^{-i\frac{4\pi}{3}} + e^{i\frac{4\pi}{3}}\ e^{i\pi l} \\ &= 1 + e^{i\pi l} + e^{i\frac{2\pi}{3}} + e^{-i\frac{2\pi}{3}}\ e^{i\pi l} \\ &= \begin{cases} \sqrt{3}\,i & \text{if } l \text{ is odd} \\ 3 & \text{if } l \text{ is even} \end{cases} \end{aligned}$$

Note that even though the odd reflections on the (11) rod are not prohibited,

they are relatively weak. This, combined with the reduced scattering cross section at larger scattering angles renders these peaks extremely weak and difficult to observe experimentally.

References

[1] H. Nakayama and H. Katayama-Yoshida. Direct conversion of graphite into diamond through electronic excited states. *J. Phys: Condens. Matter*, 15(24):R1077–R1091, 2003.

[2] T. Meguro, A. Hida, M. Suzuki, Y. Koguchi, H. Takai, Y. Yamamoto, K. Maeda, and Y. Aoyagi. Creation of nanodiamonds by single impacts of highly charged ions upon graphite. *Appl. Phys. Lett.*, 79(23):3866–3868, 2001.

[3] I. B. Khaibullin, E. I. Shtyrkov, M. M. Zaripov, R. M. Bayazitov, and M. F. Galjautdinov. Some features of laser annealing of implanted silicon layers. *Radiat. Eff.*, 36(3):225–233, 1978.

[4] R. T. Young, C. W. White, G. J. Clark, J. Narayan, W. H. Christie, M. Murakami, P. W. King, and S. D. Kramer. Laser annealing of boron-implanted silicon. *Appl. Phys. Lett.*, 32(3):139–141, 1978.

[5] C. W. White, W. H. Christie, B. R. Appleton, S. R. Wilson, P. P. Pronko, and C. W. Magee. Redistribution of dopants in ion-implanted silicon by pulsed-laser annealing. *Appl. Phys. Lett.*, 33(7):662–664, 1978.

[6] J. C. Wang, R. F. Wood, and P. P. Pronko. Theoretical analysis of thermal and mass transport in ion-implanted laser-annealed silicon. *Appl. Phys. Lett.*, 33(5):455–458, 1978.

[7] P. Baeri, S. U. Campisano, G. Foti, and E. Rimini. A melting model for pulsing-laser annealing of implanted semiconductors. *J. Appl. Phys.*, 50(2):788–797, 1979.

[8] J. A. Van Vechten, R. Tsu, F. W. Saris, and D. Hoonhout. Reasons to believe pulsed laser annealing of Si does not involve simple thermal melting. *Phys. Lett. A*, 74(6):417 - 421, 1979.

[9] J. A. Van Vechten, R. Tsu, and F. W. Saris. Nonthermal pulsed laser annealing of si; plasma annealing. *Phys. Lett. A*, 74(6):422 - 426, 1979.

[10] D. von der Linde. *Resonances - A volume in honor of the 70th birthday of Nicolaas Bloembergen.* World Scientific, Singapore, 1990.

[11] S. K. Sundaram and E. Mazur. Inducing and probing non-thermal transitions in semiconductors using femtosecond laser pulses. *Nat. Mater.*, 1(4):217–224, 2002.

[12] J. Solis, C. N. Afonso, S. C. W. Hyde, N. P. Barry, and P. M. W. French. Existence of electronic excitation enhanced crystallization in GeSb amorphous thin films upon ultrashort laser pulse irradiation. *Phys. Rev. Lett.*, 76(14):2519–2522, 1996.

[13] K. Sokolowski-Tinten, J. Solis, J. Bialkowski, J. Siegel, C. N. Afonso, and D. von der Linde. Dynamics of ultrafast phase changes in amorphous GeSb films. *Phys. Rev. Lett.*, 81(17):3679–3682, 1998.

[14] K. Nasu. *Photoinduced Phase Transitions.* World Scientific, Hackensack, 2004.

[15] S. Iwai, S. Tanaka, K. Fujinuma, H. Kishida, H. Okamoto, and Y. Tokura. Ultrafast optical switching from an ionic to a neutral state in tetrathiafulvalene-p-chloranil (TTF-CA) observed in femtosecond reflection spectroscopy. *Phys. Rev. Lett.*, 88(5):057402, 2002.

[16] E. Collet, M. Lemee-Cailleau, M. Buron-Le Cointe, H. Cailleau, M. Wulff, T. Luty, S.-Y. Koshihara, M. Meyer, L. Toupet, P. Rabiller, and S. Techert. Laser-induced ferroelectric structural order in an organic charge-transfer crystal. *Science*, 300:612–615, 2003.

[17] A. Cavalleri, Th. Dekorsy, H. H. W. Chong, J. C. Kieffer, and R. W. Schoenlein. Evidence for a structurally-driven insulator-to-metal transition in VO_2 : A view from the ultrafast timescale. *Phys. Rev. B*, 70(16):161102, 2004.

[18] P. Baum, D.-S. Yang, and A. H. Zewail. 4D visualization of transitional structures in phase transformations by electron diffraction. *Science*, 318:788–792, 2007.

[19] M. Fiebig, K. Miyano, Y. Tomioka, and Y. Tokura. Sub-picosecond photo-induced melting of a charge-ordered state in a perovskite manganite. *Appl. Phys. B*, 71:211–215, 2000.

[20] F. Schmitt, P. S. Kirchmann, U. Bovensiepen, R. G. Moore, L. Rettig, M. Krenz, J.-H. Chu, N. Ru, L. Perfetti, D. H. Lu, M. Wolf, I. R. Fisher, and Z.-X. Shen. Transient electronic structure and melting of a charge density wave in $TbTe_3$. *Science*, 321(5896):1649–1652, 2008.

[21] N. Gedik, D.-S. Yang, G. Logvenov, I. Bozovic, and A. H. Zewail. Nonequilibrium phase transitions in cuprates observed by ultrafast electron crystallography. *Science*, 316:425–429, 2007.

[22] N. Bloembergen. From nanosecond to femtosecond science. *Rev. Mod. Phys.*, 71:S283–S287, 1999.

[23] A. Damascelli. Probing the electronic structure of complex systems by ARPES. *Physica Scripta*, T109:61–74, 2004.

[24] R. F. Egerton. Electron energy-loss spectroscopy in the TEM. *Reports on Progress in Physics*, 72(1):016502, 2009.

[25] F. Carbone, B. Barwick, O.-H. Kwon, H. S. Park, J. S. Baskin, and A. H. Zewail. EELS femtosecond resolved in 4D ultrafast electron microscopy. *Chem. Phys. Lett.*, 468(4-6):107 - 111, 2009.

[26] Y. R. Shen. *The Principles Of Non-Linear Optics.* John Wiley & Sons, Hoboken, NJ, 2003.

[27] M. Bargheer, N. Zhavoronkov, M. Woerner, and T. Elsaesser. Recent progress in ultrafast x-ray diffraction. *ChemPhysChem*, 7(4):783–792, 2006.

[28] A. H. Zewail. 4D ultrafast electron diffraction, crystallography, and microscopy. *Annu. Rev. Phys. Chem.*, 57(1):65–103, 2006.

[29] C. V. Shank, R. Yen, and C. Hirlimann. Time-resolved reflectivity measurements of femtosecond-optical-pulse-induced phase transitions in silicon. *Phys. Rev. Lett.*, 50(6):454–457, 1983.

[30] C. V. Shank, R. Yen, and C. Hirlimann. Femtosecond-time-resolved surface structural dynamics of optically excited silicon. *Phys. Rev. Lett.*, 51(10):900–902, 1983.

[31] H. W. K. Tom, G. D. Aumiller, and C. H. Brito-Cruz. Time-resolved study of laser-induced disorder of Si surfaces. *Phys. Rev. Lett.*, 60(14):1438–1441, 1988.

[32] P. Saeta, J.-K. Wang, Y. Siegal, N. Bloembergen, and E. Mazur. Ultrafast electronic disordering during femtosecond laser melting of GaAs. *Phys. Rev. Lett.*, 67(8):1023–1026, 1991.

[33] K. Ishioka, M. Hase, M. Kitajima, L. Wirtz, A. Rubio, and H. Petek. Ultrafast electron-phonon decoupling in graphite. *Phys. Rev. B*, 77(12):121402, 2008.

[34] K. Sokolowski-Tinten, C. Blome, J. Blums, A. Cavalleri, C. Dietrich, A. Tarasevitch, I. Uschmann, E. Forster, M. Kammler, M. Horn von Hoegen, and D. von der Linde. Femtosecond x-ray measurement of coherent lattice vibrations near the lindemann stability limit. *Nature*, 422:287–289, 2003.

[35] E. N. Glezer, Y. Siegal, L. Huang, and E. Mazur. Laser-induced band-gap collapse in GaAs. *Phys. Rev. B*, 51(11):6959–6970, 1995.

[36] E. N. Glezer, Y. Siegal, L. Huang, and E. Mazur. Behavior of $\chi^{(2)}$ during a laser-induced phase transition in GaAs. *Phys. Rev. B*, 51(15):9589–9596, 1995.

[37] Y. Siegal, E. N. Glezer, and E. Mazur. Dielectric constant of GaAs during a subpicosecond laser-induced phase transition. *Phys. Rev. B*, 49(23):16403–16406, 1994.

[38] L. Huang, J. P. Callan, E. N. Glezer, and E. Mazur. GaAs under intense ultrafast excitation: Response of the dielectric function. *Phys. Rev. Lett.*, 80(1):185–188, 1998.

[39] K. Sokolowski-Tinten, J. Bialkowski, and D. von der Linde. Ultrafast laser-induced order-disorder transitions in semiconductors. *Phys. Rev. B*, 51(20):14186–14198, 1995.

[40] I. L. Shumay and U. Höfer. Phase transformations of an InSb surface induced by strong femtosecond laser pulses. *Phys. Rev. B*, 53(23):15878–15884, 1996.

[41] S. V. Govorkov, Th. Schro¨der, I. L. Shumay, and P. Heist. Transient gratings and second-harmonic probing of the phase transformation of a GaAs surface under femtosecond laser irradiation. *Phys. Rev. B*, 46(11):6864–6868, 1992.

[42] K. Sokolowski-Tinten, J. Bialkowski, M. Boing, A. Cavalleri, and D. von der Linde. Thermal and nonthermal melting of gallium arsenide after femtosecond laser excitation. *Phys. Rev. B*, 58(18):R11805–R11808, 1998.

[43] A. Rousse, C. Rischel, and J.-C. Gauthier. Femtosecond x-ray crystallography. *Rev. Mod. Phys.*, 73(1):17–31, 2001.

[44] C. Rischel, A. Rousse, I. Uschmann, P.-A. Albouy, J.-P. Geindre, P. Audebert, J.-C. Gauthier, E. Froster, J.-L. Martin, and A. Antonetti. Femtosecond time-resolved x-ray diffraction from laser-heated organic filmsnature. *Nature*, 390:490–492, 1997.

[45] C. W. Siders, A. Cavalleri, K. Sokolowski-Tinten, Cs. Tóth, T. Guo, M. Kammler, M. Horn von Hoegen, K. R. Wilson, D. von der Linde, and C. P. J. Barty. Detection of nonthermal melting by ultrafast x-ray diffraction. *Science*, 286(5443):1340–1342, 1999.

[46] C. Rose-Petruck, R. Jimenez, T. Guo, A. Cavalleri, C. W. Siders, F. Rksi, J. A. Squier, B. C. Walker, K. R. Wilson, and C. P. J. Barty. Picosecond-milliangstrom lattice dynamics measured by ultrafast x-ray diffraction. *Nature*, 398:310–312, 1999.

[47] J. Larsson, P. A. Heimann, A. M. Lindenberg, P. J. Schuck, P. H. Bucksbaum, R. W. Lee, H. A. Padmore, J. S. Wark, and R. W. Falcone. Ultrafast structural changes measured by time-resolved x-ray diffraction. *Appl. Phys. A*, 66:587–591, 1998.

[48] A. Rousse, C. Rischel, S. Fourmaux, I. Uschmann, S. Sebban, G. Grillon, Ph. Balcou, E. Forster, J.P. Geindre, P. Audebert, J.C. Gauthier, and D. Hulin. Non-thermal melting in semiconductors measured at femtosecond resolution. *Nature*, 410:65–68, 2001.

[49] A. M. Lindenberg, J. Larsson, K. Sokolowski-Tinten, K. J. Gaffney, C. Blome, O. Synnergren, J. Sheppard, C. Caleman, A. G. MacPhee, D. Weinstein, D. P. Lowney, T. K. Allison, T. Matthews, R. W. Falcone, A. L. Cavalieri, D. M. Fritz, S. H. Lee, P. H. Bucksbaum, D. A. Reis, J. Rudati, P. H. Fuoss, C. C. Kao, D. P. Siddons, R. Pahl, J. Als-Nielsen, S. Duesterer, R. Ischebeck, H. Schlarb, H. Schulte-Schrepping, Th. Tschentscher, J. Schneider, D. von der Linde, O. Hignette, F. Sette, H. N. Chapman, R. W. Lee, T. N. Hansen, S. Techert, J. S. Wark, M. Bergh, G. Huldt, D. van der Spoel, N. Timneanu, J. Hajdu, R. A. Akre, E. Bong, P. Krejcik, J. Arthur, S. Brennan, K. Luening, and J. B. Hastings. Atomic-scale visualization of inertial dynamics. *Science*, 308(5720):392–395, 2005.

[50] D. M. Fritz, D. A. Reis, B. Adams, R. A. Akre, J. Arthur, C. Blome, P. H. Bucksbaum, A. L. Cavalieri, S. Engemann, S. Fahy, R. W. Falcone, P. H. Fuoss, K. J. Gaffney, M. J. George, J. Hajdu, M. P. Hertlein, P. B. Hillyard, M. Horn-von Hoegen, M. Kammler, J. Kaspar, R. Kienberger, P. Krejcik, S. H. Lee, A. M. Lindenberg, B. McFarland, D. Meyer, T. Montagne, E. D. Murray, A. J. Nelson, M. Nicoul, R. Pahl, J. Rudati, H. Schlarb, D. P. Siddons, K. Sokolowski-Tinten, Th. Tschentscher, D. von der Linde, and J. B. Hastings. Ultrafast bond softening in bismuth: Mapping a solid's interatomic potential with x-rays. *Science*, 315(5812):633–636, 2007.

[51] A. M. Lindenberg, I. Kang, S. L. Johnson, T. Missalla, P. A. Heimann, Z. Chang, J. Larsson, P. H. Bucksbaum, H. C. Kapteyn, H. A. Padmore, R. W. Lee, J. S. Wark, and R. W. Falcone. Time-resolved x-ray diffraction from coherent phonons during a laser-induced phase transition. *Phys. Rev. Lett.*, 84(1):111–114, 2000.

[52] D. A. Reis, M. F. DeCamp, P. H. Bucksbaum, R. Clarke, E. Dufresne, M. Hertlein, R. Merlin, R. Falcone, H. Kapteyn, M. M. Murnane, J. Larsson, Th. Missalla, and J. S. Wark. Probing impulsive strain propagation with x-ray pulses. *Phys. Rev. Lett.*, 86(14):3072–3075, 2001.

[53] M. Bargheer, N. Zhavoronkov, Y. Gritsai, J. C. Woo, D. S. Kim, M. Woerner, and T. Elsaesser. Coherent atomic motions in a nanostructure studied by femtosecond x-ray diffraction. *Science*, 306(5702):1771–1773, 2004.

[54] M. Combescot and J. Bok. Instability of the electron-hole plasma in silicon. *Phys. Rev. Lett.*, 48(20):1413–1416, 1982.

[55] P. Stampfli and K. H. Bennemann. Theory for the instability of the diamond structure of Si, Ge, and C induced by a dense electron-hole plasma. *Phys. Rev. B*, 42(11):7163–7173, 1990.

[56] P. Stampfli and K. H. Bennemann. Time dependence of the laser-induced femtosecond lattice instability of Si and GaAs: Role of longitudinal optical distortions. *Phys. Rev. B*, 49(11):7299–7305, 1994.

[57] K. H. Bennemann. Ultrafast dynamics in solids. *J. Phys.: Condens. Matter*, 16(30):R995, 2004.

[58] P. L. Silvestrelli, A. Alavi, M. Parrinello, and D. Frenkel. Ab initio molecular dynamics simulation of laser melting of silicon. *Phys. Rev. Lett.*, 77(15):3149–3152, 1996.

[59] R. Car and M. Parrinello. Unified approach for molecular dynamics and density-functional theory. *Phys. Rev. Lett.*, 55(22):2471–2474, 1985.

[60] P. L. Silvestrelli, A. Alavi, M. Parrinello, and D. Frenkel. Structural, dynamical, electronic, and bonding properties of laser-heated silicon: An ab initio molecular-dynamics study. *Phys. Rev. B*, 56(7):3806–3812, 1997.

[61] I. Štich, R. Car, and M. Parrinello. Bonding and disorder in liquid silicon. *Phys. Rev. Lett.*, 63(20):2240–2243, 1989.

[62] A. Cavalleri, Cs. Tóth, C. W. Siders, J. A. Squier, F. Ráksi, P. Forget, and J. C. Kieffer. Femtosecond structural dynamics in VO_2 during an ultrafast solid-solid phase transition. *Phys. Rev. Lett.*, 87(23):237401, 2001.

[63] R. Saito, G. Dresselhaus, and M. S. Dresselhaus. *Physical Properties Of Carbon Nanotubes*. Imperial College Press, 1998.

[64] F. P. Bundy. Pressure-temperature phase diagram of elemental carbon. *Physica A*, 156:169–178, 1989.

[65] F. P. Bundy, H. T. Hall, H. M. Strong, and R. H. Wentorf. Man-made diamonds. *Nature*, 176:51–55, 1955.

[66] H. P. Bovenkerk, F. P. Bundy, H. T. Hall, H. M. Strong, and R. H. Wentorf. Preparation of diamond. *Nature*, 184:1094–1098, 1959.

[67] P. S. DeCarli and J. C. Jamieson. Formation of diamond by explosive shock. *Science*, 133(3467):1821–1822, 1961.

[68] F. P. Bundy and J. S. Kasper. Hexagonal diamond - a new form of carbon. *J. Chem. Phys.*, 46:3437–3446, 1967.

[69] M. C. Polo, J. Cifre, G. Sánchez, R. Aguiar, M. Varela, and J. Esteve. Pulsed laser deposition of diamond from graphite targets. *Appl. Phys. Lett.*, 67(4):485–487, 1995.

[70] W. L. Mao, H.-K. Mao, P. J. Eng, T. P. Trainor, M. Newville, C.-C Kao, D. L. Heinz, J. Shu, Y. Meng, and R. J. Hemley. Bonding changes in compressed superhard graphite. *Science*, 302:425–427, 2003.

[71] S. Fahy, S. G. Louie, and M. L. Cohen. Pseudopotential total-energy study of the transition from rhombohedral graphite to diamond. *Phys. Rev. B*, 34(2):1191–1199, 1986.

[72] G. W. Yang and J. B. Wang. Pulsed-laser-induced transformation path of graphite to diamond via an intermediate rhombohedral graphite. *Appl. Phys. A*, 72(4):475–479, 2001.

[73] S. Scandolo, M. Bernasconi, G. L. Chiarotti, P. Focher, and E. Tosatti. Pressure-induced transformation path of graphite to diamond. *Phys. Rev. Lett.*, 74:4015–4018, 1995.

[74] W. R. L. Lambrecht, C. H. Lee, B. Segall, J. C. Angus, Z. Li, and M. Sunkara. Diamond nucleation by hydrogenation of the edges of graphitic precursors. *Nature*, 364:607–610, 1993.

[75] A. D. Vita, Galli G, A. Canning, and R. Car. A microscopic model for surface-induced diamond-to-graphite transitions. *Nature*, 379:523–526, 1996.

[76] F. Banhart and P. M. Ajayan. Carbon onions as nanoscopic pressure cells for diamond formation. *Nature*, 382:433, 1996.

[77] F. Banhart. The transformation of graphitic onions to diamond under electron irradiation. *J. Appl. Phys.*, 81(8):3440–3445, 1997.

[78] Y. Lyutovich and F. Banhart. Low-pressure transformation of graphite to diamond under irradiation. *Appl. Phys. Lett.*, 74(5):659–660, 1999.

[79] Y. Miyamoto. Ultrafast reconstruction of graphite by irradiating with highly charged ions. *Appl. Phys. Lett.*, 91(11):113120, 2007.

[80] T. Mishina, K. Nitta, and Y. Masumoto. Coherent lattice vibration of interlayer shearing mode of graphite. *Phys. Rev. B*, 62(4):2908–2911, 2000.

[81] T. Kampfrath, L. Perfetti, F. Schapper, C. Frischkorn, and M. Wolf. Strongly coupled optical phonons in the ultrafast dynamics of the electronic energy and current relaxation in graphite. *Phys. Rev. Lett*, 95:187403, 2005.

[82] J. Kanasaki, E. Inami, K. Tanimura, H. Ohnishi, and K. Nasu. Formation of sp^3-bonded carbon nanostructures by femtosecond laser excitation of graphite. *Phys. Rev. Lett.*, 102:087402, 2009.

[83] U. Kreibig and M. Vollmer. *Optical Properties of Metal Clusters.* Springer, 1995.

[84] N. Yamamoto, K. Araya, and F. J. García de Abajo. Photon emission from silver particles induced by a high-energy electron beam. *Phys. Rev. B*, 64(20):205419, 2001.

[85] K. L. Kelly, E. Coronado, L. L. Zhao, and G. C. Schatz. The optical properties of metal nanoparticles: The influence of size, shape, and dielectric environment. *J. Phys. Chem. B*, 107(3):668–677, 2003.

[86] W. L. Barnes, A. Dereux, and T. W. Ebbesen. Surface plasmon subwavelength optics. *Nature*, 424:824–830, 2003.

[87] S. Link and M. A. El-Sayed. Spectral properties and relaxation dynamics of surface plasmon electronic oscillations in gold and silver nanodots and nanorods. *J. Phys. Chem. B*, 103(40):8410–8426, 1999.

[88] G. V. Hartland. Measurements of the material properties of metal nanoparticles by time-resolved spectroscopy. *Phys. Chem. Chem. Phys.*, 6:5263–5274, 2004.

[89] C. Voisin, D. Christofilos, N. Del Fatti, F. Vallée, B. Prével, E. Cottancin, J. Lermé, M. Pellarin, and M. Broyer. Size-dependent electron-electron interactions in metal nanoparticles. *Phys. Rev. Lett.*, 85(10):2200–2203, 2000.

[90] R. Jin. Controlling anisotropic nanoparticle growth through plasmon excitation. *Nature*, 425:487–490, 2003.

[91] S. Nie and S. R. Emory. Probing single molecules and single nanoparticles by surface-enhanced raman scattering. *Science*, 275:1102–1106, 1997.

[92] A. J. Haes and R. P. Van Duyne. A nanoscale optical biosensor: Sensitivity and selectivity of an approach based on the localized surface plasmon resonance spectroscopy of triangular silver nanoparticles. *J. Am. Chem. Soc.*, 124(35):10596–10604, 2002.

[93] N. Del Fatti, C. Voisin, F. Chevy, F. Vallée, and C. Flytzanis. Coherent acoustic mode oscillation and damping in silver nanoparticles. *J. Chem. Phys.*, 110(23):11484–11487, 1999.

[94] G. V. Hartland. Coherent excitation of vibrational modes in metallic nanoparticles. *Annu. Rev. Phys. Chem.*, 57:403–430, 2006.

[95] C.-K. Sun, F. Vallée, L. H. Acioli, E. P. Ippen, and J. G. Fujimoto. Femtosecond-tunable measurement of electron thermalization in gold. *Phys. Rev. B*, 50(20):15337–15348, 1994.

[96] J. H. Hodak, I. Martini, and G. V. Hartland. Spectroscopy and dynamics of nanometer-sized noble metal particles. *J. Phys. Chem. B*, 102(36):6958–6967, 1998.

[97] C. Voisin, N. Del Fatti, D. Christofilos, and F. Vallée. Ultrafast electron dynamics and optical nonlinearities in metal nanoparticles. *J. Phys. Chem. B*, 105(12):2264–2280, 2001.

[98] J. Lehmann, M. Merschdorf, W. Pfeiffer, A. Thon, S. Voll, and G. Gerber. Surface plasmon dynamics in silver nanoparticles studied by femtosecond time-resolved photoemission. *Phys. Rev. Lett.*, 85:2921–2924, 2000.

[99] P. V. Kamat, M. Flumiani, and G. V. Hartland. Picosecond dynamics of silver nanoclusters. photoejection of electrons and fragmentation. *J. Phys. Chem. B*, 102:3123–3128, 1998.

[100] A. Takami, H. Kurita, and S. Koda. Laser-induced size reduction of noble metal particles. *J. Phys. Chem. B*, 103:1226–1232, 1999.

[101] S. Inasawa, M. Sugiyama, and Y.J. Yamaguchi. Laser-induced shape transformation of gold nanoparticles below the melting point: The effect of surface melting. *J. Phys. Chem. B.*, 109:3104–3111, 2005.

[102] K. Yamada, Y. Tokumoto, T. Nagata, and F. J. Mafuné. Mechanism of laser-induced size-reduction of gold nanoparticles as studied by nanosecond transient absorption spectroscopy. *J. Phys. Chem. B*, 110(24):11751–11756, 2006.

[103] S. Link, C. Burda, B. Nikoobakht, and M. A. El-Sayed. Laser-induced shape changes of colloidal gold nanorods using femtosecond and nanosecond laser pulses. *J. Phys. Chem. B*, 104:6152–6163, 2000.

[104] A. Plech, V. Kotaidis, M. Lorenc, and J. Boneberg. Femtosecond laser near-field ablation from gold nanoparticles. *Nat. Phys.*, 2:44–47, 2006.

[105] C. B. Schaffer, A. Brodeur, and E. Mazur. Laser-induced breakdown and damage in bulk transparent materials induced by tightly focused femtosecond laser pulses. *Meas. Sci. Tech.*, 12:1784–1794, 2001.

[106] C. Guo, G. Rodriguez, A. Lobad, and A. J. Taylor. Structural phase transition of aluminum induced by electronic excitation. *Phys. Rev. Lett.*, 84(19):4493–4496, 2000.

[107] J. Miao, T. Ishikawa, B. Johnson, E. H. Anderson, B. Lai, and K. O. Hodgson. High resolution 3D x-ray diffraction microscopy. *Phys. Rev. Lett.*, 89(8):088303, 2002.

[108] K. J. Gaffney and H. N. Chapman. Imaging atomic structure and dynamics with ultrafast x-ray scattering. *Science*, 316(5830):1444–1448, 2007.

[109] M. M. Qazilbash, M. Brehm, Byung-Gyu Chae, P.-C. Ho, G. O. Andreev, Bong-Jun Kim, Sun Jin Yun, A. V. Balatsky, M. B. Maple, F. Keilmann, Hyun-Tak Kim, and D. N. Basov. Mott transition in VO_2 revealed by infrared spectroscopy and nano-imaging. *Science*, 318:1750–1753, 2007.

[110] C.-Y. Ruan, Y. Murooka, R. K. Raman, R. A. Murdick, R. J. Worhatch, and A. Pell. The development and applications of ultrafast electron nanocrystallography. *Microsc. Microanal.*, 15:323–337, 2009.

[111] R. Srinivasan, V.A. Lobastov, C.-Y Ruan, and A. H. Zewail. Ultrafast electron diffraction (UED). a new development for the 4D determination of transient molecular structures. *Helv. Chim. Acta*, 86:1761–1799, 2003.

[112] J. R. Dwyer, C. T. Hebeisen, R. Ernstorfer, V. B. Deyirmenjian, R. E. Jordan, and R. J. D. Miller. Femtosecond electron diffraction: making the molecular movie. *Phil. Trans. R. Soc. A*, 364:741–778, 2006.

[113] C.-Y. Ruan, F. Vigliotti, V. A. Lobastov, S. Chen, and A. H. Zewail. Ultrafast electron crystallography: Transient structures of molecules, surfaces, and phase transitions. *Proc. Nat. Acad. Sci. U.S.A*, 101(5):1123–1128, 2004.

[114] V. A. Lobastov, R. Srinivasan, and A. H. Zewail. Four-dimensional ultrafast electron microscopy. *Proc. Natl. Acad. Sci. USA*, 102:7069 - 7073, 2005.

[115] W. E. King, G. H. Campbell, A. Frank, B. W. Reed, J. F. Schmerge, B. J. Siwick, B. C. Stuart, and P. M. Weber. Ultrafast electron microscopy in materials science, biology, and chemistry. *J. Appl. Phys.*, 97(11):111101, 2005.

[116] J. M. Cowley. *Diffraction Physics, 3^{rd} Ed.* Elsevier, 1995.

[117] N. W. Ashcroft and N. D. Mermin. *Solid State Physics.* Brooks / Cole, 1976.

[118] C. Kittel. *Introduction to Solid State Physics, 7^{th} Ed.* John Wiley & Sons, 1995.

[119] A. Ichimiya and P. I. Cohen. *Reflection High Energy Electron Diffraction.* Cambridge University Press, UK, 2004.

[120] Z. L. Wang. *Reflection Electron Microscopy and Spectroscopy for Surface Analysis.* Cambridge University Press, UK, 1996.

[121] R. Suryana, A. Ichimiya, H. Nakahara, and Y. Saito. Surface morphology of the Si(111) surface induced by co-deposition of Si and CH_4. *J. Cryst. Growth*, 301-302:349 – 352, 2007. 14th International Conference on Molecular Beam Epitaxy - MBE XIV.

[122] P. A. Doyle and P. S. Turner. Relativistic Hartree-Fock x-ray and electron scattering factors. *Acta Cryst. A*, 24:390–397, 1968.

[123] B. E. Warren. *X-Ray Diffraction.* Dover, New York, 1990.

[124] T. Egami and S. J. L. Billinge. *Underneath the Bragg Peaks: Structural Analysis Of Complex Materials.* Pergamon Press/Elsevier, Oxford/England, 2003.

[125] C. L. Farrow, C.-Y. Ruan, and S. J. L. Billinge. Quantitative nanoparticle structures from electron crystallography data. *Phys. Rev. B*, 81(13):134104, 2010.

[126] C.-Y. Ruan, Y. Murooka, R.K. Raman, and R.A. Murdick. Dynamics of size-selected gold nanoparticles studied by ultrafast electron nanocrystallography. *Nano Lett.*, 7(5):1290–1296, 2007.

[127] O. Bostanjoglo and Th. Rosin. Ultrasonically induced magnetic reversals observed by stroboscopic electron microscopy. *Opt. Acta.*, 24(6):657–664, 1977.

[128] O. Bostanjoglo, R. P. Tornow, and W. Tornow. Nanosecond transmission electron microscopy and diffraction. *J. Phys. E*, 20(5):556, 1987.

[129] G. Mourou and S. Williamson. Picosecond electron diffraction. *Appl. Phys. Lett.*, 41(1):44–45, 1982.

[130] S. Williamson, G. Mourou, and J. C. M. Li. Time-resolved laser-induced phase transformation in aluminum. *Phys. Rev. Lett.*, 52(26):2364–2367, 1984.

[131] J. C. Williamson and A. H. Zewail. Structural femtochemistry: experimental methodology. *Proc. Nat. Acad. Sci. U.S.A*, 88(11):5021–5025, 1991.

[132] J. C. Williamson, M. Dantus, S. B. Kim, and A. H. Zewail. Ultrafast diffraction and molecular structure. *Chem. Phys. Lett.*, 196(6):529 – 534, 1992.

[133] J. D. Ewbank, W. L. Faust, J. Y. Luo, J. T. English, D. L. Monts, D. W. Paul, Q. Dou, and L. Schäfer. Instrumentation for gas electron diffraction employing a pulsed electron beam synchronous with photoexcitation. *Rev. Sci. Instrum.*, 63(6):3352–3358, 1992.

[134] J. C. Williamson, J. Cao, H. Ihee, H. Frey, and A. H. Zewail. Clocking transient chemical changes by ultrafast electron diffraction. *Nature*, 386:159–162, 1997.

[135] R. C. Dudek and P. M. Weber. Ultrafast diffraction imaging of the electrocyclic ring-opening reaction of 1,3-cyclohexadiene. *J. Phys. Chem. A*, 105(17):4167–4171, 2001.

[136] P. Reckenthaeler, M. Centurion, W. Fuss, S. A. Trushin, F. Krausz, and F. E. Fill. Time-resolved electron diffraction from selectively aligned molecules. *Phys. Rev. Lett.*, 102(21):213001, May 2009.

[137] J. C. Williamson and A. H. Zewail. Ultrafast electron diffraction. 4. molecular structures and coherent dynamics. *J. Phys. Chem.*, 98(11):2766–2781, 1994.

[138] M. Dantus, S. B. Kim, J. C. Williamson, and A. H. Zewail. Ultrafast electron diffraction. 5. experimental time resolution and applications. *J. Phys. Chem.*, 98(11):2782–2796, 1994.

[139] H. Ihee, J. Cao, and A. H. Zewail. Ultrafast electron diffraction: structures in dissociation dynamics of $Fe(CO)_5$. *Chemical Physics Letters*, 281(1-3):10 – 19, 1997.

[140] C.-Y. Ruan, V. A. Lobastov, R. Srinivasan, B. M. Goodson, H. Ihee, and A. H. Zewail. Ultrafast diffraction and structural dynamics: The nature of complex molecules far from equilibrium. *Proc. Nat. Acad. Sci. U.S.A*, 98(13):7117–7122, 2001.

[141] H. Ihee, V. Lobastov, U. M. Gomez., B. M. Goodson, R. Srinivasan, C.-Y. Ruan, and A. H. Zewail. Direct imaging of transient molecular structures with ultrafast diffraction. *Science*, 291(5503):458–462, 2001.

[142] C-Y. Ruan, V. A. Lobastov, F. Vigliotti, S. Chen, and A. H. Zewail. Ultrafast electron crystallography of interfacial water. *Science*, 304:5667, 2004.

[143] S. Chen, M. T. Seidel, and A. H. Zewail. Atomic-scale dynamical structures of fatty acid bilayers observed by ultrafast electron crystallography. *Proc. Nat. Acad. Sci. U.S.A*, 102(25):8854–8859, 2005.

[144] F. Carbone, P. Baum, P. Rudolf, and A. H. Zewail. Structural preablation dynamics of graphite observed by ultrafast electron crystallography. *Phys. Rev. Lett.*, 100(3):035501, 2008.

[145] D.-S. Yang and A. H. Zewail. Ordered water structure at hydrophobic graphite interfaces observed by 4D, ultrafast electron crystallography. *Proc. Natl. Acad. Sci. USA*, 106(11):4122–4126, 2009.

[146] B. J. Siwick, J. R. Dwyer, R. E. Jordan, and R. J. D. Miller. Ultrafast electron optics: Propagation dynamics of femtosecond electron packets. *J. Appl. Phys.*, 92:1643–1648, 2002.

[147] J. Cao, Z. Hao, H. Park, C. Tao, D. Kau, and L. Blaszczyk. Femtosecond electron diffraction for direct measurement of ultrafast atomic motions. *Appl. Phys. Lett.*, 83(5):1044–1046, 2003.

[148] J. B. Hastings, F. M. Rudakov, D. H. Dowell, J. F. Schmerge, J. D. Cardoza, J. M. Castro, S. M. Gierman, H. Loos, and P. M. Weber. Ultrafast time-resolved electron diffraction with megavolt electron beams. *Appl. Phys. Lett.*, 89(18):184109, 2006.

[149] R. Ernstorfer, M. Harb, C. T. Hebeisen, G. Sciaini, T. Dartigalongue, and R. J. D. Miller. The formation of warm dense matter: Experimental evidence for electronic bond hardening in gold. *Science*, 323(5917):1033–1037, 2009.

[150] P. Musumeci, J. T. Moody, C. M. Scoby, M. S. Gutierrez, and T. Tran. RF streak camera based ultrafast relativistic electron diffraction. *Rev. Sci. Instrum.*, 80(1):013302, 2009.

[151] J. S. Kim, T. LaGrange, B. W. Reed, M. L. Taheri, M. R. Armstrong, W. E. King, N. D. Browning, and G. H. Campbell. Imaging of transient structures using nanosecond *in situ* TEM. *Science*, 321(5895):1472–1475, 2008.

[152] A. H. Zewail. *4D Electron Microscopy. Imaging in Space and Time.* Imperial College Press, 2010.

[153] R. K. Raman, Y. Murooka, C.-Y. Ruan, T. Yang, S. Berber, and D. Tománek. Direct observation of optically induced transient structures in graphite using ultrafast electron crystallography. *Phys. Rev. Lett.*, 101(7):077401, 2008.

[154] R. A. Murdick, R. K. Raman, Y. Murooka, and C.-Y. Ruan. Photovoltage dynamics of the hydroxylated Si(111) surface investigated by ultrafast electron diffraction. *Phys. Rev. B*, 77(24):245329, 2008.

[155] C. Rullière, editor. *Femtosecond Laser Pulses: Principles and Experiments.* Springer, New York, 2005.

[156] R. A. Murdick. *Investigations on interfacial dynamics with ultrafast electron diffraction.* PhD thesis, Michigan State University, 2009.

[157] S. G. Anderson, P. Musumeci, J. B. Rosenzweig, W. J. Brown, R. J. England, M. Ferrario, J. S. Jacob, M. C. Thompson, G. Travish, A. M. Tremaine, and R. Yoder. Velocity bunching of high-brightness electron beams. *Phys. Rev. ST Accel. Beams*, 8(1):014401, 2005.

[158] T. van Oudheusden, E. F. de Jong, S. B. van der Geer, W. P. E. M. Op 't Root, O. J. Luiten, and B. J. Siwick. Electron source concept for single-shot sub-100 fs electron diffraction in the 100 keV range. *J. Appl. Phys.*, 102(9):093501, 2007.

[159] P. Baum and A. H. Zewail. Breaking resolution limits in ultrafast electron diffraction and microscopy. *Proc. Natl. Acad. Sci. USA*, 103(44):16105–16110, 2006.

[160] A. H. Zewail. Four-dimensional electron microscopy. *Science*, 328(5975):187–193, 2010.

[161] G. S. Chottiner, W. D. Jennings, and K. I. Pandya. A flexible sample transfer/insertion system for ultrahigh vacuum surface studies. *J. Vac. Sci. Technol. A*, 5:2970, 1987.

[162] H. Ehrenreich, H. R. Philipp, and B. Segall. Optical properties of aluminum. *Phys. Rev.*, 132(5):1918–1928, 1963.

[163] A. AydIn. Monte Carlo calculations of electrons in aluminum. *Appl. Radiat. Isot.*, 67(2):281 - 286, 2009.

[164] S. I. Ashitkov, M. B. Agranat, P. S. Kondratenko, S. I. Anisimov, V. E. Fortov, V. V. Temnov, K. Sokolowski-Tinten, P. Zhou, and D. von der Linde. Ultrafast structural transformations in graphite. *JETP Lett.*, 75(2):87–90, 2002.

[165] D. H. Reitze, H. Ahn, and M. C. Downer. Optical properties of liquid carbon measured by femtosecond spectroscopy. *Phys. Rev. B*, 45(6):2677–2693, 1992.

[166] K. Ishioka, M. Hase, M. Kitajima, and K. Ushida. Ultrafast carrier and phonon dynamics in ion-irradiated graphite. *Appl. Phys. Lett.*, 78(25):3965–3967, 2001.

[167] H. Park, X. Wang, S. Nie, R. Clinite, and J. Cao. Direct and real-time probing of both coherent and thermal lattice motions. *Solid State Commun.*, 136:559–563, 2005.

[168] A. Janzen, B. Krenzer, P. Zhou, D. von der Linde, and M. Horn-von Hoegen. Ultrafast electron diffraction at surfaces after laser excitation. *Surf. Sci.*, 600(18):4094–4098, 2006.

[169] B. T. Kelly. *Physics Of Graphite.* Applied Science, London, UK, 1981.

[170] J. H. Neave, B. A. Joyce, P. J. Dobson, and N. Norton. Dynamics of film growth of GaAs by MBE from RHEED observations. *Appl. Phys. A*, 31(1):1–8, 1983.

[171] G. P. Thomson. The effect of refraction on electron diffraction. *Phil. Mag.*, 6(38):939–942, 1928.

[172] L. Sturkey and L. K. Frevel. Refraction effects in electron diffraction. *Phys. Rev.*, 68(1-2):56–57, 1945.

[173] J. M. Cowley and A. L. G. Rees. Refraction effects in electron diffraction. *Proc. Phys. Soc.*, 59(2):287, 1947.

[174] E. Fitzer and U. Funk. Determination of thermal vibration amplitudes in graphite using integrated x-ray intensities correcred for thermal diffuse scattering. *Carbon*, 16:85–88, 1978.

[175] J. B. Nelson and D. P. Riley. The thermal expansion of graphite from 15°C to 800°C: part I. Experimental. *Proc. Phys. Soc.*, 57(6):477, 1945.

[176] E. A. Kellett and B. P. Richards. The *c*-axis thermal expansion of carbons and graphites. *J. Appl. Cryst.*, 4(1):1–8, 1971.

[177] X. Gonze, J. M. Beuken, R. Caracas, F. Detraux, M. Fuchs, G. M. Rignanese, L. Sindic, M. Verstraete, G. Zerah, F. Jollet, M. Torrent, A. Roy, M. Mikami, Ph. Ghosez, J. Y. Raty, and D. C. Allan. First-principles computation of material properties: the ABINIT software project. *Comput. Mat. Sci.*, 25(3):478 - 492, 2002.

[178] Y. Miyamoto, A. Rubio, and D. Tománek. Real-time ab initio simulations of excited carrier dynamics in carbon nanotubes. *Phys. Rev. Lett.*, 97(12):126104, 2006.

[179] J. M. Soler, E. A., J. D. Gale, A. García, J. Junquera, P. Ordejón, and D. Sánchez-Portal. The SIESTA method for ab initio order-n materials simulation. *J. Phys.: Condens. Matter*, 14:2745–2779, 2002.

[180] S. Passlack, S. Mathias, O. Andreyev, D. Mittnacht, M. Aeschlimann, and M. Bauer. Space charge effects in photoemission with a low repetition, high intensity femtosecond laser source. *J. Appl. Phys.*, 100:024912, 2006.

[181] X. J. Zhou, B. Wannberg, W. L. Yang, V. Brouet, Z. Sun, J. F. Douglas, D. Dessau, Z. Hussain, and Z.-X. Shen. Space charge effect and mirror charge effect in photoemission spectroscopy. *J. Electron Spectrosc.*, 142:27 – 38, 2005.

[182] T. L. Gilton, J. P. Cowin, G. D. Kubiak, and A. V. Hamza. Intense surface photoemission: Space charge effects and self-acceleration. *J. Appl. Phys.*, 68:4802–4810, 1990.

[183] A. Kubo, K. Onda, H. Petek, Z. Sun, Y. S. Jung, and H. K. Kim. Femtosecond imaging of surface plasmon dynamics in a nanostructured silver film. *Nano. Lett.*, 5(6):1123–1127, 2005.

[184] F.-J. Meyer zu Heringdorf, L. I. Chelaru, S. Mllenbeck, D. Thien, and M. Horn von Hoegen. Femtosecond photoemission microscopy. *Surf. Sci.*, 601:4700 – 4705, 2007.

[185] V. Gerstner, A. Knoll, W. Pfeiffer, A. Thon, and G. Gerber. Femtosecond laser assisted scanning tunneling microscopy. *J. Appl. Phys.*, 88:4851–4859, 2000.

[186] A. Hanisch, B. Krenzer, T. Pelka, S. Möllenbeck, and M. Horn von Hoegen. Thermal response of epitaxial thin bi films on si(001) upon femtosecond laser excitation studied by ultrafast electron diffraction. *Phys. Rev. B*, 77:125410, 2008.

[187] S. A. Hilbert, C. Uiterwaal, B. Barwick, H. Batelaan, and A. H. Zewail. Temporal lenses for attosecond and femtosecond electron pulses. *Proc. Natl. Acad. Sci. USA*, 106:10558–10563, 2009.

[188] B. W. Reed. Femtosecond electron pulse propagation for ultrafast electron diffraction. *J. Appl. Phys.*, 100:034916, 2006.

[189] B.-L. Qian and H. E. Elsayed-Ali. Acceleration element for femtosecond electron pulse compression. *Phys. Rev. E*, 65:046502, 2002.

[190] C. T. Hebeisen, G. Sciaini, M. Harb, R. Ernstorfer, T. Dartigalongue, S. G. Kruglik, and R. J. D. Miller. Grating enhanced ponderomotive scattering for visualization and full characterization of femtosecond electron pulses. *Opt. Express*, 16:3334–3341, 2008.

[191] H. Park and J. M. Zuo. Direct measurement of transient electric fields induced by ultrafast pulsed laser irradiation of silicon. *Appl. Phys. Lett.*, 94:251103, 2009.

[192] C. T. Hebeisen, G. Sciaini, M. Harb, R. Ernstorfer, S. G. Kruglik, and R. J. D. Miller. Direct visualization of charge distributions during femtosecond laser ablation of a Si (100) surface. *Phys. Rev. B*, 78:081403, 2008.

[193] D. M. Riffe, X. Y. Wang, M. C. Downer, D. L. Fisher, T. Tajima, J. L. Erskine, and R. M. More. Femtosecond thermionic emission from metals in the space-charge-limited regime. *J. Opt. Soc. Am. B*, 10:1424–1435, 1993.

[194] V. M. Silkin, J. Zhao, F. Guinea, E. V. Chulkov, P. M. Echenique, and H. Petek. Image potential states in graphene. *Phys. Rev. B*, 80(12):121408, 2009.

[195] F. Carbone, O.-H. Kwon, and A. H. Zewail. Dynamics of chemical bonding mapped by energy-resolved 4D electron microscopy. *Science*, 325:181–184, 2009.

[196] D. H. Reitze, X. Wang, H. Ahn, and M. C. Downer. Femtosecond laser melting of graphite. *Phys. Rev. B*, 40(17):11986–11989, 1989. b.

[197] K. Seibert, G. C. Cho, W. Kütt, H. Kurz, D. H. Reitze, J. I. Dadap, H. Ahn, M. C. Downer, and A. M. Malvezzi. Femtosecond carrier dynamics in graphite. *Phys. Rev. B*, 42(5):2842–2851, 1990.

[198] G. Moos, C. Gahl, R. Fasel, M. Wolf, and T. Hertel. Anisotropy of quasiparticle lifetimes and the role of disorder in graphite from ultrafast time-resolved photoemission spectroscopy. *Phys. Rev. Lett.*, 87(26):267402, 2001.

[199] M. Breusing, C. Ropers, and T. Elsaesser. Ultrafast carrier dynamics in graphite. *Phys. Rev. Lett.*, 102(8):086809, 2009.

[200] R. W. Newson, J. Dean, B. Schmidt, and H. M. van Driel. Ultrafast carrier kinetics in exfoliated graphene and thin graphite films. *Opt. Express*, 17(4):2326–2333, 2009.

[201] J. M. Dawlaty, S. Shivaraman, Mvs. Chandrashekhar, F. Rana, and M. G. Spencer. Measurement of ultrafast carrier dynamics in epitaxial graphene. *Appl. Phys. Lett.*, 92(4):042116, 2008.

[202] H. Yan, D. Song, K. F. Mak, I. Chatzakis, J. Maultzsch, and T. F. Heinz. Time-resolved raman spectroscopy of optical phonons in graphite: Phonon anharmonic coupling and anomalous stiffening. *Phys. Rev. B*, 80(12):121403, 2009.

[203] K. Nasu. sp^3 domain in graphite by visible light and photoinduced phase transitions. *Eur. Phys. J. B*, 75:415430, 2010.

[204] M. Huang, F. Zhao, Y. Cheng, N. Xu, and Z. Xu. Mechanisms of ultrafast laser-induced deep-subwavelength gratings on graphite and diamond. *Phys. Rev. B*, 79(12):125436, 2009.

[205] E.C. Samano, G. Soto, A. Olivas, and L. Cota. Dlc thin films characterized by aes, xps and eels. *Appl. Surf. Sci.*, 202:1–7, 2002.

[206] F. Tuinstra and J. L. Koenig. Raman spectrum of graphite. *J. Chem. Phys.*, 53(3):1126–1130, 1970.

[207] W. A. Yarbrough, A. R. Badzian, D. Pickrell, Y. Liou, and A. Inspektor. Diamond deposition at low substrate temperatures. *J. Cryst. Growth*, 99(1-4, Part 2):1177 - 1182, 1990.

[208] S. R. P. Silva, G. A. J. Amaratunga, E. K. H. Salje, and K. M. Knowles. Evidence of hexagonal diamond in plasma-deposited carbon films. *J. Mat. Sci.*, 29(19):4962–4966, 1994.

[209] C. Z. Wang and K. M. Ho. Structure, dynamics, and electronic properties of diamondlike amorphous carbon. *Phys. Rev. Lett.*, 71(8):1184–1187, 1993.

[210] T. C. Gunaratne, X. Zhu, V. V. Lozovoy, and M. Dantus. Influence of the temporal shape of femtosecond pulses on silicon micromachining. *J. Appl. Phys.*, 106(12):123101, 2009.

[211] S. Biswas and L. T. Drzal. A novel approach to create a highly ordered monolayer film of graphene nanosheets at the liquid-liquid interface. *Nano. Lett.*, 9:167–172, 2009.

[212] A. Plech, S. Gresillon, G.von Plessen, K. Scheidt, and G. Naylor. Structural kinetics of laser-excited metal nanoparticles supported on a surface. *Chem. Phys.*, 299(2-3):183–191, 2004.

[213] J. M. Gunn, M. Ewald, and M. Dantus. Remote two-photon emission from dendritic silver nanoclusters. *Microsc. and Microanal.*, 12:630–631, 2006.

[214] M. Ya. Schelev, M. C. Richardson, and A. J. Alcock. Image-converter streak camera with picosecond resolution. *Appl. Phys. Lett.*, 18:354–357, 1971.

[215] B. J. Siwick, J. R. Dwyer, R. E. Jordan, and R. J. D. Miller. An atomic-level view of melting using femtosecond electron diffraction. *Science*, 302:1382–1385, 2003.

[216] V. L. Colvin, A. N. Goldstein, and A. P. Alivisatos. Semiconductor nanocrystals covalently bound to metal surfaces with self-assembled monolayers. *J. Am. Chem. Soc.*, 114:5221–5230, 1992.

[217] K. C. Grabar, P. C. Smith, M. D. Musick, J. A. Davis, D. G. Walter, M. A. Jackson, A. P. Guthrie, and M. J. Natan. Kinetic control of interparticle spacing in au colloid-based surfaces: Rational nanometer-scale architecture. *J. Am. Chem. Soc.*, 118:1148–1153, 1996.

[218] T. Sato, D. G. Hasko, and H. Ahmed. Nanoscale colloidal particles: Monolayer organization and patterning. *J. Vac. Sci. Technol. B*, 15(1):45–48, 1997.

[219] T. Sato, H. Ahmed, D. Brown, and B. F. G. Johnson. Single electron transistor using a molecularly linked gold colloidal particle chain. *J. Appl. Phys.*, 82(2):696–701, 1997.

[220] S. L. Westcott, S. J. Oldenburg, T. R. Lee, and N. J. Halas. Formation and adsorption of clusters of gold nanoparticles onto functionalized silica nanoparticle surfaces. *Langmuir*, 14:5396–5401, 1998.

[221] T. Zhu, X. Fu, T. Mu, J. Wang, and Z. Liu. pH-dependent adsorption of gold nanoparticles on p-aminothiophenol-modified gold substrates. *Langmuir*, 15:5197–5199, 1999.

[222] R. R. Bhat, D. A. Fischer, and J. Genzer. Fabricating planar nanoparticle assemblies with number density gradients. *Langmuir*, 18:5640–5643, 220.

[223] W. Kern and D.A. Puotinen. Cleaning solutions based on hydrogen peroxide for use in silicon semiconductor technology. *RCA Review*, 31:187–206, 1970.

[224] W Kern, editor. *Handbook of Semiconductor Wafer Cleaning Technology - Science, Technology, and Applications.* William Andrew Publishing/Noyes, 1993.

[225] T. Sato, D. Brown, and B. F. G. Johnson. Nucleation and growth nano-gold colloidal lattices. *Chem. Commun.*, (11):1007–1008, 1997.

[226] T. Ishida, Y. Nakajima, J. Endo, D. Collard, and H. Fujita. Real-time transmission electron microscope observation of gold nanoclusters diffusing into silicon at room temperature. *Nanotechnology*, 20(6):065705, 2009.

[227] Y. Sun and Y. Xia. Shape-controlled synthesis of gold and silver nanoparticles. *Science*, 298(5601):2176–2179, 2002.

[228] N. Singh and P. K. Sharma. Debye-Waller factors of cubic metals. *Phys. Rev. B*, 3(4):1141–1148, 1971.

[229] Z. Wang, J. A. Carter, A. Lagutchev, Y. K. Koh, N.-H. Seong, D. G. Cahill, and D. D. Dlott. Ultrafast flash thermal conductance of molecular chains. *Science*, 317(5839):787–790, 2007.

[230] P. B. Hillyard, D. A. Reis, and K. J. Gaffney. Carrier-induced disordering dynamics in InSb studied with density functional perturbation theory. *Phys. Rev. B*, 77(19):195213, 2008.

[231] R. K. Raman, Z. Tao, T.-R. T. Han, and C.-Y. Ruan. Ultrafast imaging of photoelectron packets generated from graphite surface. *Appl. Phys. Lett.*, 95(18):181108, 2009.

[232] M. A. Uppal, A. Kafizas, T. H. Lim, and I. P. Parkin. The extended time evolution size decrease of gold nanoparticles formed by the Turkevich method. *New J. Chem.*, 34(7):140 –1407, 2010.

[233] H. Muto, K. Miyajima, and F. Mafune. Mechanism of laser-induced size reduction of gold nanoparticles as studied by single and double laser pulse excitation. *J. Phys. Chem. C*, 112:5810–5815, 2008.

[234] O. Gerben, P. Jóvári, L. Temleitner, and L. Pusztai. A new version of the RMC++ Reverse Monte Carlo programme, aimed at investigating the structure of covalent glasses. *J. Optoelectron. Adv. Mater.*, 9(10):3021–3027, 2007.

[235] R. J. Worhatch and C.-Y. Ruan. Unpublished work. 2010.

[236] R. L. McGreevy. Reverse monte carlo modelling. *J. Phys.: Condens. Matter*, 13(46):R877–R913, 2001.

[237] P. Grua, J. P. Morreeuw, H. Bercegol, G. Jonusauskas, and F. Vallée. Electron kinetics and emission for metal nanoparticles exposed to intense laser pulses. *Phys. Rev. B*, 68(3):035424, 2003.

[238] N. Del Fatti, C. Voisin, M. Achermann, S. Tzortzakis, D. Christofilos, and F. Vallée. Nonequilibrium electron dynamics in noble metals. *Phys. Rev. B*, 61:16956–16966, 2000.

[239] R. K. Raman, R. A. Murdick, R. J. Worhatch, Y. Murooka, S. D. Mahanti, T.-R. T. Han, and C.-Y. Ruan. Electronically driven fragmentation of silver nanocrystals revealed by ultrafast electron crystallography. *Phys. Rev. Lett.*, 104(12):123401, 2010.

[240] B. Barwick, H. S. Park, O.-H. Kwon, J. S. Baskin, and A. H. Zewail. 4D imaging of transient structures and morphologies in ultrafast electron microscopy. *Science*, 322(5905):1227–1231, 2008.

[241] A. Yurtsever and A. H. Zewail. 4D nanoscale diffraction observed by convergent-beam ultrafast electron microscopy. *Science*, 326(5953):708–712, 2009.

[242] B. Barwick, D. J. Flannigan, and A. H. Zewail. Photon-induced near-field electron microscopy. *Nature*, 462(7275):902–906, 2009.

[243] T. LaGrange, M. R. Armstrong, K. Boyden, C. G. Brown, G. H. Campbell, J. D. Colvin, W. J. DeHope, A. M. Frank, D. J. Gibson, F. V. Hartemann, J. S. Kim, W. E. King, B. J. Pyke, B. W. Reed, M. D. Shirk, R. M. Shuttlesworth, B. C. Stuart, B. R. Torralva, and N. D. Browning. Single-shot dynamic transmission electron microscopy. *Appl. Phys. Lett.*, 89(4):044105, 2006.

[244] T. LaGrange, G. H. Campbell, B.W. Reed, M. Taheri, J. B. Pesavento, J. S. Kim, and N. D. Browning. Nanosecond time-resolved investigations using the *in situ* of dynamic transmission electron microscope (*dtem*). *Ultramicroscopy*, 108(11):1441 – 1449, 2008.